A Thesis submitted for the degree of Doctor of Philosophy

A Cross Section Measurement of ν_μ Induced Charged-Current Coherent π^+ Production on Argon with the MicroBooNE Detector

Zachary G. R. Williams

May 2022

Department of Physics, University of Texas at Arlington

Contents

List of Figures

List of Tables

Acknowledgements

This is by far the most difficult thing that I have ever done in my life, and this was not at all possible without all of the love and support that I have received from my colleagues, family, and friends. I am going to acknowledge all of those who I feel deserve far more than my gratitude here.

I would like to firstly acknowledge my advisor, Dr. Jonathan Asaadi. There isn't a word for the level of patience that you have shown me during my time as your graduate student. It was an absolute pleasure to work with you, and I would not have gotten to this point without all of the great advice that you gave me. You always had either an answer to a question, or pointed me in the direction to find the answers for myself. You are a crazy busy person, and I still don't quite understand how you were able to get me through this program as well as everything else you were doing, too. I get to relish in the privileged role of being your very first graduate student through the PhD program, and I'm absolutely certain that you will have many more to follow. Thank you so much, Jonathan.

Next comes the acknowledgements for all of the colleagues I've received a tremendous amount of help from during my time working on the analysis presented in this thesis, which includes: Ryan LaZur, Ilker Parmaksiz, Elena Gramellini, Ben Jones, Jaehoon Yu, Hector Carranza, Cristian and Cristobal, Steven Gardiner, and Kirsty Duffy. I'm sure there's someone who has slipped my mind, but thank you all for your help and know I wouldn't have made it this far without it.

I am truly lucky to have the best friends a man could ever ask for and it is important to me that I thank them all here for helping me maintain my sanity during this endeavor, and I want them to know that they are indeed my chosen family. First, thank you Hunter Sullivan for sharing the burdens of graduate school with me as long as you did and for being the best friend I could ever ask for. You've always been someone I could turn to, and you've literally been there for me since the start of this journey. You helped me get through some dark times. Thank you Kelly Sullivan, for being one of the best gal pals I could have ever asked for and allowing me to rob you of time with your husband so often. And thank you again to Kelly and Hunter for making me and Humberto the godparents of your son, Bennett Sullivan, who I am also grateful for the many smiles he gave me during these last few months of graduate school. Thank you Kasey and Lera Holland for allowing Humberto and I to get away for much needed stress relief on the weekends to Chicago. It has meant the world to me to spend that time with you both. I spent the very start of graduate school flying to your wedding in Russia, and the last part of it we spent together with you both in Chicago. Thank you Austin Hickson for being one of my very best friends since sixth-grade (which I can't believe it's been that long) and continuing to help me to decompress at night after long days worrying about

neutrino physics with some video games, and for coming and visiting me up in the chilly north the multiple times you did.

Of course, it goes without saying that I wouldn't have made it this far at all without the tremendous amount of support from my family. I am so lucky to have two very supporting parents, Sharon Brim and Terry Williams, and I am so grateful for you both helping me as much as you have to get me through this. Thank you Mom for helping me with either laundry or food or moving or virtually anything a son could ever ask for. You mean the world to me. Thank you Dad for literally helping me pack up and move across the country in a u-haul together for 14+ hours, as well as always offering to help me with my homework. I also have two very supportive siblings that I love dearly and am so grateful for their love and support throughout this journey as well. Thank you Samuel John and Lauren Elizabeth. During the writing of this thesis I also spent a tremendous amount of time with my maternal grandparents: Nancy and Tommy Simpson. I am so incredibly grateful for your support as well, especially for allowing me to camp out at your house for two months during the writing of this thesis. You both mean the world to me, and I am so happy to finally finish this so you both could see me graduate. I love you all dearly.

I saved the best for last in the list of people who have gotten me here today, and this is the one person who I absolutely could not have done this without: my husband, Humberto Monsivais. You are the single most important thing in the world to me, and I can never thank you enough for all of the support and love and patience that you have shown me throughout this endeavor. You have been with me since the very beginning, and we've started a life together during the years that I've been in graduate school, and even gotten married during that time, too! You picked me back up during the many times that I wanted to give up, and you inspire me every day to be a better person and to work a little harder, because that's what you do yourself. The compassion and kindness you show is limitless, and you're the person that kept me going through it all. This work is something that I selfishly did for myself, but I dedicate it all to you, Humberto. Thank you for everything, and I can't wait to see where life takes us next.

To Humberto

Abstract

Neutrino-induced charged-current coherent pion production is an important channel for the study of neutrino-nucleus interactions. It is both a dangerous background for ν_e oscillation experiments, and a critical component required for precise understanding of neutrino-nucleus pion production in general.

This work performed a search for ν_μ-induced charged-current (CC) coherent pion production on argon in MicroBooNE from Fermilab's Booster Neutrino Beamline (BNB), which produces ν_μ with a mean energy of 0.823 GeV. A flux-integrated cross section measurement was made for this channel, and was found to be: $\sigma(\nu_\mu + Ar \to \mu^- + \pi^+ + Ar) = 1.12 \pm 0.253(\text{stat.}) \pm 0.728(\text{syst.}) \times 10^{-39}\text{cm}^2$.

1 Introduction

"Travel brings wisdom only to the wise. It renders the ignorant more ignorant than ever."

Joe Abercrombie, *Last Argument of Kings*

One of the most interesting developments in physics in the last 100 years was the proposal (in 1930) and subsequent discovery (in 1956) of the neutrino. The neutrino is electrically neutral, and nearly-massless, meaning that they only interact via the weak and gravitational forces, where these properties are the primary reasons that neutrinos are notoriously difficult to detect. There is an abundance of unanswered questions that the existence of neutrinos and their properties have raised over the past century, such as: what are their absolute masses? is the neutrino its own antiparticle? how many neutrino flavors are there? can neutrinos show the way to new, exotic particle physics beyond the standard model? It is now known that neutrinos come in three flavors (at least, there could very well be more): electron, muon, and tau. It is also now known that neutrinos propagate as mass eigenstates, which are themselves modeled as superpositions of the known flavor eigenstates. We also know the mass squared differences, Δm^2, between the three known flavor states, but we do not know their mass ordering (whether it is inverted, or normal). Beyond the information specified here, neutrinos remain largely mysterious.

The elusiveness of neutrinos have propagated the necessity of increasingly large, and increasingly more sensitive neutrino detectors. There are many such detectors (such as Cherenkov detectors), but the focus of this thesis will pertain to the liquid argon time projection chamber (LArTPC), a novel detector technology with excellent position resolution and calorimetric capabilities. Over the past several decades, this specific detector technology has rapidly developed to the point that LArTPCs are now the preferred technology for both current and next-generation neutrino detectors. The Short Baseline Neutrino (SBN) program at Fermi National Accelerator Laboratory (Fermilab) – containing the MicroBooNE, SBND, and ICARUS detectors – and the upcoming Deep Underground Neutrino Experiment (DUNE) all utilize or will utilize LArTPC technology. Due to their prevalence, and the plans for their use in next-generation neutrino experiments, a proper understanding of the LArTPC technology is vital for the ongoing research field of neutrino physics. Work that I have done on this detector technology will be presented in this thesis.

The MicroBooNE detector is a LArTPC situated along Fermilab's Booster Neutrino Beam (BNB) as a part of the SBN program. MicroBooNE's primary physics goal is to investigate the MiniBooNE low-energy excess (LEE) anomaly, but it will also pro-

vide valuable neutrino-nucleus cross section measurements, as well as LArTPC detector technology development and testing opportunities. MicroBooNE is the first hundred-tonne-scale LArTPC and the longest-running LArTPC experiment in the world (as of the composition of this thesis).

This thesis presents the results of the work that I accomplished during my time at UTA on LArTPCs, as well as an analysis using data collected by the MicroBooNE detector which sought to measure a neutrino-nucleus interaction cross section called: the flux-integrated cross section measurement of muon neutrino-induced charged-current coherent positive pion production on argon. This cross section measurement is important to understand due to coherent pion production being a potential background for appearance searches in future long-baseline neutrino oscillation experiments, as well as the fact that future long-baseline neutrino oscillation experiments will require percent level cross section uncertainties and this neutrino-nucleus interaction channel still has ambiguity at low neutrino energies. The last reason this cross section is important is that this interaction channel is interesting of its own accord, and furthering our understanding of this channel is pertinent for a full understanding of neutrino-induced coherent pion production in general.

The rest of this thesis is organized as follows: Chapter 2 presents a brief overview of neutrino physics, including historical context and the basic mathematical formalism, as well as the current state of neutrino physics. Chapter 3 presents the different forms of neutrino interactions and briefly outlines how they occur. Chapter 4 presents the theory of the main focus of this thesis, which is neutrino-induced charged-current coherent pion production, and also details the rather complicated history of the measurement of this interaction channel at low neutrino energies. Chapter 5 presents the operating principles of LArTPCs, as well as a brief historical overview of the detector technology, and discusses the work that I have done on and for LArTPCs during my time at UTA. Chapter 6 discusses the MicroBooNE detector, and Chapter 7 gives the important details for event reconstruction of neutrino interactions captured by the MicroBooNE detector. Chapter 8 follows with the details on how candidate data events are selected for this analysis, and Chapter 9 details the method of extraction for the flux-integrated cross section measurement of CC-Coh π^+ on argon at MicroBooNE. Chapter 10 lists the systematic uncertainties accounted for in this analysis, as well as how they were implemented. Chapter 11 combines the results of the previous two chapters into a total flux-integrated cross section result for the neutrino interaction channel that is the focus of this thesis. Finally, the thesis closes with Chapter 12, which details the implications, and conclusions of the cross section measurement, as well as discussing how this measurement could be improved in the future.

2 Neutrino Physics

"It's a dangerous business, Frodo, going out your door," he used to say. "You step onto the road, and if you don't keep your feet, there's no knowing where you might be swept off to."

J.R.R. Tolkien, *The Fellowship of the Ring*

This chapter covers the history of the discovery of the neutrino, the theory of the neutrino, and the current state of neutrino physics. The chapter begins with a discussion of the discovery of the neutrino, as well as a brief history of neutrino physics in Section 2.1. How neutrinos are modeled in the Standard Model (SM) is given in Section 2.2. This naturally leads to neutrino oscillations, which is discussed in detail for the three-flavor case in vacuum and in matter in Section 2.3. The Short-Baseline Anomalies are discussed in Section 2.4, and the chapter closes with a look at the current state of neutrino physics in Section 2.5.

2.1 Discovery of the Neutrino

In early 1930, Wolfgang Pauli, in a letter that he began with the now famous words: 'Dear radioactive ladies and gentlemen,' proposed the existence of a new neutral particle he called the *neutron* with a mass on the order of an electron in order to rescue the quantum theory of the nucleus from its contradictions. In particular, the main contradiction that needed to be resolved, was the demonstration by Chadwick in 1914 [14] that the spectrum of electrons released in β-decays was continuous, shown in Figure 2.1, in contrast to α- and γ-ray spectra, which both have discrete energy. W. Pauli proposed that a neutral weakly interacting fermion that is also emitted in β-decay (implying that β-decay is a three-body decay) could address the issue. When J. Chadwick discovered in 1932 the neutron as it is known today, E. Fermi renamed the Pauli particle the *neutrino*. The first published reference to the neutrino is in the Proceedings of the Solvay Conference of October 1933.

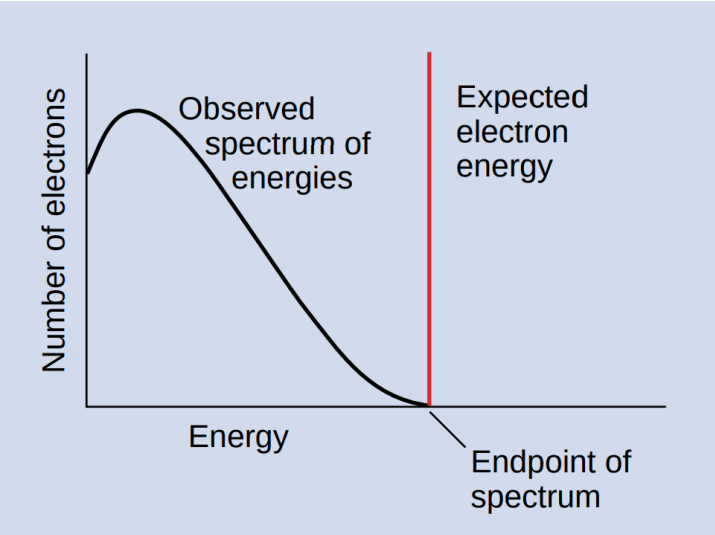

Figure 2.1: Plot showing the observed spectrum of energies for electrons (β) emitted from β-decays in comparison to the expected energy according to theory if the decay was two-body, which is shown in red.

Enrico Fermi, in 1934, made the first step towards a comprehensive theory of weak interactions with his formulated theory of β-decay, now called Fermi theory, in analogy with quantum electrodynamics (QED). The success of Fermi theory left little doubt of the neutrino's existence, but the particle had still not been observed. H. Bethe and R. Peierls, predicting the strength of the interactions of neutrinos using Fermi theory, finding it smaller than 10^{-44} cm^2 for a neutrino energy of 2 MeV they claimed that the neutrino is not impossible to observe, but would be extremely difficult, in 1934 [15].

The neutrino of Fermi's theory is massless, and the theory accurately accounted for almost all of the observed properties of β-decay, which was convincing evidence for the existence of the neutrino. In the early 1950s, Reines and Cowan attempted to devise a way to measure inverse β-decay, where an anti-neutrino can produce a positron according to this reaction:

$$\bar{\nu}_e + p^+ \rightarrow n + e^+.$$

Eventually, they settled on using the large flux of *electron anti-neutrinos* from a nuclear reactor at the Savannah River Nuclear Plant and 10 tons of equipment, including 1400 liters of liquid scintillators. This became the first reactor-neutrino experiment. In June of 1956, Reines and Cowan sent a telegram informing Pauli that they had detected neutrinos from fission fragments [16]. Reines eventually received the Nobel Prize in Physics for this discovery in 1995.

In 1962, *muon neutrinos* were discovered by Lederman, Schwartz, Steinberger, and coworkers at the Brookhaven National Laboratory. This experiment used a beam of protons focused toward a beryllium target. The resulting interaction produced a large number of pions which decayed to muons and muon neutrinos [17].

In 1973, the Gargamelle experiment at CERN discovered the weak neutral current interaction $\nu_\mu + N \to \nu_\mu +$ hadrons and $\bar{\nu}_\mu + N \to \bar{\nu}_\mu +$ hadrons, where N is a nucleon in the detector [18].

Much later in 2001, the *tau neutrinos* were detected by the DONUT experiment, which collided 800 GeV protons with a block of tungsten. This collision produced D_S mesons that subsequently decayed into tau-leptons which then produced tau neutrinos [19].

These and the experiments which followed confirmed the existence of three neutrino flavors: the electron neutrino (ν_e), the muon neutrino (ν_μ), and the tau neutrino (ν_τ), which happen to be the three neutrinos within the Standard Model. Next is a discussion of the neutrinos as they exist in the Standard Model.

2.2 Neutrinos in the Standard Model

The Standard Model of particle physics [13] is based on the gauge symmetry $SU(3) \times SU(2)_L \times U(1)_Y$ and categorizes all known fermions via the corresponding quantum numbers. They are given in Table 2.1.

Neutrinos are singlets of $SU(3)$ but belong to $SU(2)_L$ doublets together with their corresponding charged leptons. They have hypercharge $-1/2$ and do not carry electric charge, as $Q = T_3 + Y$. In the SM, neutrinos are Weyl fermions with left chirality, $\nu_{\alpha L} \equiv P_L \nu_\alpha$, $\alpha = e, \mu, \tau$. The chiral projectors are $P_L = (1 - \gamma_5)/2$ and $P_R = (1 + \gamma_5)/2$. For massless neutrinos, chirality and helicity match as the chiral projectors and the projectors on helicity components are the same up to corrections of order m/E. Left-handed neutrinos are accompanied by right-handed antineutrinos as required by the invariance of the theory under CPT (charge conjugation, parity, time reversal). Parity, the transformation of left into right and viceversa, is maximally violated in the SM as there are no right-handed neutrinos.

Left-handed neutrinos interact via the weak force according to the charged current and neutral current terms in the SM Lagrangian:

$$L_{SM} = -\frac{g}{\sqrt{2}} \sum_{\alpha=e,\mu,\tau} \bar{\nu}_{\alpha L} \gamma^\mu l_{\alpha L} W_\mu - \frac{g}{2\cos\theta_W} \sum_{\alpha=e,\mu,\tau} \bar{\nu}_{\alpha L} \gamma^\mu \nu_{\alpha L} Z_\mu + h.c., \qquad (2.1)$$

where g is the $SU(2)_L$ coupling, θ_W is the Weinberg angle, and all other symbols have the common meaning. We notice that the structure of the SM weak interaction is of the $V - A$ type.

Neutrinos come in three families. A fourth active neutrino is not allowed by the invisible width of the Z boson to which it would contribute as much as one active neutrino, $Z \to \nu_\alpha \bar{\nu}_\alpha$. The invisible width has been measured with great accuracy at LEP and leads to the following constraint on the active number of neutrinos [13]:

$$N_\nu = \frac{\Gamma_{inv}}{\Gamma_{\bar{\nu}\nu}} = 2.984 \pm 0.008. \qquad (2.2)$$

Particles	$SU(3)$	$SU(2)_L$	$U(1)_Y$
Leptons			
$\begin{pmatrix}\nu_e\\ e\end{pmatrix}_L, \begin{pmatrix}\nu_\mu\\ \mu\end{pmatrix}_L, \begin{pmatrix}\nu_\tau\\ \tau\end{pmatrix}_L$	**1**	**2**	$-1/2$
e_R, μ_R, τ_R	**1**	**1**	-1
Quarks			
$\begin{pmatrix}u\\ d\end{pmatrix}_L, \begin{pmatrix}c\\ s\end{pmatrix}_L, \begin{pmatrix}t\\ b\end{pmatrix}_L$	**3**	**2**	$1/6$
u_R, c_R, t_R	**3**	**1**	$2/3$
d_R, s_R, b_R	**3**	**1**	$-1/3$

Table 2.1: SM fermionic content and its irreducible representations with respect to the groups $SU(3)$, $SU(2)_L$, and $U(1)_Y$. **3** indicates a triplet of $SU(3)$, **2** a doublet of $SU(2)_L$ and **1** a singlet with respect to either group. Y is the hypercharge of the fields.

Additional neutrinos could be present, but they do not necessarily need to partake in SM interactions, and therefore are called sterile neutrinos.

There have been no experiments performed so far that have detected conclusive deviations from the SM, the only exception is neutrino oscillation experiments, which have shown that neutrinos indeed have mass. This is not the case in the SM, which naturally leads to a discussion of beyond the SM neutrino physics by the phenomenon known as neutrino oscillations in Section 2.3.

2.3 Neutrino Oscillations

In the presence of leptonic mixing and non-degenerate neutrino masses, the phenomenon of neutrino oscillations takes place. In both production and detection neutrinos are described by their flavor states, but in propagation through space, they are described by their mass states. The flavor states are a coherent superposition of massive states which have different masses. The massive states propagate over long distances with slightly different phases, which can amount to a change in the flavor state over distance. Thus making it possible to detect a different neutrino flavor state than the flavor state that the neutrino was produced originally. There are two ways that this happens as neutrinos propagate in nature: traversing a vacuum, or traversing through matter. The theory of neutrino oscillations in vacuum is discussed in Section 2.3.1, and the theory of neutrino oscillations through matter is discussed in Section 2.3.2.

2.3.1 Neutrino Oscillations in Vacuum

As was stated above, neutrino oscillations work on the premise that neutrinos propagate as *mass eigenstates* (which is denoted ν_k, with $k = 1, 2, 3$), but interact and are detected in their *flavor eigenstates* (which is denoted ν_α, with $\alpha = e, \mu, \tau$). Each of the flavor eigenstates is a superposition of the three mass eigenstates, which can be expressed by

$$|\nu_\alpha\rangle = \sum_k U^*_{\alpha k} |\nu_k\rangle , \tag{2.3}$$

where the unitary matrix U is known as the Pontecorvo-Maki-Nakagawa-Sakata (PMNS) matrix, given by

$$U = \begin{pmatrix} U_{e1} & U_{e2} & U_{e3} \\ U_{\mu 1} & U_{\mu 2} & U_{\mu 3} \\ U_{\tau 1} & U_{\tau 2} & U_{\tau 3} \end{pmatrix} , \tag{2.4}$$

in the case of three-flavor oscillations. As an example, here is the expression of the electron flavor eigenstate as the superposition of the three mass eigenstates:

$$|\nu_e\rangle = U^*_{e1} |\nu_1\rangle + U^*_{e2} |\nu_2\rangle + U^*_{e3} |\nu_3\rangle .$$

The PMNS matrix can also be written in terms of three flavor-space mixing angles θ_{12}, θ_{23}, and θ_{13}, and three charge-parity (CP)-violating phases, δ_{CP}, α_1, and α_2:

$$U = \begin{pmatrix} 1 & 0 & 0 \\ 0 & c_{23} & s_{23} \\ 0 & -s_{23} & c_{23} \end{pmatrix} \begin{pmatrix} c_{13} & 0 & s_{13} e^{-i\delta_{CP}} \\ 0 & 1 & 0 \\ -s_{13} e^{i\delta_{CP}} & 0 & c_{13} \end{pmatrix} \begin{pmatrix} c_{12} & s_{12} & 0 \\ -s_{12} & c_{12} & 0 \\ 0 & 0 & 1 \end{pmatrix} \begin{pmatrix} e^{i\frac{\alpha_1}{2}} & 0 & 0 \\ 0 & e^{i\frac{\alpha_2}{2}} & 0 \\ 0 & 0 & 1 \end{pmatrix} , \tag{2.5}$$

where $c_{ij} = \cos\theta_{ij}$, and $s_{ij} = \sin\theta_{ij}$. This matrix has been intentionally broken into four components to improve readability and interpretation, as well as because the different mixing angles are measured by different types of neutrino oscillation experiments. The first matrix (on the far left) includes only the mixing angle θ_{23}, which is measured by atmospheric neutrino oscillation experiments. The third matrix (on the middle-right) includes only the mixing angle θ_{12}, which dominates the mixing of solar neutrinos, thus is measured by solar neutrino oscillation experiments. The second matrix (on the middle-left) is known as the cross-mixing matrix, and depends on two parameters: the mixing angle θ_{13} and the CP-violating phase δ_{CP}. A non-zero δ_{CP} will lead to a complex matrix U and different probabilities for the CP-conjugate oscillations $P(\nu_\alpha \to \nu_\beta) \neq P(\bar{\nu}_\alpha \to \bar{\nu}_\beta)$, which would be a significant finding for neutrino physics and physicists.

The final matrix in Equation 2.5 (on the far right) contains the termed "Majorana" CP-violating phases. These lead to physical effects only for the case of Majorana neutrinos (i.e. where neutrinos are their own antiparticle) and do not conserve lepton number. Even in the case of Majorana neutrinos, these CP-violating phases do not affect the oscillation probability, which depends on $\sum_i U^*_{\alpha i} U_{\alpha j}$, so the Majorana phases cancel. It

is not possible to determine whether neutrinos are their own antiparticles from oscillation measurements; other experiments (such as the search for neutrinoless double beta decay being conducted or planned by the MAJORANA [20], GERDA [21], CUORE [22], SNO+ [23], NEXT [24], and nEXO [25] collaborations, among others) are needed to answer this question. If the neutrinos are instead different from anti-neutrinos, they are "Dirac" particles and acquire their mass in a similar way as other fermions in the Standard Model do.

If we consider orthonormal massive neutrino states ($\langle \nu_k | \nu_j \rangle = \delta_{kj}$), the unitarity of the mixing matrix implies that the flavor states are also orthonormal: $\langle \nu_\alpha | \nu_\beta \rangle = \delta_{\alpha\beta}$. Since the massive neutrino states ν_k are eigenstates of the Hamiltonian, $H |\nu_k\rangle = E_k |\nu_k\rangle$, with energy

$$E_k = \sqrt{\mathbf{p}^2 + m_k^2}, \tag{2.6}$$

then the Schrodinger equation

$$i\frac{d}{dt} |\nu_k(t)\rangle = H |\nu_k(t)\rangle , \tag{2.7}$$

implies that the massive neutrino states evolve in time as plane waves:

$$|\nu_k(t)\rangle = e^{-iE_k t} |\nu_k\rangle . \tag{2.8}$$

Considering now a flavor state $|\nu_\alpha(t)\rangle$ which describes a neutrino created with a definite flavor α at time $t = 0$. From Equations (2.3) and (2.8), the time evolution of this state is given by

$$|\nu_\alpha(t)\rangle = \sum_k U^*_{\alpha k} e^{-iE_k t} |\nu_k\rangle , \tag{2.9}$$

such that

$$|\nu_\alpha(0)\rangle = |\nu_\alpha\rangle .$$

The massive states can be expressed in terms of flavor states inverting Equation (2.3):

$$|\nu_k\rangle = \sum_\alpha U_{\alpha k} |\nu_\alpha\rangle , \tag{2.10}$$

where the relation $U^\dagger U = \mathbf{1}$ has been used. Substituting the last relation into Equation (2.9) one gets:

$$|\nu_\alpha(t)\rangle = \sum_{\beta=e,\mu,\tau} \left(\sum_k U^*_{\alpha k} e^{-iE_k t} U_{\beta k} \right) |\nu_\beta\rangle . \tag{2.11}$$

Hence, the superposition of massive neutrino states $|\nu_\alpha(t)\rangle$, and the pure flavor state given in Equation (2.3) at $t = 0$, becomes a superposition of different flavor states at $t > 0$. The transition probability of $|\nu_\alpha\rangle \to |\nu_\beta\rangle$ as a function of time is given by:

$$P_{\nu_\alpha \to \nu_\beta}(t) = |\langle \nu_\beta | \nu_\alpha \rangle|^2 = \sum_{k,j} U^*_{\alpha k} U_{\beta k} U_{\alpha j} U^*_{\beta j} e^{-i(E_k - E_j)t}. \tag{2.12}$$

For ultra-relativistic neutrinos, one could expand Equation (2.6) considering $m_k \sim 0$ to obtain $E_k \simeq E + m_k^2/2E$, where $E = |\mathbf{p}|$. Given the mass difference Δm^2_{kj} it is possible to write:

$$E_k - E_j \simeq \frac{\Delta m^2_{kj}}{2E}. \tag{2.13}$$

In neutrino oscillation experiments, the propagation time t is not measured. What is known is the distance L between the source and the detector. Since ultra-relativistic neutrinos propagate almost at the speed of light, it is possible to approximate $t = L$. Therefore, the transition probability can be approximated as:

$$P_{\nu_\alpha \to \nu_\beta}(t) = \sum_{k,j} U^*_{\alpha k} U_{\beta k} U_{\alpha j} U^*_{\beta j} e^{-i\frac{\Delta m^2_{kj} L}{2E}}. \tag{2.14}$$

The oscillation probability thus depends both on quantities fixed by nature (PMNS matrix elements and differences of the square of the masses Δm^2) and on parameters fixed by experiments (the path the neutrino travels L, i.e. the source-detector distance, and the neutrino energy E). Moreover, oscillation experiments are only sensitive to the difference of the squares of the masses and not to the absolute neutrino mass.

The now well-accepted picture of neutrino mixing involves three underlying mass states, with three mixing angles defining the linear superpositions that make up each of the three weak, or flavor, states. The magnitude of the mass-squared splitting between states ν_1 and ν_2 is known from the KamLAND reactor experiment [26], and the much-larger splitting between the third, ν_3 state and the $\nu_1 - \nu_2$ pair is known from atmospheric and long-baseline experiments [13]. However, pure neutrino oscillations are sensitive only to the magnitude of the mass splitting, not to its sign. Defining the ν_1 state as having the largest admixture of the electron flavor eigenstate, the sign of the mass splitting between states ν_2 and ν_1 is determined to be positive ($\Delta m^2_{21} > 0$) using the pattern of neutrino oscillations through the varying-density solar medium [13]. However, the corresponding sign of $\Delta m^2_{32} \sim \Delta m^2_{31}$ remains unknown. That is, there are two potential orderings, for the neutrino mass states: the so-called *normal ordering*, in which ν_3 is the heaviest, and the *inverted ordering*, in which ν_3 is the lightest, as shown in Figure 2.2.

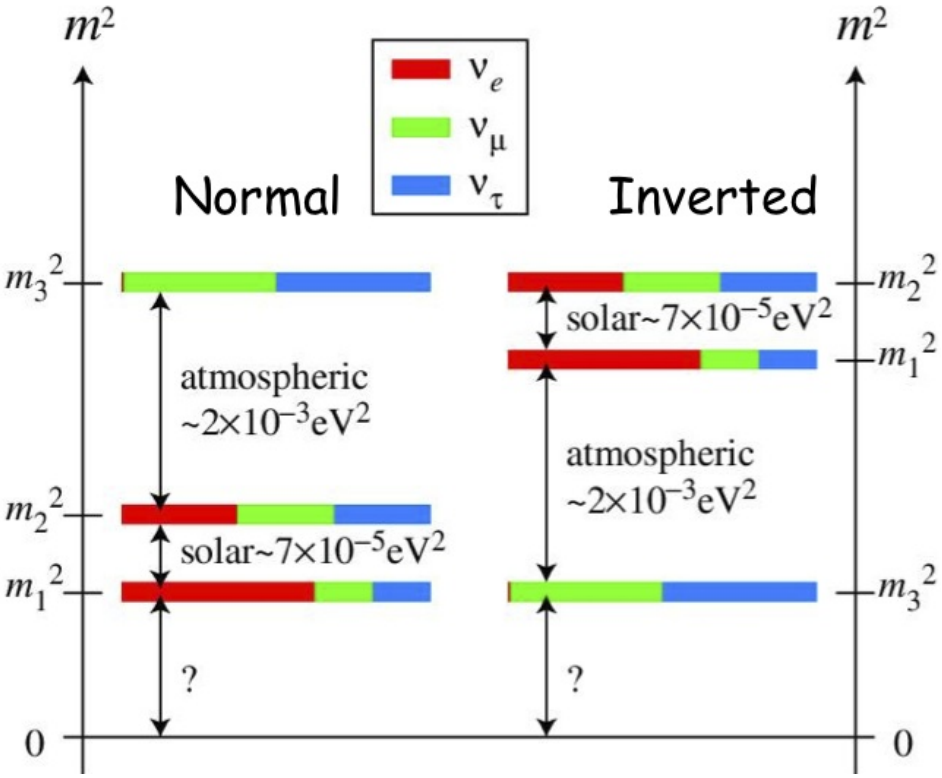

Figure 2.2: Pictorial representation of the possible neutrino mass orderings.

2.3.2 Neutrino Oscillations Within Matter

Neutrinos propagating in matter are subject to a potential due to the coherent forward elastic scattering with the particles in the medium (electrons and nucleons). Coherent scattering happens when the neutrino wave function interacts with the matter as a whole, such as when the scattered waves from the nuclei in the matter interfere with each other.

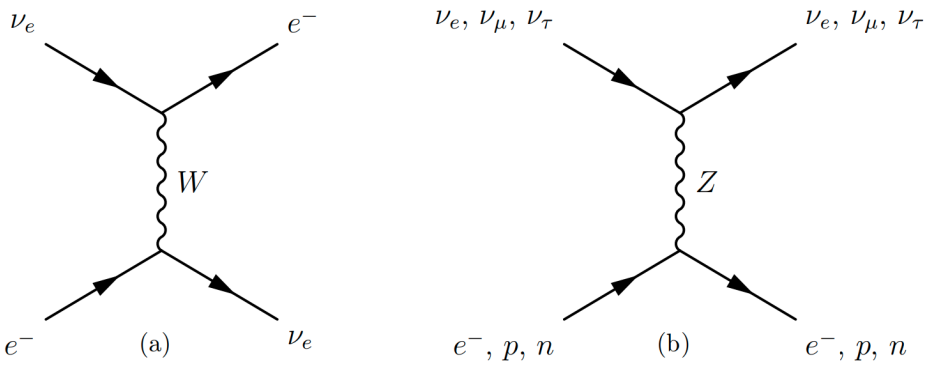

Figure 2.3: Feynman diagrams depicting examples of a CC (a) and NC (b) neutrino interaction.

When active flavor neutrinos propagate in matter, their evolution equation is affected by both charged-current (CC) and neutral-current (NC) scatterings [27]. The Feynman diagrams of CC and NC scattering are shown in Figure 2.3. This phenomenon was first proposed by Wolfenstein [28] and is now known as the Mikheyev-Smirnov-Wolfenstein (MSW) effect.

A full account of how exactly these matter effects alter neutrino oscillations probabilities is beyond the scope of this thesis (although it is well described in other sources, e.g. [27]).

An important implication of matter effects in neutrino oscillations is that their impact is different for neutrinos and antineutrinos (since the CC interaction shown in Figure 2.3 is not available for antineutrinos) due to the lack of positrons in the Earth. This can mimic a CP violation $P(\nu_\alpha \to \nu_\beta) \neq P(\bar{\nu}_\alpha \to \bar{\nu}_\beta)$ effect which does not say anything interesting about matter-antimatter asymmetry at a fundamental level. It is therefore essential to account for matter effects when attempting to determine δ_{CP} to identify genuine neutrino-sector CP violation.

Moreover, whilst vacuum oscillations are only sensitive to the square of the neutrino mass splitting, matter effects are sensitive to the signs of the mass splittings. Current and future experiments will have sensitivity to a mass ordering measurement. While T2K [29] has very little sensitivity to the ordering, due to the shorter baseline, NOνA [30] has the potential to make a measurement at the $2 - 3\sigma$ level, if the value of the CP phase parameter δ_{CP} is maximal. A combination of current experiments at different baselines (e.g. T2K+NOνA) could help to further disentangle the competing effects of CP violation and matter-induced neutrino-antineutrino differences. However, the future DUNE [31] experiment will identify the mass ordering, removing the ambiguities.

2.3.3 Overview of Neutrino Oscillation Experiments

Neutrino oscillation experiments are classified based on the different sources of neutrinos that have been used, and can be broken down into the experiment types listed below.

Reactor Neutrino Experiments

These experiments exploit the large isotropic fluxes of electron anti-neutrinos produced in nuclear reactors by β decays of heavy nuclei (mainly fission fragments of ^{235}U, ^{238}U, ^{239}Pu, and ^{241}Pu). Typical energy of reactor $\bar{\nu}_e$'s is of the order of a few MeV.

Atmospheric Neutrino Experiments

Primary cosmic rays interact with the upper layers of the atmosphere producing a large flux of pions and kaons that then decay in the atmosphere into muons and muon neutrinos. Many muons further decay into electrons and muon neutrinos before hitting the ground. Atmospheric neutrino experiments are designed to detect these ν_μ.

Solar Neutrino Experiments

These experiments detect the electron neutrinos generated in the core of the Sun by the thermonuclear reactions that power the Sun. Solar neutrino experiments are designed to detect these ν_e and are sensitive to extremely small values of Δm^2 ($\Delta m^2_{21} = 7.37^{+0.59}_{-0.44} \times 10^{-5} eV^2$), much smaller than the sensitivity of the other experiment discussed above.

Accelerator Experiments

These experiments make use of beams of muon neutrinos produced by the decay of pions, kaons, and muons created by a proton beam hitting a target. They are further classified into *appearance* experiments if they look at electron neutrinos oscillated from the initial muon neutrinos, or *disappearance* experiments if they look at the reduction in muon neutrino events due to oscillations. These experiments are the focus of this thesis and will be better described in Chapter 6.

2.4 Short-Baseline Anomalies

A series of short-baseline neutrino oscillation experiments provided unexpected results. The results they obtained are inconsistent or in strong tension with the predictions obtained from the three neutrino oscillation paradigm. In this section, these experiments are split into three categories:

- Accelerator neutrino experiments
- Radio-chemical experiments
- Nuclear reactor experiments.

2.4.1 Accelerator Neutrino Experiments

The Liquid Scintillator Neutrino Detector (LSND) observed an excess of $\bar{\nu}_e$ events from a well understood $\bar{\nu}_\mu$ source in 2001 [1]. At the same period, the KARMEN experiment studied neutrino supplied via the decay of pions produced when a proton beam strikes a target. It operated from 1990 until March 2001, searching for the appearance and disappearance of electron neutrinos. KARMEN did not observe any oscillation signal. limits were set on neutrino oscillation parameters [32], which are in tension with the LSND experiment and were followed up by MiniBooNE.

Liquid Scintillator Neutrino Detector

The first tension with the three-neutrino framework arose in the 1990s by the LSND experiment at Los Alamos [33]. The neutrino beam was produced by firing a 0.8 GeV prootn beam into a target. The charged pions produced are stopped in the beam dump

where they decay at rest. As illustrated in Figure 2.4, this leads to a well understood source of muon antineutrinos of 0 MeV to 53 MeV.

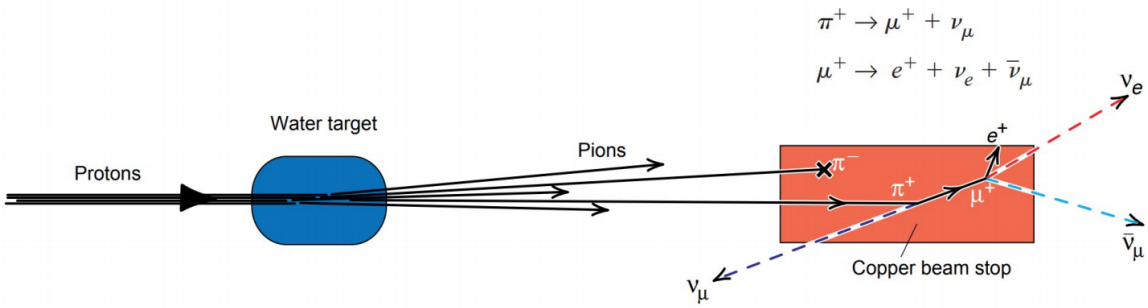

Figure 2.4: Neutrino beam used by the LSND experiment. A proton beam is fired at a water target, where they produce pions. Most of the pions travel half a meter in the air before striking a copper beam stop and coming to rest. Nearly all of the negative pions are absorbed by copper nuclei before they decay, but each positive pion decays at rest to a muon and a muon neutrino. The muons also come to rest in the beam stop and decay to a muon antineutrino, a positron, and an electron antineutrino. The neutrinos fly off in all directions isotropically. Illustration from [1].

A liquid scintillator detector was positioned 31 m away from the target. The process searched for was inverse beta decay:

$$\bar{\nu}_\mu \xrightarrow{oscillation} \bar{\nu}_e + p \to e^+ + n. \tag{2.15}$$

The signature of such an event is illustrated on the left panel of Figure 2.5.

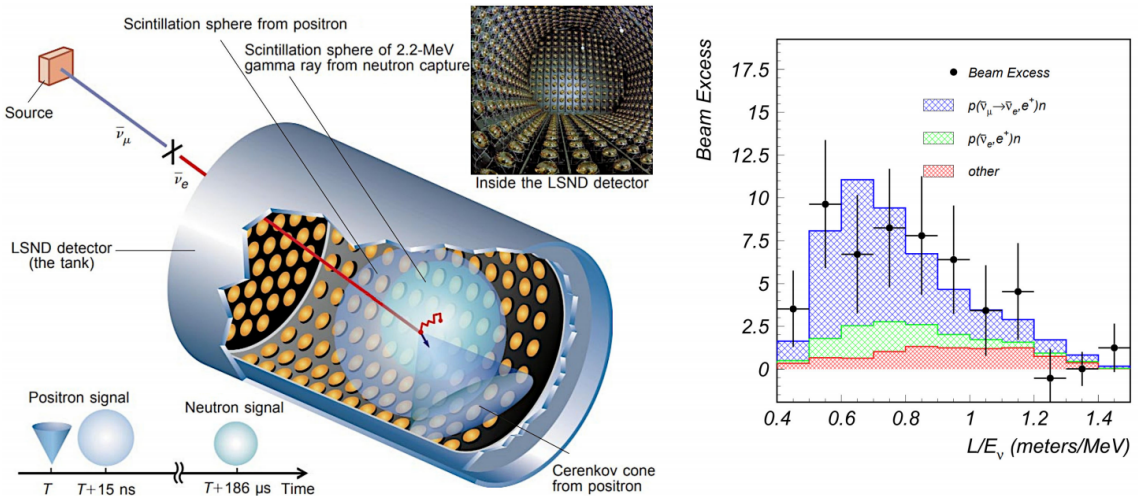

Figure 2.5: (Left) Signature of a $\bar{\nu}_e$ event in LSND. A muon antineutrino produced at the source oscillates en-route to the detector and appears as an electron antineutrino. The neutrino scatters off a free proton in the oil, creating a positron and a neutron. The positron travels faster than the speed of light in the oil and so produces a Cherenkov cone. As it loses energy through collisions with atoms in the oil, the positron also produces a sphere of scintillation light. The neutron survives about 186 microseconds and wanders $\mathcal{O}(1\text{m})$ before it is absorbed by a nucleus, emitting a 2.2 MeV gamma ray that also produces a sphere of scintillation light. This succession of events is the signature of an electron antineutrino. (Right) The observed excess of candidate $\bar{\nu}_e$ events. The blue part of the histogram is the contribution due to a potential additional oscillation. Figure from [1].

The LSND experiment reported an anomalous event excess in the $\bar{\nu}_\mu \to \bar{\nu}_e$ appearance channel, the result is shown on the right panel of Figure 2.5 [1]. This could be interpreted as an oscillation with $\Delta m^2 \approx 1$ eV. Such a scale is clearly incompatible with Δm^2_{21} and Δm^2_{32} and could be explained with the presence of sterile neutrinos ($\bar{\nu}_\mu \to \nu_{\text{sterile}} \to \bar{\nu}_e$). At the same time, the results of the KARMEN and Bugey experiments excluded parts of the allowed low Δm^2 region [32, 34]. Within the constraints of the former, the LSND signal is best fitted through an additional sterile neutrino oscillation with a mass splitting of the order of 1 eV [35].

MiniBooNE

The MiniBooNE experiment, located at Fermilab, was designed with the goal to validate the LSND measurement [36]. The neutrino beam used will be the topic of Section 6.1. For current purposes, it is important to note that the Booster Neutrino Beam is able to run in both neutrino and antineutrino modes, and that the muon (anti)neutrino energy is peaked around 800 MeV. To be sensitive to the signal seen by LSND, the baseline was

taken to be 541 m, leading to a very similar L/E value.

The detector consists of a 12 m diameter sphere filled with 10 million liters of mineral oil. The active volume is surrounded by a sphere, instrumented with 1280 8 inch PMTs. An additional 240 PMTs are located in the outer veto region and used for cosmic activity rejection. Particles travelling through the mineral oil at a speed exceeding the speed of light in the medium will emit Cherenkov light. The kinetic energy threshold for Cherenkov production depends on the mass of the particle, making MiniBooNE fairly insensitive to protons and neutrons compared to light particles sucha s electrons and muons. Between the latter two, particle identification is made based on the shape of the Cherenkov cone captured by the PMT system, as illustrated in Figure 2.6.

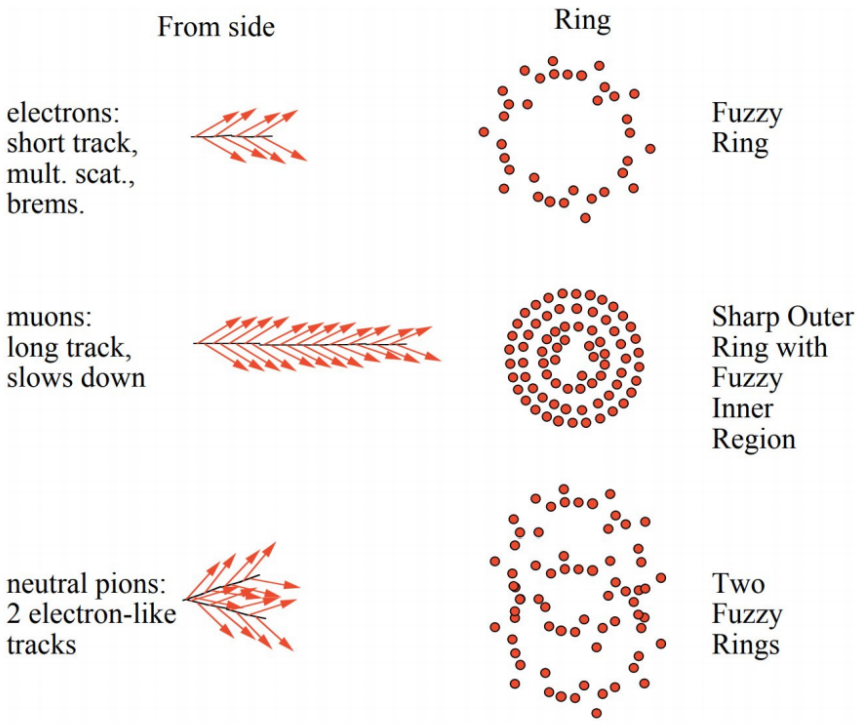

Figure 2.6: Paricle Identification in MiniBooNE. Schematic showing the different signatures of event topologies as seen by the PMT system of MiniBooNE. Electrons scatter, creating a fuzzy ring. Muons follow a more straight trajectory, leading to a sharper ring structure. The photons from $\pi^0 \to \gamma\gamma$ decays produce electrons through scattering and therefore creating similar signatures. Figure from [2].

Apart of particle observance through the direct emission of Cherenkov light, detection can happen through secondary processes. Due to the nature of electromagnetic shower formation, high energetic photons will undergo scattering and pair-production. The produced electons – and positrons – in these processes emit Cherenkov light if their energy is above threshold. Therefore, the signature of photons and electrons is indistin-

guishable in MiniBooNE. Neutrons could, in principle, be detected by 2.2 MeV γs that result from delayed (lifetime of 186 μs) neutron capture on protons within the mineral oil. In practice, this is below the detection threshold arising from radioactivity, PMT noise, etc.

For energy calibration, MiniBooNE relied on the typical Michel electron spectrum peaked at $m_\mu/2 = 52.8$ MeV. Furthermore, the invariant mass from the $\pi^0 \to \gamma\gamma$ was also reconstructed to validate the energy response around 135 MeV.

The interaction looked for by the MiniBooNE sterile neutrino search was:

$$\nu_\mu \xrightarrow{oscillation} \nu_e + n \to e^- + p \tag{2.16}$$

$$\bar{\nu}_\mu \xrightarrow{oscillation} \bar{\nu}_e + p \to e^+ + n \tag{2.17}$$

Here, the final state electron from the Charged Current (CC) neutrino scattering is observed through a fuzzy Cherenkov ring signature. Being a different detector technology, the systematic uncertainties of MiniBooNE are completely different from those of the LSND experiment. Nonetheless, having a similar L/E value and sensitivity to the same neutrino interaction channel, MiniBooNE can test $\mathcal{O}(1\text{eV})$ sterile neutrino hypothesis.

After 15 years of data-taking, the MiniBooNE experiment reported results from an analysis of ν_e appearance data from 12.84×10^{20}POT in neutrino mode. If interpreted as an excess of ν_e charged-current quasielastic events, the size of the excess is 381.2 ± 85.2, corresponding to 4.5σ in the energy range 200 MeV to 1250 MeV. Combining these data with the $\bar{\nu}_e$ appearance data from 11.27×10^{20}POT in antineutrino mode, a total of $(\nu_e + \bar{\nu}_e)$ charged-current quasielastic event excess of 460.5 ± 99.0 events (4.7σ) is observed. The MiniBooNE data are consistent in energy and magnitude with the excess of events reported by LSND, and the significance of the excesses of the two experiments combined is 6.0σ [2]. The final result in neutrino mode is shown in the left panel of Figure 2.7. The right panel investigates the compatibility of the LSND and MiniBooNE in the light of the sterile neutrino hypothesis.

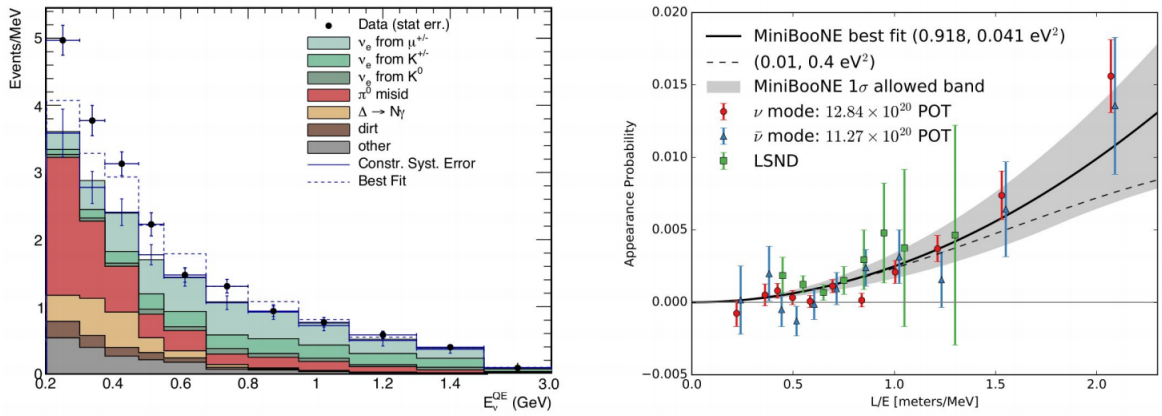

Figure 2.7: (Left) The low-energy excess as observed by MiniBooNE in neutrino mode. The reconstructed neutrino energy under the hypothesis that the charged-current interaction is quasielastic. The excess in data is clearly visible at low energies. The dotted line corresponds to the prediction when a sterile neutrino is included in the model. (Right) The allowed parameter space by the LSND and MiniBooNE (in neutrino and antineutrino mode) for a sterile neutrino. Figure from [2].

It is important to stress the quasielastic hypothesis in the MiniBooNE result. The selected events are interpreted under the assumption of scattering with a single free nucleon. In the case of an electron neutrino interaction, the energy can be reconstructed using the final state lepton:

$$E_\nu^{QE} = \frac{2m_n E_e + m_p^2 - m_n^2 - m_e^2}{2(m_n - E_e + \cos\theta\sqrt{E_e^2 - m_e^2})}, \tag{2.18}$$

where m_n, m_p, and m_e are the mass of the neutron, proton, and the electron. θ is the angle of the outgoing lepton with respect to the incoming neutrino direction. In reality, intranuclear processes such as pion absorption complicate the energy reconstruction. It is therefore possible that the energy reconstruction of the observed excess events is underestimated and corresponds to higher true neutrino energies.

MiniBooNE Backgrounds

In the low-energy region where the excess manifests itself, three background categories can mimic the Low Energy Excess (LEE) as observed by MiniBooNE:

- Intrinsic ν_e: The ν_e component of the beam, coming from $\mu^\pm$, $K^\pm$, and K^0, is the irreducible background of the experiment, since it can't be distinguished from ν_μ oscillating into ν_e. This component of the flux is partially constrained by measuring the ν_μ interactions.

- Misidentified π^0: The background from misidentified π^0 events represents the largest component. These events are particularly challenging to reconstruct since very forward-boosted photons will appear in the detector as a single fuzzy ring. The MiniBooNE collaboration has constrained this contribution by reconstructing the invariant π^0 mass of the event and obtaining a sample with a purity $> 90\%$ of NC π^0 events. The total uncertainty on the NC background is 7% [37].

- Misidentified $\Delta \rightarrow N\gamma$: A neutral current resonant interaction can produce a Δ resonance, which has a rare electromagnetic decay channel $\Delta \rightarrow N\gamma$, where $N = n, p$. This channel is also constrained by the NC π^0 in-situ measurement. The uncertainty on this component is 12% [37].

Both the π^0 and the $\Delta \rightarrow N\gamma$ backgrounds arise formt he inability of a Cherenkov detector to distinguish between photons and electrons, which is one of the most powerful capabilities of a LArTPC, which will be discussed in Chapter 5.

2.4.2 Radio-Chemical Neutrino Detection Experiments

Two solar neutrino experiments, GALLEX [38] and SAGE [39], used intense neutrino sources (^{51}Cr, ^{37}Ar) during the detector calibration. These sources decay through electron capture, producing an electron neutrino and emitting γ-radiation. The sources were shielded to stop the gamma-radiation and act as a clean neutrino source. Both GALLEX and SAGE observed an approximate 24% event deficit in the ν_e disappearance channel. This deficit is often referred to as the *Gallium anomaly* and can also be understood by neutrino oscillations with 1 eV sterile neutrinos. A fit of the data in terms of neutrino oscillations favors at about 2.3σ short-baseline electron neutrino disappearance with respect to the null hypothesis of no oscillations [40, 41].

2.4.3 Reactor Antineutrino Anomaly (RAA)

In 2011 Mueller et al. [42] as well as Huber [43] published new nuclear reactor antineutrino reference spectra computed from electron spectrum measurements but with revised conversion techniques. Both found a 3% increase in the reactor flux compared to the previous predictions, which had been applied as standard for more than 20 years. A reanalysis of the measured versus the predicted neutrino flux was performed using the antineutrino flux measurements at 100m baseline and less. Together with an updated neutrino interaction cross section, the computation resulted in an observed-to-predicted ratio of 0.935 ± 0.024 [44], which is the so-called Reactor Antineutrino Anomaly (RAA) [45]. Figure 2.8 displays the data of several reactor experiments together with two hypothetical fits, one in the case of three neutrinos, the other includes one sterile neutrino. Clear preference is given to the $3 + 1$ neutrino hypothesis.

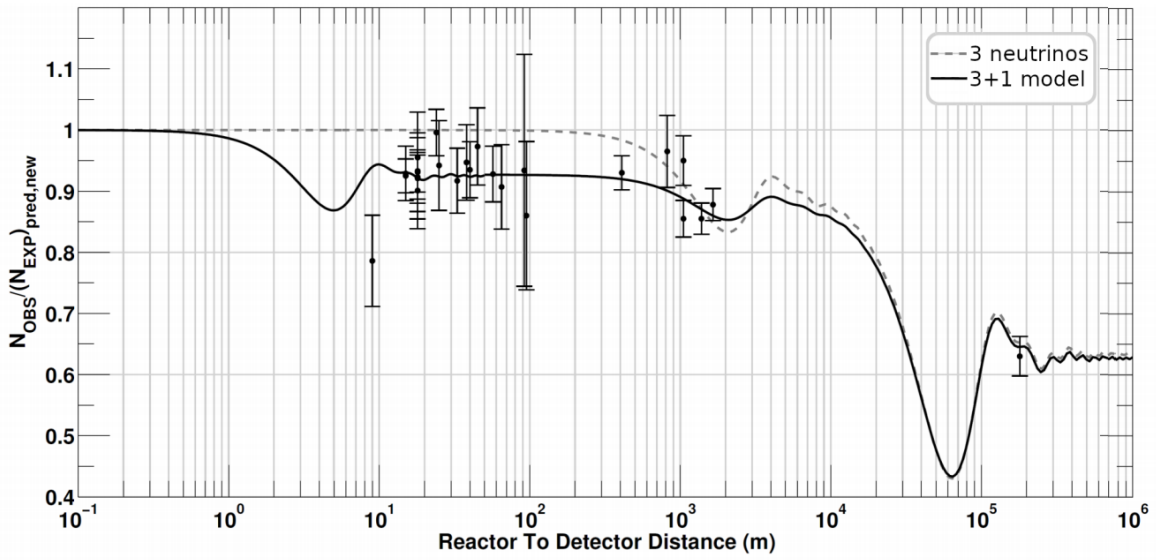

Figure 2.8: Illustration of the short-baseline reactor antineutrino anomaly. The graph shows the ratio of the observed to the expected rate, from the recent reactor neutrino flux calculations without neutrino oscillations, for all reactor neutrino experiments at various baselines. The dashed line corresponds to the classic 3 neutrino oscillation scenario, while the solid line corresponds to the $3+1$ model (3 active neutrinos + 1 sterile neutrino) with $\Delta m^2 \approx 1$ eV. The bump around 3 km is due to the well-measured atmospheric neutrino oscillation, the one around 100 km is the solar neutrino oscillation. Figure from [3].

The differences found in the short-baseline reactor experiments could indicate unaccounted physics in the propagation and detection of neutrinos, such as sterile neutrinos. On the contrary, the differences could also be introduced by errors on the predicted reactor spectra. Upcoming very short-baseline experiments will test if the discovered overall deficit in antineutrino rate is linked to neutrino flavor oscillations into a light sterile state. Even without new physics, data from different reactor types will bring valuable insights into the nature of the reactor shape distortion, bypassing the use of summation spectra and, accordingly, their large uncertainties.

2.4.4 Current Status and Global Fits

Combined with cosmological evidence for an additional relativistic degree of freedom before recombination [46, 47, 48], the gallium, LSND/MiniBooNE neutrino disappearance anomalies and the Reactor Antineutrino Anomaly provide substantial arguments for sterile neutrinos. An overview of the significance of these anomalies is given in Table 2.2. Even though hints for a sterile neutrino are observed in several channels by a large set of experiments employing widely varying detector technologies, the picture

is far from clear. The lack of observation of a sterile neutrino oscillation in the muon disappearance channels creates tension between different data sets.

Experiment	Channel	Significance
LSND	$\nu_\mu \to \nu_e$	3.8σ
MiniBooNE	$\nu_\mu \to \nu_e$	4.5σ
MiniBooNE	$\bar{\nu}_\mu \to \bar{\nu}_e$	2.8σ
GALLEX/SAGE	ν_e disappearance	2.3σ
Reactors	$\bar{\nu}_e$ disappearance	2.7σ

Table 2.2: Significance of experimental anomalies from neutrino experiments. LSND and MiniBooNE are accelerator-based short-baseline experiments. GALLEX/SAGE are radioactive source experiments. The others are reactor experiments and represent the Reactor Antinuetrino Anomaly (RAA). A detailed overview of the anomalies and their significance is given in [12].

Global fits have found a large improvement in the $\Delta\chi^2 = \chi^2_{null} - \chi^2_{3+1}$, indicating the data favors a correction that behaves like an additional oscillation [49]. An internal inconsistency arises when the goodness of fit is evaluated on the appearance and disappearance data-sets separately. There are several possible explanations for the tension:

1. There are no sterile neutrinos. In this case, the separate data-sets must suffer from biases and unevaluated systematic uncertainties. Those biases, over different channels and detection technologies accidentally match the effect produced by a sterile neutrino.

2. There is one light sterile neutrino as explained in the simplest $3 + 1$ extension. In this scenario, some data-sets suffer from unidentified experimental effects. In the case of MiniBooNE, for example, the result is systematic limited, increasing the likeliness of unaccounted uncertainties in the result. Furthermore, it is worth noting that null results providing limits, such as the disappearance searches, have received less scrutiny.

3. There is additional new physics in the neutrino sector. More complicated models such as a decaying sterile neutrino or a $3 + N$ model introduce additional degrees of freedom and are able to relieve tension in the data.

From a theoretical point of view, it is worth noting that, light sterile neutrinos do not show up in a natural way in most beyond the Standard Model theories. The popular type-I see-saw model, for example, which provides an explanation of the small neutrino couplings, predicts only heavy sterile neutrinos ($m > 10^{10}$ GeV). If light sterile neutrinos indeed exist, they would suggest new frontiers in both experimental and theoretical physics.

2.5 The Current State of Neutrino Physics

All of the many experiments that have been listed have provided many points of data for neutrino oscillations, and neutrinos in general. In particular, neutrino oscillation has been observed from many sources: the sun, reactors, Cosmic Ray (CR) interactions, and accelerator beams [13]. A summation of the measurements of current parameters modeling the 3-Flavor Oscillation model (which sufficiently describes the majority of neutrino oscillation phenomenon that have been observed) are given in Table 2.3.

Summary of 3-Flavor Oscillation Parameters				
	Normal Hierarchy		**Inverted Hierarchy**	
Parameter	1σ BF	3σ range	1σ BF	3σ range
$\theta_{12}(^\circ)$	$33.44^{+0.77}_{-0.74}$	$31.27 - 35.86$	$33.45^{+0.78}_{-0.75}$	$31.27 - 35.87$
$\theta_{23}(^\circ)$	$49.2^{+0.9}_{-1.2}$	$40.1 - 51.7$	$49.3^{+0.9}_{-1.1}$	$40.3 - 51.8$
$\theta_{13}(^\circ)$	$8.57^{+0.12}_{-0.12}$	$8.20 - 8.93$	$8.60^{+0.12}_{-0.12}$	$8.24 - 8.96$
$\delta_{CP}(^\circ)$	197^{+27}_{-24}	$120 - 369$	282^{+26}_{-30}	$193 - 352$
$\Delta m^2_{21}(10^{-5}eV^2)$	$7.42^{+0.21}_{-0.20}$	$6.82 - 8.04$	$7.42^{+0.21}_{-0.20}$	$6.82 - 8.04$
$\Delta m^2_{31}(10^{-3}eV^2)$	$2.517^{+0.026}_{-0.027}$	$2.435 - 2.598$	$2.498^{+0.028}_{-0.028}$	$2.414 - 2.518$

Table 2.3: Table summarizing the best-fit (BF) three-flavor oscillation parameters, along with 3σ ranges. Values taken from [13].

With these values noted, it is important to remark that there are still a lot of unanswered questions in the realm of neutrino physics that need to be addressed. The remaining questions would find their answers through these conditions:

- Determining the nature (either Dirac or Majorana) of massive neutrinos.
- Determining the mass ordering (whether the sign of Δm^2_{31} or Δm^2_{32} is negative or positive).
- Determining, or obtaining significant constraints on, the absolute scale of neutrino masses.
- Determining the status of CP symmetry in the lepton sector.
- Determining if there is a fourth, sterile neutrino.

There are many different experiments that are currently working on, or have been proposed to perform these investigations. An important factor for future long-baseline experiments is a proper experimental understanding of neutrino-nucleus interactions as well as their cross sections. One of the neutrino-nucleus interaction cross sections that

need to be understood better is the signal channel of this analysis, which is one of the motivations for this thesis measurement.

The next chapter, Chapter 3, will give a brief discussion on many different types of neutrino-nucleus interactions, how they occur, as well as a short introduction to the neutrino-nucleus interaction that is the primary focus of this thesis.

3 Neutrino Interactions

Neutrinos are not composed of quarks, they are neutral particles, and they have mass. This means that neutrinos can only interact via the weak and gravitational forces. The gravitational effect is extremely difficult to measure, so, to study neutrinos, the weak interactions are employed. The weak force is mediated by the W and Z bosons. Whenever a neutrino interaction involves the $W^{\pm}$, that type of interaction is known as a *charged current* (CC) interaction, and neutrino interactions that involve the Z are known as *neutral current* (NC) interactions (both are depicted in the Feynman Diagrams shown in Figure 3.1). CC neutrino interactions are easily identified by the outgoing lepton that emerges from the interaction. For example, a CC ν_e interaction will produce an outgoing electron in the final state, which would be the same expectation for ν_μ and ν_τ interactions except they would have their corresponding lepton in the final state instead of an electron. For NC interactions, the interacting neutrino will appear in both the initial and final state, and the exchange of the Z boson is responsible for the mediation of the transfer of energy. In general, CC and NC interactions proceed as

$$\nu_l + A \rightarrow l^- + X \quad \text{(CC)} \tag{3.1}$$

$$\nu_l + A \rightarrow \nu_l + X \quad \text{(NC)} \tag{3.2}$$

where ν_l represents a neutrino of flavor $l = e, \mu, \tau$, A is the target nucleus, l is the charged outgoing lepton (in CC interactions only), and X represents the final-state particles of the corresponding interactions. In addition to CC and NC, GeV-scale neutrino interactions (the focus of this thesis is one of these) are further subdivided into distinct interaction types depending on the incident neutrino energy and how it interacts with a target nucleus.

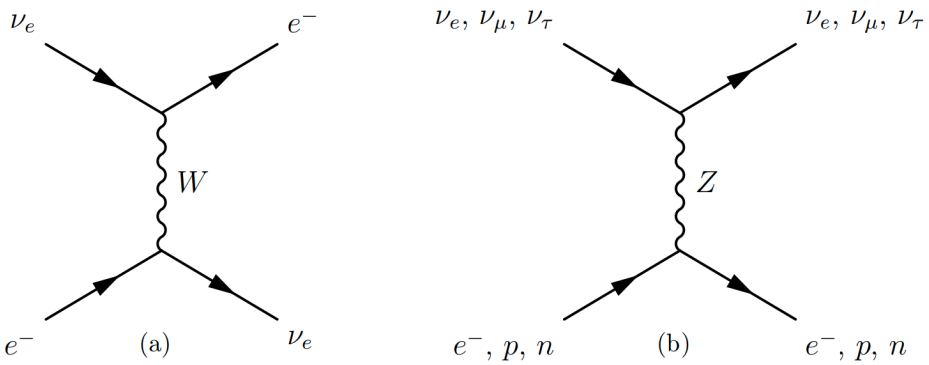

Figure 3.1: Feynman diagrams depicting examples of a CC (a) and NC (b) neutrino interaction.

This chapter discusses many different forms of neutrino interactions and gives a short description of how the different interactions occur. Section 3.1 will discuss many different higher energy neutrino interaction modes, as well as give a brief description of the neutrino interaction channel that is the focus of this thesis.

3.1 Neutrino Interaction Modes

The description of neutrino scattering between 0.1 – 20 GeV can be described by several distinct neutrino scattering mechanisms. The possibilities fall into three main categories, also shown in Figure 3.2.

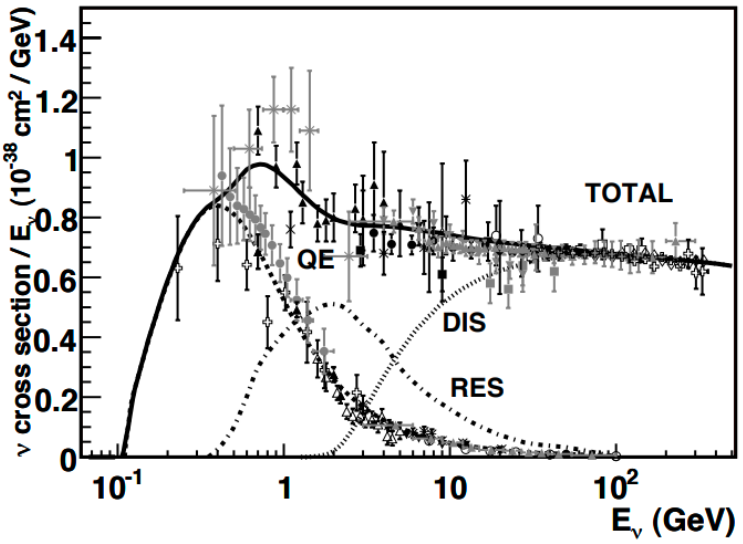

Figure 3.2: Total neutrino per nucleon CC cross sections (for an isoscalar target) divided by neutrino energy and plotted as a function of energy. The data points show the results of different experiments. Also shown are the various contributing processes that will be described in the next sections. These contributions include QE scattering (dashed), resonance production (dot-dash), and DIS scattering (dotted).

At the mean neutrino energy that is investigated by this thesis ($\sim$ 0.8GeV), the main neutrino interaction channel occurring is Quasi-Elastic (QE) scattering, which will be discussed in Section 3.1.1. The next most frequent interaction channel is Resonance (RES) Production, which will be detailed in Section 3.1.2, and is followed by Deep Inelastic Scattering (DIS) discussed in Section 3.1.3. The least common interaction channel is Coherent Pion Production (COH), which is discussed in Section 3.1.4. The last section briefly discusses other interaction channels that can occur at these neutrino energies in Section 3.1.5.

3.1.1 Quasi-Elastic Interactions

For $\sim$ 1GeV neutrino energies, the most common interaction mode is the Quasi-Elastic (QE) mode, which can be seen in Figure 3.2. In QE interactions, an incoming neutrino interacts with the nucleus, modifying the quark flavor content of a nucleon in the process, as shown in Figure 3.3. A more general charged current Quasi-Elastic (CCQE) interaction is given by:

$$\nu_l + n \rightarrow l^- + p \tag{3.3}$$

$$\bar{\nu}_l + p \rightarrow l^- + n \tag{3.4}$$

where n and p represents a neutron and proton, respectively. For NC elastic (NCE) interaction, a neutrino transfers energy to a single nucleon via Z boson exchange, so the interaction proceeds as:

$$\nu_l + N \rightarrow \nu_l + N \tag{3.5}$$

where N represents a nucleon. Note that NCE interactions also produce a nuclear recoil which is not shown in Equation 3.5. CCQE interactions are significantly easier to recognize than NCE interactions due to the presence of an outgoing charged lepton. For NCE, the signal is generally a single neutron or proton in the final state, which can be difficult to distinguish from background.

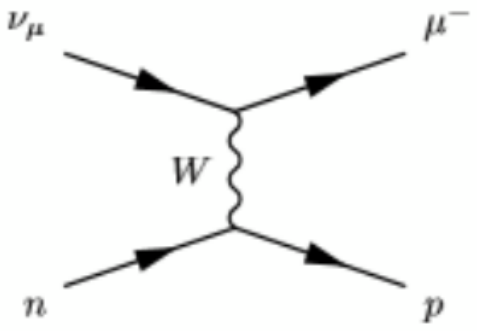

Figure 3.3: Feynman diagram that depicts CCQE. As is evident in the diagram, a ν_μ comes in and interacts with a nucleon (n) in a target nucleus and ejects a nucleon (p) and a lepton (μ^-).

Most Monte Carlo event generators use the Llewellyn-Smith model [50] for CCQE interactions, although the more recent Nieves model [51] appears to offer better agreement between simulation and data for some experiments with larger target nuclei [52].

3.1.2 Resonance Production

Given enough energy, and if the neutrino-nucleus center of mass energy exceeds the mass of a delta baryon, neutrinos can send the struck nucleon to an excited state. In this case, the neutrino interaction produces a baryon resonance (N^*). The baryon resonance quickly decays, most often to a nucleon and single pion final state:

$$\nu_l + N \rightarrow l + N^* \rightarrow l + \pi + N', \tag{3.6}$$

where N,$N' = n$,p. Other higher multiplicity decay modes are also possible as baryonic resonances created in neutrino-nucleon interactions can potentially decay to multi-pion final states. At the lowest energies, the process is dominated by production of the $\Delta(1232)$, which is the first excited state of a nucleon, as shown for example in Figure 3.4.

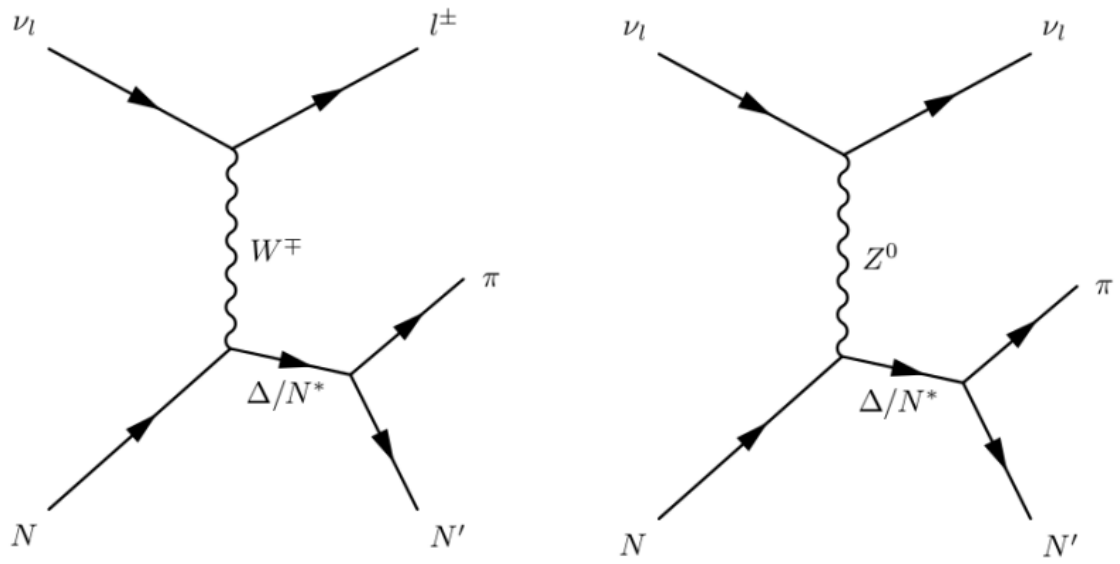

Figure 3.4: Feynman Diagrams for Resonant Production, where CC-Res is on the left, and NC-Res is on the right.

Charged-Current Resonance Production

Charged-Current Resonant Production (CCRes), as shown in Figure 3.4, is a neutrino-nucleus interaction that produces a baryon resonance via the W-boson (in the case of MicroBooNE, this is a $\Delta(1232)$ resonance) which then decays to a pion. Thus the final states under consideration here are:

$$\nu_\mu p \to \mu^- \Delta^{++} \to \mu^- p \pi^+$$

$$\nu_\mu n \to \mu^- \Delta^{+} \to \mu^- p \pi^0$$

$$\nu_\mu n \to \mu^- \Delta^{+} \to \mu^- n \pi^+$$

Neutral-Current Resonance Production

Neutral-Current Resonant Production (NCRes), as shown in Figure 3.4, is a neutrino-nucleus interaction that produces a baryon resonance via the Z-boson (in the case of MicroBooNE this is $\Delta(1232)$ resonance) which then decays to a pion. Thus the final states under consideration here are:

$$\nu_\mu p \to \nu_\mu p \Delta^{+} \to \nu_\mu n \pi^+$$

$$\nu_\mu p \to \nu_\mu p \Delta^{+} \to \nu_\mu p \pi^0$$

$$\nu_\mu n \to \nu_\mu n \Delta^0 \to \nu_\mu n \pi^0$$

$$\nu_\mu n \to \nu_\mu n \Delta^0 \to \nu_\mu n p \pi^-$$

Historically, the most commonly used resonant model in simulation has been the Rein-Sehgal model [53]. The more recent Berger-Sehgal model [54] improves on the older model by including experimental pion scattering data and leptonic mass correction terms.

3.1.3 Deep Inelastic Scattering

In deep inelastic scattering, the neutrino scatters off a quark in the nucleon via the exchange of a virtual W or Z boson producing a lepton (or a neutrino for the NC version) and a hadronic system in the final state. This breaks apart the nucleon, producing a jet of hadrons in an interaction mode known as Deep Inelastic Scattering (DIS). This is the dominant neutrino interaction mode for neutrinos with energy above about 10 GeV. Both CC and NC processes are possible:

$$\nu_\mu N \to \mu^- X \quad \text{(CC)}, \tag{3.7}$$

$$\nu_\mu N \to \nu_\mu X \quad \text{(NC)}. \tag{3.8}$$

There are only a few neutrinos undergoing DIS interactions at MicroBooNE energies, and for this reason, this interaction mode is not described in detail here. Details on these interactions can be found in [55] and in this thesis they are modelled according to the GENIE neutrino event generator.

3.1.4 Coherent Pion Production

In addition to resonant pion production, neutrinos can produce pions by interacting coherently with the nucleons forming the target nucleus. Neutrino-nucleus coherent pion production is an inelastic interaction that produces a lepton and a pion in the forward direction while leaving the nucleus in its initial state. This interaction has both a charged-current (CC) and neutral-current (NC) form, which are briefly detailed in the subsections below. The CC version of this interaction channel is depicted in the Feynman diagram in Figure 3.5. This is one of the most rare neutrino-nucleus interaction channels, and the channel has a complicated history which will be further discussed in Chapter 4.

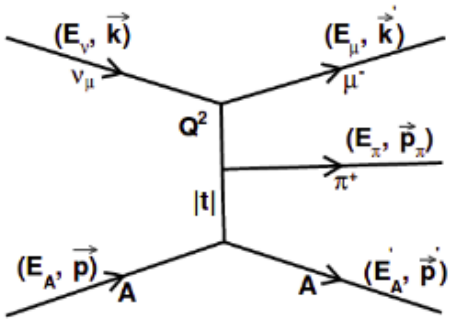

Figure 3.5: Feynman Diagram of Coherent Pion Production.

Charged-Current Coherent Pion Production

The charged-current coherent pion production processes are represented by Equation 3.9, where A is the nucleus.

$$\nu_l + A \rightarrow l^- + \pi^+ + A$$

$$\bar{\nu}_l + A \rightarrow l^+ + \pi^- + A \tag{3.9}$$

A cross section measurement of the CC version of this interaction channel on argon is the primary focus of this thesis.

Neutral-Current Coherent Pion Production

The neutral-current coherent pion production processes are represented by Equation 3.10, where A is the nucleus.

$$\nu_l + A \rightarrow \nu_l + \pi^0 + A$$

$$\bar{\nu}_l + A \rightarrow \bar{\nu}_l + \pi^0 + A \tag{3.10}$$

3.1.5 Other Interaction Modes

Neutrino interactions can also produce final states involving strange quarks. At neutrino energies below 2 GeV, Cabibbo suppressed single kaon production $\nu_\mu N \rightarrow \mu^- K^+ N$ is the dominant K^+ production mechanism. At higher energies, K^+ mesons arise via associated production accompanied by strangeness = -1 baryons (Λ, $\Sigma^\pm$) or mesons (K^-, $\bar{K}^0$) such that there is no net change in strangeness ($\Delta S = 0$). This can occur through an intermediate resonance state or in DIS by hadronisation, the production of mesons and baryons from the struck quark. Measuring neutrino-induced kaon production is of interest primarily as a source of potential background for proton decay searches. Proton decay modes containing a final state kaon, $p \rightarrow K^+\nu$, have large branching ratios

in many SUSY GUT models. Because there is a non-zero probability that an atmospheric neutrino interaction can mimic such a proton decay signature, estimating these background rates has become an increasingly important component to such searches.

Neutrino interactions which resemble CCQE can also arise from "two-particle two-hole" (2p2h) processes [51]. In these processes, a neutrino scatters on a pair of nucleons which are interacting with each other via meson-exchange currents (MEC). Older versions of MC event generators do not account for MEC interactions. Recent versions of the widely-used GENIE event generator [56] include a model of CC 2p2h interactions based on the work of Nieves *et al.* [51]. For NC, the only 2p2h treatment available in GENIE is the empirical Dytman model described in Reference [57].

With the many different forms of neutrino-nucleus interactions that are likely to be encountered now presented, focus can now be returned to the signal channel of the analysis presented in this thesis: CC-Cohπ^+ production. The next chapter, Chapter 4, will go into further detail on some of the various models of CC-Cohπ^+ production, it will list the motivations for furthering our understanding of the interaction channel, as well as give a history on the measurements made of this channel and the channel's controversial history.

4 A Controversial History

"The most important step a man can take. It's not the first one, is it? It's the next one. Always the next step."

Brandon Sanderson, *Oathbringer*

This chapter covers the rather complicated history of the neutrino-nucleus scattering interaction called Charged-Current Coherent Pion Production, CC-Coh π^+, as well as the theories of the interaction (including the Adler's theorem models of Rein-Sehgal and Berger-Sehgal, and an example of a *microscopic* model, which were specifically created to describe neutrino interactions for neutrino energies less than roughly $\sim$ 2GeV). The chapter closes with some of the motivations for furthering our understanding of this interaction channel.

The chapter begins by defining CC-Coh π^+ interactions in Section 4.1, and then proceeds to lay out some of the controversial history of measurements for the channel in Section 4.2. A rather in depth look at the Adler's theorem models of Rein-Sehgal and Berger-Sehgal, as well as a so called *microscopic* class of model for describing CC-Coh π^+ are all detailed in Section 4.3. The chapter concludes by discussing the many motivations for furthering our understanding of CC-Coh π^+ in Section 4.4.

4.1 Defining Neutrino-Induced Charged-Current Coherent Pion Production

Neutrino-Induced Charged-Current Coherent Pion Production (CC-Coh) occurs whenever a neutrino (ν_l) of some lepton flavor l interacts coherently with a target nucleus and ejects a charged pion (π) and a lepton (l) of the same flavor as the interacting ν_l. This type of neutrino interaction has two key characteristics:

- the target nucleus is left in its ground state due to there being virtually no four-momentum transfer to the nucleus,
- and the two particles that are produced are both forward boosted with a small opening angle between them.

This can be said like so: charged-current coherent pion production in neutrino-nucleus scattering, represented by Equation 4.1 and depicted by the Feynman diagram in Figure 4.1, is a process in which the neutrino scatters coherently from an entire nucleus,

leaving the nucleus unchanged. No quantum numbers are exchanged and there is little four-momentum, $|t|$, transfer to any nucleon. Due to these restrictions the outgoing lepton and pion are aligned with the beam direction and no other hadrons are produced.

$$\nu_\mu + A \rightarrow \mu^- + \pi^+ + A \tag{4.1}$$

This particular neutrino-nucleus interaction channel has a bit of a controversial history, and needs to be studied further to help discern the ambiguity in the proposed models for the channel. This channel is the main subject of this thesis and a discussion of the controversial history follows in Section 4.2.

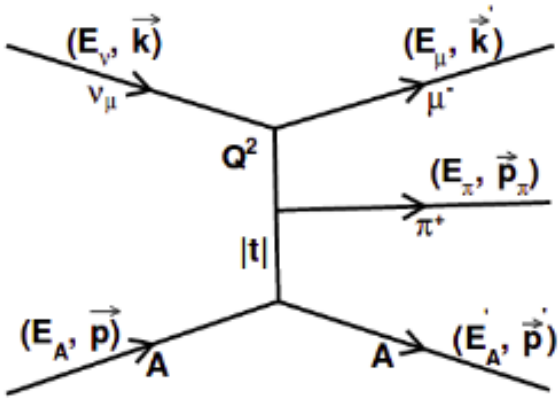

Figure 4.1: Feynman Diagram of ν_μ-Induced Charged-Current Coherent π^+ Production.

4.2 The Controversial History

The first observation of coherent pion production was reported in February 1983 by the Aachen-Padova spark-chamber experiment [58] in CERN's PS neutrino or antineutrino beam. While studying a sample of solitary π^0s produced in their ν_μ and $\bar{\nu}_\mu$ beams they observed a significant excess of events in the forward-going direction, an excess that was not present in another sample in which the π^0 was produced along with a proton. They identified this excess as NC coherent pion production: a theoretical description of which had first been published by K.S. Lackner [59] four years earlier in the context of determining the structure of the weak neutral-current.

In response to Aachen-Padova's discovery, Dieter Rein and Lalit Sehgal developed a theoretical model for coherent pion production [60], building on Lackner's paper and their own recent work on resonance pion production. Their predictions agreed with the cross section extracted by Aachen-Padova, as well as one from a retrospective re-analysis of data from the Gargamelle experiment [61].

Over the following decade five more experiments observed and measured both CC and NC coherent pion production with neutrinos and antineutrinos. Many giving exceptionally clean and clear signals of coherent production. Over a wide range of neutrino

energies all experimental data were consistent with predictions from the Rein-Sehgal model, within the resolution of the experiments.

The resurgance of neutrino physics that accompanied the discovery of oscillations at the end of the 20th century also brought about a series of experiments at lower neutrino energies than had been studied previously. In stark contrast to previous experiments, K2K's search for CC coherent pion production at E_ν of 1.3 GeV found no evidence CC-Cohπ production. This surprising result was later confirmed by SciBooNE, which also set cross section limits well below the level predicted by the Rein-Sehgal model implemented in NEUT (the interaction simulation both experiments were using). Measurements of NC coherent pion production were successfully made in both MiniBooNE and SciBooNE, but even here the cross sections reported were substantially smaller than the values expected from the Rein-Sehgal implementations in NEUT and NUANCE.

These inconsistencies at lower neutrino energies sparked new models to be produced to describe CC coherent pion production at lower neutrino energies, which moved the predicted cross section to lower levels than what was predicted by the Rein-Sehgal model. More recently, CC coherent pion production has been observed by the MINERνA experiment for neutrino energies between 1.5 GeV and 20.0 GeV. T2K has also recently published the first measurement of this channel below neutrino energies of 1.5 GeV.

Difficulty in achieving simultaneous agreement with data at high and low energies, coupled with frailties of Rein-Sehgal at lower neutrino energies, suggest an alternative model may be required to describe coherent pion production. Though, it may be premature to rule out the Rein-Sehgal model for a number of reasons:

- K2K reported their CC coherent limit at $E_\nu \sim 1.3$GeV using an early version of the model which did not take into account the muon's mass.
- Both SciBooNE and K2K searched for CC coherent in the Q^2 distribution, instead of the more characteristic $|t|$.
- the cross section and pion kinematics predicted by the Rein-Sehgal model can vary significantly depending on the inputs used.

There are several models of coherent pion production in circulation now. At present, existing experimental data is nowhere near sufficient to discriminate between them. Further discussion of the classes of models for CC coherent pion production follow in Section 4.3.

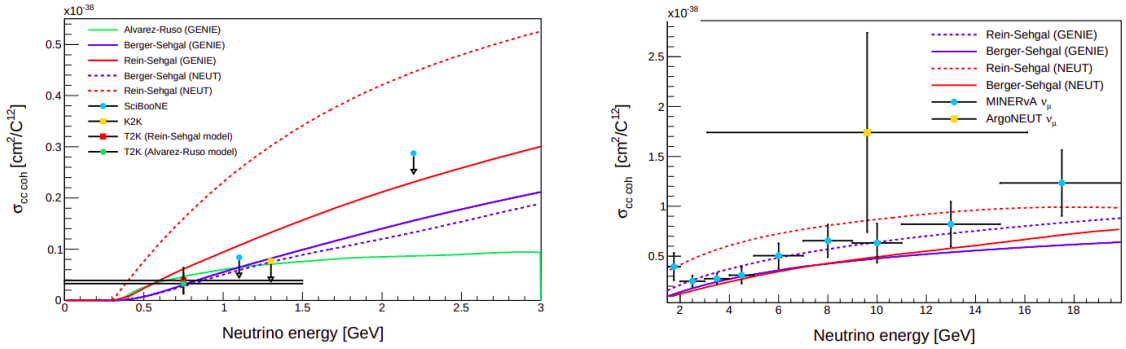

Figure 4.2: Left: comparison of the Rein-Sehgal (red), Berger-Sehgal (blue), and the Alvarez-Ruso *et al.* (green) models as predicted by NEUT (dashed) and GENIE (solid) against the K2K, SciBooNE, and T2K results. Right: comparison of the Rein-Sehgal and Berger-Sehgal models against the MINERνA and ArgoNEUT results.

4.3 The Classes of Models for Charged-Current Coherent Pion Production

The classes of models of CC-Coh π^+ can be broken into two distinct categories: models that use Adler's Theorem which are discussed in Section 4.3.1, and so-called *microscopic* models which are discussed in Section 4.3.2.

4.3.1 Adler's Theorem Models

The first class of models uses Adler's Partially Conserved Axial-Vector Current (PCAC) Theorem [62] to relate the coherent scattering cross section at $Q^2 = -q^2 = -(p_\nu - p_\mu)^2 = 0$ with the pion-nucleus elastic scattering cross section. The most popularly used model of this form is the Rein-Sehgal model [60, 63], and the next most frequent is the Berger-Sehgal model [64], and both of these models are given a more detailed description below. The validity of these models below neutrino energies of roughly 2 GeV is limited.

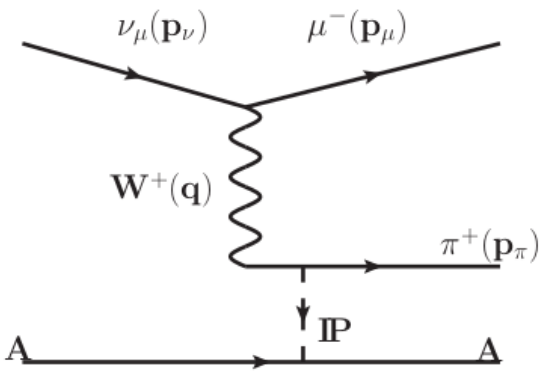

Figure 4.3: Feynman diagram depicting an Adler's PCAC theorem class of CC-Coh π^+.

The Rein-Sehgal Model

The Rein-Sehgal Model was originally constructed to model Neutral-Current Coherent π^0 production, and was extended to pertain to the Charged-Current version. This model is very widely used in neutrino oscillation experiments and is the most commonly used model of CC-Coh π^+, in general. Based on Adler's PCAC theorem, the differential cross section for neutrino-induced Coherent π production when $Q^2 = 0$ is:

$$\left.\frac{d^3\sigma(\nu A \to lA\pi)}{dxdyd|t|}\right|_{Q^2=0} = \frac{G_F^2}{\pi^2} f_\pi^2 m_N E_\nu (1-y) \left.\frac{d\sigma(\pi A \to \pi A)}{d|t|}\right|_{E_\nu y = E_\pi}, \tag{4.2}$$

where $x = Q^2/2m_N\nu$ and $y = \nu/E_\nu$ are the Bjorken kinematic variables, ν is the energy transfer, $|t|$ is the square of the four-momentum transferred to the nucleus, G_F is the weak coupling constant, f_π is the pion decay constant, and m_N is the mass of the nucleon. Adler's PCAC allows this relation of the forward neutrino differential cross section at the nucleus A to the pion differential cross section of the process $\pi A \to \pi A$.

Now, this is a feasible expression only for the forward going case ($Q^2 = 0$), and to make the expression usable for non-forward going cases ($Q^2 \neq 0$), Rein-Sehgal used the vector dominance model by attaching a propagator term $\left(\frac{m_A^2}{Q^2+m_A^2}\right)^2$ to the differential cross section, and the new equation became:

$$\left.\frac{d^3\sigma(\nu A \to lA\pi)}{dxdyd|t|}\right|_{Q^2\neq 0} = \frac{G_F^2}{\pi^2} f_\pi^2 m_N E_\nu (1-y) \left(\frac{m_A^2}{Q^2+m_A^2}\right)^2 \left.\frac{d\sigma(\pi A \to \pi A)}{d|t|}\right|_{E_\nu y = E_\pi}, \tag{4.3}$$

where m_A is the axial vector mass, and this new expression is not strictly confined to the forward going case ($Q^2 = 0$).

The pion-nucleus differential cross section is expressible as:

$$\frac{d\sigma(\pi A \to \pi A)}{d|t|} = A^2 |F_A(t)|^2 \left.\frac{d\sigma(\pi N \to \pi N)}{d|t|}\right|_{|t|=0},$$

where A is the atomic number of the nucleus, and $F_A(t)$ is the nuclear form factor (including the effect of pion absorption). Through the use of the optical theorem, the pion-nucleon differential cross section in the forward direction is given by:

$$\left.\frac{d\sigma(\pi N \to \pi N)}{d|t|}\right|_{|t|=0} = \frac{1}{16\pi}\left[\sigma_{tot}^{\pi N}\right]^2(1+r^2), \;\; r = \frac{\mathrm{Re}[f_{\pi N}(0)]}{\mathrm{Im}[f_{\pi N}(0)]}.$$

In the model, an average cross section from measurements of pion-deuteron scattering is incorporated as $\sigma_{tot}^{\pi N}$. For the nuclear form factor, a simple form of:

$$|F_A(t)|^2 = e^{-b|t|}F_{abs}$$

is adopted, where b is related to the nuclear radius R, given by:

$$b = \frac{1}{3}R^2, \; (R = R_0 A^{1/3}).$$

The term F_{abs} is a $|t|$-independent attenuation factor representing the effect of pion absorption in the nucleus, expressed as:

$$F_{abs} = e^{-\langle x\rangle\lambda},$$

where $\langle x\rangle$ and λ are the average path length traversed by the pion produced in the nucleus, and the absorption length, respectively. By assuming that the nucleus is a homogeneous sphere with uniform density, $\langle x\rangle$ and λ are calculated as:

$$\langle x\rangle = \frac{3}{4}R, \; \lambda = A\left(\frac{3}{4\pi R^3}\right)\sigma_{inel}^{\pi N},$$

where $\sigma_{inel}^{\pi N}$ is the pion-nucleon inelastic cross section. This leads to:

$$F_{abs} = exp\left(-\frac{9A^{1/3}}{16\pi R_0^2}\sigma_{inel}^{\pi N}\right).$$

Therefore, the differential cross section for Coherent π production by Rein-Sehgal is:

$$\frac{d^3\sigma(\nu A \to lA\pi)}{dxdyd|t|} = \frac{G_F^2}{\pi^2}f_\pi^2 m_N E_\nu(1-y)\left(\frac{m_A^2}{Q^2+m_A^2}\right)^2\frac{A^2}{16\pi}\left[\sigma_{tot}^{\pi N}\right]^2(1+r^2)e^{-b|t|}F_{abs}. \quad (4.4)$$

There is an important modification that must be taken into account whenever the mass of the out-going lepton is non-zero. This modification is expressed as a simple multiplicative correction factor;

$$C = \left(1 - \frac{1}{2}\frac{Q_{min}^2}{Q^2+m_\pi^2}\right)^2 + \frac{1}{4}y\frac{Q_{min}^2(Q^2-Q_{min}^2)}{(Q^2+m_\pi^2)^2}, \quad (4.5)$$

where

$$Q_{min}^2 = m_l^2\frac{y}{1-y}.$$

The range of the variable Q^2 is:

$$Q^2_{min} < Q^2 < 2m_N E_\nu y_{max}$$

where y lies between $y_{min} = m_\pi/E_\nu$ and $y_{max} = 1 - m_l/E_\nu$. Thus, the differential cross section with the lepton mass correction is expressed as:

$$\left.\frac{d^3\sigma(\nu A \to lA\pi)}{dxdyd|t|}\right|_{m_l \neq 0} = C\theta(Q^2 - Q^2_{min})\theta(y - y_{min})\theta(y_{max} - y)\left.\frac{d^3\sigma(\nu A \to lA\pi)}{dxdyd|t|}\right|_{m_l=0}. \tag{4.6}$$

The lepton mass correction is only applied to the charged current channel and is not applied to the neutral current channel. The Rein-Sehgal model sets the axial vector mass, m_A, to 1.0 GeV/c^2, and the nuclear radius parameter, R_0, is set to 1.0 fm. An important result of the Rein-Sehgal model is that the cross section has an atomic number, A, dependence on the order of $A^{1/3}$ [65].

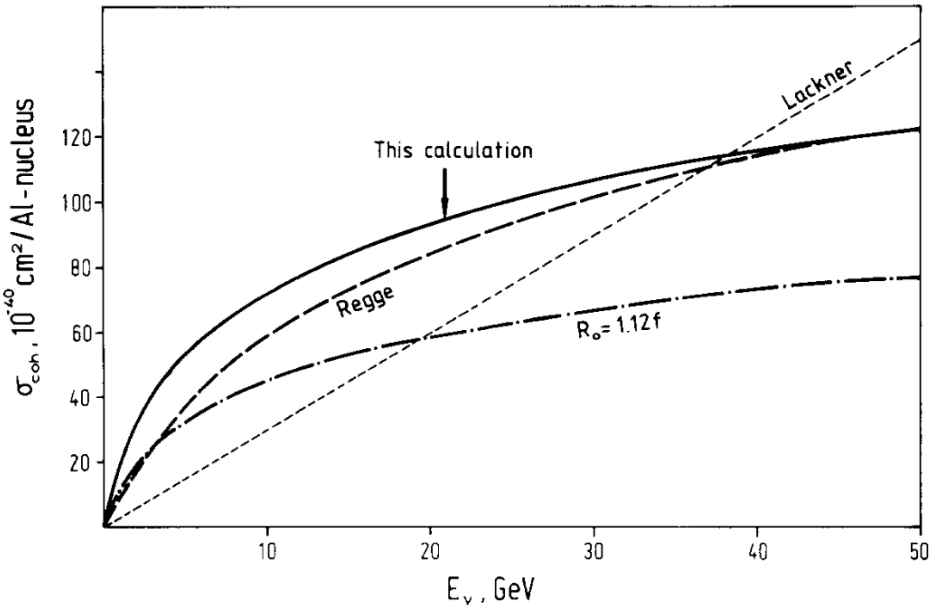

Figure 4.4: Energy dependence of the total coherent π^0 cross section for ^{27}Al corresponding to this calculation with $R_o = 1.0fm$, and with $R_o = 1.12fm$. Figure from [4].

The Berger-Sehgal Model

The Berger-Sehgal Model is a newer Adler's PCAC based model that uses data from pion-nucleus elastic scattering, and is a modification of the Rein-Sehgal Model. In the Berger-Sehgal Model, the parameterization of the $\pi^\pm A$ elastic scattering cross section is instead fit to charged pion-carbon ($\pi^\pm C$) elastic scattering data and scaled to other

nuclei. This approach avoids some of the uncertainties from modeling nuclear effects, *e.g.* pion absorption, in the Rein-Sehgal parameterization. In the Berger-Sehgal Model, coherent cross sections scale as $A^{2/3}$ with the atomic number, which differs from the Rein-Sehgal scaling of $A^{1/3}$ [64].

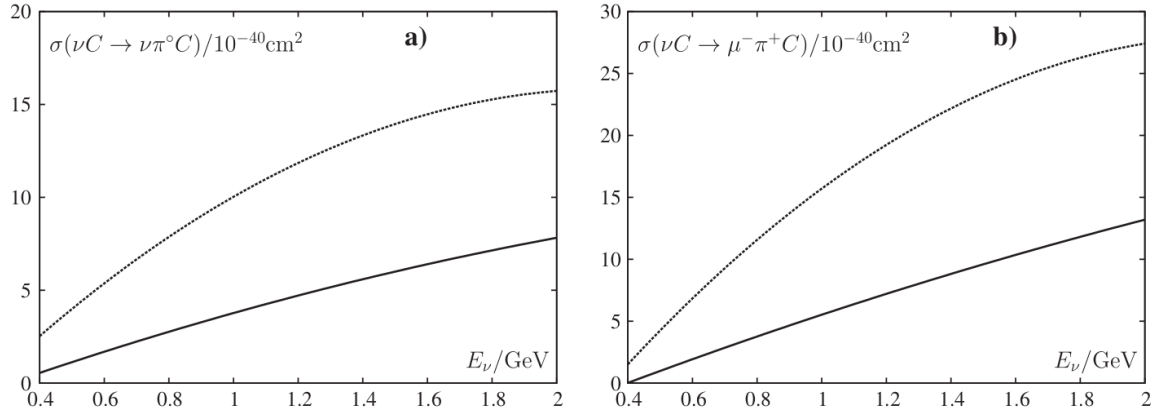

Figure 4.5: Cross section per nucleus of coherent π production by neutrinos off carbon nuclei using the Berger-Sehgal model, (a) is the NC reaction $\nu_\mu + {}^{12}\mathrm{C} \to \nu_\mu + {}^{12}\mathrm{C} + \pi^0$, and (b) the CC reaction $\nu_\mu + {}^{12}\mathrm{C} \to \mu^- + {}^{12}\mathrm{C} + \pi^+$. The upper curve is calculated using the hadronic Rein-Sehgal model, the lower curve using the Berger-Sehgal parametrization of pion carbon scattering data. Figure from [5].

4.3.2 Microscopic Models

The second class of models, known as *microscopic* models, was developed specifically for neutrino energies less than $2GeV$. These models are based on the single nucleon process $\nu_l N \to l^- N \pi^+$, which is dominated by Δ production at low energies as shown in the diagram in Figure 4.6. Where PCAC models describe coherent pion production off of a nucleus in terms of a single interaction channel with that nucleus, a microscopic model describes the process in terms of a coherent sum of neutrino-nucleon interactions where the final-state nucleon is constrained to remain in the same quantum state. The model discussed here is the Alvarez-Ruso *et al* [6, 7], which has only recently been implemented in a neutrino event generator, and is the only microscopic model that's been implemented thus far.

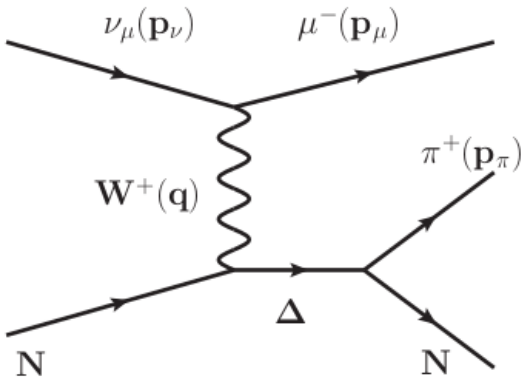

Figure 4.6: Feynman diagram depicting a microscopic model class of CC-Coh π^+. Figure from [6, 7].

The Alvarez-Ruso et al. Microscopic Model

The complete Alvarez-Ruso model includes four neutrino-nucleus pion producing channels, two of which involve intermediate propagation of a Δ, and two the propagation of a nucleon. The first paper on the model described CC coherent pion production [7, 66], and included only the s-channel Δ mode which dominates the reaction. This was extended to include the other three modes in the second paper on NC coherent [6, 67], for which they become more relevant.

Two significant nuclear effects are also taken into account. First, the properties of Δ's, such as their mass and decay width, are modified by their presence inside a nuclear environment. Second, the outgoing pion is also affected by the nuclear environment, treated as a "distortion" of its wavefunction by a nuclear potential (this is effectively a more careful treatment of the pion absorption included in Rein-Sehgal for low energy pions). The results of the model are depicted in Figure 4.7, where the CC coherent pion production cross section is plotted as a function of E_ν for a variety of nuclear targets.

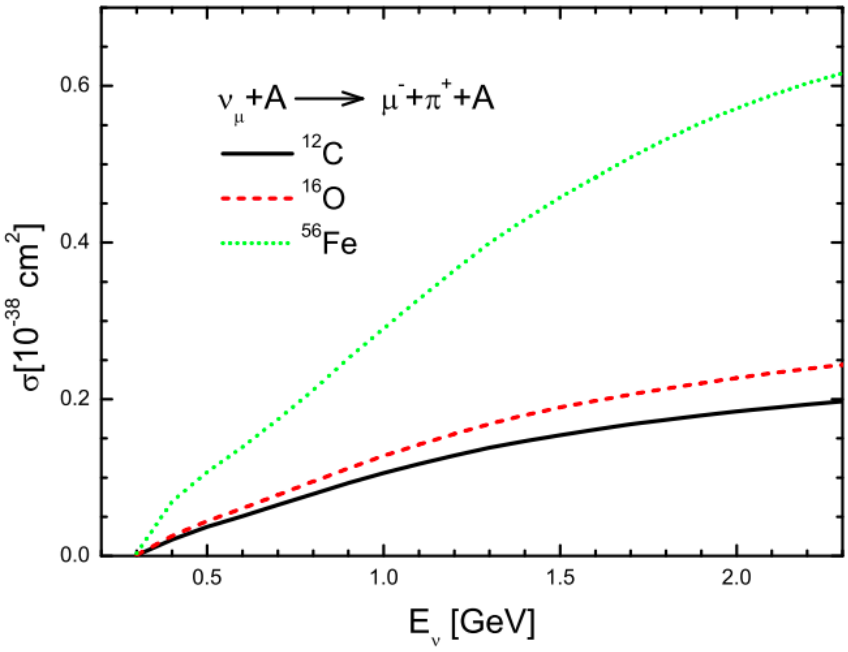

Figure 4.7: Alvarez-Ruso *et al* CC-Coh π^+ cross section as a function of neutrino energy (E_ν) on a variety of target nuclei.

4.4 The Motivations for Studying This Channel

The main motivations for studying CC-Coh π^+ are as follows:

- SciBooNE (in BNB, same as MicroBooNE) and K2K failed to observe the channel, but set upper limits.
- T2K, at comparable neutrino energy, did observe CC-Coh π^+.
- Higher energy experiments have observed CC-Coh π^+ and have shown that it is satisfactorily modeled using Rein-Sehgal, but Rein-Sehgal is **NOT** satisfactory at low neutrino-energy ($< 2GeV$).
- MicroBooNE is in the unique position to shed light on what's happening at lower neutrino-energies.

Further motivations for studying this interaction channel includes:

- NC-Coh π^0 is a ν_μ-induced background for $\nu_\mu \rightarrow \nu_e$ oscillations. The NC version of Coherent π production is modeled the same way as the CC version, and understanding the differences is vital for appearance measurements.

- Coherent π production has been considered to be used as a standard candle, due to its relative simplicity, to help constrain neutrino fluxes and neutrino-energy reconstruction for oscillation analyses, but a better understanding of this channel would be necessary to do this.
- The misidentification of π^+s as protons distorts the reconstructed neutrino-energy distribution in ν_μ disappearance searches.

Now that the signal channel of this analysis has been defined, and the motivations for furthering our understanding have been given, it is time to move on to discussing the detector technology that will be used to make the cross section measurement of CC coherent pion production. The next chapter, Chapter 5, will discuss liquid argon time projection chambers (LArTPC).

5 Liquid Argon Time Projection Chambers

This chapter details liquid argon time projection chambers (LArTPCs) and the work that has been done on them for this thesis analysis, both in software and hardware. The chapter starts with a brief historical review of LArTPC technology, such as its invention as well as the invention of the time projection chamber (TPC), in Section 5.1. Next, the chapter continues in Section 5.2 where a discussion of the properties of liquid argon that make it useful as a detector medium occurs. The chapter then discusses the working principles of LArTPCs in Section 5.3. The chapter closes with a look at the work done on the technology during the course of this analysis, in terms of both hardware and software, in Section 5.4.

5.1 Brief Historical Review of LArTPC Technology

The time projection chamber (TPC) concept was invented by David Nygren in the late 1970s [68]. In 1977, Carlo Rubbia devised a LArTPC, operating under many of the same principles as Nygren's initial TPC design, but using liquid argon as a sensitive medium instead of a gas [69]. Developments in this technology continue to push LArTPCs to the forefront for current and upcoming neutrino detectors. The properties of argon that make it the ideal medium for LArTPCs is discussed in Section 5.2 next.

5.2 Liquid Argon Properties

The properties of the noble element argon make it ideal for use in a TPC. It is chemically inert, which allows the ionization electrons to drift large distances without being absorbed. It is relatively cheap, readily available ($\approx 1\%$ of the air, by weight), stable and has a relatively low mean ionization potential (23.6 eV). In addition, the high density of argon allows for a compact detector with a good event rate compared with lighter mediums such as water. Further tables, and a more in depth description of the properties of liquid argon can be found in [70].

Section 5.2.1 discusses the ways in which scintillation light is produced in liquid argon by charged particles that traverse the liquid argon. Section 5.2.2 briefly talks about the ionization potential of liquid argon, and how the ionization potential is modeled. Section 5.2.3 discusses the ways that ionized electrons are drifted through liquid argon and how there is non-negligible diffusion that occurs as the electrons are moved through

argon, both longitudinal and transverse. Section 5.2.4 briefly talks about the impacts of impurities in liquid argon and how electrons attach to those impurities.

5.2.1 Scintillation

A charged particle crossing liquid argon causes ionization and excitation of the argon atoms, yielding free electrons and the emission of scintillation light. Scintillation light is observed in the Vacuum Ultra-Violet (VUV) range in a band centered at 128nm with a FWHM of about 10nm, and is attributed to the emission of excited diatomic molecules (excimers). Figure 5.1 shows the two chains through which scintillation light can be produced in liquid argon.

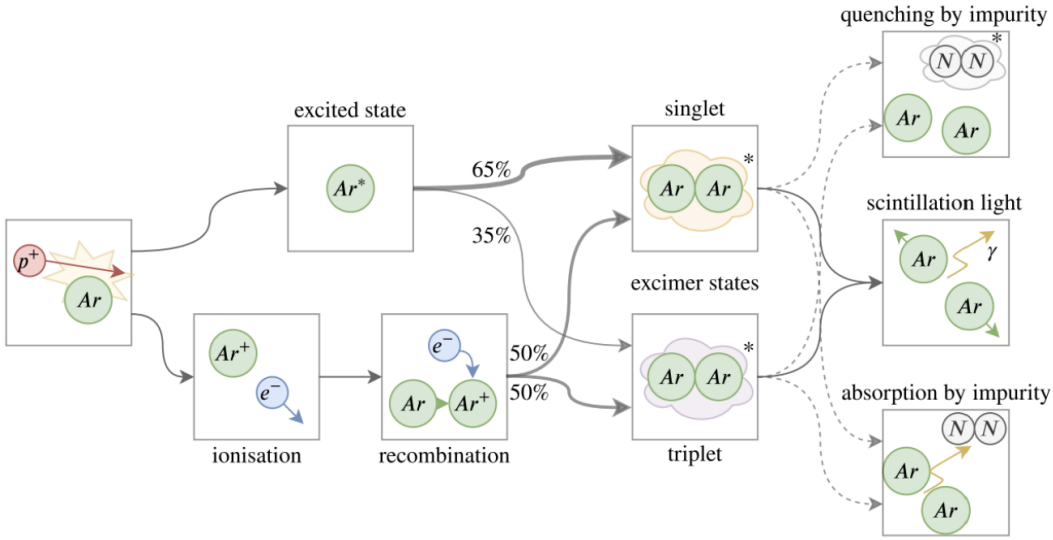

Figure 5.1: Scintillation light production in Liquid Argon. A charged particle excites (upper sequence) or ionizes (lower sequence) the argon atoms. The first process gives rise to self-trapped exciton luminescence while the latter can lead to recombination luminescence. In both of these mechanisms, the scintillation light production requires the formation of excimers. The production of scintillation light can be suppressed through quenching or absorption by impurities, such as nitrogen, as shown on the panels on the right. Figure from [8].

The two chains through which scintillation light can be produced in liquid argon are:

1. **Self-trapped exciton luminescence:** Charged particles travelling in the liquid argon leave a fraction of the argon atoms in excited states. These excitons form a short-lived dimeric molecule with another argon atom, called dimers or excimers. The majority of those are in the singlet state $^1\Sigma_u$, and approximately one-third correspond to the triplet state $^3\Sigma_u$.

2. **Recombination luminescence:** Alternatively, the charged particles can ionize the argon atoms, creating free electrons. When free electrons recombine with the positive Ar atoms, these can again create excited dimers. In this process the creation of the singlet or triplet excimer states are equally likely.

The $^1\Sigma_u$ singlet gives rise to a fast scintillation light component with a decay time of $\approx$ 6ns while the $^3\Sigma_u$ triplet has a decay time of $\approx$ 1500ns. This means that liquid argon scintillation light will consist of fast and slow components that are well separated, and both are peaked in the VUV region at 128nm. It is an important note that impurities in the liquid argon can reduce the amount of scintillation light through quenching and absorption, as is shown in Figure 5.1.

5.2.2 Ionization

The average energy required to produce an electron-ion pair in LAr is $W_i = 23.6 \pm 0.3eV$ [71, 72]. This value is smaller than that obtained in gaseous argon ($W_g = 26.4$ [73]), which indicates the presence of a conduction band in the condensed state [71].

Charge recombination in liquid argon is important for the operating principles of LArTPCs due to the fact that you want to drift the ionization electrons over to the sense wires. There are several different recombination models that have been proposed [74, 75, 76]. These models have a brief description following.

The Jaffe [75] "columnar" model is approximated by the same expression as the so-called Birk's law describing the quenching effects in scintillators:

$$Q = Q_0(1 + \frac{k_E}{\varepsilon})^{-1}, \tag{5.1}$$

where Q is the collected charge, Q_0 the initial ionization charge, ε is the electric field and k_E is a constant to be obtained from a fit to data. This model has been successfully used for high drift fields.

An explicit dependence on the stopping power $< dE/dx >$ and a normalization constant have been introduced by [76], where:

$$Q = A\frac{Q_0}{1 + k/\varepsilon < dE/dx >}, \tag{5.2}$$

where A and k are parameters to be fit. This phenomenological expression, when fit to the ICARUS 3t data [77] for drift fields of $0.2 - 0.5$kV/cm, yields [78] $A = 0.800 \pm 0.003$, and $k = 0.0486 \pm 0.0006$ kV/cm g/(cm^2 MeV).

The so-called box model [74] predicts:

$$Q = Q_0\frac{1}{\xi}\ln(1 + \xi) \tag{5.3}$$

where ξ is a parameter that is proportional to the ionization charge density and inversely proportional to the electric field. This expression has been successfully used [74] to fit

the dependence of charge recombination for low energy electrons as a function of an electric field up to 10 kV/cm.

The recombination phenomenon's importance for liquid argon results from its direct affects on the discrimination of particle types on the basis of their stopping power and achievable energy resolution. Further understanding and measurements of this effect need to be made.

5.2.3 Drift and Diffusion

The drift velocity of electrons in LAr depends primarily on the electric field strength. A weaker dependence on the temperature has been measured. The addition of small amounts of impurities to LAr causes the drift velocity to increase.

Knowledge of the diffusion coefficient D is especially important for long drift times because it directly affects the accuracy of the drift time measurement and the transverse smearing of the reconstructed tracks in a LArTPC. The spread of an isolated group of electrons increases with drift time t as $\sigma = \sqrt{2Dt}$. For gases, the diffusion coefficient in a direction parallel to an electric field (D_L) differs from that in the transverse direction (D_T). For argon gas D_L is substantially lower than D_T.

5.2.4 Electron Attachment to Impurities

In the presence of electronegative impurities, the concentration of free elections $[e]$ in LAr decreases exponentially with time according to:

$$\frac{d[e]}{dt} = -k_s[S][e] \Rightarrow [e] = [e_0]e^{-k_s[S]t} = [e_0]e^{-t/\tau_e} \tag{5.4}$$

where $[S]$ is the concentration of electronegative impurities, k_s is an electron attachment rate constant and $\tau_e = 1/(k_s[S])$ is the electron lifetime. Knowledge of the effect of oxygen is particularly important because it is one of the main contaminants in commercial LAr. The attachment rate constants to oxygen have been measured as a function of the electric field strength [70].

5.3 Liquid Argon Time Projection Chambers

LArTPCs can be broken down into four main components: the cryogenic and liquid argon purification system, the electronic readout and wire plane system, the light collection system, and the drift electric field and feedthrough system. The operating principle of these machines is a relatively simple concept and is illustrated by Figure 5.2. The large open cuboid-shaped volume is filled with ultra-pure liquid argon. A homogeneous electric field is created by a high voltage cathode on one side and a grounded anode on the opposite side. Any charged particle that traverses the liquid argon will excite and ionize the medium, producing scintillation light which can be detected by the light collection system, and ionization electrons which can be drifted over and readout by sense

wires. The purity of the argon is extremely important such that the drifted electrons can guarantee an on the order of milliseconds readout window drift time before the electrons have a chance to recombine.

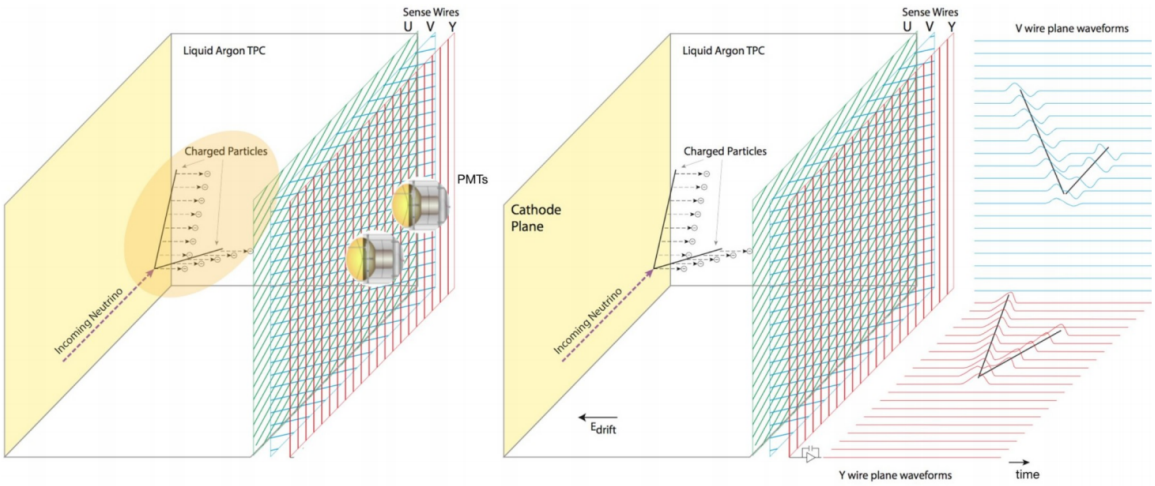

Figure 5.2: Operating principle of the LArTPC as a neutrino detector, where an incoming neutrino comes in, interacts with the liquid argon, and produces two charged particle tracks that both produce scintillation light and ionization electrons as they traverse the liquid argon. (Left) The fast scintillation light is collected by the PMT system. (Right) The slow drift of ionization electrons across the TPC volume to the wire planes by the drift electric field. A depiction of the charge collected on the sense wires is also shown on the far right. Figure from [9]

These next sections further discuss the four main components of LArTPCs in more detail, and give their importance more emphasis.

5.3.1 Cryogenic and Liquid Argon Purification Systems

Due to the relatively small span of temperature that argon is a liquid under, a cryogenic system to maintain the low temperature of the argon to maintain it as a liquid is absolutely vital to the successful operation of a LArTPC. Without a cryogenic system, there would not be liquid argon for the TPC.

As has been mentioned above, another vital aspect for the successful operation of a LArTPC is the purity of the liquid argon employed in the cryogenic vessel. Low purity argon used in a LArTPC can cause a number of problems, where the most harmful aspects would be the quenching of scintillation light, and the diminished drift time of ionization charge in the TPC, both causing decreased resolution capabilities of the detector.

5.3.2 Readout and Wire Plane Systems

Perhaps the most important aspect of a LArTPC is the readout and charge collection system. Most LArTPCs currently use a wire plane system, where wire planes composed of wires that are equally spaced are used to induce an electrical signal on from drifting the ionization electrons from a charged particle traversing the detector, such that it can be readout and reconstructed to reproduce a 3D image of the particle interaction. The minimum number of wire planes necessary in order to reconstruct a 3D image is at least two, but in the case of the LArTPC used for this thesis' analysis, three wire planes are used, where two planes are induction planes (the charge induces a bipolar signal on the wires) and the last plane is the collection plane where the charge is deposited. The specifics of the LArTPC used in the analysis of this thesis will be discussed more in Chapter 6.

5.3.3 Light Collection Systems

The scintillation light that is produced by charged particles traversing the liquid argon of a LArTPC (discussed in Section 5.2.1) can be used in a number of ways. It can be used as a trigger where if your detector is operating downstream of a neutrino beamline, coincidence of the fast scintillation light with the time of the beam spill can act as a cosmic background discriminant for neutrino event detection. The timing information from the detection of scintillation light is also employed in the reconstruction of the time-projected dimension of a LArTPC.

5.3.4 Drift Electric Field and Feedthrough Systems

LArTPCs require a drift high-voltage system in order to provide a uniform and stable drift electric field over which to drift the ionization electrons from charged particle tracks. Without one, there would not be a way to drift the ionization charge to the sense wires of the LArTPC, and thus there would not be any electrical signal to reconstruct into tracks. Monitoring of this electric field is also important for reconstruction of the third-dimension of a LArTPC detector as a result of the drift velocity's dependence on the electric field. A common way of making a uniform and stable drift electric field in a LArTPC is by using voltage divider steps between the cathode and anode of a LArTPC.

5.4 Work I Have Done on LArTPCs

This short section is intended to describe the many different projects worked on during the course of this thesis. Though not all of them came to publication, the learning that resulted has been invaluable and is worth documenting here. These subsections will be broken into parts based on the experiment that I worked on at the time.

5.4.1 LArIAT/PixLAr Experiment

The work that I did for the Liquid Argon TPC In A Testbeam (LArIAT) Experiment can be summarized as follows:

- Helped to construct and install the third set of the wire planes used in the LArTPC of the experiment.
- Took many hours of shifts of data taking times for the experiment.
- Helped with a proton calorimetry study.
- I helped install the Pixel planes for the PixLAr implementation of the LArIAT experiment, as well as taking many hours of shifts for data taking in this implementation.

5.4.2 SBND Experiment

The work that I did for the Short Baseline Neutrino Detector (SBND) Experiment can be summarized as follows:

- Tested the cold electronics and ASICs deployed in the SBND experiment.
- Helped to create a database for the results of the cold electronics testing for the different ASICs tested.

5.4.3 ICARUS Experiment

The work that I did for the ICARUS Experiment can be summarized as follows:

- I was responsible for the installation of the Drift HV System for the detector.
- I was also responsible for the pORC review, as well as the modifications necessary to the Drift HV system for it to work at Fermilab. Such as the installation of the electrical racks and the power supplies as well as the cabling of the entire Drift HV system.
- I helped install all of the top feedthroughs of the detector for the readout of the wire planes and connections of the cryogenic system.
- I also tested all of the feedthrough boards of the wire plane feedthroughs for shorts and electrical connectivity.
- I served as the Drift HV WG Convener for almost two years and helped the transition from installation into commissioning of the system.
- I shifted and helped with data taking for ICARUS a number of times as well as served as the on-call Drift HV expert for over a year.
- I helped to implement the control software of the Drift HV system, and took it to an operational point.

5.4.4 MicroBooNE Experiment

The work that I did for the Micro Booster Neutrino Experiment, or MicroBooNE (which is the detector of this thesis and will be detailed more in Chapter 6), can be summarized as follows:

- Performed a study to set the threshold for hits in both MC and Data for MCC9.
- Took many hours of shifts for data taking for the experiment.
- Served as a member of the production team, where I was responsible for generating MC and Data reconstruction samples for different analyses on the experiment.
- This thesis, or a flux-integrated cross section measurement of neutrino-induced charged-current coherent pion production on argon, is also a result of work I've done on MicroBooNE.

5.4.5 Time at UTA

The work that I did for the lab at UTA on projects that pertain to LArTPC research with Dr. Asaadi and the rest of the group can be summarized as follows:

- I was responsible for the design and construction of the first implementation of the argon purification system (it was a monstrosity).
- I helped with many iterations of the argon purity monitor meant to be deployed in the argon purification system.
- I helped with the data taking and experimental setup of the TPB solubility study, which resulted in the paper that concludes this chapter.

Published by IOP Publishing for Sissa Medialab

Received: *April 11, 2018*
Revised: *February 5, 2019*
Accepted: *February 8, 2019*
Published: *February 18, 2019*

2019 JINST 14 P02021

Emanation and bulk fluorescence in liquid argon from tetraphenyl butadiene wavelength shifting coatings

J. Asaadi, B.J.P. Jones,[1] **A. Tripathi, I. Parmaksiz, H. Sullivan and Z.G.R. Williams**

Department of Physics, University of Texas at Arlington, Arlington, Texas 76019, U.S.A.

E-mail: ben.jones@uta.edu

Abstract: We study the stability of three types of popularly employed TPB coatings under immersion in liquid argon. TPB emanation from each coating is quantified by fluorescence assay of molecular sieve filter material after a prolonged soak time. Two of the coatings are shown to emanate a detectable concentration of TPB into argon over a 24 hour period, which corresponds to tens of parts per billion in argon by mass. In an independent setup, the dissolved or suspended TPB is shown to produce a wavelength shifting effect in the argon bulk. Interpretations of these results and implications for present and future liquid argon time projection chamber experiments are discussed.

Keywords: Neutrino detectors; Noble liquid detectors (scintillation, ionization, double-phase); Scintillators, scintillation and light emission processes (solid, gas and liquid scintillators)

ArXiv ePrint: 1804.00011

Corresponding author.

https://doi.org/10.1088/1748-0221/14/02/P02021

Contents

2019 JINST 14 P02021

1 Tetraphenyl butadiene coatings in liquid argon TPC experiments

Liquid argon time projection chambers (LArTPCs) play a central role in modern neutrino physics [1–4] and dark matter searches [5–8]. As well as being an excellent active medium for time projection chamber operation, liquid argon is also a bright scintillator, with a yield of tens of thousands of photons per MeV. This scintillation light is emitted in the vacuum ultraviolet (VUV) range (128 nm) which presents challenges for its detection. Although argon itself is highly transparent at this wavelength, the majority of commercially available optical detectors such as SiPMs and photomultiplier tubes are not sensitive in this spectral range.

Although some devices now exist with VUV sensitivity [9–11], this problem has traditionally been solved in large-scale systems by employing a wavelength shifting coating to convert VUV light into a visible range where it can be detected by conventional sensors. One of the most commonly used fluors is the organic compound tetraphenyl butadiene (TPB). Various properties of TPB that are relevant to operation of LArTPCs have been studied, including its efficiency at 128 nm [12–14], photo-degradation rates and mechanism [15–17] and emission time profile [18]. However, a full understanding of the behaviour of TPB in running experiments is still evolving. Given the reliance of future particle physics programs on the proper performance of TPB coated elements over many years, a strong understanding of the long term stability and behaviour of TPB in liquid argon is vital.

In this work we study the stability of TPB coatings in liquid argon. A primary goal is to establish whether TPB remains solidly affixed to coating surfaces, or rather may become dissolved or suspended in the argon bulk, for several commonly used types of coating in neutrino detectors. Previous work has established that TPB coatings are unstable, and perhaps partially soluble, in liquid xenon [19]. If this phenomenon were similarly exhibited in liquid argon, it could have significant implications for present and future neutrino and dark matter experiments. If TPB is lifted from surfaces into the bulk, either through solvation or as particulates in suspension, it may:

- Lead to wavelength shifting behavior in the bulk, or to direct excitation transfer to dissolved or suspended TPB molecules;

- Create a loss of performance of coatings over time;
- Cause TPB deposition onto surfaces other than those that are typically considered active.

These effects may lead to detrimental effects on experimental performance, or in some cases be put to constructive use if well controlled and understood.

This paper is organized as follows. In section 2 we describe the coatings under study and their uses in experiments. In section 3 the relative stability of these coatings in liquid argon is studied, with TPB loss and subsequent accretion in filters demonstrated and quantified. Then in section 4, light emission from TPB-loaded argon is measured, demonstrating that TPB steadily detaches from the surface into the bulk, and maintains its wavelength shifting character in this process. Finally section 5 presents a brief discussion of the interpretation and implications of our results.

2 Coatings tested in this study

Three types of coating were used in this study, which reflect three types of TPB application widely employed in large LArTPC experiments for neutrino physics. Samples were acquired directly from the collaborators who prepared them for their respective experiments and strongly resemble those used in operating detectors. These are:

Evaporatively coated foil ("Foils"). Such foils resemble those used in the LArIAT experiment [20, 21]. To form these coatings, a thickness of 300 $\mu g cm^{-2}$ TPB is evaporatively deposited onto highly reflective VIKUITI sheeting [22] at 220°C in vacuum. This leads to a bright white, highly efficient but somewhat mechanically fragile coating.

Over-saturated TPB in polystyrene painted coating on acrylic ("TPB+PS"). This coating resembles the TPB-coated plates of the MicroBooNE experiment, prepared according to the recipe described in [1, 23]. To form these coatings a solution of 1 g TPB and 1 g polystyrene is prepared in 50 ml toluene with small addition of ethanol as a surfactant. As the toluene dries, the TPB becomes over-saturated in the polystrene matrix, leading to large white crystals of TPB on the plate surface. This produces a milky white, high efficiency coating that is more mechanically robust against scratches or abrasions than the evaporative coatings.

High surface quality TPB coated acrylic ("Lightguides"). This coating resembles those used in the light guiding paddles [24–27] of the MicroBooNE experiment [1] and proposed for the SBND [4], DUNE [8] and ProtoDUNE [28] experiments. The coatings in this study were prepared similarly to those in ref. [29]. In this case 0.1 g acrylic and 0.1 g TPB were dissolved in 50 ml toluene and a UV-transmitting acrylic bar is soaked in the solution and then drawn. This produces a surface with a high optical quality but much lower wavelength shifting efficiency than either evaporative or TPB+PS coatings. This surface finish allows such coatings to be used in guiding light from a large surface area to a small number of optically sensitive devices. In well-prepared coatings, the TPB layer is effectively invisible and mechanically robust.

With thanks to Janet Conrad and Andrzej Szelc.

2019 JINST 14 P02021

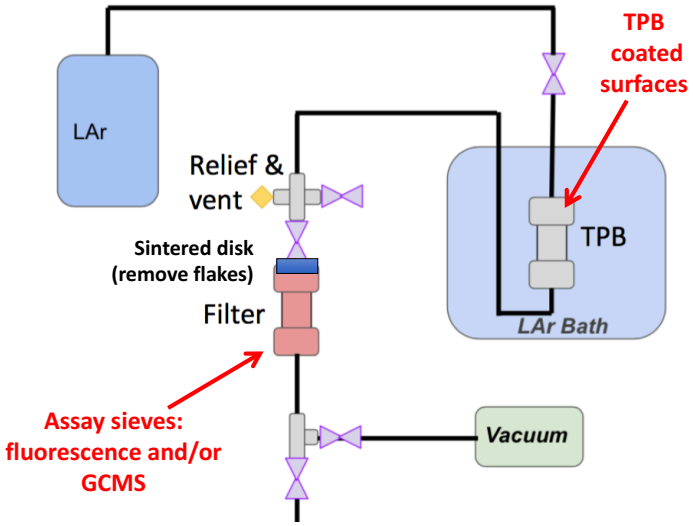

Figure 1. Labelled schematic of the apparatus used to study TPB emanation and collection in the filters.

3 Comparison of coating robustness by fluorescence assay

If TPB does emanate from coatings into either suspension or solution in argon, the filtration systems employed to clean this argon may remove it. In particular, molecular sieves provide a large surface area of material onto which suspended TPB molecules or particles may adsorb. To test the robustness of TPB coated surfaces in argon, a small cylinder of volume 119 cc containing a TPB coated element of ~103 cm^2 coated surface area was filled with liquid argon (AirGas Ultra High Purity, ≤1 ppm O2, ≤1 ppm H2O, ≤5 ppm N2) and allowed to sit for a specified number of hours. After this time has elapsed, the liquid was driven by a back-pressure of clean argon through a column of Sigma Aldrich 4A molecular sieves between two sintered steel disks. The argon was dumped into a dewar for evaporation to atmosphere, then the system was isolated and allowed to warm up to room temperature. Prior to each run the internal surfaces were cleaned with toluene, and the system was evacuated using a turbo-molecular pump to vacuum quality $< 10^{-4}$ Torr. Toluene will be our solvent of choice throughout this work, given its known excellent solubility for TPB. A sketch of this system is shown in figure 1.

Once at room temperature, the filter column was opened and the sieve material extracted in layers with approximately 90 g each, which were transposed into clean beakers. The full filter column contained approximately 6 layers, and the first five were included in this study, the latter being discarded due to its non-uniform mass depending on filter fill. Each beaker was capped with clean aluminum foil and shaken to mix the material. A small quantity from each sample was discarded to produce samples of relatively uniform mass of 85±2 g, and each was weighed to milligram precision on an analytic balance. The samples were soaked in 100 ml of toluene for 1 hour, being stirred with a clean glass rod after 0, 30 and 50 minutes. After this soak, each solution was filtered through fine-grade filter paper to remove non-soluble sieve dust, into another set of clean beakers. These smaller beakers were left in a dark fume hood overnight such that the toluene solvent completely evaporated. After evaporation a small amount of visible white residue

2019 JINST 14 P02021

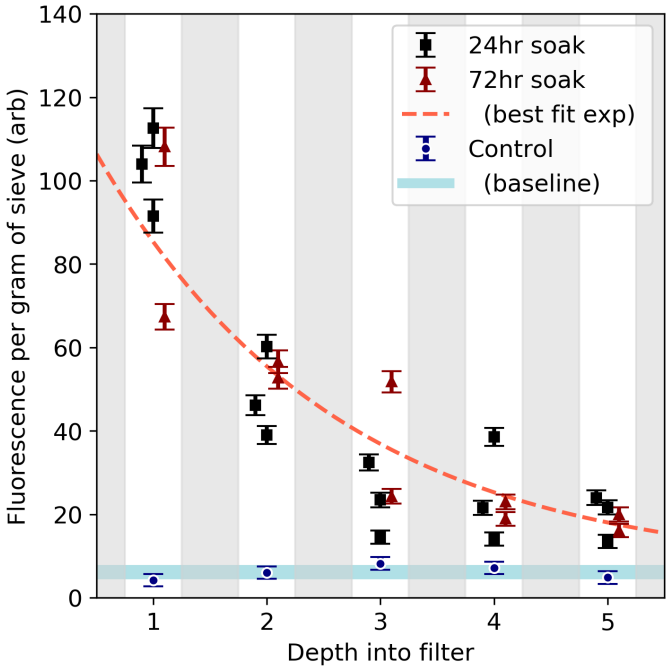

Figure 2. Fluorescence intensity vs depth into the filter for the various foil samples.

was observed. This residue was present with clean sieves as well as used ones, so is not believed to be directly connected to the TPB absorption.

The residue was re-solvated in 10±0.2 ml of toluene, leading to a concentrated solution of the compounds extracted from the sieves. The samples were then pipetted into clean, capped quartz vials, which were individually scanned for fluorescence at 350 nm with 5 nm emission and excitation slit widths in an Agilent Cary Eclipse spectrophotometer. The integrated fluorescence intensity between 400 and 600 nm was recorded for each sample. Figure 2 shows the fluorescence intensity vs depth into the filter for the various samples of wavelength shifting foil, normalized to the initial sieve sample mass, for illustration. The steadily decreasing intensity as a function of position in the filter strongly supports the interpretation that the filters are removing TPB from the argon flow. The error bars of figure 2 include quantified contributions from the stability of the spectrometer (absolute scale of 1.48 in arb. units); the initial toluene volume (100±2 ml yielding a 2% uncertainty); the fraction of toluene actually extracted from the wet sieves (measured to be 0.73±0.02 yielding a 2.7% uncertainty); and the volume of toluene used in resolvation of the residue (10±0.2 ml yielding a 2% uncertainty). The uncertainty in the tested sieve mass was also evaluated, but was negligible in all cases.

To ensure that the observed fluorescence emission was indeed from TPB, three of the solvated residue samples were tested with gas chromatography coupled to mass spectrometry (GCMS) using a similar protocol to that described in [15]. A strong TPB peak was observed, with no other notable dissolved species.

A control run with no TPB element in front of the filter yielded an effectively fluorescence-free result, further supporting this interpretation. Although the fluorescence from this control run was

2019 JINST 14 P02021

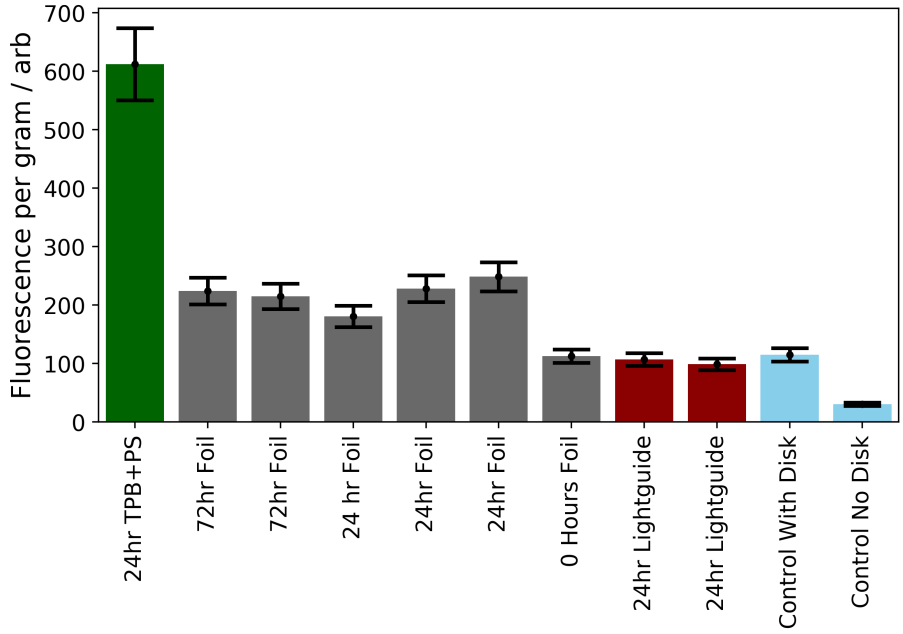

Figure 3. Integrated fluorescence intensity for the various samples tested in this study.

minimal (shown in figure 3 in blue), we subsequently observed that even following a cleaning procedure involving a 30 minute soak in toluene and several washes, the sintered disks in front of the filter column retained some TPB from the previous run, which then propagated into the filter column with a clean argon flush. This sets a lower limit on the amount of fluorescence that indicates clearly the presence of displaced TPB. The relative intensity of fluorescence observed from each tested sample including both control configurations is shown in figure 3.

It is notable that neither of the light-guide samples displayed TPB in excess of the control runs with the sintered disk, and so these do not appear to emanate TPB at a level above the sensitivity of our procedure. Also notable is that the zero-hour flush, where argon was pushed over a foil and through the column with no soak time, also does not exhibit strong fluorescence above the background level. After either 24 and 72 hours of argon soak, the foils did cause a significant fluorescence increase in the column, though the observed increase after 72 hours was not significantly in excess of that after 24 hours. Finally, the TPB+PS plate demonstrated by far the largest fluorescence enhancement. Although the statistics in this test are low, the relatively stable behavior within the foil samples shows that the fluorescence measurement procedure is repeatable at the 10% level. Since the foil runs were taken at various times after different prior system configurations, this uncertainty includes the contribution from the memory effect of the sintered disk described above. An error bar of this magnitude is associated to each bar in figure 3.

The actual mass of TPB absorbed into the sieves can be determined from the fluorescence measurements by comparison with calibration samples. Samples of TPB in toluene were prepared and scanned using the same procedure as the sieve residue. These data are shown in figure 4, left. A straight line is fit to the data, allowing the fluorescence intensity of be interpreted as a measurement of the mass of TPB dissolved in toluene. This can then be used to infer the mass density of TPB

2019 JINST 14 P02021

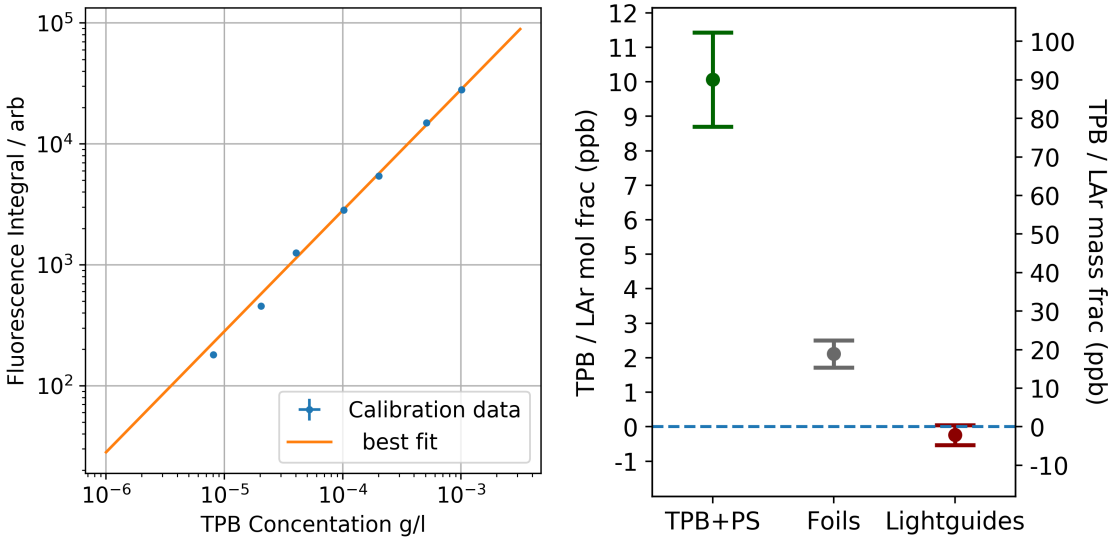

Figure 4. Left: calibration data mapping fluorescence intensity vs TPB concentration in toluene. Right: molar and mass fractions of TPB dissolved or suspended in LAr implied by these data.

in the original liquid argon volume after the soak. The fluorescence integral on the vertical axis of figure 4, left is in the same units as the y axis of figure 2 after multiplying by the mass in grams (~85 g), thus the relevant range for this study is 10^3–10^4 in these units. Figure 4, right shows the estimated concentration of TPB in liquid argon apparently emanated by each sample type inferred from these data. The bulk concentration may also have dependencies on parameters such as exposed surface area and coating history, so these quantities should be considered as an example rather than a universal property. Each concentration measurement shown in figure 4 represents only a lower limit on the TPB present in the argon, since an unknown amount will be deposited onto surfaces other than the assayed material, including the sintered disk and the vessel walls. These data suggest that TPB emanates into argon at the tens of ppb level by mass, from both the foil and TPB+PS coatings. The emanation from the light guide coating, if present, is below our sensitivity due to the memory effect of the sintered disk.

4 Light emission from TPB-loaded argon

In order to test if the TPB emanated from these coatings could be a source of extraneous light in LArTPC experiments, we set up an apparatus to establish whether visible light could be detected from an ultraviolet source when TPB coated material had been allowed to soak in a pure argon bath. The experimental setup used four Hamamatsu S10362-11-050P MPPCs situated at the bottom of a cylindrical cryostat with a total volume of ~70,600 cm^3. Below the MPPCs, TPB coated material was enclosed between two pieces of G10 such that the wavelength shifting surface was not optically apparent to either the light source or the MPPCs. Light from a QPhotonics UVTOP 255 nm LED [30] was delivered into the cryostat via a UV-transmitting fiber optic. This fiber optic was aligned to shine onto a non-reflective, black surface ~15 cm above the MPPC. This volume is

2019 JINST 14 P02021

filled with high purity liquid argon, and sits within an outer, open liquid argon bath for refrigeration, while the visible light yield in the internal cryostat is monitored.

Measurements were made by recording the number of MPPC signals above threshold every thirty seconds for a period of twenty minutes. For each measurement, the average of the number of counts in the thirty second interval and its standard deviation is reported. These measurements were repeated every twelve hours over a forty eight hour period for each of the configurations reported below.

At the beginning of each run, the LED was disconnected from the fiber optic to establish the rate of accidental background events. This background category includes events deriving from stray ambient light, electronics noise, MPPC dark current, or scintillation from radioactivity or cosmic rays. The ambient rates were consistent across all measurements in the multi-day data taking period, with 18.32 counts ±4.45, shown in figure 5 in red for the control run as "No LED, No TPB".

A benchmark measurement was made with no TPB coated element in the system, but the LED connected and pulsed. The system was kept in this configuration for forty-eight hours to confirm the stability of the system. Some stray light was observed in this case, with a 130.0 ± 11.7 counts observed (shown in figure 5 in black as "LED ON, No TPB"). This light is believed to derive from the blue tail of the UV LED reflecting in the vessel, which although much less intense than the UV spectrum, is within the sensitivity range of the MPPC. As a further benchmark, the vessel was warmed up and the non-reflective surface was replaced with TPB+PS plate ∼ 6 cm from the fiber optic, directly illuminated. The vessel was filled with argon and measurements were again made over a forty-eight hour period with 670.8 ± 28.2 counts was recorded. This is shown in green on figure 5 as "LED directed at TPB plate" and provides a reference point corresponding to a bright, efficient wavelength shift. Subsequent measurements can then be referenced against these two extreme cases.

After these initial characterizations, the vessel was cleaned and samples of TPB+PS with equal surface area to those used in section 3 were inserted into the chamber below the MPPC's. The aim of this trial was to search for evidence for scintillation light due to TPB in solution/suspension. The vessel was again filled with argon with the fiber aligned to the black, non-reflective beam stop. A measurement of the MPPC rate was made immediately after filling, for LED on and off. The LED on rate was found to be 137.0 ± 13.8, consistent with the control "NO TPB" measurement and the LED off rate was found to be 17.2 ± 4.3, also consistent with the control measurement. These measurements were repeated every twelve hours for forty-eight hours for LED on and off. The LED ON/OFF data are shown with blue circles and red squares respectively, in figure 5. The amount of light observed for a fixed LED intensity is observed to grow gradually over the 48 hour time window, consistent with the hypothesis of TPB emanation from the coatings into the bulk, as observed in the filter assay studies. To test the stability of the system, the vessel was evacuated, the TPB samples removed, and the setup cleaned before being filled with fresh argon for a further benchmark set of LED on and LED off measurements. The LED on rate was found to be 131.3 ± 11.2 and the LED off rate was 16.4 ± 4.7, both of which are consistent with the previous control measurements, strongly suggesting that the additional light originates from TPB emanation.

It is notable that the timescale of emanation is multiple hours, consistent with the null results from the "zero hour" filter assay and non-null results from the "24 hour" assay test in section 3; and also that the displaced TPB appears to be not only a visible light source but also a rather bright one with 429.2 ± 22.3 counts after 48 hours, around half the intensity of the directly illuminated coating.

2019 JINST 14 P02021

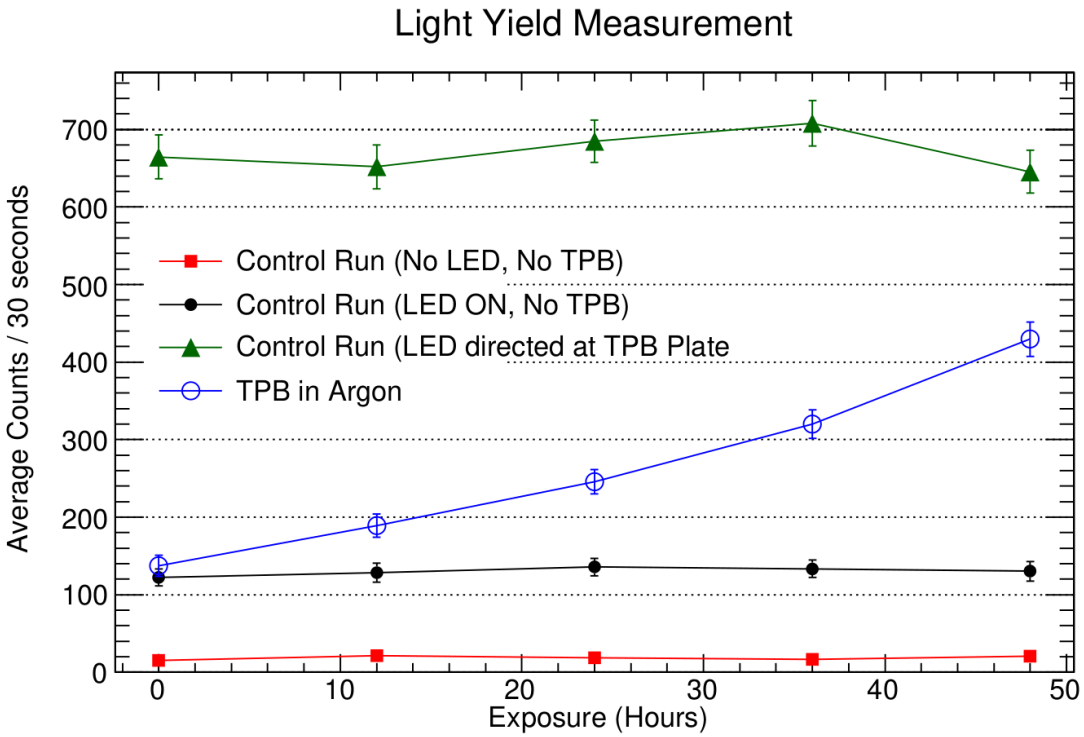

Figure 5. Light yield vs time in LAr. See text for detailed description.

Preliminary studies of pulse timing indicate components of the wavelength shifted light with long time constants, in the milliseconds range. This may represent a phosphorescent behaviour that is suppressed when TPB is densely packed on a surface but uninhibited in weak solutions. The details of these time constants will be studied in future work.

5 Discussion

We have conclusively demonstrated that TPB emanates from certain coating types that are commonly used in liquid argon particle physics experiments, when submerged in liquid argon over hour to day timescales. This emanated TPB is removed from the argon bulk by molecular sieves, and detaches most strongly from coatings where the fluor is not protected by a polymer matrix. This has possible implications for running and proposed particle physics experiments that use either painted or evaporative coatings.

The amount of TPB that becomes dissolved or suspended is in the range of tens of parts per billion by mass. This is sufficient to cause bulk fluorescence in the argon, and this fluorescence has been demonstrated using 255 nm excitation by LED. The bulk fluorescence for an argon sample near saturation is found to be of similar magnitude to the brightness of an exposed coating, suggesting that this may be a significant visible light source in experiments where TPB is present.

Although our data demonstrate TPB emanation, they are unable to distinguish between a true solvation effect or a suspension of larger particulates. These two possibilities can be considered as points in a continuum, with colloidal suspensions of very small particles behaving almost

2019 JINST 14 P02021

indistinguishably from a true solution in all practical cases of interest. The previous reported instability of TPB films in liquid xenon [19] was also not conclusively characterized. If that effect were to be attributed to solubility, then the expected scaling of Van-Der-Waals (VDW) forces between these two noble elements according to the London Dispersion Equation [31] would suggest similar qualitative effects should be expected in argon, the ratio of VDW forces being around a factor of ~2.6, assuming the ionization energy of TPB to be around 5 eV and the well known polarizibilities of argon and xenon atoms.

Because solubility/emanation is likely to depend on parameters including liquid flow rate, history of coating preparation and handling, fill procedure, time since installation, filtration method, and potentially also purity, evacuation, purge, or bake-out procedure, it is not possible to make quantitative predictions for any given experiment, given our present level of understanding. However, the previously unreported phenomena presented in this paper may have significant implications in running and planned detectors, and further consideration of these effects in more targeted experimental configurations appears well motivated.

There is also a notable possibility that dissolved or suspended TPB in argon may represent an opportunity rather than a burden. If a suitable filtration and circulation system could be implemented to maintain a specific steady-state concentration, this would remove the need for additional wavelength shifting elements such as light guides, coated plates or foils. Such a detector with an inherently wavelength shifting noble medium could achieve higher efficiency of light collection via reduced solid-angle losses, and also enjoy tuneable optical parameters after installation, among other benefits. Such a light detection concept may be promising for future large LArTPCs and cryogenic scintillation experiments.

Acknowledgments

We thank Janet Conrad and Andrzej Szelc for providing samples and useful feedback and encouragement during this work, and Flavio Cavanna for insightful comments. The equipment used in these studies was procured for the MicroBooNE, DUNE and NEXT programs. The UTA group is supported by the Department of Energy under contract numbers DE-SC0011686 and DE-SC0017721.

References

[1] MicroBooNE collaboration, *Design and Construction of the MicroBooNE Detector*, 2017 *JINST* **12** P02017 [arXiv:1612.05824].

[2] SBND collaboration, *Developing LAr Scintillation Light Collection Ideas in the Short Baseline Neutrino Detector*, 2016 *JINST* **11** C02018.

[3] ICARUS collaboration, *Design, construction and tests of the ICARUS T600 detector*, *Nucl. Instrum. Meth.* **A 527** (2004) 329.

[4] MicroBooNE, LAr1-ND, ICARUS-WA104 collaboration, *A Proposal for a Three Detector Short-Baseline Neutrino Oscillation Program in the Fermilab Booster Neutrino Beam*, arXiv:1503.01520.

2019 JINST 14 P02021

[5] ArDM collaboration, *Commissioning of the ArDM experiment at the Canfranc underground laboratory: first steps towards a tonne-scale liquid argon time projection chamber for Dark Matter searches*, *JCAP* **03** (2017) 003 [arXiv:1612.06375].

[6] WARP collaboration, *Warp liquid argon detector for dark matter survey*, *New Astron. Rev.* **49** (2005) 265 [astro-ph/0405342].

[7] DarkSide collaboration, *First Results from the DarkSide-50 Dark Matter Experiment at Laboratori Nazionali del Gran Sasso*, *Phys. Lett.* **B 743** (2015) 456 [arXiv:1410.0653].

[8] DUNE collaboration, *Long-Baseline Neutrino Facility (LBNF) and Deep Underground Neutrino Experiment (DUNE)*, arXiv:1512.06148.

[9] E. Erdal, L. Arazi, M.L. Rappaport, S. Shchemelinin, D. Vartsky and A. Breskin, *First demonstration of VUV-photon detection in liquid xenon with THGEM and GEM-based Liquid Hole Multipliers*, *Nucl. Instrum. Meth.* **A 845** (2017) 218 [arXiv:1603.07669].

[10] T. Igarashi, M. Tanaka, T. Washimi and K. Yorita, *Performance of VUV-sensitive MPPC for Liquid Argon Scintillation Light*, *Nucl. Instrum. Meth.* **A 833** (2016) 239 [arXiv:1505.00091].

[11] V. Zabrodskii et al., *SiPM prototype for direct VUV registration*, *Nucl. Instrum. Meth.* **A 787** (2015) 348.

[12] C. Benson, G. Orebi Gann and V. Gehman, *Measurements of the intrinsic quantum efficiency and absorption length of tetraphenyl butadiene thin films in the vacuum ultraviolet regime*, *Eur. Phys. J.* **C 78** (2018) 329 [arXiv:1709.05002].

[13] V.M. Gehman et al., *Fluorescence Efficiency and Visible Re-emission Spectrum of Tetraphenyl Butadiene Films at Extreme Ultraviolet Wavelengths*, *Nucl. Instrum. Meth.* **A 654** (2011) 116 [arXiv:1104.3259].

[14] R. Francini et al., *VUV-Vis optical characterization of Tetraphenyl-butadiene films on glass and specular reflector substrates from room to liquid Argon temperature*, arXiv:1304.6117.

[15] B.J.P. Jones, J.K. VanGemert, J.M. Conrad and A. Pla-Dalmau, *Photodegradation Mechanisms of Tetraphenyl Butadiene Coatings for Liquid Argon Detectors*, 2013 *JINST* **8** P01013 [arXiv:1211.7150].

[16] C.S. Chiu et al., *Environmental Effects on TPB Wavelength-Shifting Coatings*, 2012 *JINST* **7** P07007 [arXiv:1204.5762].

[17] R. Acciarri, N. Canci, F. Cavanna, E. Segreto and A.M. Szelc, *Aging studies on thin tetra-phenyl butadiene films*, 2013 *JINST* **8** C10002.

[18] E. Segreto, *Evidence of delayed light emission of TetraPhenyl Butadiene excited by liquid Argon scintillation light*, *Phys. Rev.* **C 91** (2015) 035503 [arXiv:1411.4524].

[19] P. Sanguino, F. Balau, A.B. do Rego, A. Pereira, and V. Chepel, *Stability of tetraphenyl butadiene thin films in liquid xenon*, *Thin Solid Films* **600** (2016) 65.

[20] F. Spagliardi, *Developing Light Collection Enhancements and Wire Tensioning Methods for LArTPC Neutrino Detectors*, MSc Thesis, Manchester University, Manchester U.K. (2017).

[21] LArIAT collaboration, *LArIAT: Liquid Argon TPC in a Test Beam*, FERMILAB-PROPOSAL-1034 (2013).

[22] A. Langenkämper et al., *Low-Temperature Relative Reflectivity Measurements of Reflective and Scintillating Foils used in Rare Event Searches*, *Nucl. Instrum. Meth.* **A 884** (2018) 40 [arXiv:1703.07152].

2019 JINST 14 P02021

[23] C.M. Ignarra, *Sterile Neutrino Searches in MiniBooNE and MicroBooNE*, Ph.D. Thesis, Massachusetts Institute of Technology, Cambridge U.S.A. (2014).

[24] L. Bugel et al., *Demonstration of a Lightguide Detector for Liquid Argon TPCs*, *Nucl. Instrum. Meth.* **A 640** (2011) 69 [arXiv:1101.3013].

[25] Z. Moss et al., *Improved TPB-coated Light Guides for Liquid Argon TPC Light Detection Systems*, 2015 *JINST* **10** P08017 [arXiv:1410.6256].

[26] D. Whittington, S. Mufson and B. Howard, *Scintillation Light from Cosmic-Ray Muons in Liquid Argon*, 2016 *JINST* **11** P05016 [arXiv:1408.1763].

[27] B. Howard et al., *A Novel Use of Light Guides and Wavelength Shifting Plates for the Detection of Scintillation Photons in Large Liquid Argon Detectors*, *Nucl. Instrum. Meth.* **A 907** (2018) 9 [arXiv:1710.11233].

[28] DUNE collaboration, *The Single-Phase ProtoDUNE Technical Design Report*, arXiv:1706.07081.

[29] Z. Moss et al., *A Factor of Four Increase in Attenuation Length of Dipped Lightguides for Liquid Argon TPCs Through Improved Coating*, arXiv:1604.03103.

[30] Q-Photonics, *Deep UV light emitting diode, 0.3–0.4 mW @ 255 nm*, (2018), http://www.qphotonics.com/Deep-UV-LED-255nm-UVTOP255TO39HS.html.

[31] J.O. Hirschfelder, C.F. Curtiss, R.B. Bird and M.G. Mayer, *Molecular theory of gases and liquids. Vol. 26*, Wiley, New York U.S.A. (1954).

2019 JINST 14 P02021

6 The Micro Booster Neutrino Experiment

This chapter covers the technical details of the Micro Booster Neutrino Experiment (or MicroBooNE), as well as its primary physics goals. MicroBooNE was proposed to resolve the Low Energy Excess (LEE) observed by the Mini Booster Neutrino Experiment (MiniBooNE). The chapter begins with a description of the primary beamline from which MicroBooNE receives neutrinos, the Booster Neutrino Beamline (BNB), in Section 6.1. A detailed description of the LArTPC that is MicroBooNE's detector is given in Section 6.2, which is followed by a discussion of the triggers and the data stream used by MicroBooNE in Section 6.3. The readout electronics and the data format collected by MicroBooNE are discussed in Section 6.4, and the detector simulation is discussed in Section 6.5. The chapter closes with a brief description of the detector operations in Section 6.6.

6.1 The Booster Neutrino Beamline

The Booster Neutrino Beamline (or BNB) is one of the neutrino beams that MicroBooNE receives, and is produced from the Fermi National Accelerator Laboratory's (Fermilab) accelerator complex. The BNB is the same beamline used by MiniBooNE, as well. The accelerator complex is composed of four accelerators that work in tandem: the linear accelerator (Linac), the Booster, the Recycler, and the Main Injector. These accelerators produce two primary proton beams, a low energy (8 GeV) proton beam from the Booster, and a high-energy (120 GeV) beam from the Main Injector. Hitting a target, these proton beams produce secondary beams of pions, kaons, muons, and neutrinos that serve a variety of experiments [79].

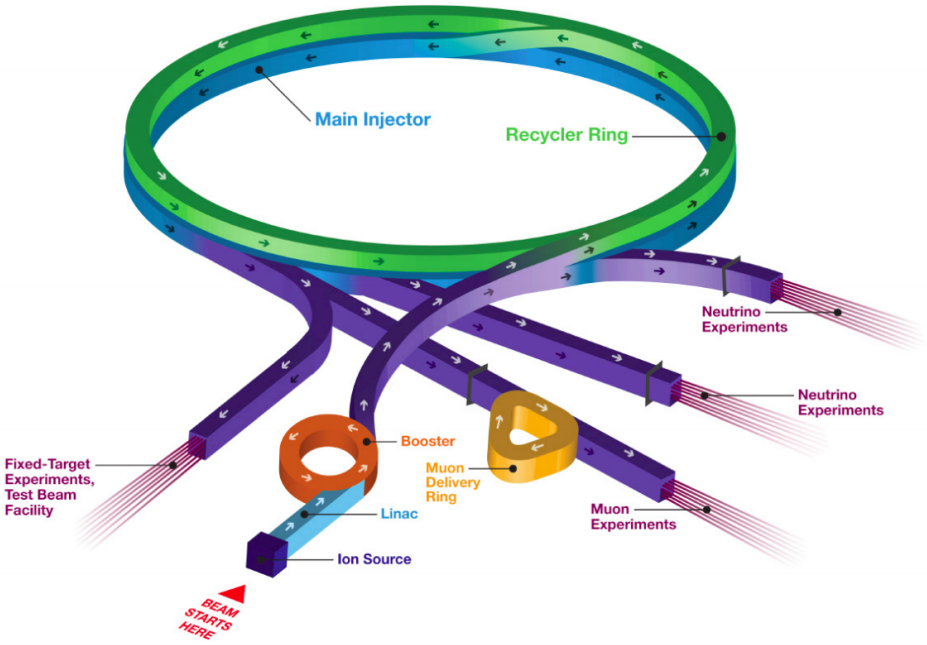

Figure 6.1: Cartoon depiction of Fermilab's accelerator complex.

This section describes in some detail the production process of neutrinos through the BNB beamline. Three sections will describe the main stages involved: the production and extraction of an 8 GeV proton beam, in Section 6.1.1; the beam target and focusing horn which lead to a secondary meson beam, in Section 6.1.2; and the composition of the neutrino beam reaching the MicroBooNE detector, in Section 6.1.3.

6.1.1 Primary Proton Beam

The BNB produces a neutrino beam using the protons from the Booster synchrotron which have a momentum of $8.89 GeV/c$. These protons strike a beryllium target that is embedded in a pulsed electromagnet, called the horn which is depicted in Figure 6.2.

The Booster proton beam begins upstream as a beam of negatively charged hydrogen ions H^-. The H^- ions are then subjected to a linear accelerator that uses alternating electromagnetic fields which accelerates them to 400 MeV of kinetic energy. Electrons are removed from the H^- ions through the use of a carbon foil. After, the bare protons enter the 474-meter-circumference Booster synchrotron, which operates at a frequency of 15 Hz. Once here, the protons are accelerated up to 8.89 GeV/c momentum. The protons are bunched in "beam spills" containing roughly 4×10^{12} protons spaced throughout a 1.6 μs time window per spill. The protons are then directed toward a thick beryllium target, which is described in Section 6.1.2.

The absolute number of Protons on Target (POT) is measured by two toroids that reside upstream of the target and are part of a larger beam monitoring system. The uncertainty on the POT is on the order of 2%. Additional beam characteristics are

monitored by beam position monitors, a multi-wire chamber, and a resistive wall monitor. This system measures beam intensity, timing, width, position, and direction of the proton beam.

6.1.2 Beam Target and Focusing Horn

Protons from the primary proton beam come in and strike a beryllium target which is embedded in a pulsed electromagnet, called the horn which is depicted in Figure 6.2. The beryllium target is composed of seven identical cylindrical segments of beryllium, to produce a cylinder 71.1 cm long and 0.51 cm in radius. The cylindrical segments are contained within a sleeve (1.37 cm inner radius, 0.9 cm thickness) also made of beryllium, which is connected to each segment via three beryllium fins. Within the sleeve, air is circulated in order to help cool the target.

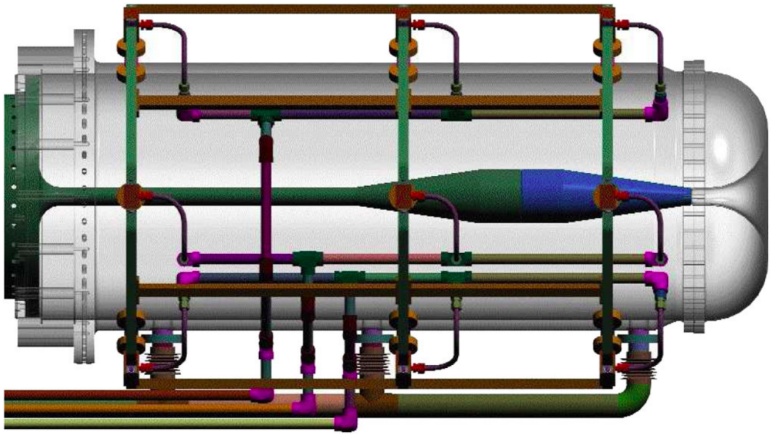

Figure 6.2: Diagram of the magnetic focusing horn used in the BNB.

Once the target is struck by the incoming protons, secondary particles are produced, including pions and kaons, which happen to represent the primary source of neutrinos and anti-neutrinos. After their production, and in order to enhance the neutrino beam, these secondaries are focused by a toroidal electromagnet (horn) placed around the target. Inside the horn, a toroidal magnetic field provides a restoring force for particles of a certain charge, and defocuses particles of the opposite charge, thus enhancing a ν_μ beam while reducing $\bar{\nu}_\mu$ background (or vice versa) originating from the decays of the secondary particles. The more focused the mesons are before the decay, the more focused will the neutrino beam be once it reaches the detector, which results in enhancing the flux. The focusing horn is made of aluminum and is pulsed with a 174 kA current. A drawing of the horn structure is shown in Figure 6.2.

The horn is 185 cm long and is composed of an inner and an outer conducting cylinder. A positive current travels down the inner conductor, arches back towards the front via the outer conductor, thus producing a magnetic field perpendicular to the beam direction within its volume which falls off as $1/r$. The inner conductor is oriented just

outside the beryllium target. Right outside the inner conductor, the strength of the magnetic field reaches 1.5 Tesla. Since the horn heats up due to the pulsed current and radiation, during operation the inner conductor is constantly being cooled with nozzles that spray water on it. As was breifly mentioned above, the direction of the current can be switched to focus the positively charged secondaries, or the negatively charged secondaries, ultimately producing a beam primarily of neutrinos ("neutrino mode") or antineutrinos ("antineutrino mode"), respectively. The BNB beamline is schematically shown in Figure 6.3. The horn also has a small field-free region, called the neck of the horn. This enables the incoming particles to pass through that region without being affected by the magnet. The neck also allows the remaining proton beam to pass through it, without impinging with the horn.

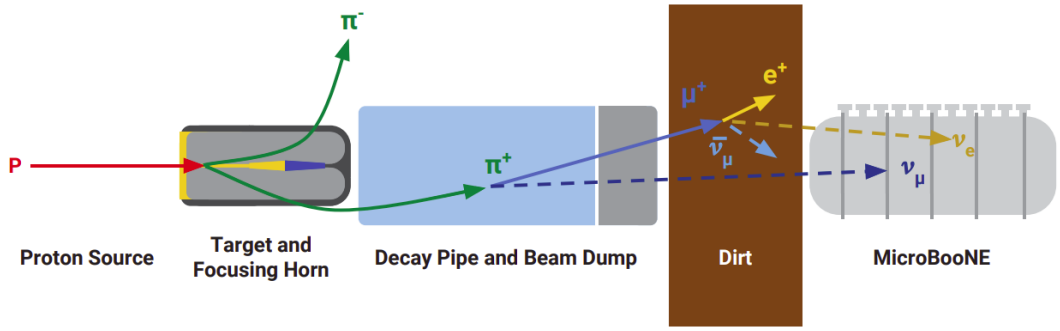

Figure 6.3: Diagram of the Booster Neutrino Beamline.

After being focused, the charged pions and kaons travel through a 50-meter decay region: a cylindrical volume of air, in which pions and kaons decay, producing the tertiary neutrino beam which will eventually reach the detector downstream. Any remaining charged particles which have not yet decayed are blocked by an absorber made of concrete. The absorber stops the hadron component of the beam, while the neutrinos and some of the muons from the decayed mesons will pass through it. All of this brings the beam to the point where is is almost entirely composed of neutrinos, which will propagate through the dirt before reaching the detector downstream.

6.1.3 Beam Composition

For the analysis of this thesis, a data set collected when the horn was pulsed with a positive current was used. This results in the positively charged mesons being focused towards the beam axis, while negatively charged mesons are deflected away. The most abundant of the mesons produced by the protons that are collided with the beryllium target are positively charged pions (π^+) which results in a π^+ beam. There is a small contribution of positively charged kaons (K^+) and muons (μ^+) to the beam, but the K^+ and μ^+ are left free to decay. The main branching ratio (BR) for π^+ decay results in the π^+ decaying to a μ^+ and a ν_μ, thus resulting in a predominantly ν_μ beam. At the same

time, contamination from other neutrino states in pion decay are caused by either $\bar{\nu}_\mu$ or by ν_e coming from the decay of muons ($\mu^+ \to e^+ + \bar{\nu}_\mu + \nu_e$). There also happens to be a small contamination in the beam of $\bar{\nu}_\mu$ from μ^- which are very forward going (or very energetic) and were therefore not deflected by the horn.

Booster Neutrino Beam Composition and Predicted Flux at MicroBooNE								
	ν_μ		$\bar{\nu}_\mu$		ν_e		$\bar{\nu}_e$	
Flux ($^\circ/cm^2/POT$)	5.2×10^{-10}		3.3×10^{-11}		2.9×10^{-12}		3.0×10^{-13}	
Fraction		93.6%		5.9%		0.52%		0.05%
Composition	π^+:	96.7%	π^-:	89.7%	$\pi^+ \to \mu^+$:	51.6%	K^0_L:	70.7%
	K^+:	2.7%	$\pi^+ \to \mu^+$:	4.5%	K^+:	37.3%	$\pi^- \to \mu^-$:	19.3%
	other:	0.6%	*other*:	5.8%	*other*:	11.1%	*other*:	10.0%

Table 6.1: Predicted neutrino flux at the MicroBooNE detector with the horn in neutrino mode. The composition of the channels is built up from different parent mesons, the two most important ones are given.

Neutrinos produced by the decay of kaons ($K^\pm$, K^0, K^0_L) also happen to contribute to the flux. As a result of the smaller kaon production rate in the target this is a minor contribution to the total neutrino flux that will reach the experiment. Almost the entire flux of ν_μ with energy below 2.5 GeV is contributed by events which originate from pion decay, while kaons contribute almost exclusively to ν_μ beyond this energy. Most importantly, because of the broader range of decay channels, kaons contribute significantly to the ν_e flux, even at lower energies. A small fraction of $\bar{\nu}_e$ also arises from kaon decay.

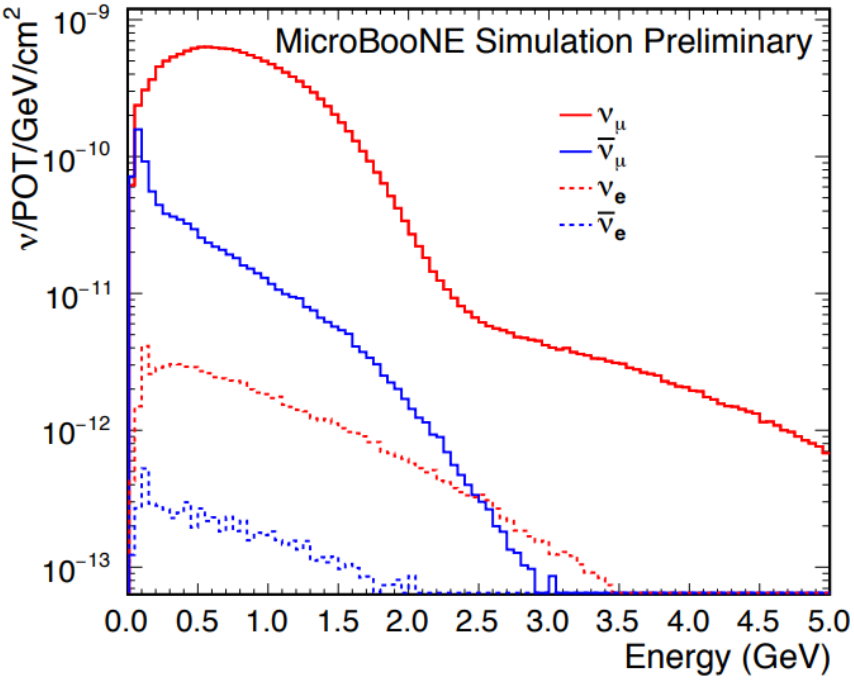

Figure 6.4: Neutrino Flux at MicroBooNE.

In the end, the neutrino beam produced at the BNB is a 93.6% ν_μ beam, with a contamination of $\bar{\nu}_\mu$ (5.86%), ν_e (0.52%), and $\bar{\nu}_e$ (0.05%). Figure 6.4 shows the neutrino flux split in the contributions from the four neutrino states as modelled by the MiniBooNE beam simulation and calculated at the MicroBooNE detector. Table 6.1 is a table of the beam composition that shows the contamination as well for the BNB. Next will be a discussion of the detector used for the analysis of this thesis, in Section 6.2.

6.2 The MicroBooNE Detector

The MicroBooNE detector is a liquid argon time projection chamber (LArTPC), located 470m downstream from the target of the BNB. The MicroBooNE LArTPC drifts and collects charge to produce fine-grained images of the ionization that was liberated by charged particles traversing a volume of highly-purified liquid argon. This section will describe the design and implementation of the LArTPC of MicroBooNE.

6.2.1 The Time Projection Chamber

The TPC used in the MicroBooNE experiment, shown in Figure 6.5, is a rectangular parallelepiped with dimensions 2.3 m (height) × 2.6 m (width) × 10.4 m (length, along the beam direction). The coordinate system adopted is shown in Figure 6.6. The 8256 stainless steel sense wires forming the three anode planes have a plane-to-plane spacing

of 3 mm, and the wires on each plane are separated with a 3 mm wire pitch. The wires are connected to application-specific integrated circuits (ASICs) which operate at a liquid argon temperature of 87K. While crossing the first two wire planes, consisting of 2400 wires at angles ±60 degrees relative to the vertical, ionization electrons induce a signal on them (thus, they are called the induction planes). Subsequently, the electrons are collected (thus, it is called the collection plane) by the third plane, made of 3456 vertically-oriented wires. The electric field is created by a series of 64 2.54-cm diameter stainless steel pipes shaped into a rectangular loop, forming the field cage. The negatively charged cathode is held at a high voltage (operating voltage is 70 kV), and this voltage is incrementally stepped down across the field cage tubes with a voltage divider chain, with an equivalent resistance of 250 MΩ between each tube. The distance from center-to-center of adjacent field cage loops is 4 cm. This creates a uniform electric field within the LArTPC. The technical details of the TPC are also listed in Table 6.2 for easier reference.

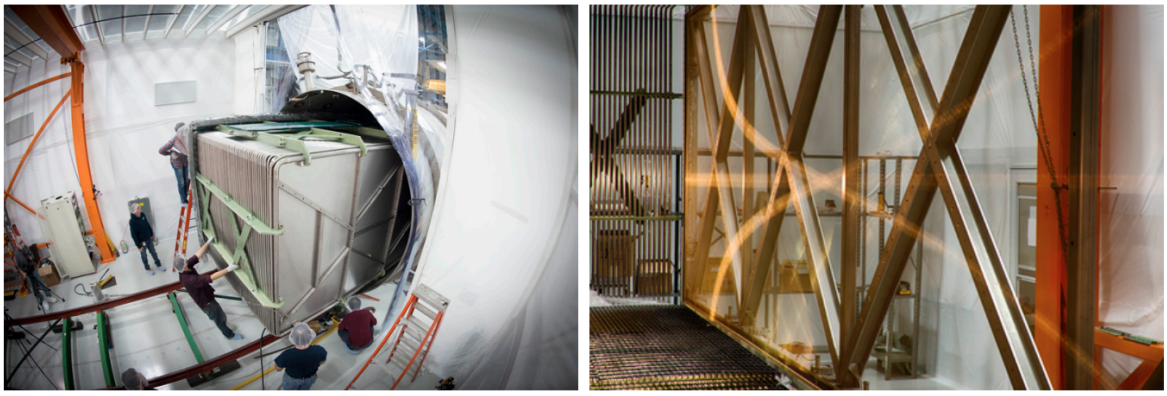

(a) (b)

Figure 6.5: The MicroBooNE TPC when it was inserted in the cryostat (a). The cathode is visible on the front right and the field cage, made of tubes, can also be seen. The inside of the TPC (b). The three wire planes are visible along the anode on the right, and the field cage tubes at the back.

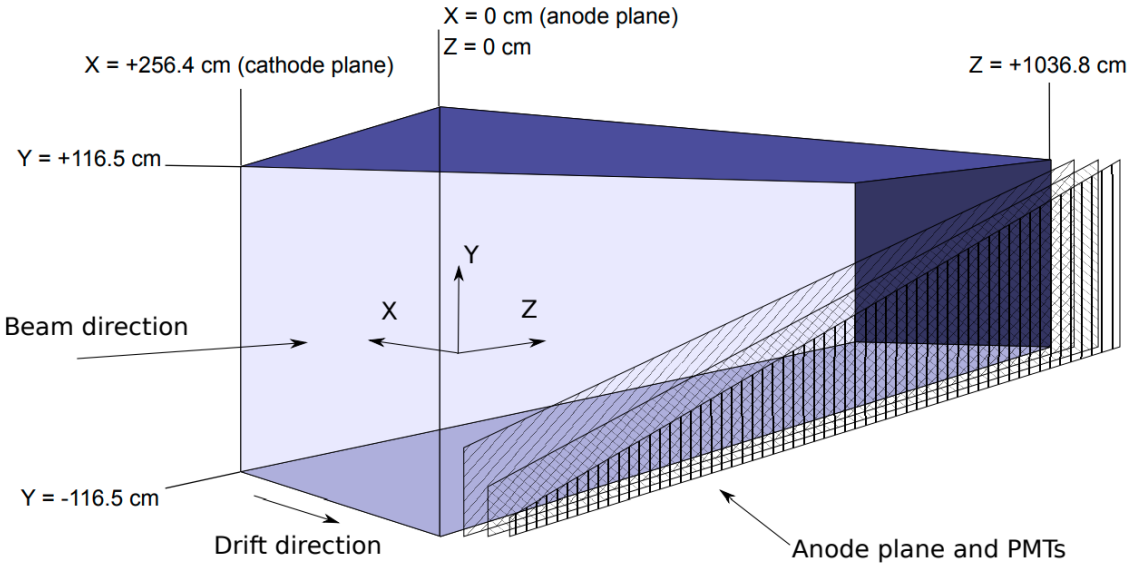

Figure 6.6: Drawing of MicroBooNE's TPC. The TPC is placed with its longest side in the beam direction. The anode-plane on which wires where signals are formed is on the right-hand side, as seen from the beam. The cathode, where the drift high voltage is applied, is on the left.

The next section will describe the ionization electron signal, or charge signal, that is produced by the drifted ionization electrons to the wire planes, in Section 6.2.2.

6.2.2 Charge Signal

The ionization electrons that are produced in the TPC are subsequently detected as induced currents as a result of their drifting by sense-wires placed on the anode-plane of the detector. As a result of the bias voltages which are applied to all three wire-planes to ensure full transparency of the first two induction planes, the same ionization electrons produce signals on wires on all three wire-planes. As the ionization electrons are drifted by the first two wire-planes, they induce a bipolar signal. The signal produced on the wires on the final plane, which the electrons are collected on, is unipolar. Starting with a waveform from a single wire (Figure 6.7, step (a)), it is possible to visualize particles trajectories by displaying such waveforms next to the waveforms from all the other wires, as done in steps (b) and (c) of Figure 6.7. This figure only shows part of the detector, where a ν_μ CC candidate vertex was identified. Figure 6.8 shows the complete candidate event, with the final state muon coming to a stop and decaying. In this figure, moving from left to right, all of the waveforms from the collection plane wires are displayed. For a single wire, the y axis shows the recorded waveform in a drift-time coordinate. The particle trajectory points that are visible in the lower part of the image are closer to the anode plane as a result of the electrons from that point having to take less time to drift and be collected on the collection plane wires. The y axis in this figure can

LArTPC Design Parameters and Nominal Operating Conditions	
Parameter	Value
# Anode planes	3
Anode planes spacing	$3mm$
Wire pitch	$3mm$
Wire type	SS, diam. $150\mu m$
Wire coating	$2\mu m$ Cu, $0.1\mu m$ Ag
Design Wire tension	$6.9N \pm 1.0N$
# wires (total)	8256
# Induction0 plane (U) wires	2400
# Induction1 plane (V) wires	2400
# Collection plane (Y) wires	3456
Wire orientation (w.r.t. vertical)	$+60^{\circ}$, -60°, 0° (U, V, Y)
Cathode voltage (nominal)	$-128kV$
Bias voltages (U, V, Y)	$-200V$, $0V$, $+440V$
Drift-field	$500V/cm$
Max. Drift Time, Cathode to U (at $500V/cm$)	$1.6ms$
# Field-cage steps	64
Ring-to-ring voltage step	$2.0kV$

Table 6.2: MicroBooNE LArTPC design parameters and nominal operating conditions.

then be seen as the drift direction in the detector, while the x axis shows the direction along the neutrino beam, as collection plane wires are displaced perpendicularly to this direction. In summary, Figure 6.8 shows a bird-eye view of particles interacting in the MicroBooNE detector.

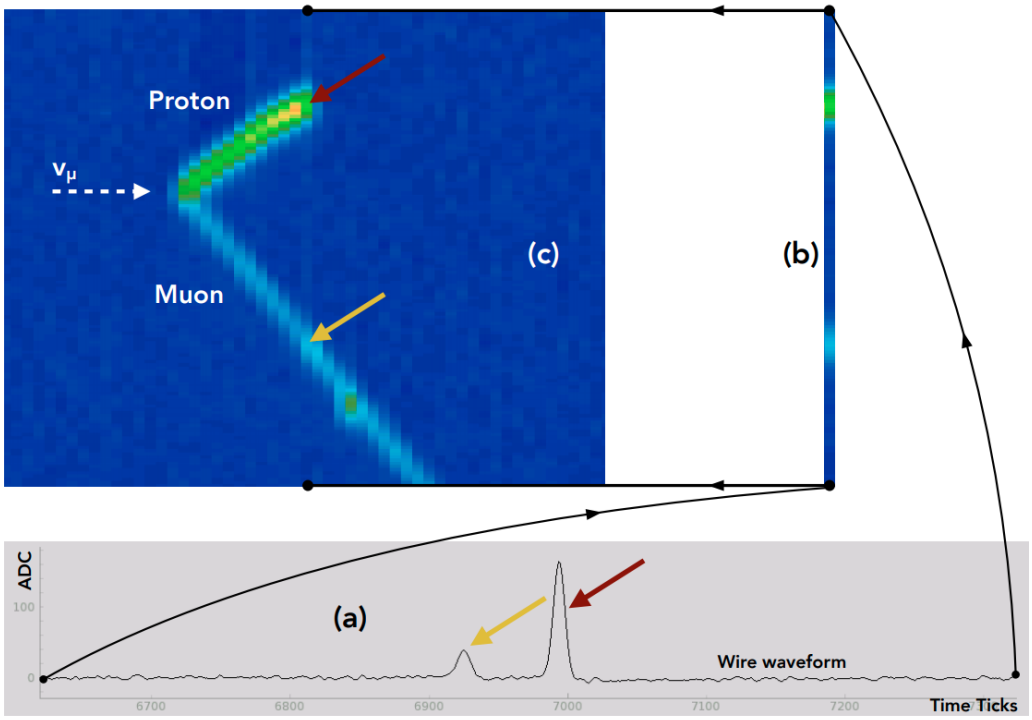

Figure 6.7: Figure (a) shows a waveform from a collection plane wire (after noise filtering). Figure (b) and (c) shows how the MicroBooNE event display is constructed, by displaying waveforms from each wire one next to the other. The display shows a candidate interaction vertex from a ν_μ CC interaction, where the final state proton and muon are visible.

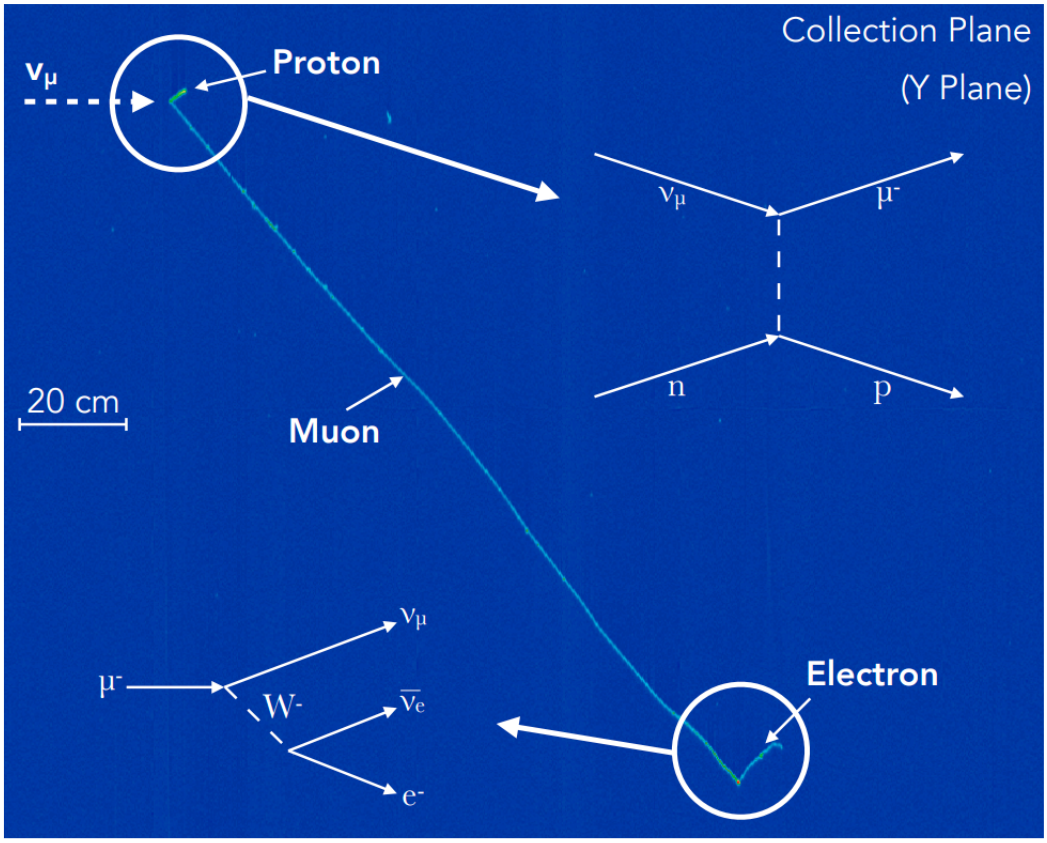

Figure 6.8: Event display showing raw data from a small region of the TPC volume from the collection plane. The display shows a candidate ν_μ CC interaction, where the final state proton and muon are visible. The x axis shows the collection plane wires (increasing wire-number from left to right) and the y axis shows the drift-coordinate (increasing drift-time moving upwards). The scale bar applies to both the horizontal and vertical coordinates. The color map shows the amount of collected charge on each wire per time tick. In this display the muon candidate is spatially contained in the detector and it decays. The Michel electron coming from the decay is also visible.

With the charge signal now discussed, the next aspect of the LArTPC of MicroBooNE to discuss is the light collection system, which follows in Section 6.2.3.

6.2.3 Light Collection System

The light produced by neutrino interactions in MicroBooNE is an important input for both event selection and reconstruction. One of the critical capabilities the light collection system provides is the ability to form a beam-event trigger when a pulse of light is observed in coincidence with the beam spill. Because typically only one beam spill in 600 will produce a neutrino interaction in the detector, such a trigger will substantially reduce the overall data output rate.

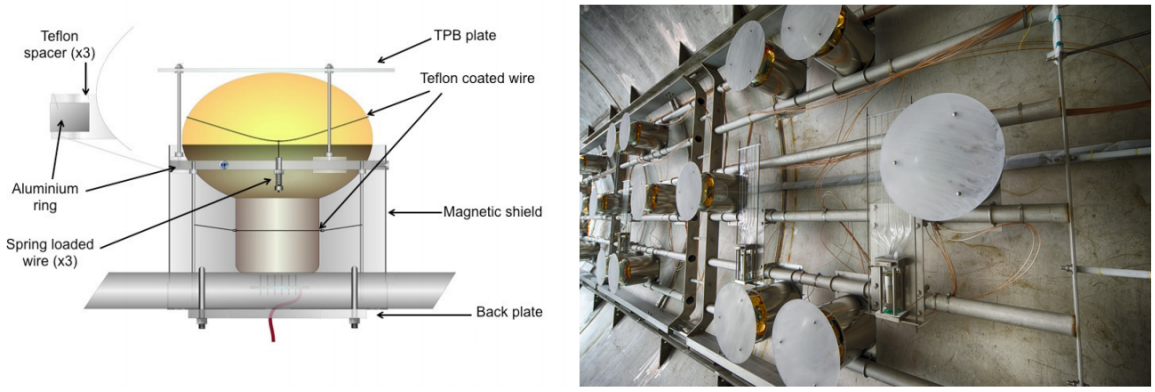

Figure 6.9: A diagram of the PMTs in MicroBooNE on the left, and a photo of the PMTs installed in the cryostat with the TPB plates installed in front of them on the right.

The light collection system consists of primary and secondary sub-systems. The primary light collection system is made up of "optical units," each one consisting of a PMT located behind a wavelength-shifting plate (coated in TPB, which was discussed in the previous Chapter). In total, 32 optical units were installed, yielding 0.9% photocathode coverage. The secondary system consists of four light guide paddles. These paddles were introduced for R&D studies for future LArTPCs, and are placed near the primary optical units to allow a comparison of their performances. A flasher system, used for calibration, consists of optical fibers bringing visible light from an LED to each PMT face.

As a result of the optical system not being used beyond its capabilities of a beam-event trigger in this study, the discussion is ended here for this subsystem of the MicroBooNE LArTPC. Next will be a discussion of the triggers and the data stream of MicroBooNE, in Section 6.3.

6.3 Triggers and Data Stream

Every event in MicroBooNE starts with a hardware trigger. The Fermilab accelerator division sends signals to MicroBooNE every time there is a neutrino beam spill. This trigger, called the "BNB" trigger, causes a window to open the PMT readout that lasts for 23.4 μs, and a window in the TPC readout that lasts 4.8 ms. The beam trigger efficiency is 99.8%. The data sample originating from the trigger is here called the "beam-on" data sample.

The majority of the spills do not produce a neutrino interaction in the detector. Indeed, simulations show that approximately only 1 in 600 beam spills produces a neutrino interaction in the detector. In order to reduce the amount of recorded data, not every spill is saved. A software trigger looks at light activity on the PMTs in time-coincidence with the 1.6 μs beam spill reaching the detector. This activity may be caused by a neu-

trino interaction, coincident CR activity, or some other coincident sources. The software trigger reduces the data rate by a factor of 20. The signal efficiency loss through the trigger condition is negligibly small.

An additional trigger used in this work is the so-called "EXT" trigger, that mimics a BNB trigger in the absence of neutrino beam. This trigger allows to record CR data in order to measure the cosmogenic background that will affect the analysis. The data sample collected with this trigger is here called the "beam-off," or "EXT" data sample, and will be labeled as such in future plots shown for this analysis.

An optical pre-filter is also run in order to help reduce the data volume that TPC reconstruction algorithms is applied to. This filter checks for optical activity within the time window of the beam and requires a minimum threshold of 20 Photo-Electron (PE) in the beam time window.

The MicroBooNE simulation (described in Section 6.5), only includes simulation of events that contain neutrino interactions and does not contain events with only CRs. In order to be compared to the beam-on data sample, events from the beam-off data stream are added to the simulation, normalising by the number of hardware triggers. The event distributions presented in this thesis will show simulation compared to plus beam-off data compared to beam-on data. The next section, Section 6.4, will briefly discuss the readout electronics and the data format for MicroBooNE.

6.4 Readout Electronics and Data Format

MicroBooNE's readout electronics are responsible for forming, digitising, and recording signals associated with the TPC and PMT systems. Thus this is one of the most vital subsystems of the detector.

The MicroBooNE TPC electronics system is separated into "cold" electronics, which are submerged in liquid argon, and "warm" electronics, which are located outside of the cryostat. The cold electronics are responsible for amplifying and shaping signals produced on the sense wires. Performing these operations in a cold environment and in close proximity to the wires allows MicroBooNE to obtain a high signal-to-noise ratio, essential to obtain accurate particle identification with low detection thresholds. The warm electronics are responsible for digitising signals, and compressing and formatting the data before it is sent to the data acquisition system.

The analogue signals from the 8256 sense wires in the TPC pass through Complementary Metal-Oxide-Semiconductor (CMOS) analogue front end ASICs which operate on cold motherboards at liquid argon temperatures. The signals are then shaped and amplified by cold intermediate amplifiers before passing through a warm feed-through. The signals are received by custom-designed LArTPC readout modules, which digitize and process them. The TPC wire signals are digitized at 16 MHz and then down-sampled in the digitization process to 2 MHz (500 ns time-ticks). The TPC system reads out three 1.6 ms frames of wire signal data associated with one event. This time is chosen based on how long it takes for ionization electrons from the cathode side of the TPC to drift to the anode wires (this time is 1.6 ms with the design drift field of 500 V/cm, but 2.3

ms as a result of the current MicroBooNE drift field of 173 V/cm). One frame before and two frames after the trigger are collected, ensuring that there is a large enough amount of data to identify a neutrino interaction, as well as all CR signals that arrive soon enough before or after the neutrino needing to be reconstructed in analyses, too.

Similarly to the TPC, the PMT signals undergo separate shaping with a 60 ns peaking time to allow for the digitization of several samples on the rising edge of a signal for more precise timing reconstruction abilities. The PMT signals are digitized at 64 MHz (15.625 ns time-ticks) and are then split into high-gain and low-gain channels which carry 18% and 1.8% of the total signal amplitude, respectively, to extend the dynamic range of the Analog-to-Digital Converter (ADC). The PMT system records data in two different formats: (i) in an unbiased way for a duration of 1500 samples (23.4 μs) which is opened by the beam-gate signal received on the trigger board. Neutrinos are expected to arrive $\approx 4\mu$s after this window is opened; (ii) in a discriminated way (called "cosmic discriminator") before and after the 23.4 μs window. This is needed in order to reduce the amount of recorded data. Discriminated waveforms are read out for an interval of 6.4 ms, which well covers the 4.8 ms TPC readout window: [-1.6,+3.2] ms. The cosmic discriminator only saves waveforms that go above a threshold of 130 ADC ($\approx 6.5 effective PE$), $and it only saves 40 samples (\approx 0.6\mu$s). A dead-time of 45 samples follows every time a cosmic-discriminated waveform is recorded.

Thus that is how data is readout using the readout electronics and the data format of the collected experimental data. The next section, Section 6.5, will discuss the way that events are simulated within the LArTPC for analyses of MicroBooNE.

6.5 Simulation

Beamline and detector simulations are intended to represent truth level estimations of neutrino production and interaction processes. These estimations serve as a baseline for comparison with collected data, as well as to estimate the backgrounds in the selected data samples. They are referred to as Monte Carlo (MC) simulations. There are a number of systems to model, and details to account for, in order to ensure the simulation precisely captures the state of the detector.

The flux of neutrinos at the MicroBooNE detector is simulated using a framework built by the MiniBooNE collaboration. Neutrino interactions in the MicroBooNE detector are simulated using the GENIE event generator, which generates the primary interaction inside the argon nucleus, the production of all final-state particles in the nucleus (hadronisation), and the transport and rescattering of the final-state particles through the nucleus (FSI). GENIE v3 was used for the MC presented in the analysis of this thesis, and Table 6.3 lists the nuclear models employed in GENIE v3.

The simulation of the MicroBooNE detector is based on Geant4 [80] and includes particle propagation, drift of ionisation electrons to the wire planes, as well as propagation of scintillation light to the PMTs. Ionisation due to CRs also leads to a distortion of the electric field within the detector. The effect is the build-up of slow-moving positive ions in a detector which gives rise to the so-called "space charge" effect. This effect leads

Interaction	Model
Nuclear Model	Local Fermi Gas
Quasielastic scattering	Nieves w/ dipole axial FF
CC MEC	Nieves
NC MEC	Empirical
NC elastic	Ahrens
Resonance	Berger-Sehgal
Coherent pion production	Berger-Sehgal
Deep inelastic scattering	Bodek-Yang
Hadronization	AGKY
Final-state interactions	hA2018

Table 6.3: Table listing the nuclear models employed in GENIE v3.

to a displacement in the reconstructed position of signal ionization electrons, as well as variations in the amount of charge quenching experienced by ionization throughout the volume of the TPC. The MicroBooNE detector simulation includes the space-charge effect. All simulation is carried out within the LArSoft framework [81].

Finally, now that the simulation of events within the MicroBooNE detector has been discussed, the detector operations and a description of the data set that is used in the analysis of this thesis will follow in Section 6.6.

6.6 Detector Operations

The MicroBooNE detector has been recording neutrino beam data since August 2015, with over 1.3×10^{21} protons-on-target (POT) collected to date. Figure 6.10 shows the amount of Protons on Target (POT) collected since the start of operations. The CC-Coherent Pion Production cross section analysis presented in this thesis utilizes 6.87×10^{20} POT of data (called "Run 1+2+3"), collected from February to March 2018. More recent data, not used in this analysis, benefits from the installation of a CR tagger system. To date, MicroBooNE has performed five full runs of data-taking, with scheduled shutdowns and maintenance performed in between runs.

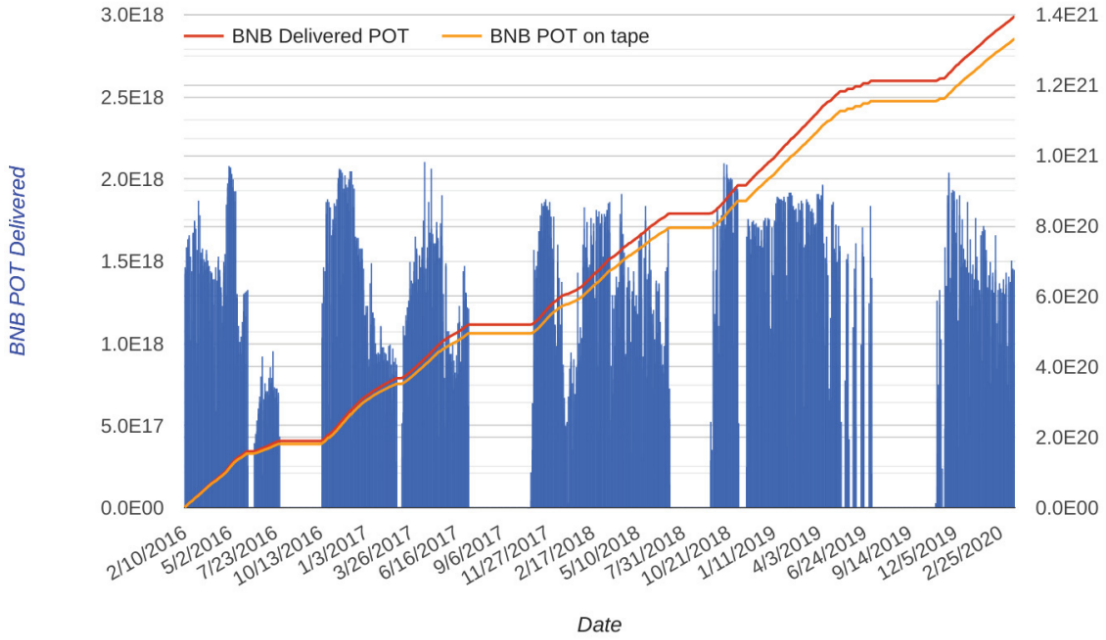

Figure 6.10: Cumulative POT collected by MicroBooNE during Runs 1-5, excluding the period before the software trigger was applied. The total POT delivered across all five runs with the software trigger is 1.39×10^{21}, while the POT written to tape is 1.33×10^{21}.

The next chapter, Chapter 7, details the process of taking the raw data from the light collection system, as well as the wireplanes, and turning that information into reconstructed events with tracks, showers, vertices, flashes, and more.

7 Event Reconstruction

After discussing the MicroBooNE detector, as well as the simulation of events in Chapter 6, it is now time to move to reconstructing the particle interactions, or "event" of interest to this analysis. There are three primary reconstruction algorithms that are used by MicroBooNE analyses: the Pandora pattern recognition algorithm [82], a deep neural network algorithm known as Deep Learning (DL) [83], and the novel Wire-Cell (WC) reconstruction algorithm [84].

This chapter covers the TPC and optical reconstruction that is applied to all data events in order to go from raw data recorded by the detector to high-level reconstructed objects, like particle tracks (used extensively in this analysis' sample selection) and optical flashes of light, necessary for the preselection portion of this analysis. Section 7.1 and 7.2 describes the TPC and optical reconstruction respectively. The neutrino reconstruction is described in Section 7.3, and is followed by the methods of muon momentum reconstruction in Section 7.4. The chapter closes with a brief discussion of the four-momentum transfer reconstruction in Section 7.5.

7.1 Optical Reconstruction

The optical reconstruction collects raw waveforms recorded by individual PMTs and combines them to reconstruct "flashes," which represent optical activity in time across several PMTs, usually caused by a single neutrino or CR interaction in the TPC. This process can be broken into three distinct steps: Signal Processing (Section 7.1.1), Baseline Estimation (Section 7.1.2), and Pulse Finding and Flash Reconstruction (Section 7.1.3). Once the flash reconstruction is finished, the flash can then be used to identify candidate neutrino interactions through a process called Flash Matching (Section 7.1.4).

7.1.1 Signal Processing

The first step performed in the optical reconstruction consists in merging the high and low gain channels into a "saturation-corrected" waveform which tries to correct saturating high-gain pulses by using information from the low-gain channel.

7.1.2 Baseline Estimation

The baseline estimation of the waveform is performed in two different ways depending on whether the waveform is coming from the cosmic or the beam discriminator. If

the waveform comes from the cosmic discriminator, a constant value is used for the baseline, which is simply set to the first ADC value in the first recorded sample. If the waveform comes from the beam discriminator, a more complex algorithm is used. A loop is done over all the waveform ADC recorded values, and the Standard Deviation (STD) of neighboring values is calculated. If the STD is low, is shows that there is no optical activity in that region. In such regions, the baseline is set to the same waveform ADC values. A loop along the waveform entries is done and, where a region with high STD is found, the baseline is estimated by doing a linear interpolation between the two low-STD adjacent regions. This procedure takes care of estimating the right baseline if there are fluctuations. An example of baseline estimation can be seen in Figure 7.1.

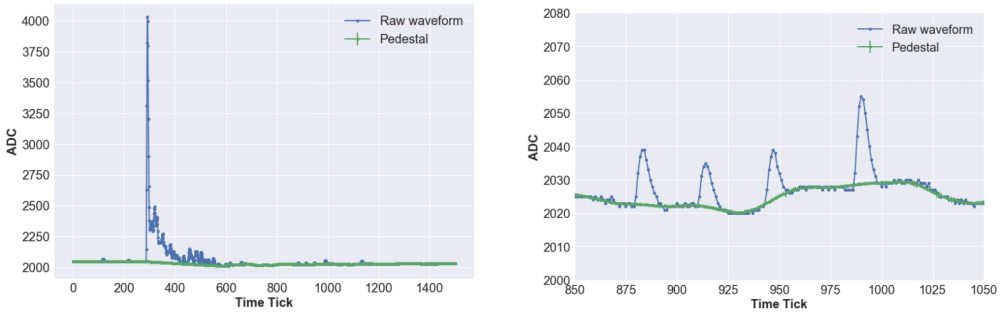

Figure 7.1: An example of PMT raw waveform from data in blue and the estimated baseline in green (Left), and an enlargement of the waveform to show single PE peaks (Right).

7.1.3 Pulse Finding and Flash Reconstruction

Once the baseline is determined, an algorithm that looks at the waveform ADCs going above a configurable threshold is run, in order to find pulses. Then, the flash reconstruction takes the identified pulses associated to each PMT as input. The time range is divided into configurable intervals and pulses falling in the same time interval are identified. Once coincident pulses are found, an integration window of 8μs is applied in order to collect all the late light. To avoid that another flash is claimed by coincident late light pulses, an 8μs dead time window is also applied. In the case of two candidates flashes with a time difference smaller than 8μs, only the one that deposits more PE is saved.

The most interesting flashes are those happening during the 1.6μs beam spill window, as the majority of them are induced by neutrino interactions. It is not possible to have multiple reconstructed flashes in that time window. In fact, it is smaller than 8μs dead time window described above. In the case of more than one neutrino interactions or neutrino interactions with one or more CRs happening during the beam spill window, two scenarios are possible. For simplicity, let's assume there are two interactions happening during that time, then: (i) if the first interaction deposits less PEs than the second one, the pulses of the first will be ignored, and a flash will be claimed with the pulses of the second one (although late light pulses of the first may contaminate the second

claimed pulse), (*ii*) if the first interaction deposits more PEs than the second one, then a flash will be claimed at the time of the first interaction, and the pulses of the second interaction will be added to the first claimed pulse.

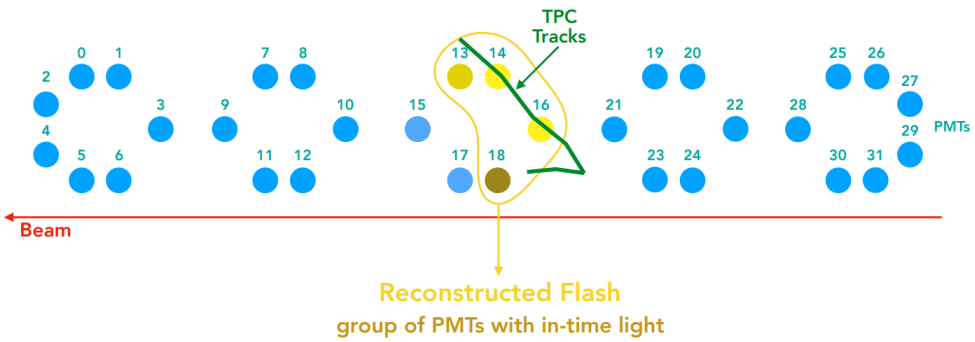

Figure 7.2: Schematic of flash reconstruction. The blue circles represent the MicroBooNE PMTs, and the red line an example of a particle track in the detector. The yellow PMTs that see light in time coincidence coming from the track, are clustered together to form a flash.

The flash reconstruction also performs a constant background subtraction of 2 PE per PMT to account for a measured 250 kHz noise, that is then integrated over the 8μs flash time window. Figure 7.2 shows a sketch of the flash reconstruction.

7.1.4 Flash Matching

The flashes that have been reconstructed can then be used in neutrino interaction identification through the process of flash matching. For each PMT, the reconstructed optical activity is compared to the predicted activity for each candidate interaction in the event. The interaction whose optical activity most closely matches expectation (based on a χ^2 test) is then "matched" to the reconstructed flash. This flash-matching technique reduces background by an order of magnitude, significantly improving MicroBooNE's ability to distinguish neutrino interactions against a large cosmic background [85].

7.2 TPC Reconstruction

This section very briefly describes the reconstruction steps that lead to TPC reconstructed objects in MicroBooNE, the most common of these being tracks, and electromagnetic (EM) showers (vertices are also a common reconstructed object). Tracks tend to show as relatively straight and narrow lines traversing the TPC volume, such as the long muon track shown in Figure 6.8. At MicroBooNE energies, the most common track-producing particles are muons, charged pions, and protons. Unlike tracks, showers tend to produce a cascade of particles in a roughly conical shape. EM showers in MicroBooNE are generally produced by either electrons or photons. Electrons shower

immediately when produced, and thus the showers are usually attached to the interaction vertex. Photons will propagate invisibly over some distance before converting to an e^+ and e^- pair, which then create showers themselves. This means that photon showers show a distinct gap between interaction vertex and the shower starting point. This analysis only makes use of tracks and vertices.

The starting input for TPC reconstruction consists of waveforms in the drift time of charge induced or deposited on the sense wires. These waveforms are passed through a filtering algorithm that was developed to reduce the noise introduced by the electronics. An example of the noise filtering algorithm in action is shown in Figure 7.3. The output of the noise filtering algorithm is then fed into another algorithm designed to identify candidate peaks in the waveforms by requiring that the peak of the waveform goes above a configurable threshold (I was actually the person that configured this threshold for the MC and data for the reconstruction algorithm that was used in this analysis, called MCC9).

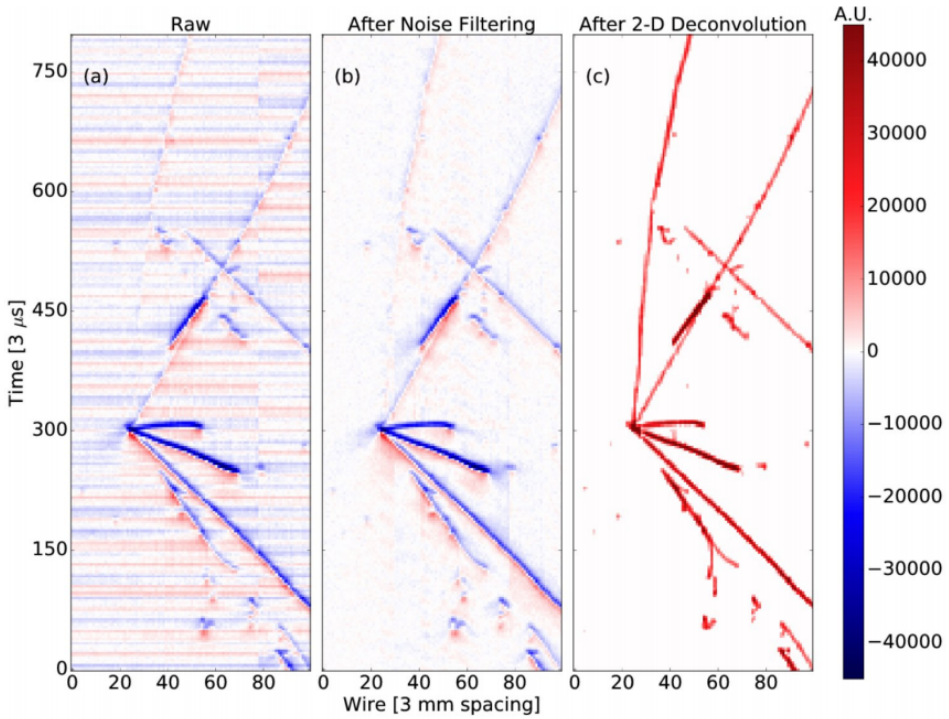

Figure 7.3: An example neutrino candidate event display from MicroBooNE data (event 41075, run 3493) showing a U plane view. (a) The raw waveform image in units of average baseline subtracted ADC scaled by 250 per 3μs. (b) The image after software noise-filtering in units of average baseline subtracted ADC scaled by 250 per 3μs. (c) The image after *2D* deconvolution in units of electrons per 3μs. Prolonged signals associated with near-vertical tracks, such as the one at the top left of each event display window, are recovered after the deconvolution step. Additionally, the image quality near the neutrino interaction vertex improves after the $2D$ deconvolution, which is expected to lead to improvements in the pattern recognition. Figure from [10].

The candidate peaks are then fitted with a Gaussian shape in order to obtain a "hit" representing the charge deposited on a wire by an incident track. Hits are objects with charge deposition information, a peak time, and a peak width, and serve as the basic input to the more complicated reconstruction algorithms that cluster the hits into tracks and showers. Hits are then grouped into clusters. The purpose of this is to group hits which correspond to the same particles signature, i.e. a track or shower. MicroBooNE utilizes the Pandora multi-algorithm pattern recognition framework, which handles the clustering of hits, as well as the reconstruction of 3D objects like tracks and showers.

The output of Pandora is structured in Particle Flow reconstructed particles, called "PFParticles," each one corresponding to a distinct track or shower and their heirarchy, which identifies parent-daughter relationships and describes the particle flow in the observed interactions. A neutrino is created as part of the heirarchy and forms the primary parent particle for a neutrino interaction. LArTPCs also provide excellent calorimetric

information. Calorimetry can be used to make a measurement of a particle energy deposition, which is useful to construct the particle identification (PID). The calorimetry is used in this analysis to help distinguish between muon candidate tracks from proton candidate tracks, as well as to help distinguish pion candidate tracks from proton candidate tracks.

7.3 Neutrino Reconstruction

Before neutrino reconstruction, Pandora is run in PandoraCosmic mode to identify hits that are flagged as being associated to CRs. The hits belonging to the CRs identified by the PandoraCosmic algorithms are removed from the data set and Pandora is run again, but this time in the PandoraNu configuration. PandoraNu reconstruction aims to identify a neutrino interaction vertex and uses it to aid the reconstruction of all particles emerging from the vertex position. There is careful treatment to reconstruct tracks and showers. A parent neutrino particle is created and the reconstructed visible particles are added as daughters of the neutrino.

Reconstruction of the neutrino interaction vertex begins with the creation of a list of possible vertex positions. A score is assigned to each vertex and only the one with the highest score is selected. The score is made by the product of three factors [86]: (*i*) the energy kick score, which creates a variable similar to the transverse energy and suppresses vertices with high scores since primary particles produced in the interaction should all point back towards the true interaction vertex; (*ii*) the asymmetry score, which suppresses candidates incorrectly placed along single, straight clusters, by counting the numbers of hits deemed upstream and downstream of the candidate position; (*iii*) the beam weighting score, which uses the beam direction and prefers vertices on the upstream side.

After vertex reconstruction, Pandora reconstructs tracks and showers and returns a list of reconstructed PFParticles. The final step in the PandoraNu reconstruction is to organise the reconstructed particles into a hierarchy. The primary particle is the neutrino PFParticle, which has no track nor shower associated but stores the neutrino candidate vertex. Any PFParticles deemed to be associated with the interaction vertex are added as primary daughters of the neutrino particle. Other particles, if exist, are added as daughter to the existing primary daughters of the neutrino PFParticle. Each hierarchy results in a single reconstructed neutrino particle, with the reconstructed daughter particles. More information is available in [86].

7.4 Muon Momentum Reconstruction

There are several different techniques that can be used to measure the muon momentum in a LArTPC: Momentum by Track Length, Momentum by Calorimetry Information, and Momentum by Multiple Coulomb Scattering.

Momentum by Track Length The momentum p can be measured from the muon

track length. The relationship between kinetic energy K and muon track length according to [11] is shown in Figure 7.4. The red line shows the interpolation used for this analysis. The particle momentum is obtained by $p = \sqrt{K^2 + 2mK}$, with m being the muon mass. This requires the track to be spatially contained in the TPC.

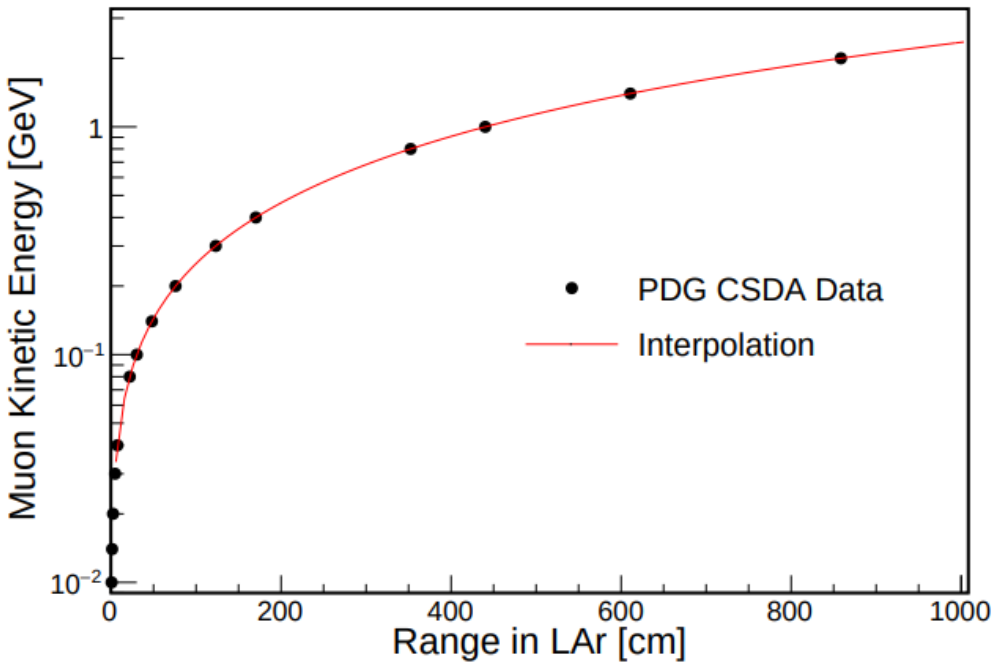

Figure 7.4: Muon kinetic energy vs. range in liquid argon according to the Particle Data Group data [11]. The red line shows the interpolation used for this analysis.

Momentum by Calorimetry Information By looking at the deposited charge on the wires, the quantity dE/dx of a particle can be measured along the particle trajectory, and can then be integrated in x to get the energy of the particle, and so the momentum $p = \sqrt{E^2 - m^2}$. This requires the track to be spatially contained in the TPC.
Momentum by Multiple Coulomb Scattering The momentum can be estimated by looking at the amount of muon scatters in argon and comparing it to the theory, then retrieving the RMS of the scattering angle as a function of p [87]. This method is powerful as it can also be applied to muons exiting the TPC.

While the first and second methods can only be applied to tracks that are spatially contained in the detector, the last one can be applied to all tracks. Since a large fraction of muons will exit the detector at the BNB energies, it is important to not restrict the analysis to only contained muons. Momentum by MCS will, therefore, be used for the analysis in this thesis for tracks that are not contained, and the previous two methods will be used on spatially contained tracks.

7.5 Four-Momentum Transfer Reconstruction

CC-Coh π^+ interactions can be identified by requiring that the observed final state consists only of a charged lepton and pion (the target nucleus is not observed since the energy transferred to the nucleus is small) and small $|t|$. This second identification characteristic, $|t|$ being small, needs to be made of reconstructed information. This is how that is accomplished for this analysis. From the assumption of zero energy transfer to the nucleus, $|t|$ can be approximated as

$$|t| = \left|(p_\nu - p_\mu - p_\pi)^2\right| \approx \left(\sum_{i=\mu,\pi} E_i - p_{i,L}\right)^2 + \left|\sum_{i=\mu,\pi} \vec{p}_{i,T}\right|^2 \tag{7.1}$$

where p_{ν_l}, p_l, and p_π are the four-momenta of the neutrino, charged lepton, and pion, respectively (these are found using the muon momentum reconstruction techniques mentioned above), and $\vec{p}_T$ and p_L are the transverse and longitudinal momenta with respect to the incoming neutrino direction. Thus, the $|t|$ is now reconstructed and can be used in event selection. A stacked histogram showing the data and MC agreement for this variable is shown in Figure 7.5.

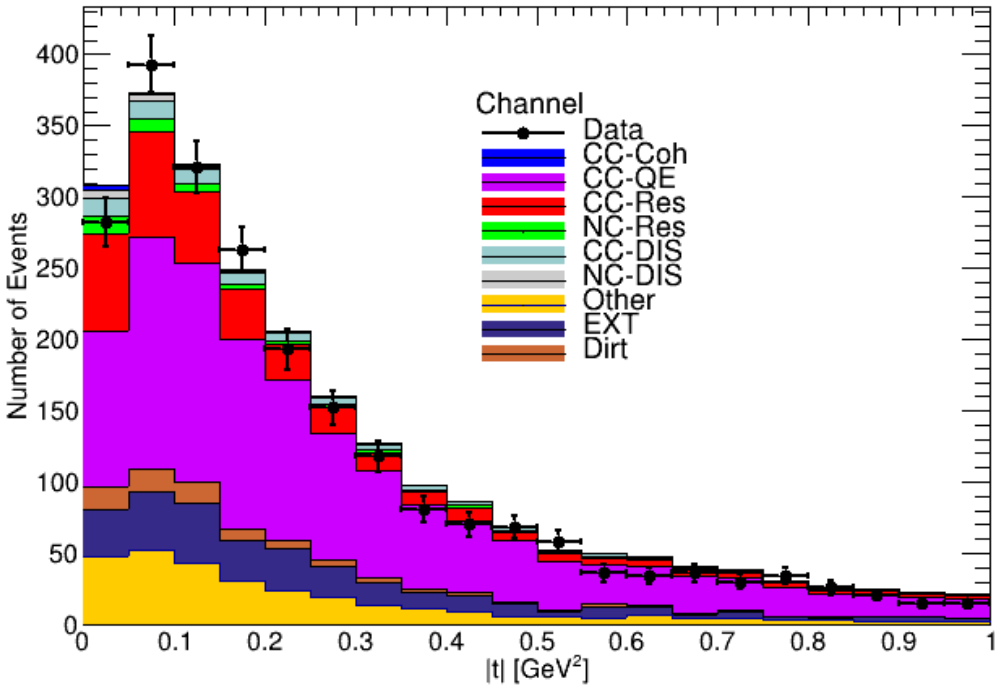

Figure 7.5: This is the stacked histogram of $|t|$ for events that passed the 2-Track filter. The error shown is only statistical error for the data sample.

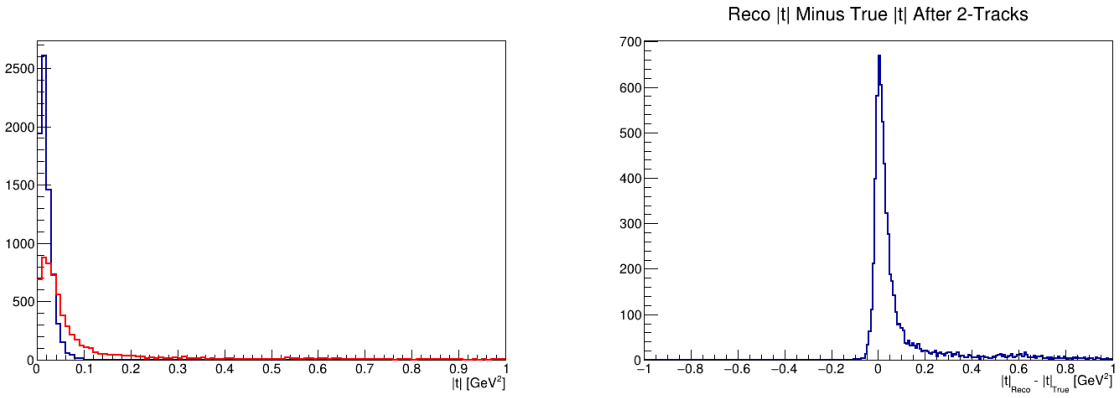

Figure 7.6: $|t|$ of the Enhanced CC-Coh π^+ sample where blue is $|t|_{True}$ and red is $|t|_{Reco}$ for events that have passed the 2-Track selection (Left) and the difference between $|t|_{Reco} - |t|_{True}$ for events that have passed the 2-Track selection, or the $|t|$ resolution (Right).

Figure 7.6 shows the resolution acquired for $|t|$, which comes out to be around $\approx 0.025 GeV^2$, and a selection utilizing this can be made. The next chapter of this thesis, Chapter 8, details the event selection implemented in order to choose CC-Coh π^+ production events, which will be used to calculate a flux-integrated cross section for this neutrino-nucleus interaction channel.

8 Event Selection

This chapter covers the selections implemented to accept CC-Coherent Pion Production events for this analysis. Due to the scarcity of this channel, obtaining a high purity sample of CC-Coh π^+ events is a difficult task. Significant work has gone into the development of this selection, which will be detailed below.

The first selection that is made is the implementation of a previous MicroBooNE analysis that selects a CC-Inclusive sample, which is discussed in Section 8.1. Once the CC-Inclusive sample is obtained, steps are taken to select a CC-Coh π^+ sample. This is done by first making a 2-Track Requirement (Section 8.2), which is followed by what has been called a Cone Angle Selection (Section 8.3). The Vertex Activity Selection immediately follows and is discussed in Section 8.4, and then comes the Pion Candidacy Selection discussed in Section 8.5. The last part of the selection is the Opening Angle Selection, which is discussed in Section 8.6, and concludes the selection of CC-Coh π^+ events. How the four-momentum ($|t|$) is measured is discussed in Section 8.7. The performance of the selection is discussed in Section 8.8, and the chapter concludes with a summary of the results of the event selection for CC-Coh π^+ in Section 8.9.

8.1 The CC-Inclusive Preselection

A version of the CC-Inclusive analysis selection that has been made on MicroBooNE data before is implemented as the preselection for this analysis. More details about the selection can be found in the thesis of the analyser that constructed the CC-Inclusive selection [8]. This selection is implemented in order to select a sample that has a high purity of CC-Inclusive events, implying that the NC backgrounds have been rejected. The possibility that two different neutrino interactions occurred in the same readout window of the detector is small enough that this is not considered for this analysis. Each readout window is assumed to have had only one neutrino interaction, if any.

8.1.1 Muon Candidacy Requirements

This step of the selection aims to tag the muon within a CC-Inclusive interaction. If no suitable muon-candidate is found, the event is discarded. There are many parameter requirements for a track to be designated as a muon candidate, and the first qualification for a track is the track score.

Track Score

The aim of this requirement is to remove electromagnetic shower activity, and ensure the candidate muon track is indeed "track-like." The track score is a statistical tool that gives a score for how closely a corresponding collection of hits resembles a particle track, or a track-like behavior (value close to 1), over a shower-like behavior (value close to 0). The track must have a track score greater than 0.85 in order for it to be designated as a muon candidate. Figure 8.1 shows the track scores for a general MC sample and a CC-Coh π^+ enhanced sample generated for this analysis.

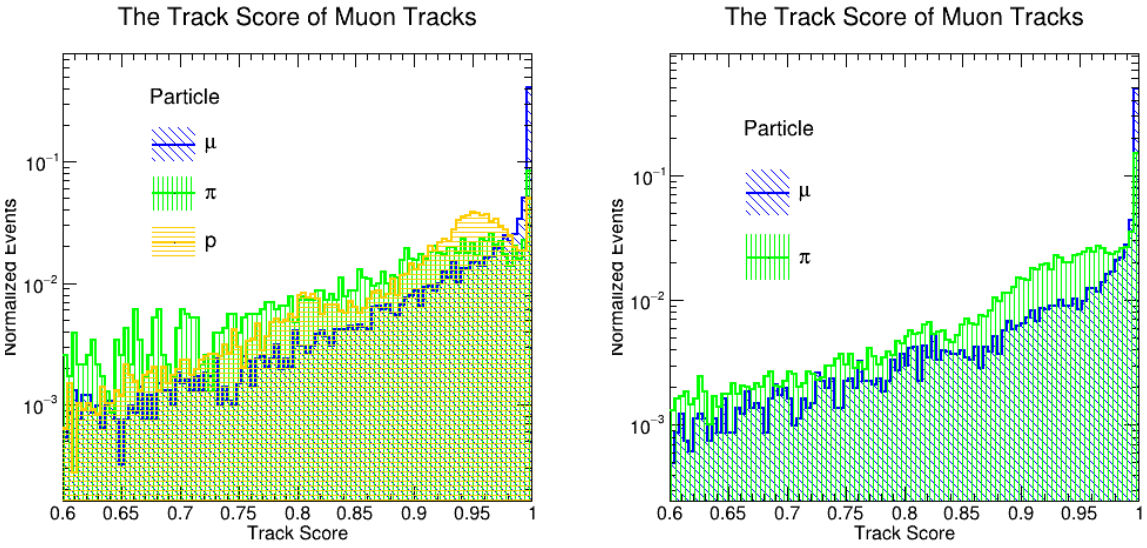

Figure 8.1: Track Scores for the CC-Inclusive Events (Left) and CC-Coherent Events (Right).

Vertex Distance

This requirement is intended to ensure that the beginning of the candidate muon track starts within a short distance of the location of the reconstructed neutrino vertex, in order to be sure that the track originated from the candidate neutrino interaction at that vertex. If the candidate muon track starts more than $4cm$ from the reconstructed neutrino interaction vertex, it will not be designated as a potential muon candidate track. The vertex distances can be seen in Figure 8.2.

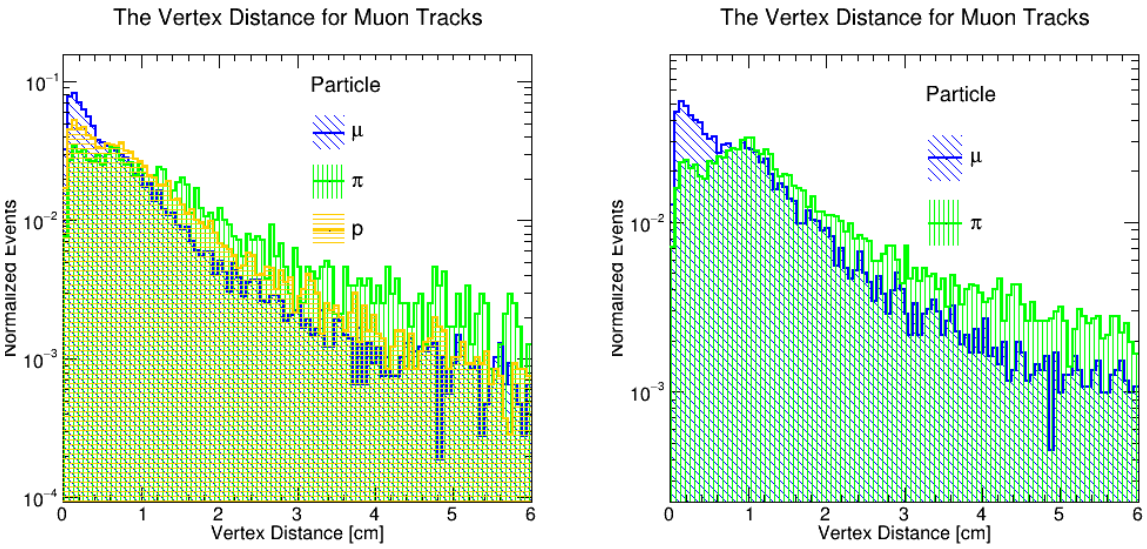

Figure 8.2: Vertex Distances for the CC-Inclusive Events (Left) and CC-Coherent Events (Right).

Generation

This requirement is intended to ensure that the Pandora pattern recognition network identified this candidate muon track as being a product of a neutrino interaction. The generation requirement is that it is equal to 2 according to Pandora, which means that Pandora believes the track is a daughter of an interaction. If not, the track will not be designated as a muon candidate.

Track Length

This requirement is intended to ensure a quality muon track is selected as the potential muon candidate and it, in combination with the vertex distance selection, excludes the possibility for mis-reconstructed events – often with cosmic impurities or near unresponsive wire regions – to be selected. The length of track chosen for this selection is $20cm$. If a track does not have at least $20cm$ of length, it will not be designated as a muon candidate. Figure 8.3 shows the track lengths of potential muon candidates for both the general MC sample and the CC-Coh π^+ sample that was specifically produced for this analysis.

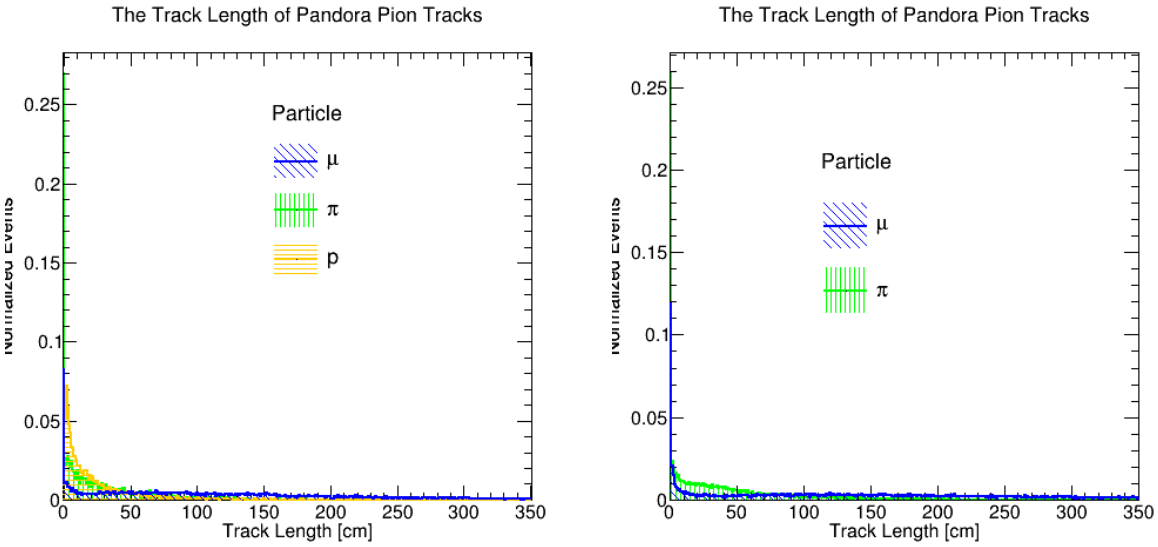

Figure 8.3: Pandora Reconstructed Track Lengths for the CC-Inclusive Events (Left) and CC-Coherent Events (Right).

Figure 8.4 shows the track lengths with a logarithmic y-axis of potential muon candidates for both the general MC sample and the CC-Coh π^+ sample that was specifically produced for this analysis.

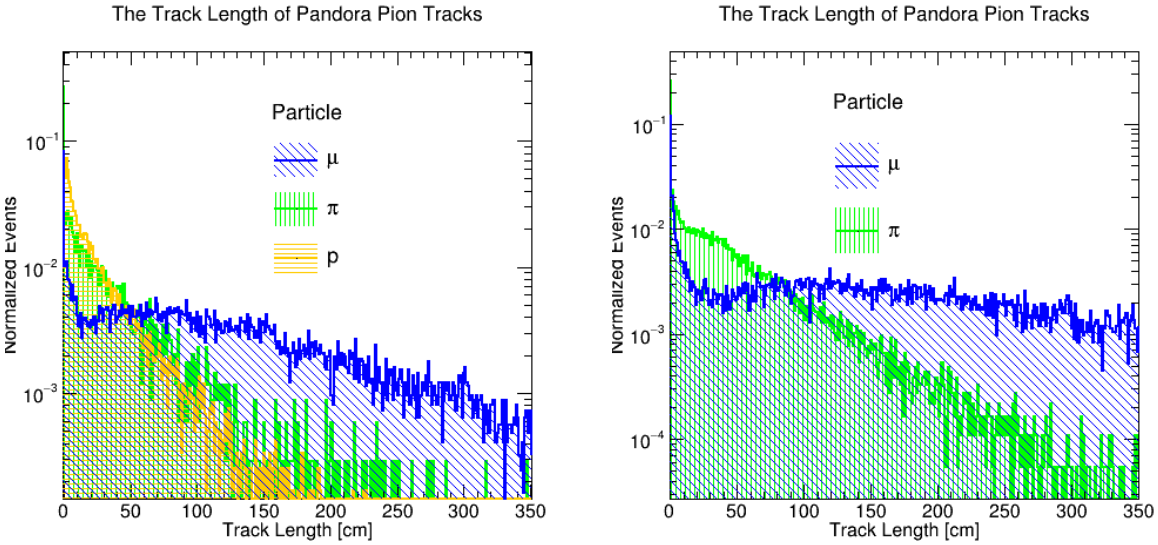

Figure 8.4: Pandora Reconstructed Track Lengths for the CC-Inclusive Events (Left) and CC-Coherent Events (Right) with a logarithmic y-axis.

Proton χ^2_p

The proton χ^2_p is a statistical hypothesis test intended to describe how closely a reconstructed track resembles a proton, when the track is hypothesized to be a proton. A

lower number implies that the reconstructed track more closely resembles a proton, than not a proton. This requirement is intended to ensure the selection of muon candidate tracks that do not resemble protons, thus should eliminate proton tracks that could be misidentified as a muon track. The requirement placed on the muon candidate is that it should have a $\chi^2_p > 60$. Figure 8.5 shows the χ^2_p for the MC sample on the left, and for an enhanced CC-Coh π^+ sample on the right.

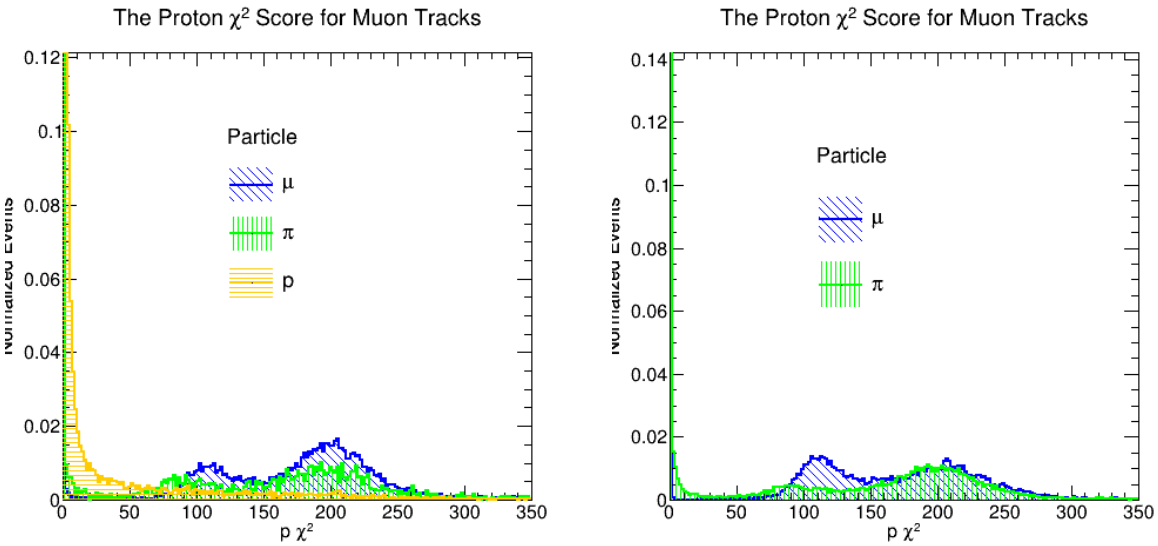

Figure 8.5: Proton χ^2 Scores for the CC-Inclusive Events (Left) and CC-Coherent Events (Right).

Muon χ^2_μ

The muon χ^2_μ is a statistical hypothesis test intended to describe how closely a reconstructed track resembles a muon, when the track is hypothesized to be a muon. A lower number implies that the reconstructed track more closely resembles a muon, than not a muon. This requirement is intended to ensure the selection of muon candidate tracks that do resemble muons, thus should eliminate non-muon like tracks that could be misidentified as a muon track. The requirement placed on the muon candidate is that it should have a $\chi^2_\mu < 30$. Figure 8.6 shows the χ^2_μ for the MC sample on the left, and for an enhanced CC-Coh π^+ sample on the right.

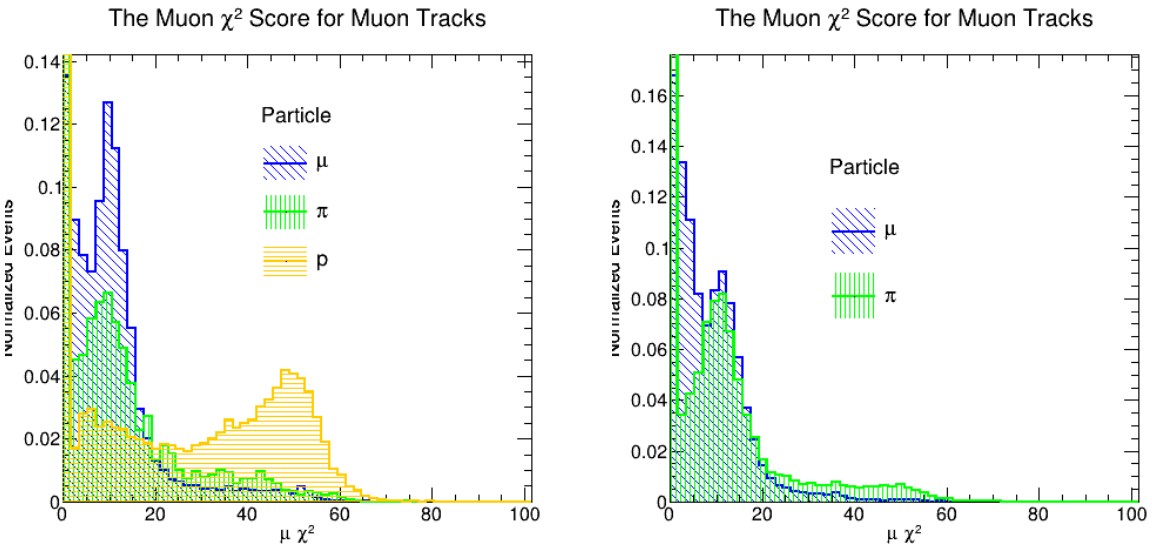

Figure 8.6: Muon χ^2 Scores for the CC-Inclusive Events (Left) and CC-Coherent Events (Right).

Proton χ^2_p Over Muon χ^2_μ (χ^2_p/χ^2_μ)

This ratio requirement for a candidate muon track is again intended to rule out non-muon like track through the use of a combination of both the χ^2_p and the χ^2_μ as a ratio: χ^2_p/χ^2_μ. The muon candidate track must have a $\chi^2_p/\chi^2_\mu > 7$ in order to be classified as a muon candidate. These ratios are shown in Figure 8.7, where on the left is for the MC sample, and the right is for an enhanced CC-Coh π^+ sample specifically generated for this analysis.

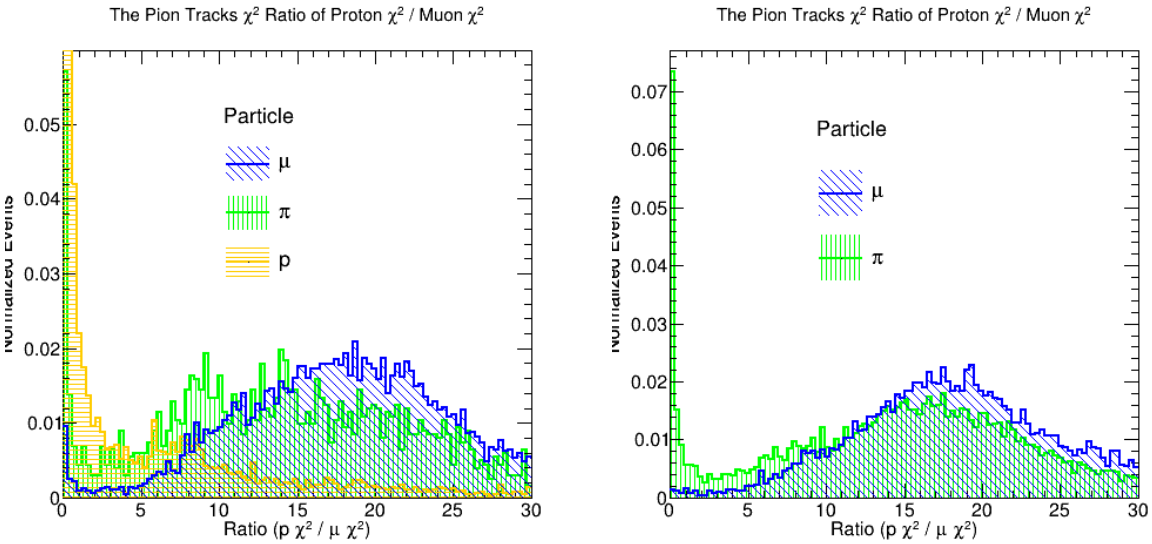

Figure 8.7: χ^2 Ratio for the CC-Inclusive Events (Left) and CC-Coherent Events (Right).

Should a candidate track have all of the above qualities, it is classified as the muon candidate for the event. If an event has two or more muon candidate tracks, the longest track is chosen as the muon candidate. This happens very rarely.

8.1.2 Further Selection

If the event has a muon candidate, additional cuts are applied to reduce the *BNB External* contribution, and to increase the purity of the CC-Inclusive selection. This section details the additional selections implemented to accomplish those goals.

Pandora PDG Code

The returned Pandora PDG code for the event must be that of a muon neutrino (ν_μ), which is a code of 14. This is done to ensure that the event is the result of a ν_μ interaction according to Pandora.

Start Vertex of Daughters

The reconstructed starting vertex of all daughter tracks must be within at least 10cm of the borders of the fiducial volume for an event. This is to ensure there is enough space for a proper reconstruction of the corresponding daughter track to be in consideration for the event.

Fiducial Volume

The reconstructed neutrino vertex must be within the defined fiducial volume chosen for this analysis. The fiducial volume used in this analysis is:

- X-axis (drift direction): [10, 246.4] cm,
- Y-axis (vertical direction): [-106.5, 106.5] cm,
- Z-axis (beam direction): [10, 986.8] cm.

This fiducial volume corresponds to a value of $49.19 \times 10^6 \text{cm}^3$, or 49.19m^3. This volume is used to ensure that tracks and hits that are reconstructed are of good quality and do not come within an appreciable distance of dead wires in the MicroBooNE TPC, or start too close to a boundary of the detector where space-charge effects are the largest.

Flash χ^2_{Flash} and Topological Score

The Flash χ^2_{Flash} and Topological Score selection is an or requirement, where the event was either required to have a $\chi^2_{Flash} < 10$ or a neutrino Topological Score > 0.25. Both of these are again statistical tests where the returned values imply how closely the corresponding hit or track resembles a hit that corresponds to a flash, or that the track is topologically consistent with a neutrino-induced event. If the event had either or both

of these two conditions met, it moved on to the next step of the selection which is a flat topological score selection on the event.

Topological Score

This is the last requirement for an event to pass the CC-Inclusive preselection used in this analysis. This value represents the output of a support-vector machine designed to classify events as either neutrino-like (value close to 1) or cosmic-like (value close to 0). The event is required to have a neutrino Topological Score > 0.06. If the event passes this selection as well as all the others above, then it passed the CC-Inclusive preselection and moves on to the actual CC-Coh π^+ selection which took tremendous effort to put together for this analysis, and was by far the most difficult portion of this thesis work.

8.2 2-Tracks Requirement

If an event has passed the CC-Inclusive pre-selection defined above, the next selection it must pass is what is called the 2-track requirement. This step in the selection is intended to explicitly target events that have a topology that would align with a neutrino interacting and producing two MIP-like, forward-boosted tracks, such as would be the case for CC-Coh events. This requires that exactly two reconstructed tracks come within $10cm$ of the reconstructed neutrino vertex in the event, and no more. If an event has more, or less than two tracks within the $10cm$ of the reconstructed neutrino vertex, it is dropped.

8.3 Cone Angle Selection

The Cone Angle is the angle that's between the vector addition of any two tracks in an event and the beam direction (z-direction), and we find this angle for a track in an event by looping through every track in an event and selecting the smallest angle found as the Cone Angle for that track. We then find the smallest Cone Angle of the event, and retain that as the Cone Angle for the event. The process of finding the Cone Angle is depicted in the diagram shown in Figure 8.8.

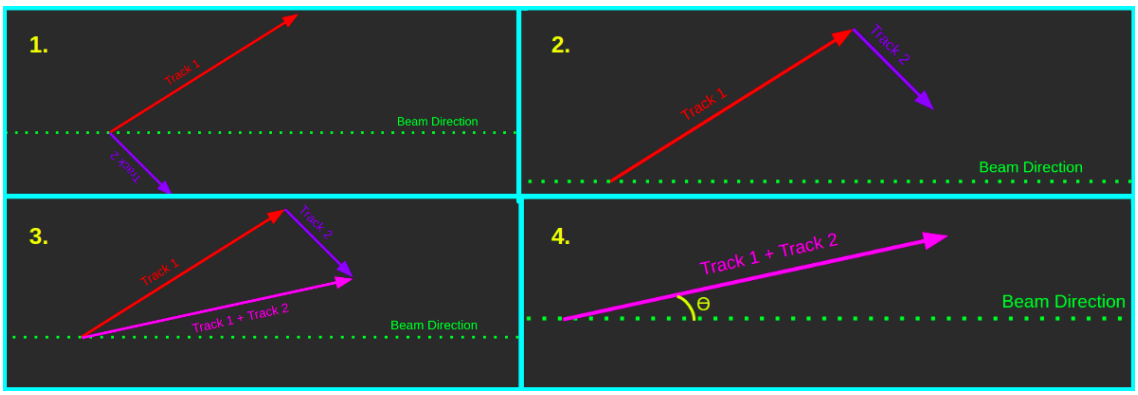

Figure 8.8: Diagram that illustrates how the Cone Angle is found.

Looking at Figure 8.8, and starting at the top left (#1) we have two tracks in an event. Then, now at #2, we vector add these two tracks, and now, in #3, we have the vector addition of the two tracks. Lastly, in #4 at the bottom right of the figure, we calculate the angle between our new vector and the beam direction, and the θ shown in the figure would be the Cone Angle. The Cone Angle of the events that have passed the 2-Track filter is shown in the stacked histogram of Figure 8.9.

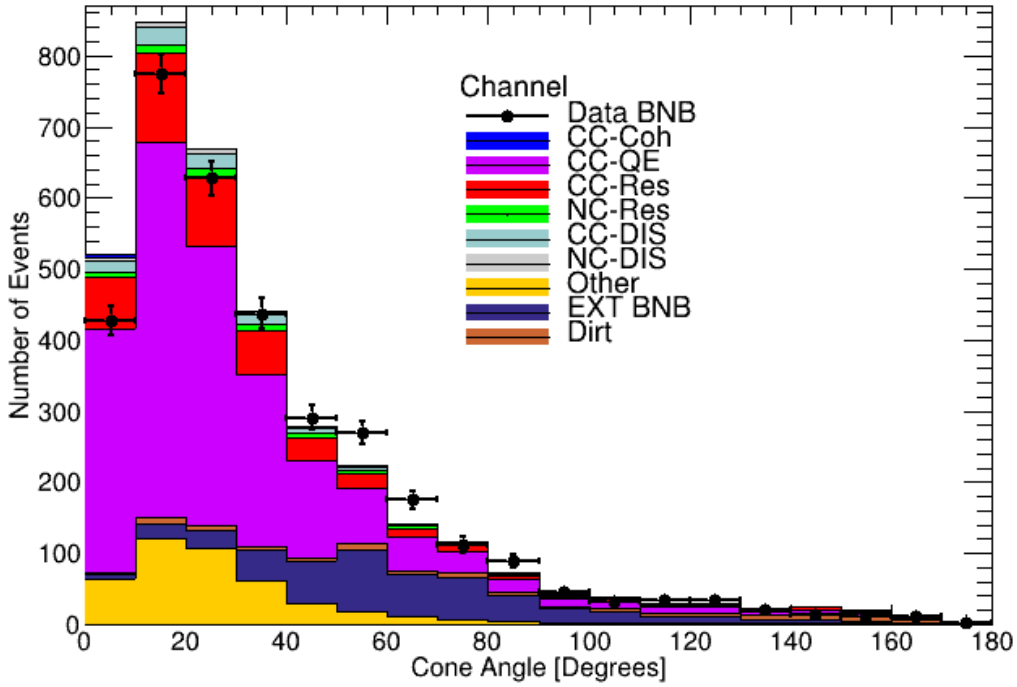

Figure 8.9: This is the stacked histogram of the cone angle for events that have passed the 2-Track filter.

Figure 8.10 shows the rejection percentage of background events and the passing percentage of events for signal events if the selection is made at that value. This plot is specifically for the Cone Angle for events that have passed the 2-Track filter. Using this plot, the requirement that the Cone Angle$< 20°$ was chosen.

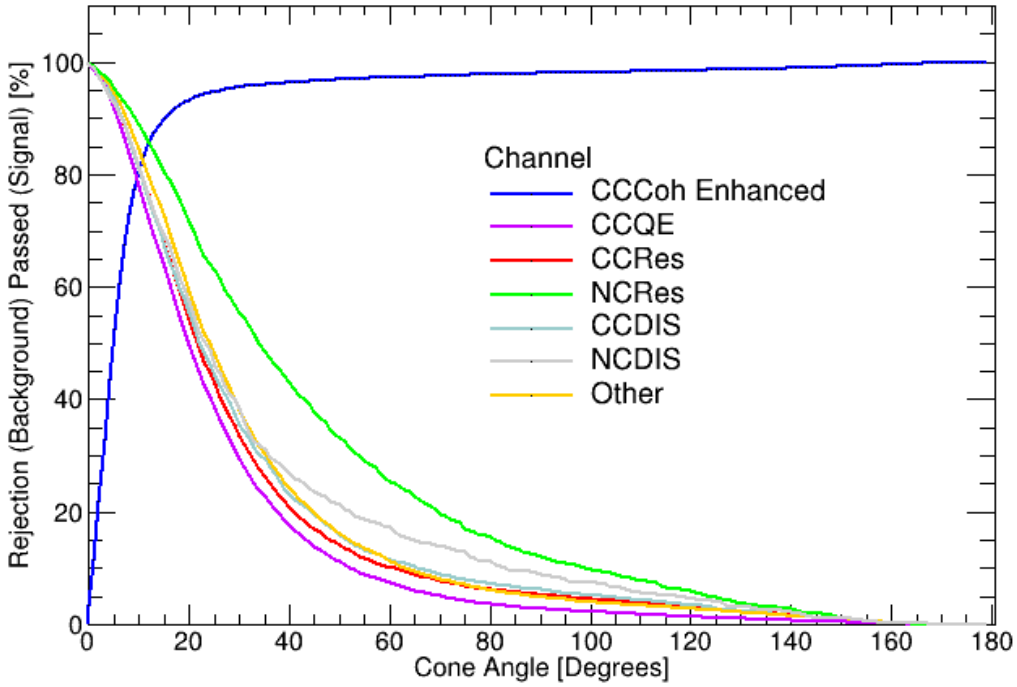

Figure 8.10: Rejection (for background events) and passing (for signal or CC-Coh π^+ events) percentages for if the cut was placed at the value in the plot. This plot is for the Cone Angle of events that have passed the 2-Track selection.

8.4 Vertex Activity Selection

The Vertex Activity has the potential to be one of the best identifiers for CC-Coh π^+ events, because our signal channel has the characteristic that there is very little four-momentum transfer to the nucleus, thus the contribution to the Vertex Activity for CC-Coh π^+ events should simply be from two particle tracks where both are MIPs.

This selection is broken into two segments that combine to make the total vertex activity selection: the vertex activity using track associated hits only (Section 8.4.1), and the vertex activity using all hits within a region around the reconstructed neutrino vertex (Section 8.4.2). Both are detailed below.

8.4.1 Vertex Activity Using Track Associated Hits

The Vertex Activity is a summation of the amount of energy deposited within a bubble from the hits that have been associated to reconstructed tracks that is drawn around the neutrino vertex for an event. If an energy deposit does not fall within this bubble, or if it was not associated with a reconstructed track, it is not included in the Vertex Activity calculation. The bubble radius used in this study was $10cm$, this was the result of a study to see how the vertex activity changed for various bubble sizes. Figure 8.11 depicts a bubble of radius $R = 10cm$ drawn around a neutrino vertex, and the energy deposits associated to reconstructed tracks in this bubble would be summed to give the Vertex Activity in that region.

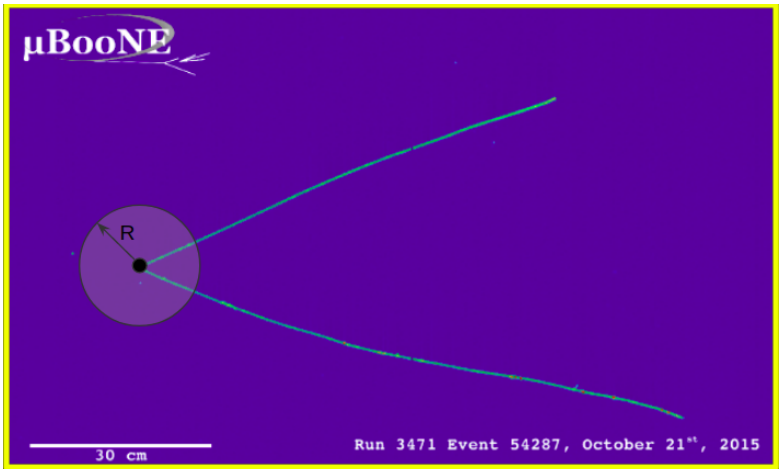

Figure 8.11: Vertex Activity graphic for hits associated to reconstructed tracks.

The VA in MeV of the events that have passed the 2-Track filter is shown in Figure 8.12. The algorithm to calculate the VA did not exist for MicroBooNE before, and so was specifically developed by myself for this analysis. The algorithm takes in reconstructed track information, finds the corresponding hits associated with the track and their positional information, and then loops through the hits associated with the track to see if the corresponding hit deposition along that point of the track falls within the $10cm$ bubble drawn around the reconstructed neutrino vertex position. If it does, the energy is added to the VA summation found for the event.

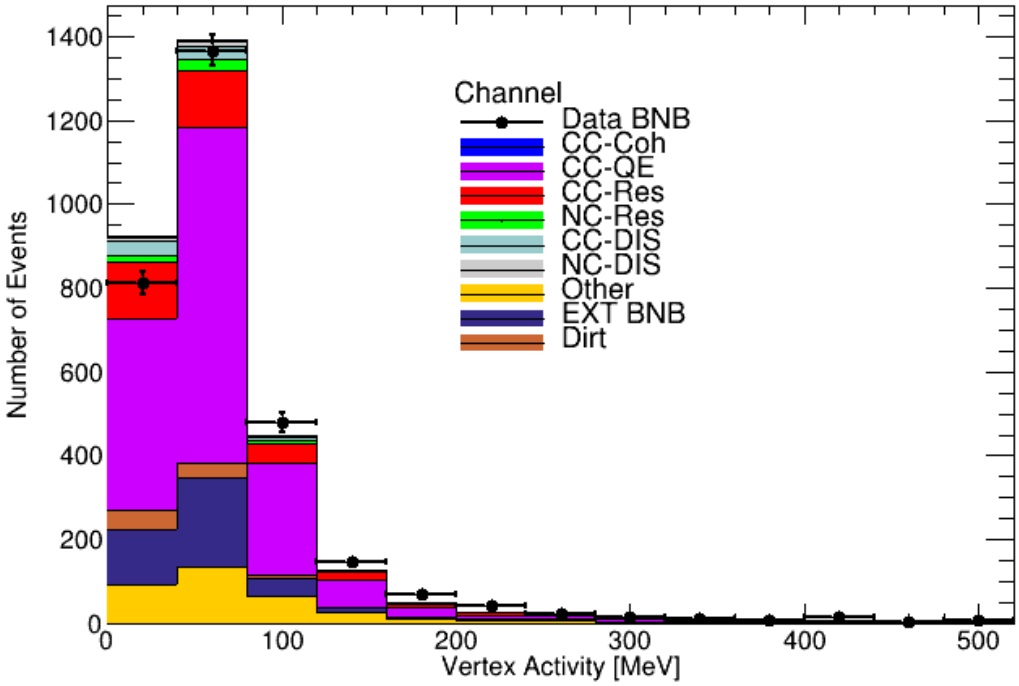

Figure 8.12: This is the stacked histogram of the vertex activity within the 10cm bubble drawn around the reconstructed neutrino vertex using just track associated hits for events that have passed the 2-Track filter.

Figure 8.13 shows the rejection percentage of background events and the passing percentage of events for signal events if the selection is made at that value. This plot is specifically for the VA of all hits associated to tracks within the 10cm bubble around the reconstructed neutrino vertex for events that have passed the 2-Track filter. Using this plot, the requirement that the VA < 50MeV was chosen.

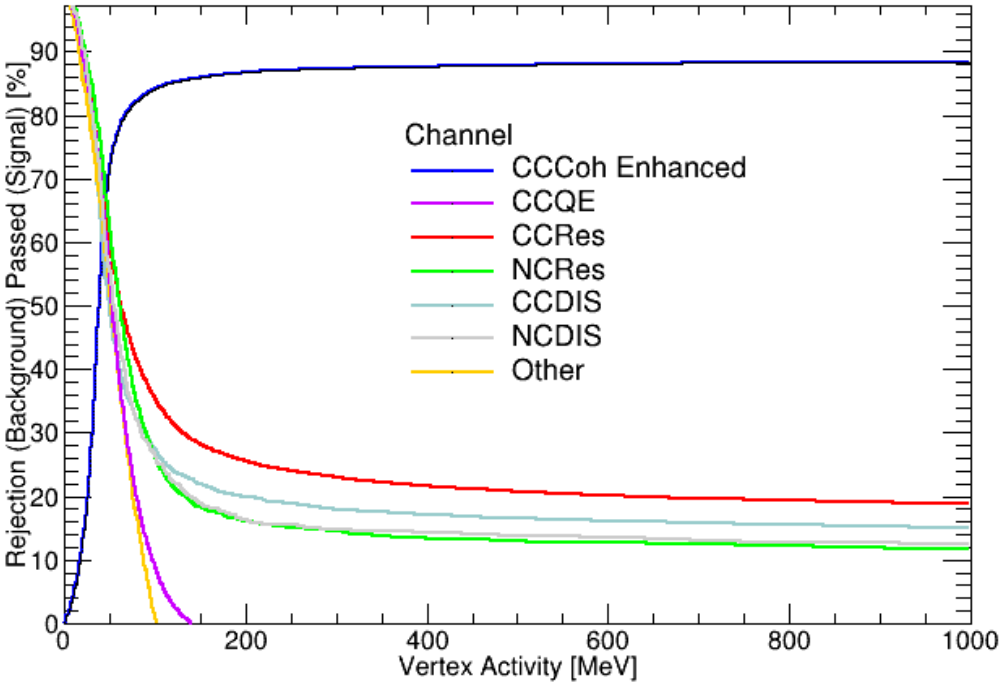

Figure 8.13: Rejection (for background events) and passing (for signal or CC-Coh π^+ events) percentages for if the cut was placed at the value in the plot. This plot is for the VA of all hits associated to tracks within the 10cm bubble around the reconstructed neutrino vertex.

8.4.2 Vertex Activity Using All Collection Plane Hits

The vertex activity selection discussed above only makes use of the hits that are associated to reconstructed tracks within the bubble drawn around the reconstructed neutrino vertex, which eliminates some of the distinguishing ability between CC-Coh π^+ events and background due to the backgrounds causing more hits within the bubble that will not necessarily be associated to tracks (this occurs for a number of reasons). That is why this second version of a vertex activity selection is added in addition to the selection above to make a total vertex activity selection.

This version of the vertex activity sums all of the hits that occur on the collection plane that come within some specified number of wires and time ticks of the reconstructed neutrino vertex. The VA in ADC of the events that have passed the 2-Track filter is shown in Figure 8.14.

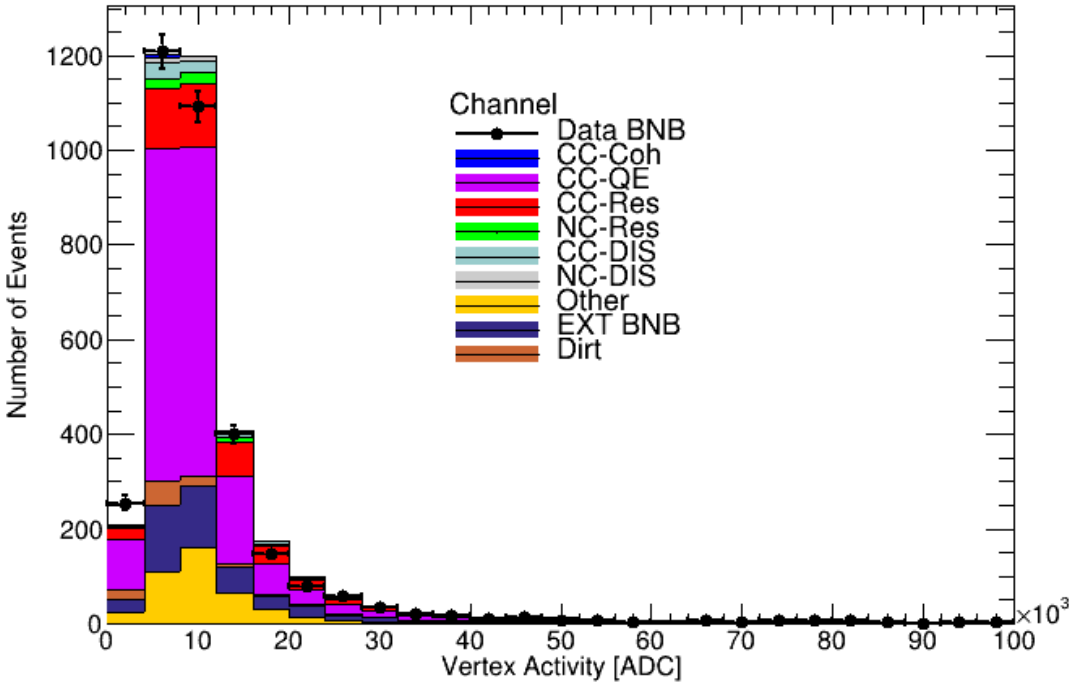

Figure 8.14: This is the stacked histogram of the vertex activity using all hits of the collection plane within the specified number of wires and ticks of the reconstructed neutrino vertex for events that have passed the 2-Track filter.

The algorithm that takes the information from reconstructed hits and converts this information into this version of the vertex activity calculation did not exist within the MicroBooNE code environment, previously. I developed this algorithm, and subsequently applied it to the reconstruction for this analysis. The algorithm takes as input the time and hit integral charge information, as well as the wire number associated with the hit and converts it into a spatial position that can be compared with the position of the reconstructed neutrino vertex. This portion of the vertex activity only looks at the collection plane information, so this limits the spatial conversion to a 2-D reconstructed position of the hit (the xz position of the hit) due to the orientation of the vertical wires of the collection plane. This means that the vertex activity selection includes all of the hits within a right-circular cylinder whose center of the circle portion of the cylinder corresponds to the location of the reconstructed neutrino vertex and the lengthwise of the cylinder encompasses the entire y-axis of the detector. This makes it possible that some hits that are associated with reconstructed cosmic tracks above or below (in the y-axis) the reconstructed neutrino vertex are also included in this version of the VA selection.

Figure 8.15 shows the rejection percentage of background events and the passing percentage of events for signal events if the selection is made at that value. This plot is specifically for the VA of all hits within the defined region around the reconstructed

neutrino vertex for events that have passed the 2-Track filter. Using this plot, the requirement that the VA < 6750ADC was chosen.

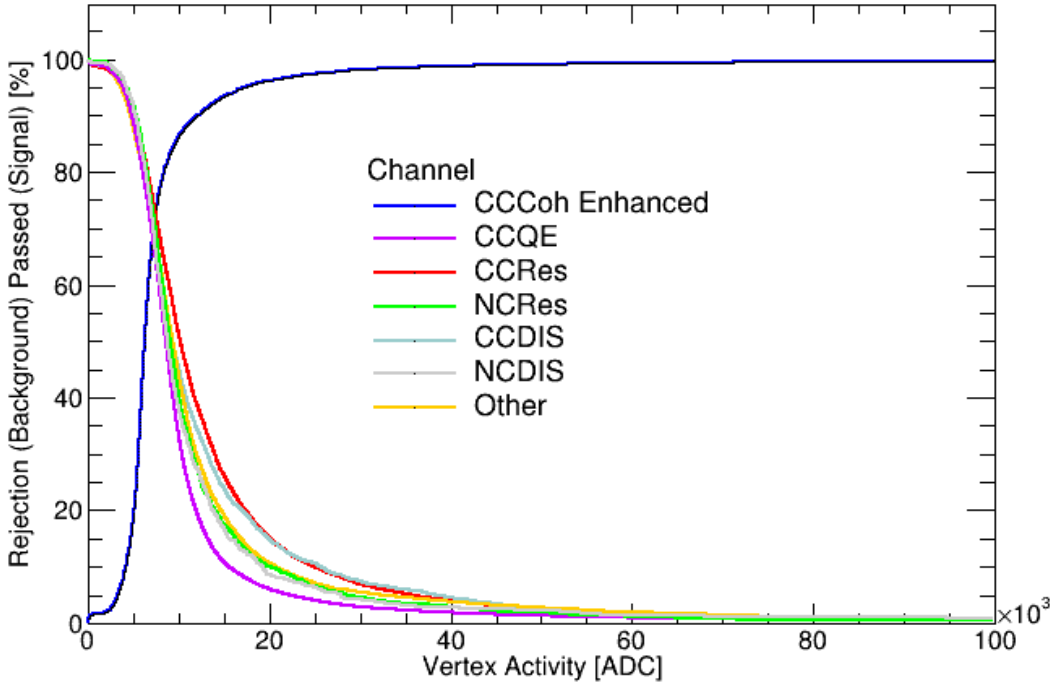

Figure 8.15: Rejection (for background events) and passing (for signal or CC-Coh π^+ events) percentages for if the cut was placed at the value in the plot. This plot is for the VA of all hits in the collection plane in the defined region around the reconstructed neutrino vertex.

Of all of the selections made in this analysis' event selection, the VA selections are the most "off-the-knee" of the passing/rejection plots shown in this chapter. This could very well cause large uncertainties to arise in detector modeling due to these selections being close to the detector resolution limits in charge and energy deposition regions, as well as positional resolution. The VA selections are highly suspect for detector uncertainties that are discussed later in this thesis, and should be investigated in future iterations of this analysis.

8.5 Pion Candidacy Selection

The second track in the selection that is not the muon candidate tagged above, is considered the pion candidate. We implement two new requirements of the pion candidate track that it must pass in order for the event to proceed in the selection. The first condition makes use of the same χ^2_μ and χ^2_p used above for the muon candidate track,

and the second requirement uses the log-likelihood ratio (LLR) developed by another MicroBooNE analyzer. Both are discussed below.

8.5.1 Pion Candidacy Using χ^2_μ and χ^2_p Values of the Pion Candidate Track

Like was done for the muon candidate above, similar restrictions based on the χ^2_μ and χ^2_p are implemented to select good pion candidate tracks. Figure 8.16 shows the 2D histogram of the pion candidate tracks where the y-axis is the χ^2_μ and the x-axis is χ^2_p for events that have passed the 2-Track selection stage. Based on this plot, the selection is made to select pion candidate tracks that look more like a muon than a proton. This is done by requiring that the pion candidate track in an event (which is the track that wasn't tagged as the official muon candidate track) has $\chi^2_\mu < 20$ and $\chi^2_p > 50$.

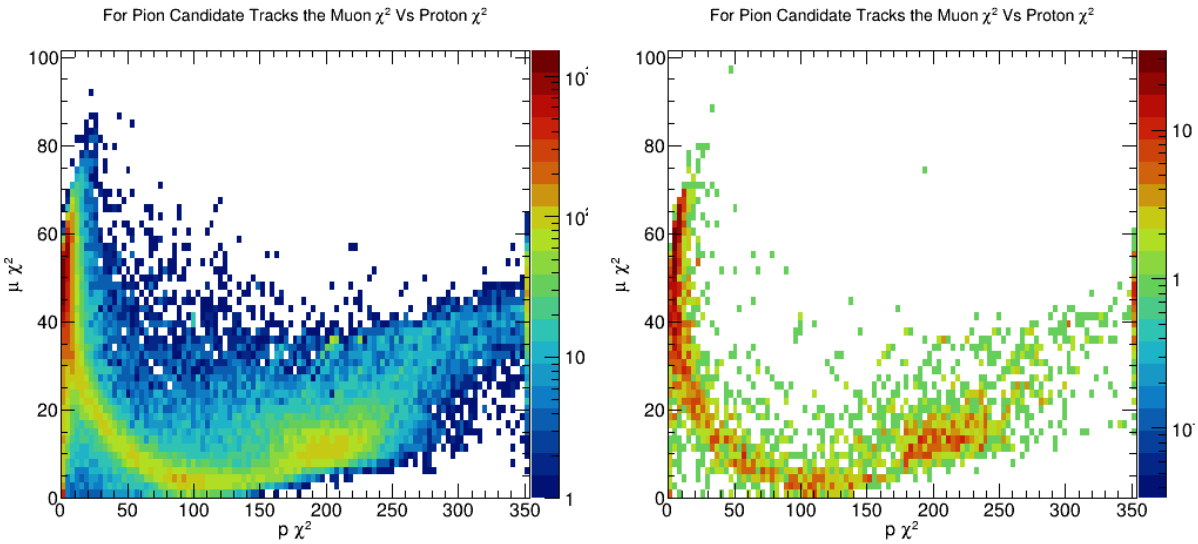

Figure 8.16: χ^2_μ vs χ^2_p for events that pass the 2-Track selection, where the left is for MC and right is the open 5E19 POT Run 1 unblinded data sample.

Again, these χ^2 values are the same as those mentioned above that were used in the muon candidacy selection of the CC-Inclusive pre-selection. They are statistical hypothesis tests that return a value for the corresponding tracks based on whether the track was assumed to be either a muon, or a proton.

8.5.2 Pion Candidacy Using the Log-Likelihood Ratio

The second portion of the pion candidacy comes from using the Log-Likelihood Ratio (LLR) that was developed by another analyzer in the MicroBooNE collaboration. This variable is calculated by comparing track hit information from all three TPC wire planes to theoretical templates for muons and protons. The logarithm of a likelihood ratio for

these two particle identification hypotheses is then converted to a score. The returned value spans from either $[-1, 1]$, and the implication is if the returned value is close to -1 then the track looks like a proton track and if the returned value is close to 1 then the track looks like a muon. Figure 8.17 shows the histogram for pion candidate tracks for events that have passed the 2-Track selection stage.

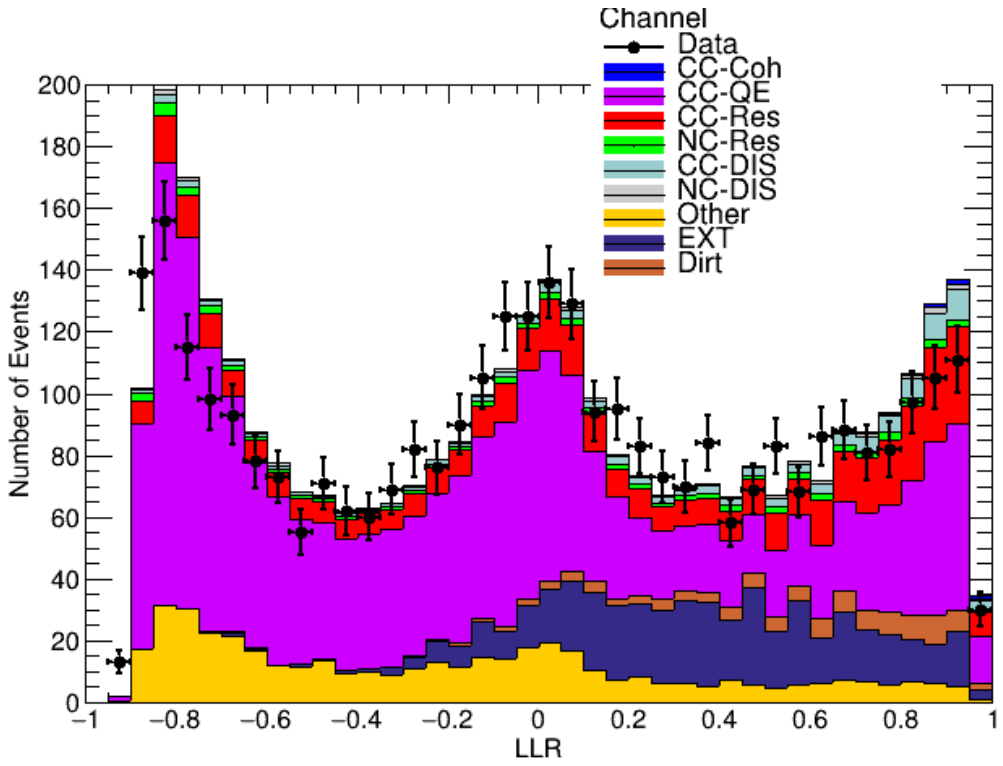

Figure 8.17: This is the stacked histogram of the LLR of the pion candidate tracks for events that have passed the 2-Track filter. The closer that this returned value is to -1 means that the track looks like a proton, and the closer that this returend value is to 1 means that the track looks like a muon, or MIP.

Figure 8.18 shows the rejection percentage of background events and the passing percentage of events for signal events if the selection is made at that value. This plot is specifically for Niccolo's LLR of the pion candidate track for events that have passed the 2-Track filter. Using this plot, the requirement that the LLR of the pion candidate track > 0.7 was chosen.

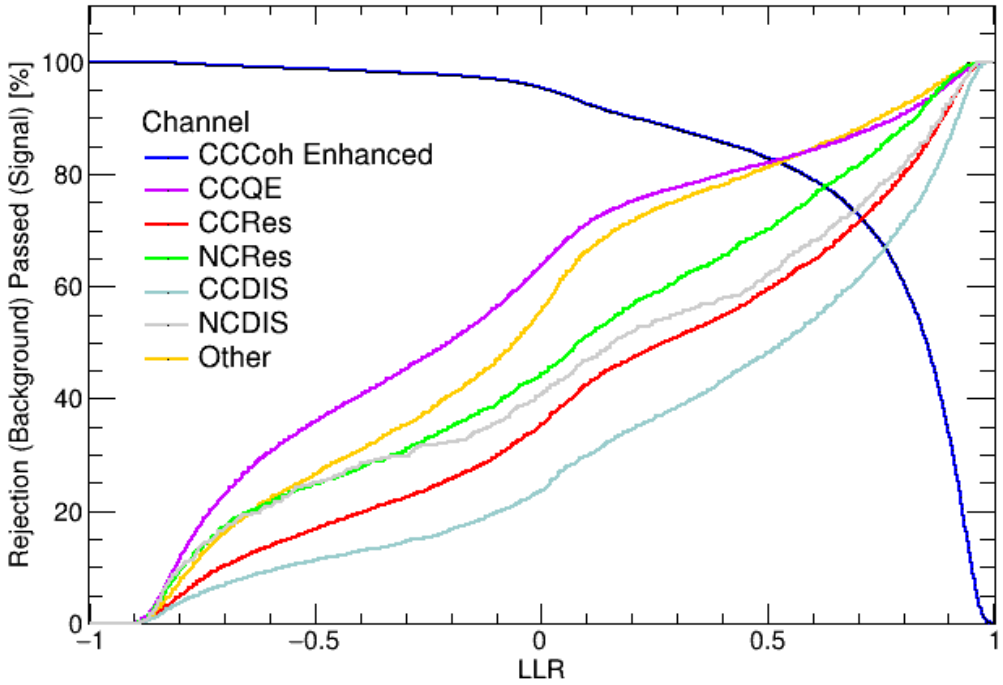

Figure 8.18: Rejection (for background events) and passing (for signal or CC-Coh π^+ events) percentages for if the cut was placed at the value in the plot. This plot is for Niccolo's LLR selection.

8.6 Opening Angle Selection

What is called the Opening Angle ($\theta_{\mu\pi}$) in this selection is the angle between the reconstructed muon-candidate track and the reconstructed pion-candidate track that have been labeled as such based off of the selections made above. This selection was thought of as a way of taking advantage of the small opening angle between the μ and π that is characteristic of the CC-Coh π^+ channel. The opening angle is calculated using:

$$\theta_{\mu\pi} = \cos^{-1}\left(\frac{\vec{p}_\mu \cdot \vec{p}_\pi}{|\vec{p}_\mu||\vec{p}_\pi|}\right), \tag{8.1}$$

where $\vec{p}_\mu$, and $\vec{p}_\pi$ are the momentum vectors for the muon and pion, respectively. The Opening Angle of the events that have passed the 2-Track filter is shown in Figure 8.19.

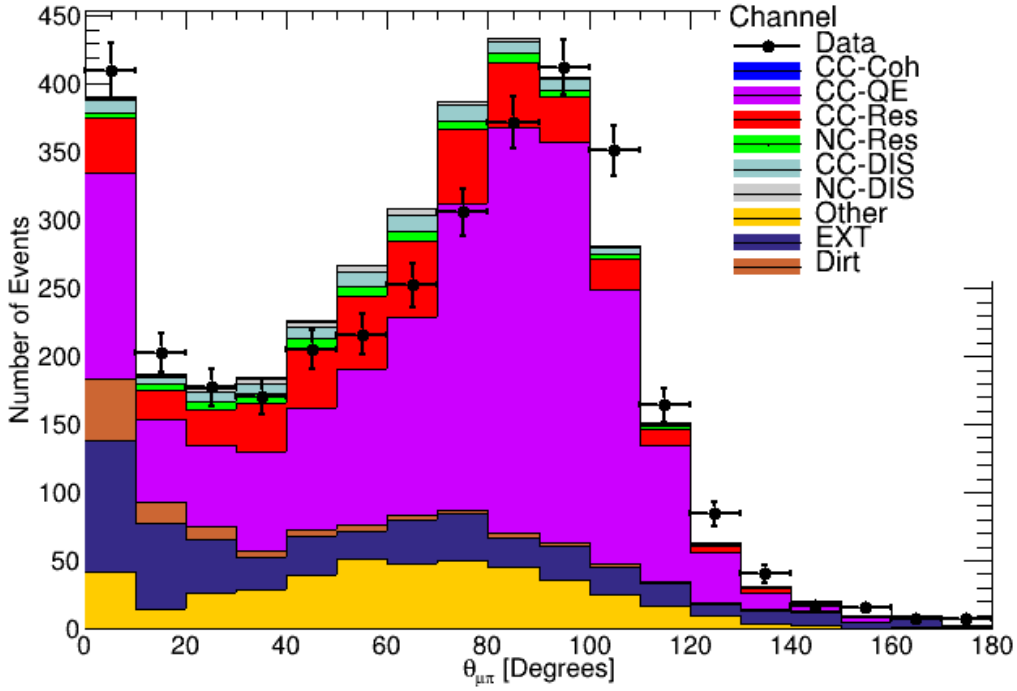

Figure 8.19: This is the stacked histogram of the opening angle between the two tracks of the 2-Track filter for events that have passed the 2-Track filter.

Figure 8.20 shows the rejection percentage of background events and the passing percentage of events for signal events if the selection is made at that value. This plot is specifically for the Opening Angle for events that have passed the 2-Track filter. Using this plot, the requirement that $\theta_{\mu\pi} < 60°$ was chosen.

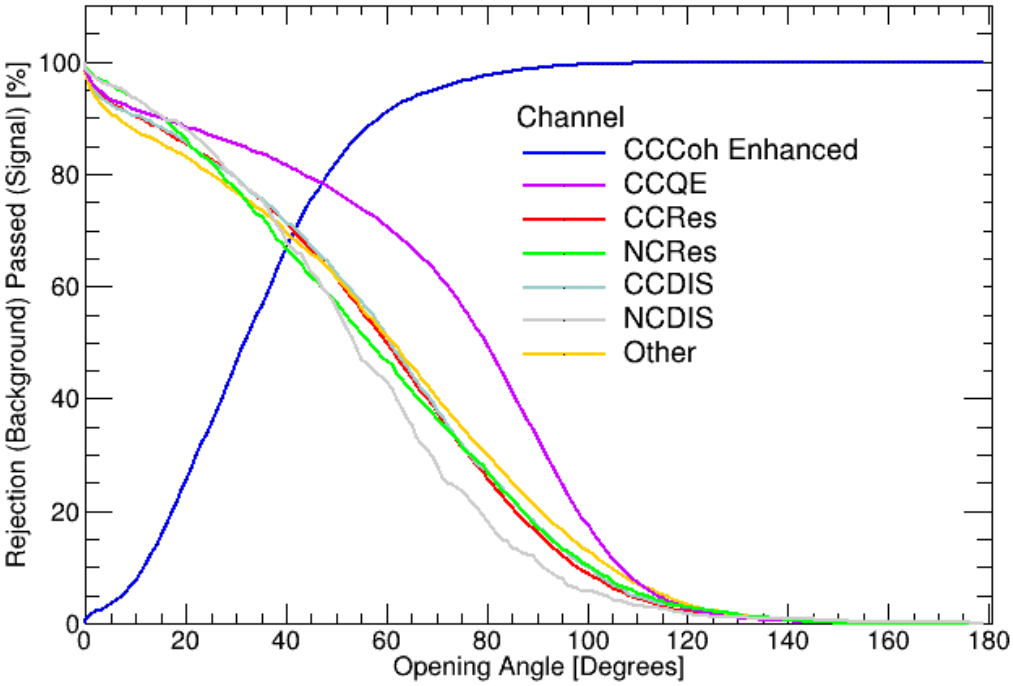

Figure 8.20: Rejection (for background events) and passing (for signal or CC-Coh π^+ events) percentages for if the cut was placed at the value in the plot. This plot is for Opening Angle selection.

8.7 Four-Momentum Measurement

CC-Coh π^+ interactions can be identified by requiring that the observed final state consists only of a charged lepton and pion (the target nucleus is not observed since the energy transferred to the nucleus is small) and small $|t|$. From the assumption of zero energy transfer to the nucleus, $|t|$ can be approximated as

$$|t| = \left|(p_\nu - p_\mu - p_\pi)^2\right| \approx \left(\sum_{i=\mu,\pi} E_i - p_{i,L}\right)^2 + \left|\sum_{i=\mu,\pi} \vec{p}_{i,T}\right|^2 \tag{8.2}$$

where p_{ν_l}, p_l, and p_π are the four-momenta of the neutrino, charged lepton, and pion, respectively, and $\vec{p}_T$ and p_L are the transverse and longitudinal momenta with respect to the incoming neutrino direction.

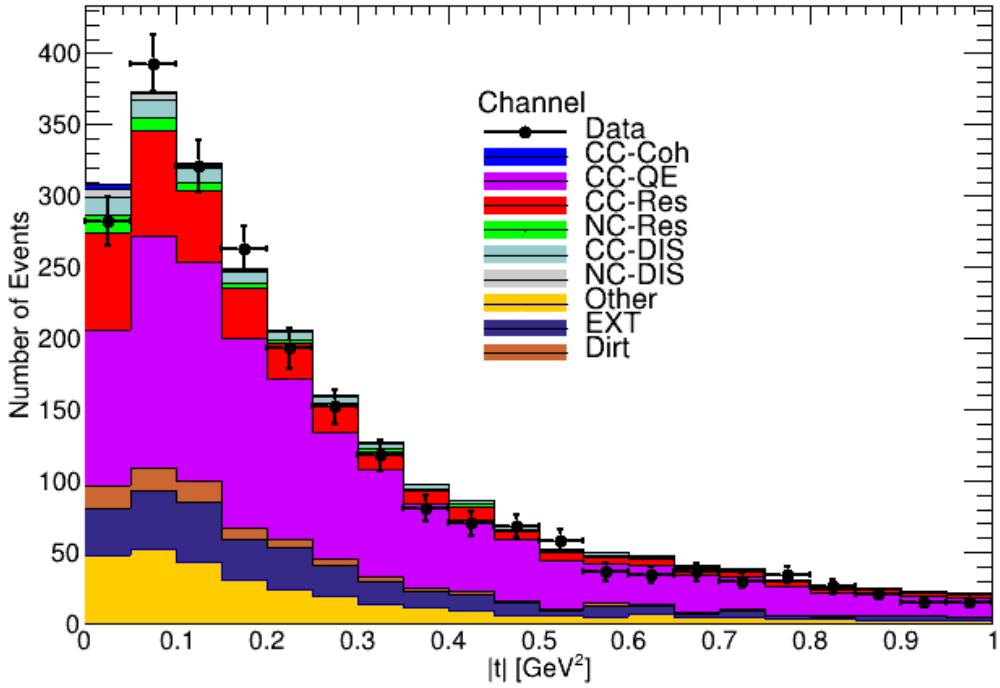

Figure 8.21: This is the stacked histogram of $|t|$ for events that passed the 2-Track filter.

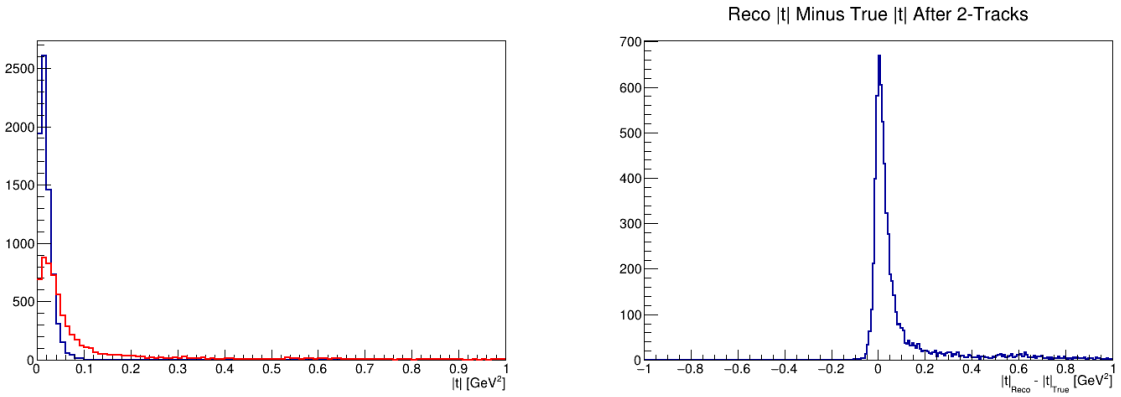

Figure 8.22: $|t|$ of the Enhanced CC-Coh π^+ sample where blue is $|t|_{True}$ and red is $|t|_{Reco}$ for events that have passed the 2-Track selection (Left) and the difference between $|t|_{Reco} - |t|_{True}$ for events that have passed the 2-Track selection, or the $|t|$ resolution (Right).

Using the resolution in Figure 8.22, a selection requiring that $|t| < 0.10\text{GeV}^2$ is chosen (which is approximately $\approx 4\times$ the resolution found in $|t|$ for the MicroBooNE detector). If an event does not have this requirement, it is dropped from the selection. This value

is chosen to significantly improve the purity of the selected sample, while maintaining a relatively high efficiency.

8.8 Event Selection Performance

The performance of this event selection is quantified in terms of both efficiency (ϵ) and purity (p). The efficiency of the event selection can be described by this equation:

$$\epsilon = \frac{\text{Selected } \nu_\mu \text{ CC-Coh } \pi^+ \text{ interactions with true vertex in the FV}}{\text{Generated } \nu_\mu \text{ CC-Coh } \pi^+ \text{ interactions with true vertex in the FV}}, \tag{8.3}$$

and the purity can be described by this equation:

$$p = \frac{\text{Selected } \nu_\mu \text{ CC-Coh } \pi^+ \text{ interactions with true vertex in the FV}}{\text{All selected events}}. \tag{8.4}$$

The event selection efficiency is shown in Figure 8.23 as a function of the true neutrino energy ($E_{\nu_\mu}^{\text{True}}$), and a step-by-step breakdown of the selected number of events passing the different stages of this selection is shown in Table 8.1, scaled to 6.878×10^{20} POT. The overall selection efficiency is 12.8%, with a purity of 16%.

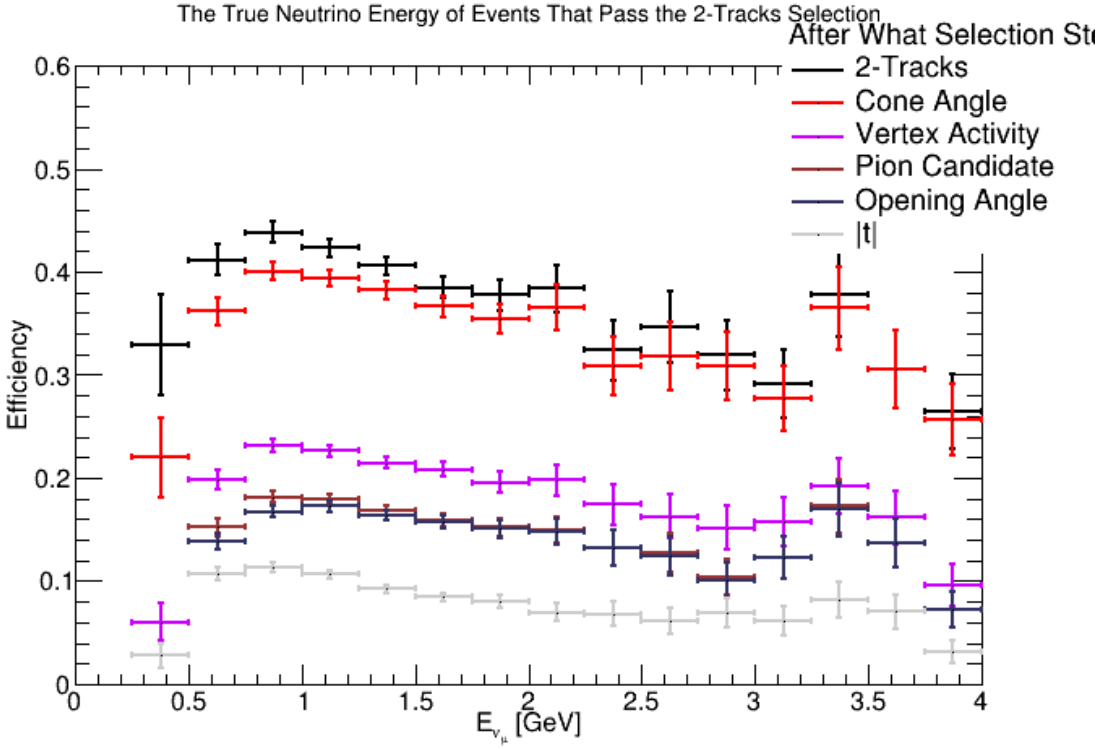

Figure 8.23: Event selection efficiency as a function of $E_{\nu_\mu}^{\text{True}}$ for each stage of the selection. This is for the CC-Coh π^+ enhanced sample that we made for this analysis.

Selected Number of Events Scaled to 6.878×10^{20} POT											
6.878×10^{20} POT	**Data**	**CCCoh**	**CCQE**	**CCRes**	**NCRes**	**CCDIS**	**NCDIS**	**Other**	**MC Total**	**Dirt**	**BNB EXT**
Num. Within Fiducial Volume	324672	261	72843	42576	14174	10467	4404	31144	176989	14377	92512
CC-Inclusive Preselection	122007	157	42491	21732	2000	4533	900	14133	86524	2699	12994
2-Tracks Selection	63245	105	28201	6937	1024	1465	425	6379	44750	1594	7472
Cone Angle Selection	21780	97	13114	3013	269	616	171	2693	20070	188	438
Vertex Activity Selection	3987	55	2241	460	47	132	34	266	3269	137	149
Pion Candidacy Selection	1038	43	524	228	15	76	13	58	972	67	41
Opening Angle Selection	710	41	337	154	12	47	9	57	670	66	41
Four-Momentum Transfer Selection	286	33	68	72	4	10	5	12	211	25	8

Table 8.1: The number of selected events broken down by interaction channel and scaled to match the data sample of 6.878×10^{20} POT.

8.9 Event Selection Summary

The above sections have shown the event selection implemented in order to select a sample of CC-Coh π^+ events for a flux-integrated cross section measurement of the channel. The selection results in an efficiency of 12.8%, and a purity of 16%. This selection was developed to maximize both the efficiency and purity for this interaction channel and represents the majority of the work that went into the analysis for this thesis. Approximately 286 data events pass this selection, and after the background subtraction of 211 events, we are left with 75 potential CC-Coh π^+ events. Figure 8.24 depicts the four-momentum transfer for the full Runs $1 + 2 + 3$ data sample that was used in this thesis with a variable binning through the opening angle selection. The lowest bin is composed of the events that pass the full selection.

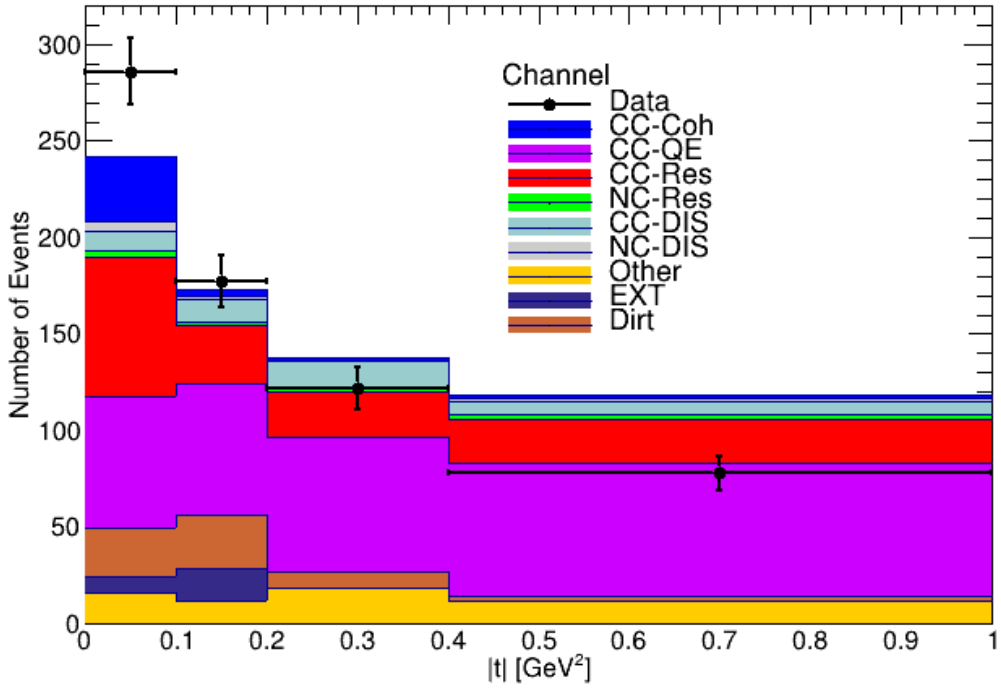

Figure 8.24: This is the stacked histogram of $|t|$ for events that passed the opening angle selection with a variable binning. Recall that the four-momentum transfer selection requires $|t| < 0.10\text{GeV}^2$, which means only the lowest bin in this figure passes the full selection.

Now that the full selection has been detailed, and it has been shown to be a flat selection across neutrino energy (see Figure 8.23), the next chapter, Chapter 9, will use the selection presented here to show how the cross section measurement will be calculated with errors only resulting from statistical uncertainties. Further examination of systematic uncertainties will come in Chapter 10.

9 Cross Section Extraction

This chapter covers the method of extraction of the cross section that this analysis attempts to measure for CC-Coh π^+, which is the primary physics goal of this thesis. Section 9.1 discusses how exactly the total cross section for CC-Coh π^+ is calculated, followed by the actual result of the total calculation (without systematic uncertainties) in Section 9.2, which also closes the chapter.

9.1 Cross Section Calculation

The total flux-integrated cross section (σ) is calculated using the following equation:

$$\sigma = \frac{N - B}{\epsilon \cdot T \cdot \Phi_{\nu_\mu}}, \tag{9.1}$$

where N is the number of selected events, B is the number of selected background events (from simulation and beam-off data), ϵ is the efficiency of the event selection (overall, including acceptance), T is the number of target nuclei, Φ_{ν_μ} is the BNB muon neutrino flux integrated over energy and scaled to the corresponding POT received for the analysis.

9.1.1 BNB Integrated Flux

The BNB ν_μ flux in neutrino mode running is shown in Figure 9.1. The flux is simulated using the MiniBooNE framework as described in [88]. The total integrated flux scaled to 6.878×10^{20} POT is

$$\Phi_{\nu_\mu} = 5.07 \times 10^{11} \text{cm}^{-2}. \tag{9.2}$$

The mean neutrino energy for the BNB flux is

$$\langle E_{\nu_\mu} \rangle = 823 \text{MeV}, \tag{9.3}$$

with 68% of the values falling into the energy range of $823 - 498 = 325$MeV and $823 + 502 = 1325$MeV.

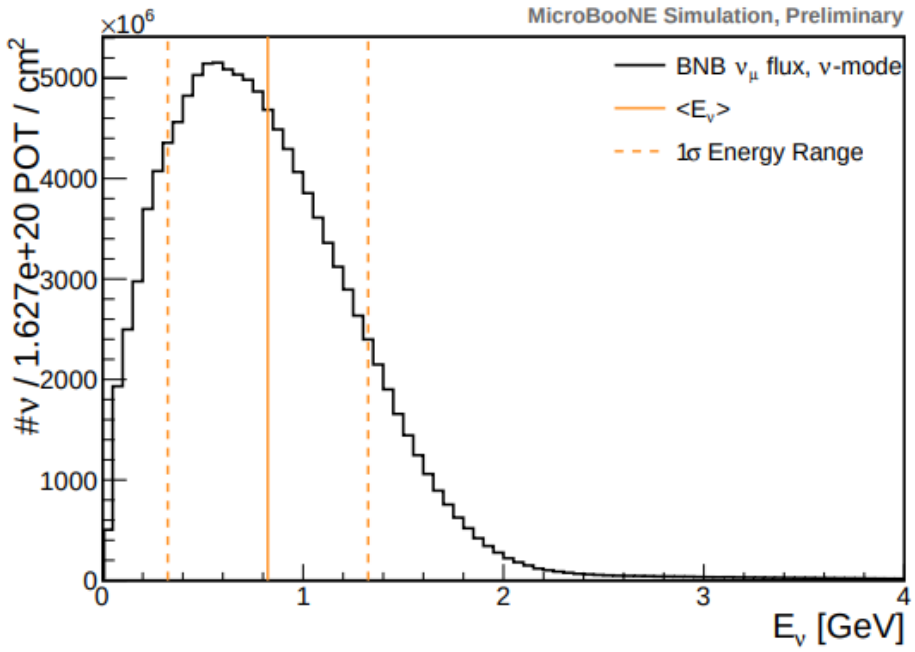

Figure 9.1: The BNB ν_μ flux in neutrino mode at the MicroBooNE detector center, scaled to 1.592×10^{20} POT. The lines mark the mean neutrino energy and the 1σ range.

9.1.2 Number of Target Nuclei

The amount of material that the incoming neutrinos could have interacted with is called the number of target nuclei, T, and the number of observed interactions depends on this number. The assumption that the entire volume of the MicroBooNE detector consists solely of argon nuclei is made, and that the average density sufficiently describes the entire fiducial volume chosen for this analysis.

With those assumptions, the number of target nuclei, T, is found using this equation:

$$T = \frac{\rho_{Ar} \times V \times N_A}{m_{mol}} \tag{9.4}$$

where ρ_{Ar} is the density of liquid argon, V is the fiducial volume, N_A is Avogadro's Number, and m_{mol} is the number of grams per mole of argon. These numbers are summarized in Table 9.1.

Using the values in Table 9.1 in Equation 9.4, the value for T is found to be $T = 1.03 \times 10^{30}$ target nuclei. The volume is assumed to be pure argon because the number of contaminants in the detector has been measured to be less than 50 particles per trillion [89]. The systematic uncertainty on this estimation is discussed in Section 10.4.

Parameter	Value
ρ_{Ar}	1.3836 g/cm^3
V	49.19×10^6 cm^3
N_A	6.022×10^{23} molecules/mol
m_{mol}	39.95 g/mol

Table 9.1: Parameter list used to calculate the number of target nucleons.

9.2 Total Cross Section

The total cross section can be calculated using Equation 9.1 and the variables discussed in the sections above, which have been tabulated in Table 9.2 and Table 9.3.

Variable	Value
Φ_{ν_μ}	5.07×10^{11} cm^{-2}
T	1.03×10^{30}
ϵ	0.128 ± 0.0145 (stat.)

Table 9.2: Parameter list used to calculate the total cross section. The integrated flux corresponds to an exposure of 6.878×10^{20} POT. The systematic uncertainties on the flux and number of targets are discussed in the next chapter.

Name	Variable	Value
Measured Event Number	N	286 ± 17
ν_μ CC-Coh Events	S	33 ± 1
Cosmic Only (from off-beam)	-	8 ± 1
Dirt (from MC)	-	25 ± 5
Non ν_μ CC-Coh Events (from MC)	-	179 ± 11
Total Background	B	211 ± 16

Table 9.3: Number of events list used to calculate the total cross section. The numbers correspond to an exposure of 6.878×10^{20} POT.

With $N = 286 \pm 17$ selected data events and $B = 211 \pm 16$ estimated background events, the data extracted cross section per nuclei is found to be:

$$\sigma(\nu_\mu + Ar \rightarrow \mu^- + \pi^+ + Ar) = 1.12 \pm 0.253(\text{stat.}) \times 10^{-39}\text{cm}^2. \quad (9.5)$$

The MC cross section predicted by GENIE can be obtained by

$$\sigma_{MC} = \frac{S}{\epsilon \cdot T \cdot \Phi_{\nu_\mu}}, \tag{9.6}$$

where S is the number of selected signal events, $S = 33 \pm 1$, which gives

$$\sigma_{MC} = 4.97 \pm 0.148(\text{stat.}) \times 10^{-40}\text{cm}^2. \tag{9.7}$$

The percent difference between the two cross section is $(\sigma - \sigma_{MC})/\sigma_{MC} = 125\%$, which is covered by the systematic uncertainty which will be shown in the next couple of chapters.

Now that the method of calculating a cross section has been presented, and the cross section has been calculated with the statistical uncertainty shown, the only thing left to include is the systematic uncertainties that could impact this result. Chapter 10 will discuss the systematic uncertainties taken into account for this analysis.

10 Systematic Uncertainties

This chapter covers the methods of evaluating the systematic uncertainties considered for the CC-Coh π^+ cross section extraction, and their results. Section 10.1 discusses the systematic uncertainties that correspond to the flux modeling. Section 10.2 discusses the systematics involved with calculating hadronic reinteractions. Section 10.3 covers the systematics associated with the method of POT counting employed by this analysis, and Section 10.4 discusses the systematics involved with calculating the number of target nuclei that is used in the cross section extraction. The systematics that result from detector modeling are detailed in Section 10.5, and the method of evaluating the systematics of the neutrino generator used by MicroBooNE, called GENIE, is discussed in Section 10.6. The last systematic uncertainty considered by this analysis, which is on the DIRT events simulation, is discussed in Section 10.7. The chapter closes with a summary of the total systematic uncertainty for the analysis in Section 10.8.

10.1 Flux Systematics

To evaluate the Flux systematic, this analysis uses a *multisim* technique, which consists of generating several MC replicas, each one called "universe," where the model parameters are varied within their uncertainties. These universes are constructed by reweighting the baseline MC. What changes in the cross section computation is the MC, i.e. efficiency, and subtracted background events. This results in a 20.9% uncertainty on the cross section measurement as a result of the Flux Systematics. This result is shown in Figure 10.2 for the affect on the number of background events (recall that only the events in the first bin pass the event selection of this analysis).

10.2 Hadronic Re-Interaction Systematics

To evaluate the hadronic re-interaction systematic, this analysis uses a *multisim* technique, which consists of generating several MC replicas, each one called "universe," where the hadron re-interaction model parameters used in GEANT4 are varied within their uncertainties. These universes are constructed by reweighting the baseline MC. What changes in the cross section computation is the MC, i.e. efficiency, and subtracted background events.

Protons, charged pions, and neutrons all lose energy through ionization but also hadronic scatters with argon nuclei. Hadronic scatters lead to "hard" direction changes, or production of new particles. The interaction length at a given energy is given by:

$$\lambda(E) = \frac{1}{\sigma(E) * \rho}, \tag{10.1}$$

where $\sigma(E)$ is the interaction cross section and ρ is the particle number density. For any small piece of pion track, the survival probability (the probability that it does not interact) is

$$P_{surv}(E, E + \Delta E) = e^{-\Delta L/\lambda(E)}, \tag{10.2}$$

where ΔL is the length of a slice $\Delta L = \Delta E/(dE/dx)$. Multiplying $P_{surv}(E, E + \Delta E)$ for all the pion track segments, the total survival probability at a given initial energy $P_{surv}(E_{init})$ can be obtained. The interaction probability is then $P_{int}(E_{int}) = 1 - P_{surv}(E_{init})$. To account for uncertainty in the cross section $\sigma(E)$, such cross section is changed according to its uncertainty and the survival probability is recalculated for a given start momentum, obtaining P'_{surv}. The weight given to an interacting hadron is:

$$w = \frac{1 - P'_{surv}(E_{init})}{1 - P_{surv}(E_{init})}, \tag{10.3}$$

while the weight given to a non-interacting hadron is:

$$w = \frac{P'_{surv}(E_{init})}{P_{surv}(E_{init})}. \tag{10.4}$$

This reweighting is performed on a per-event basis and the result for the impact on number of background events in the MC is shown in Figure 10.2. The relative systematic uncertainty on the total cross section, only due to particle re-interaction uncertainties, amounts to 3.16%.

10.3 POT Counting Systematics

An additional uncertainty is due to the POT counting. The primary proton beam is monitored using two toroids measuring its intensity (protons-per-pulse). According to the MiniBooNE flux paper, the proton flux measured in the two toroids agree within 2%. This is included as an additional uncertainty on the normalisation of the cross section, added in quadrature to all the elements of the final total uncertainties for both signal and background, except for the EXTBNB background.

10.4 Number of Target Nuclei Systematics

The fiducial volume on the MC truth is defined as:

- X-axis (drift direction): [10, 246.4] cm,
- Y-axis (vertical direction): [-106.5, 106.5] cm,

- Z-axis (beam direction): [10, 986.8] cm.

The total fiducial volume is 49,185,005.8 cm^3. Considering a ± 1 cm random variation on each of the six boundaries, the root mean square of the volume is about 0.35%. The argon density depends on the temperature. Taking into account the difference between 87 K ($1.3973 g/cm^3$) and 89 K ($1.3849 g/cm^3$), the relative difference is below 0.9%. The abundance of Argon-40 is above 99.6%. Therefore, the total number of argon nuclei in the fiducial volume is about 1.21×10^{30} with about 1% relative uncertainty. The number of target nuclei is applied to the signal part in extracting the cross section. Since this uncertainty is very small compared to the other uncertainties, its impact on the background prediction is ignored.

10.5 Detector Systematics

The detector systematics were analyzed by producing multiple samples that vary certain parameters of the detector, where only one detector parameter at a time is changed by its uncertainty (this is called a *unisim* case). Therefore, the difference between the central value cross section and the cross section calculated with the new MC runs gives an indication of the systematic uncertainty on the cross section.

The detector systematics are broken down into 9 different samples that vary a set of parameters of the detector that correspond to particular named samples. The results of these variations are summarized in Table 10.1. The 9 different detector variation samples are named and given a short description here:

- **Wire-Mod X:** variations apply data-driven transformations to the simulated width and amplitude of deconvolved TPC wire waveforms. Specifically, parameters varied that influence the x-position.
- **Wire-Mod YZ:** variations apply data-driven transformations to the simulated width and amplitude of deconvolved TPC wire waveforms. Specifically, parameters varied that influence the (y, z)-position. These two are linked due to the fact that they are reconstructed from wire information, that when the wire parameters are varied, both dimensions would vary.
- **Wire-Mod θ_{XZ}:** variations apply data-driven transformations to the simulated width and amplitude of deconvolved TPC wire waveforms. Specifically, variations that influence the θ_{XZ} of reconstructed objects, such as the hit width and area.
- **Wire-Mod θ_{YZ}:** variations apply data-driven transformations to the simulated width and amplitude of deconvolved TPC wire waveforms. Specifically, variations that influence the θ_{YZ} of reconstructed objects, such as the hit width and area.
- **LY Down:** overall 25% decrease in light yield.
- **LY Attenuation:** alternate attenuation length that mostly impacts Run3 data due to the change in argon purity seen in Run3 data.

- **LY Rayleigh:** Rayleigh scattering parameter changes for the light yield.
- **SCE:** alternative space charge map is used in the reconstruction.
- **Recomb2:** alternative recombination model is used in the modified box model [90].

It is important to note that these contributions to the systematic uncertainty are added in quadrature. This ignores any correlations between the different samples. This is the largest source of systematic uncertainty, and has a 53.4% uncertainty on the total cross section measurement. This result is shown in Figure 10.2 for the affect on the number of background events (recall that only the events in the first bin pass the event selection of this analysis).

Detector Systematic Uncertainties		
Variation	Background Variation [%]	Cross Section Uncertainty [%]
CV	0.0	0.0
wire-mod X	3.83	9.15
wire-mod YZ	-2.77	-6.62
wire-mod θ XZ	1.31	3.13
wire-mod θ YZ	-11.4	-27.3
LY down	-3.85	-9.19
LY atten	-7.96	-19.0
LY Rayleigh	-1.05	-2.51
SCE	-8.05	-19.2
Recomb2	-14.2	-33.9
Total	22.4	53.4

Table 10.1: Sources of detector systematics and their impact on the selected number of events in the analysis' signal region.

The largest systematic uncertainty on the cross section calculation is found to be the different recombination model, and the next highest being the wire-mod θ_{YZ}. Both of these are consistent with having a potentially large impact from the selections made for the VA in the analysis being "off-the-knee," as was briefly mentioned before. The recombination changes can drastically change the amount of energy or charge deposited and then found in the VA for the event. The changes in wire-mod θ_{YZ} could potentially impact the second version of the VA due to its reliance on only the XZ-plane, so large changes in what is located within the YZ-plane and their angles can push hits into and out of the summed region of the VA, thus wildly affecting the events that pass that stage of the selection.

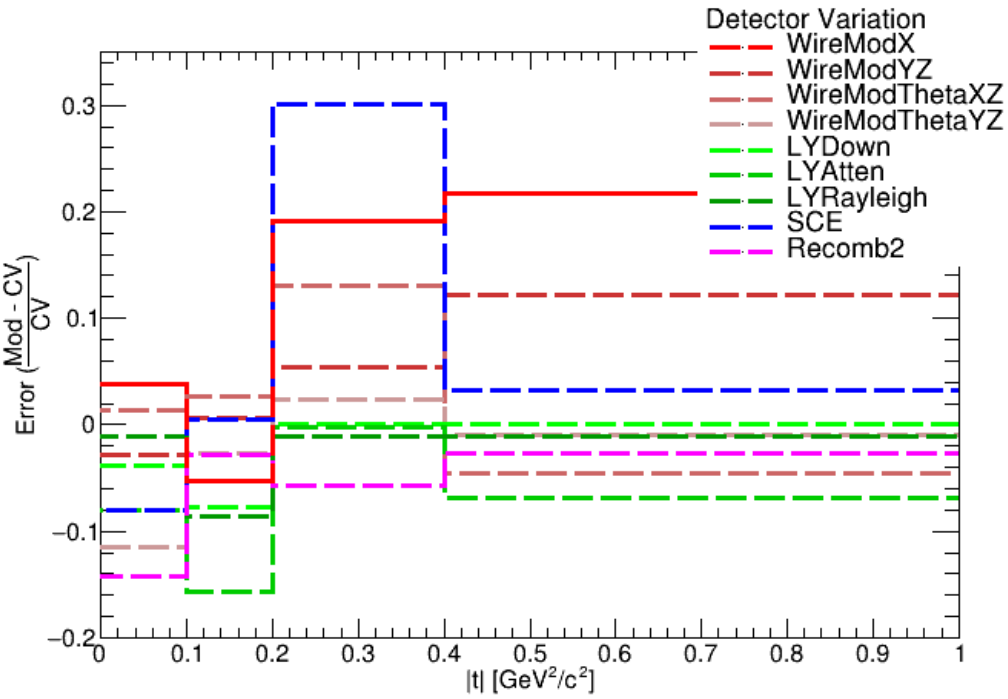

Figure 10.1: Error on background numbers plotted for $|t|$ with a variable bin width of all of the detector systematic variations. Shown are the effects on background numbers from detector variation systematic uncertainties.

Again, to reiterate, future iterations of this analysis should investigate the changes in the detector systematic uncertainties that result from a less stringent requirement on both versions of the VA selection (aka move the selections onto the knee in the passing/rejection plots). It is my belief that this would have a drastic improvement in this uncertainty, but wasn't investigated further due to time constraints of this analysis.

10.6 GENIE Systematics

To evaluate the GENIE systematic, this analysis uses a *multisim* technique, which consists of generating several MC replicas, each one called "universe," where the model parameters are varied within their uncertainties. These universes are constructed by reweighting the baseline MC. What changes in the cross section computation is the MC, i.e. efficiency, and subtracted background events.

The GENIE simulator provides a built-in framework of event reweighting for evaluating systematic uncertainties in an analysis. Given a certain physics parameter P with estimated prior uncertainty δP, the effect on the final cross section if this parameter is changed to $P' = P + x_p \delta P$, where x_p is a systematic parameter, is shown in this section.

Here, the effect of reweighting all GENIE parameters at the same time is studied in order to evaluate the systematic uncertainty on the measurement. The result of

the GENIE systematic uncertainties is a 25.5% uncertainty on the total cross section measurement. This result is shown in Figure 10.2 for the affect on the number of background events (recall that only the events in the first bin pass the event selection of this analysis). This value of uncertainty is consistent with what other MicroBooNE analyses have seen, and if further details on what GENIE parameters are varied is wanted, one can look to [91].

10.7 Dirt Systematics

The DIRT events are neutrino interactions originated from outside the cryostat. The biggest uncertainty associated with the DIRT events are the modeling of the outside materials. In addition to the systematic uncertainties associated with flux/Xs and detector, we assign a conservative relative 50% uncertainty to DIRT events. This results in a 16.7% uncertainty on the total cross section measurement.

10.8 Systematic Uncertainties Summary

This chapter covered the estimation of the systematic uncertainties that could affect the ν_μ CC-Coh π^+ cross section measurement considered for this analysis. The uncertainties for GENIE, the flux, and hadronic re-interaction were estimated using a *multisim* approach, and resulted in a 25.5%, a 20.9%, and a 3.16% cross section uncertainty respectively. The uncertainty on the detector utilized a *unisim* technique and the contributions were added in quadrature to arrive at a 53.4% uncertainty on the total cross section, which is the largest contribution to the systematics considered in this analysis. All of the above mentioned systematics are depicted in Figure 10.2 for their affect on the number of background events (only the first bin passes the event selection of this analysis). The collaboration agreed to an approximate 50% mismodeling for the Dirt portion of the background, which corresponds to a 16.7% uncertainty on the total cross section. The MC Statistical uncertainty results in a 5.04% uncertainty. The number of target nuclei resulted in a 1% uncertainty, and the POT Counting resulted in a 2% uncertainty. The efficiency uncertainty results in a 0.55% uncertainty. All of these are summarized in Table 10.2. When added in quadrature, these systematics correspond to a 65.2% uncertainty from the systematics considered to affect this cross section measurement. The next chapter will show the total cross section for ν_μ CC-Coh π^+ with both statistical and systematic uncertainties.

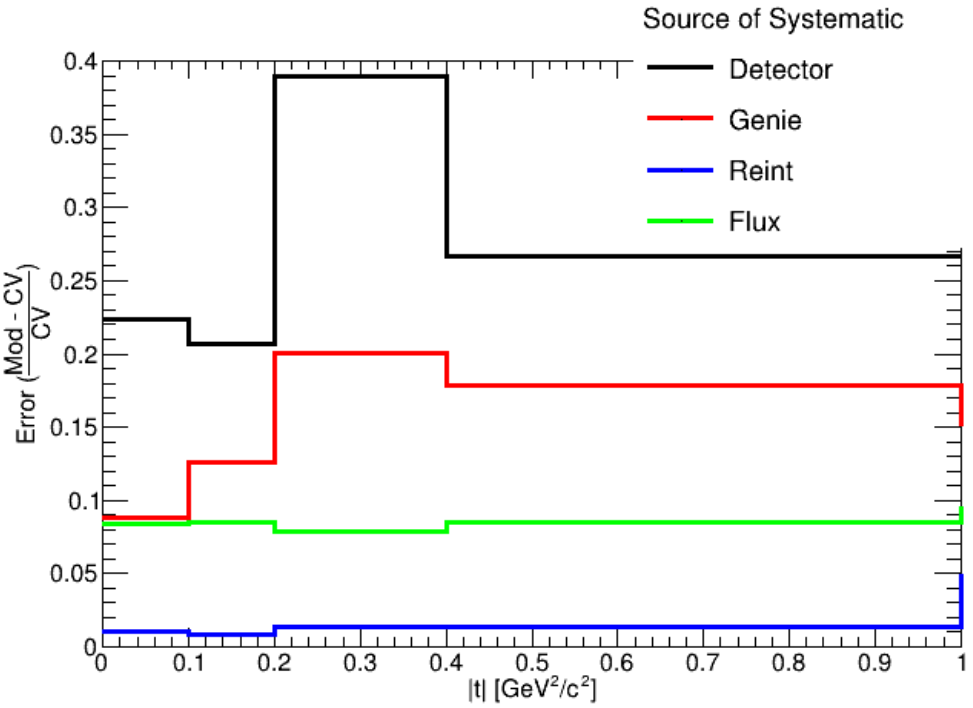

Figure 10.2: Error on background numbers plotted for $|t|$ with a variable bin width. Shown are the affects on background numbers from Detector, Flux, Reinteraction, and GENIE systematic uncertainties. Recall that only the first bin of this figure passes the event selection used in this analysis.

All Considered Systematic Uncertainties	
Source of Uncertainty	Cross Section Uncertainty
Detector	53.4%
GENIE	25.5%
Reinteraction	3.16%
Flux	20.9%
Dirt Uncertainty	16.7%
POT Counting	2%
Number of Target Nuclei	1%
Efficiency Uncertainty	0.55%
MC Statistics	5.04%
Total Systematic Uncertainty	65.2%

Table 10.2: All systematic uncertainties accounted for in this analysis. The total systematic uncertainty is found by summing all of the contributions in quadrature.

11 Cross Section Results

"It's the questions we can't answer that teach us the most. They teach us how to think."

Patrick Rothfuss, *The Wise Man's Fear*

The previous two chapters were devoted to the discussion of the cross section extraction method (Chapter 9), and to the systematic uncertainties that could affect the cross section measurement of this thesis (Chapter 10). This chapter presents the final results and the main purpose of this thesis: the muon-neutrino induced charged-current coherent positive pion production flux integrated cross section measurement on argon with both statistical and systematic uncertainties.

Section 11.1 shows the total cross section measurement results and the plot of that value with the ν_μ flux received by MicroBooNE and the predicted GENIE tune cross section for comparison.

11.1 The Final Cross Section

The total flux-integrated cross section for CC-Coh π^+ production on argon per nucleus using 6.878×10^{20} POT of collected data by MicroBooNE and accounting for both statistical and systematic uncertainties (from Chapter 10) is found to be:

$$\sigma(\nu_\mu + Ar \to \mu^- + \pi^+ + Ar) = 1.12 \pm 0.253(\text{stat.}) \pm 0.728(\text{syst.}) \times 10^{-39}\text{cm}^2. \quad (11.1)$$

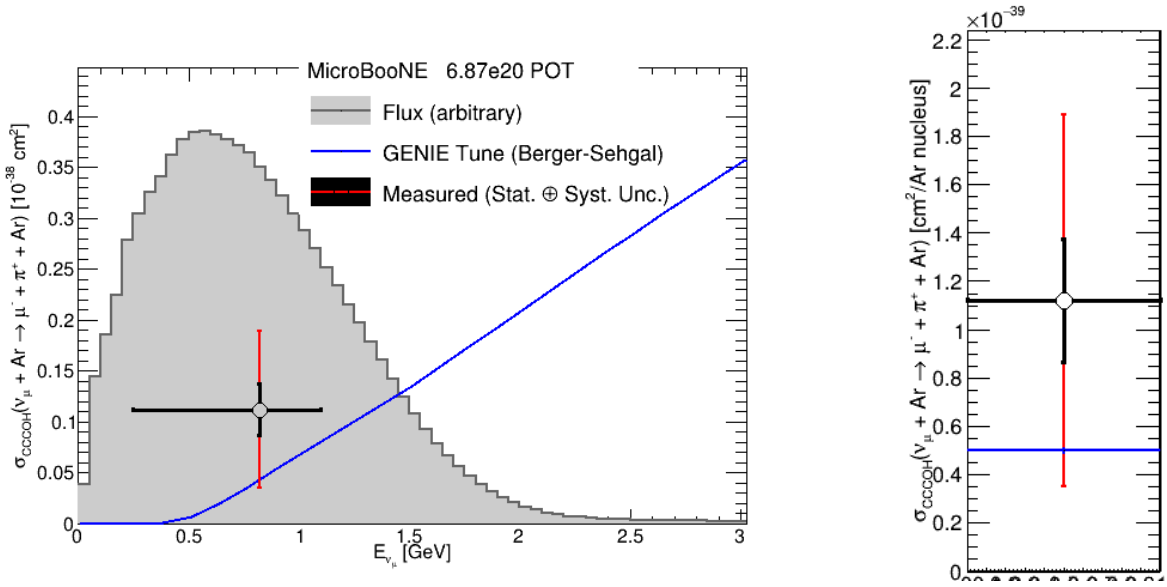

Figure 11.1: (Left) Predicted ν_μ CC-Coh π^+ production cross section on argon per argon nucleus as a function of neutrino energy. The predicted GENIE tune cross section for CC-Coh π^+ (which uses the Berger-Sehgal model) is shown in blue. For comparison, the neutrino flux at MicroBooNE (scaled arbitrarily) is shown in gray. The total flux-integrated cross section is shown as the data point where the black vertical bar is the statistical uncertainty, and the red vertical bar is the quadrature adding of both the statistical and systematic uncertainties. (Right) The total measured flux-integrated cross section for CC-Coh π^+ production is shown as the data point where the black vertical bar is the statistical uncertainty, and the red vertical bar is the quadrature adding of both the statistical and systematic uncertainties. The GENIE tune is plotted in blue as well for easy comparison.

The cross section is also shown in Figure 11.1, which shows the measured cross section in comparison to the cross section predicted by the GENIE tune (which uses the Bergher-Sehgal model). Thus, this is the main result of this thesis. There are potential improvements that could be made to the analysis in the future, both in terms of the systematic and statistical uncertainties quoted. Both of these and the conclusions drawn will be discussed in the concluding chapter of this thesis: Chapter 12.

12 Conclusions and Outlook

"Well, here at last, dear friends, on the shores of the sea comes the end of our fellowship in Middle-earth. Go in peace! I will not say: do not weep; for not all tears are an evil."

J.R.R. Tolkien, *The Return of the King*

Further investigation of neutrinos, especially in the form of neutrino oscillation experiments, can help provide vital clues to the future development of particle physics. These future oscillation experiments are limited by the precision of our understanding of neutrino-nucleus interactions. Of particular interest is the interaction channel called neutrino induced coherent pion production due to its potential as a source of background to ν_e oscillation searches. Furthering our understanding of this channel also helps with the broader goal of understanding neutrino induced pion production in general.

Over the past years, many experiments have measured the total flux-integrated cross section of CC-Cohπ^+ production. This interaction channel has had a controversial history, which was discussed in Chapter 4. This controversial history along with the recent measurements made by the T2K, MINERνA, and ArgoNeuT collaborations helped motivate more measurements of this channel, which was the primary goal of this thesis, ideally helping to shed light on the motivations for studying this channel further that were listed in Chapter 4, as well.

This thesis has presented a search for CC-Cohπ^+ as well as the highest statistics measurement to date of the total flux-integrated cross section measurement of CC-Cohπ^+ production on argon at a mean neutrino energy of 0.823GeV. The data used was collected using the MicroBooNE LArTPC in the Fermilab Booster neutrino beam and corresponds to 6.878×10^{20} protons on target of exposure. The results of the cross section are depicted in Figure 11.1. The total flux-integrated cross section was found to be:

$$\sigma(\nu_\mu + Ar \rightarrow \mu^- + \pi^+ + Ar) = 1.12 \pm 0.253(\text{stat.}) \pm 0.728(\text{syst.}) \times 10^{-39}\text{cm}^2. \quad (12.1)$$

The implication of this result is that the systematic and statistical uncertainties are large enough that the Berger-Sehgal model implemented in this version of the MicroBooNE MC cannot be ruled out as an accurate explanation of CC coherent pion production at the neutrino energy of this result. Another implication is that there is still more work to be done on this channel in the future, but a confirmation measurement along the same beamline as SciBooNE (who did not observe this interaction channel)

is an important result. The result also helps further our understanding of CC-Cohπ^+ production, in general due to it being the largest statistics measurement of this channel on argon to date. The associated systematic uncertainties of this measurement are too large to give model distinguishing capability, but this result shows how LArTPC technology continues to produce valuable physics results for current generation neutrino experiments. This thesis has shown some of the work being done for future neutrino experiments that will utilize LArTPC technology as well.

There are a number of future improvements that can be made in this analysis. One of the primary examples is an improvement in the detector systematics, as was discussed in Section 10.5. These large systematic uncertainties are likely to be a product of the selection choices implemented for this analysis. Another future improvement includes a reduction in the statistical uncertainty, which can only be accomplished by the inclusion of more data. The inclusion of both Runs 4 and 5 of MicroBooNE would effectively double the amount of POT received for the analysis, but implementation of these runs is still an in progress work being done by the MicroBooNE collaboration and will require significantly more work before it could be included in this analysis due to the experiment's blinding policy.

The publication of this work is actively being pursued, and the plan is to push this result to a PRD publication.

Bibliography

[1] A. Aguilar, L. B. Auerbach, R. L. Burman, D. O. Caldwell, E. D. Church, A. K. Cochran, J. B. Donahue, A. Fazely, G. T. Garvey, R. M. Gunasingha, R. Imlay, W. C. Louis, R. Majkic, A. Malik, W. Metcalf, G. B. Mills, V. Sandberg, D. Smith, I. Stancu, M. Sung, R. Tayloe, G. J. VanDalen, W. Vernon, N. Wadia, D. H. White, and S. Yellin, "Evidence for neutrino oscillations from the observation of $\overline{\nu}_e$ appearance in a $\overline{\nu}_\mu$ beam," *Phys. Rev. D*, vol. 64, p. 112007, Nov 2001.

[2] A. A. Aguilar-Arevalo, B. C. Brown, L. Bugel, G. Cheng, J. M. Conrad, R. L. Cooper, R. Dharmapalan, A. Diaz, Z. Djurcic, D. A. Finley, R. Ford, F. G. Garcia, G. T. Garvey, J. Grange, E.-C. Huang, W. Huelsnitz, C. Ignarra, R. A. Johnson, G. Karagiorgi, T. Katori, T. Kobilarcik, W. C. Louis, C. Mariani, W. Marsh, G. B. Mills, J. Mirabal, J. Monroe, C. D. Moore, J. Mousseau, P. Nienaber, J. Nowak, B. Osmanov, Z. Pavlovic, D. Perevalov, H. Ray, B. P. Roe, A. D. Russell, M. H. Shaevitz, J. Spitz, I. Stancu, R. Tayloe, R. T. Thornton, M. Tzanov, R. G. Van de Water, D. H. White, D. A. Wickremasinghe, and E. D. Zimmerman, "Significant excess of electronlike events in the miniboone short-baseline neutrino experiment," *Phys. Rev. Lett.*, vol. 121, p. 221801, Nov 2018.

[3] A. Gando, Y. Gando, S. Hayashida, H. Ikeda, K. Inoue, K. Ishidoshiro, H. Ishikawa, M. Koga, R. Matsuda, S. Matsuda, T. Mitsui, D. Motoki, K. Nakamura, Y. Oki, M. Otani, I. Shimizu, J. Shirai, F. Suekane, A. Suzuki, Y. Takemoto, K. Tamae, K. Ueshima, H. Watanabe, B. D. Xu, S. Yamada, Y. Yamauchi, H. Yoshida, T. Banks, B. E. Berger, M. Cribier, P. Decowski, J. A. Detwiler, M. Durero, D. Dwyer, Y. Efremenko, S. Enomoto, V. Fischer, B. K. Fujikawa, J. Gaffiot, V. M. Gelis, H. J. Karwowski, Y. G. Kolomensky, A. Kozlov, V. N. Kornoukhov, T. Lasserre, J. G. Learned, A. Letourneau, D. Lhuillier, J. Maricic, D. M. Markoff, S. Matsuno, G. Mention, R. Milincic, T. ODonnell, I. S. Saldikov, L. Scola, G. V. Tikhomirov, C. Veyssiere, M. Vivier, and S. Yoshida, "White paper: Celand - investigation of the reactor antineutrino anomaly with an intense 144ce-144pr antineutrino source in kamland," 2013.

[4] D. Rein and L. M. Sehgal, "Coherent pi0 Production in Neutrino Reactions," *Nucl. Phys. B*, vol. 223, pp. 29–44, 1983.

[5] C. Berger and L. M. Sehgal, "Partially conserved axial vector current and coherent pion production by low energy neutrinos," *Phys. Rev. D*, vol. 79, p. 053003, Mar 2009.

[6] L. Alvarez-Ruso, L. S. Geng, and M. J. V. Vacas, "Neutral current coherent pion production," *Phys. Rev. C*, vol. 76, p. 068501, Dec 2007.

[7] L. Alvarez-Ruso, L. S. Geng, S. Hirenzaki, and M. J. V. Vacas, "Charged current neutrino-induced coherent pion production," *Phys. Rev. C*, vol. 75, p. 055501, May 2007.

[8] W. V. D. Pontseele, "Search for electron neutrino anomalies with the microboone detector." `https://inspirehep.net/files/740e89044c87e3ec602cedd0c5163470`, 2020.

[9] B. Fleming, "The MicroBooNE Technical Design Report," 2 2012.

[10] C. Adams, R. An, J. Anthony, J. Asaadi, M. Auger, S. Balasubramanian, B. Baller, C. Barnes, G. Barr, M. Bass, F. Bay, A. Bhat, K. Bhattacharya, M. Bishai, A. Blake, T. Bolton, L. Camilleri, D. Caratelli, I. C. Terrazas, R. Carr, R. C. Fernandez, F. Cavanna, G. Cerati, H. Chen, Y. Chen, E. Church, D. Cianci, E. Cohen, G. Collin, J. Conrad, M. Convery, L. Cooper-Troendle, J. Crespo-Anadón, M. D. Tutto, D. Devitt, A. Diaz, M. Dolce, S. Dytman, B. Eberly, A. Ereditato, L. E. Sanchez, J. Esquivel, J. Evans, A. Fadeeva, B. Fleming, W. Foreman, A. Furmanski, D. Garcia-Gamez, G. Garvey, V. Genty, D. Goeldi, S. Gollapinni, E. Gramellini, H. Greenlee, R. Grosso, R. Guenette, P. Guzowski, A. Hackenburg, P. Hamilton, O. Hen, J. Hewes, C. Hill, J. Ho, G. Horton-Smith, A. Hourlier, E.-C. Huang, C. James, J. J. de Vries, L. Jiang, R. Johnson, J. Joshi, H. Jostlein, Y.-J. Jwa, D. Kaleko, G. Karagiorgi, W. Ketchum, B. Kirby, M. Kirby, T. Kobilarcik, I. Kreslo, Y. Li, A. Lister, B. Littlejohn, S. Lockwitz, D. Lorca, W. Louis, M. Luethi, B. Lundberg, X. Luo, A. Marchionni, S. Marcocci, C. Mariani, J. Marshall, D. M. Caicedo, A. Mastbaum, V. Meddage, T. Mettler, T. Miceli, G. Mills, A. Mogan, J. Moon, M. Mooney, C. Moore, J. Mousseau, M. Murphy, R. Murrells, D. Naples, P. Nienaber, J. Nowak, O. Palamara, V. Pandey, V. Paolone, A. Papadopoulou, V. Papavassiliou, S. F. Pate, Z. Pavlovic, E. Piasetzky, D. Porzio, G. Pulliam, X. Qian, J. Raaf, V. Radeka, A. Rafique, L. Rochester, M. Ross-Lonergan, C. R. von Rohr, B. Russell, D. W. Schmitz, A. Schukraft, W. Seligman, M. Shaevitz, J. Sinclair, A. Smith, E. Snider, M. Soderberg, S. Söldner-Rembold, S. Soleti, P. Spentzouris, J. Spitz, J. S. John, T. Strauss, K. Sutton, S. Sword-Fehlberg, A. Szelc, N. Tagg, W. Tang, K. Terao, M. Thomson, M. Toups, Y.-T. Tsai, S. Tufanli, T. Usher, W. V. D. Pontseele, R. V. de Water, B. Viren, M. Weber, H. Wei, D. Wickremasinghe, K. Wierman, Z. Williams, S. Wolbers, T. Wongjirad, K. Woodruff, T. Yang, G. Yarbrough, L. E. Yates, B. Yu, G. Zeller, J. Zennamo, and C. Zhang, "Ionization electron signal processing in single phase LArTPCs. part II. data/simulation comparison and performance in MicroBooNE," *Journal of Instrumentation*, vol. 13, pp. P07007–P07007, jul 2018.

[11] "Muons in liquid argon (ar)."

[12] S. Gollapinni, "Accelerator-based short-baseline neutrino oscillation experiments," 2015.

[13] M. Tanabashi, K. Hagiwara, K. Hikasa, K. Nakamura, Y. Sumino, F. Takahashi, J. Tanaka, K. Agashe, G. Aielli, C. Amsler, M. Antonelli, D. M. Asner, H. Baer, S. Banerjee, R. M. Barnett, T. Basaglia, C. W. Bauer, J. J. Beatty, V. I. Belousov, J. Beringer, S. Bethke, A. Bettini, H. Bichsel, O. Biebel, K. M. Black, E. Blucher, O. Buchmuller, V. Burkert, M. A. Bychkov, R. N. Cahn, M. Carena, A. Ceccucci, A. Cerri, D. Chakraborty, M.-C. Chen, R. S. Chivukula, G. Cowan, O. Dahl, G. D'Ambrosio, T. Damour, D. de Florian, A. de Gouvêa, T. DeGrand, P. de Jong, G. Dissertori, B. A. Dobrescu, M. D'Onofrio, M. Doser, M. Drees, H. K. Dreiner, D. A. Dwyer, P. Eerola, S. Eidelman, J. Ellis, J. Erler, V. V. Ezhela, W. Fetscher, B. D. Fields, R. Firestone, B. Foster, A. Freitas, H. Gallagher, L. Garren, H.-J. Gerber, G. Gerbier, T. Gershon, Y. Gershtein, T. Gherghetta, A. A. Godizov, M. Goodman, C. Grab, A. V. Gritsan, C. Grojean, D. E. Groom, M. Grünewald, A. Gurtu, T. Gutsche, H. E. Haber, C. Hanhart, S. Hashimoto, Y. Hayato, K. G. Hayes, A. Hebecker, S. Heinemeyer, B. Heltsley, J. J. Hernández-Rey, J. Hisano, A. Höcker, J. Holder, A. Holtkamp, T. Hyodo, K. D. Irwin, K. F. Johnson, M. Kado, M. Karliner, U. F. Katz, S. R. Klein, E. Klempt, R. V. Kowalewski, F. Krauss, M. Kreps, B. Krusche, Y. V. Kuyanov, Y. Kwon, O. Lahav, J. Laiho, J. Lesgourgues, A. Liddle, Z. Ligeti, C.-J. Lin, C. Lippmann, T. M. Liss, L. Littenberg, K. S. Lugovsky, S. B. Lugovsky, A. Lusiani, Y. Makida, F. Maltoni, T. Mannel, A. V. Manohar, W. J. Marciano, A. D. Martin, A. Masoni, J. Matthews, U.-G. Meißner, D. Milstead, R. E. Mitchell, K. Mönig, P. Molaro, F. Moortgat, M. Moskovic, H. Murayama, M. Narain, P. Nason, S. Navas, M. Neubert, P. Nevski, Y. Nir, K. A. Olive, S. Pagan Griso, J. Parsons, C. Patrignani, J. A. Peacock, M. Pennington, S. T. Petcov, V. A. Petrov, E. Pianori, A. Piepke, A. Pomarol, A. Quadt, J. Rademacker, G. Raffelt, B. N. Ratcliff, P. Richardson, A. Ringwald, S. Roesler, S. Rolli, A. Romaniouk, L. J. Rosenberg, J. L. Rosner, G. Rybka, R. A. Ryutin, C. T. Sachrajda, Y. Sakai, G. P. Salam, S. Sarkar, F. Sauli, O. Schneider, K. Scholberg, A. J. Schwartz, D. Scott, V. Sharma, S. R. Sharpe, T. Shutt, M. Silari, T. Sjöstrand, P. Skands, T. Skwarnicki, J. G. Smith, G. F. Smoot, S. Spanier, H. Spieler, C. Spiering, A. Stahl, S. L. Stone, T. Sumiyoshi, M. J. Syphers, K. Terashi, J. Terning, U. Thoma, R. S. Thorne, L. Tiator, M. Titov, N. P. Tkachenko, N. A. Törnqvist, D. R. Tovey, G. Valencia, R. Van de Water, N. Varelas, G. Venanzoni, L. Verde, M. G. Vincter, P. Vogel, A. Vogt, S. P. Wakely, W. Walkowiak, C. W. Walter, D. Wands, D. R. Ward, M. O. Wascko, G. Weiglein, D. H. Weinberg, E. J. Weinberg, M. White, L. R. Wiencke, S. Willocq, C. G. Wohl, J. Womersley, C. L. Woody, R. L. Workman, W.-M. Yao, G. P. Zeller, O. V. Zenin, R.-Y. Zhu, S.-L. Zhu, F. Zimmermann, P. A. Zyla, J. Anderson, L. Fuller, V. S. Lugovsky, and P. Schaffner, "Review of particle physics," *Phys. Rev. D*, vol. 98, p. 030001, Aug 2018.

[14] J. Chadwick, "Intensitätsverteilung im magnetischen Spectrum der β-Strahlen von

radium B + C," *Verhandl. Dtsc. Phys. Ges.*, vol. 16, p. 383, 1914.

[15] H. Bethe and R. Peierls, "The neutrino," *Nature*, vol. 133, no. 3366, pp. 689–690, 1934.

[16] F. Reines, C. L. Cowan, F. B. Harrison, A. D. McGuire, and H. W. Kruse, "Detection of the free antineutrino," *Phys. Rev.*, vol. 117, pp. 159–173, Jan 1960.

[17] G. Danby, J.-M. Gaillard, K. Goulianos, L. M. Lederman, N. Mistry, M. Schwartz, and J. Steinberger, "Observation of high-energy neutrino reactions and the existence of two kinds of neutrinos," *Phys. Rev. Lett.*, vol. 9, pp. 36–44, Jul 1962.

[18] F. Hasert, S. Kabe, W. Krenz, J. Von Krogh, D. Lanske, J. Morfin, K. Schultze, H. Weerts, G. Bertrand-Coremans, J. Sacton, W. Van Doninck, P. Vilain, U. Camerini, D. Cundy, R. Baldi, I. Danilchenko, W. Fry, D. Haidt, S. Natali, P. Musset, B. Osculati, R. Palmer, J. Pattison, D. Perkins, A. Pullia, A. Rousset, W. Venus, H. Wachsmuth, V. Brisson, B. Degrange, M. Haguenauer, L. Kluberg, U. Nguyen-Khac, P. Petiau, E. Belotti, S. Bonetti, D. Cavalli, C. Conta, E. Fiorini, M. Rollier, B. Aubert, D. Blum, L. Chounet, P. Heusse, A. Lagarrigue, A. Lutz, A. Orkin-Lecourtois, J. Vialle, F. Bullock, M. Esten, T. Jones, J. McKenzie, A. Michette, G. Myatt, and W. Scott, "Observation of neutrino-like interactions without muon or electron in the gargamelle neutrino experiment," *Physics Letters B*, vol. 46, no. 1, pp. 138–140, 1973.

[19] K. Kodama, N. Ushida, C. Andreopoulos, N. Saoulidou, G. Tzanakos, P. Yager, B. Baller, D. Boehnlein, W. Freeman, B. Lundberg, J. Morfin, R. Rameika, J. Yun, J. Song, C. Yoon, S. Chung, P. Berghaus, M. Kubantsev, N. Reay, R. Sidwell, N. Stanton, S. Yoshida, S. Aoki, T. Hara, J. Rhee, D. Ciampa, C. Erickson, M. Graham, K. Heller, R. Rusack, R. Schwienhorst, J. Sielaff, J. Trammell, J. Wilcox, K. Hoshino, H. Jiko, M. Miyanishi, M. Komatsu, M. Nakamura, T. Nakano, K. Niwa, N. Nonaka, K. Okada, O. Sato, T. Akdogan, V. Paolone, C. Rosenfeld, A. Kulik, T. Kafka, W. Oliver, T. Patzak, and J. Schneps, "Observation of tau neutrino interactions," *Physics Letters B*, vol. 504, no. 3, pp. 218–224, 2001.

[20] W. Xu, N. Abgrall, F. T. Avignone, A. S. Barabash, F. E. Bertrand, V. Brudanin, M. Busch, M. Buuck, D. Byram, A. S. Caldwell, Y.-D. Chan, C. D. Christofferson, C. Cuesta, J. A. Detwiler, Y. Efremenko, H. Ejiri, S. R. Elliott, A. Galindo-Uribarri, G. K. Giovanetti, J. Goett, M. P. Green, J. Gruszko, I. Guinn, V. E. Guiseppe, R. Henning, E. W. Hoppe, S. Howard, M. A. Howe, B. R. Jasinski, K. J. Keeter, M. F. Kidd, S. I. Konovalov, R. T. Kouzes, B. D. LaFerriere, J. Leon, J. MacMullin, R. D. Martin, S. J. Meijer, S. Mertens, J. L. Orrell, C. O'Shaughnessy, N. R. Overman, A. W. P. Poon, D. C. Radford, J. Rager, K. Rielage, R. G. H. Robertson, E. Romero-Romero, M. C. Ronquest, B. Shanks, M. Shirchenko, N. Snyder, A. M. Suriano, D. Tedeschi, J. E. Trimble, R. L. Varner, S. Vasilyev, K. Vetter, K. Vorren, B. R. White, J. F. Wilkerson, C. Wiseman, E. Yakushev, C.-H. Yu, and V. Y. and,

"The majorana demonstrator: A search for neutrinoless double-beta decay of76ge," *Journal of Physics: Conference Series*, vol. 606, p. 012004, may 2015.

[21] G. Collaboration, M. Agostini, M. Allardt, A. M. Bakalyarov, M. Balata, I. Barabanov, N. Barros, L. Baudis, C. Bauer, N. Becerici-Schmidt, E. Bellotti, S. Belogurov, S. T. Belyaev, G. Benato, A. Bettini, L. Bezrukov, T. Bode, D. Borowicz, V. Brudanin, R. Brugnera, D. Budjáš, A. Caldwell, C. Cattadori, A. Chernogorov, V. D'Andrea, E. V. Demidova, A. di Vacri, A. Domula, E. Doroshkevich, V. Egorov, R. Falkenstein, O. Fedorova, K. Freund, N. Frodyma, A. Gangapshev, A. Garfagnini, C. Gooch, P. Grabmayr, V. Gurentsov, K. Gusev, A. Hegai, M. Heisel, S. Hemmer, G. Heusser, W. Hofmann, M. Hult, L. V. Inzhechik, J. J. Csáthy, J. Jochum, M. Junker, V. Kazalov, T. Kihm, I. V. Kirpichnikov, A. Kirsch, A. Klimenko, K. T. Knöpfle, O. Kochetov, V. N. Kornoukhov, V. V. Kuzminov, M. Laubenstein, A. Lazzaro, V. I. Lebedev, B. Lehnert, H. Y. Liao, M. Lindner, I. Lippi, A. Lubashevskiy, B. Lubsandorzhiev, G. Lutter, C. Macolino, B. Majorovits, W. Maneschg, E. Medinaceli, Y. Mi, M. Misiaszek, P. Moseev, I. Nemchenok, D. Palioselitis, K. Panas, L. Pandola, K. Pelczar, A. Pullia, S. Riboldi, N. Rumyantseva, C. Sada, M. Salathe, C. Schmitt, B. Schneider, J. Schreiner, O. Schulz, B. Schwingenheuer, S. Schönert, A.-K. Schütz, O. Selivanenko, M. Shirchenko, H. Simgen, A. Smolnikov, L. Stanco, M. Stepaniuk, C. A. Ur, L. Vanhoefer, A. A. Vasenko, A. Veresnikova, K. von Sturm, V. Wagner, M. Walter, A. Wegmann, T. Wester, H. Wilsenach, M. Wojcik, E. Yanovich, P. Zavarise, I. Zhitnikov, S. V. Zhukov, D. Zinatulina, K. Zuber, and G. Zuzel, "$2\nu\beta\beta$ decay of 76ge into excited states with GERDA phase i," *Journal of Physics G: Nuclear and Particle Physics*, vol. 42, p. 115201, sep 2015.

[22] C. Arnaboldi, F. Avignone III, J. Beeman, M. Barucci, M. Balata, C. Brofferio, C. Bucci, S. Cebrian, R. Creswick, S. Capelli, L. Carbone, O. Cremonesi, A. de Ward, E. Fiorini, H. Farach, G. Frossati, A. Giuliani, D. Giugni, P. Gorla, E. Haller, I. Irastorza, R. McDonald, A. Morales, E. Norman, P. Negri, A. Nucciotti, M. Pedretti, C. Pobes, V. Palmieri, M. Pavan, G. Pessina, S. Pirro, E. Previtali, C. Rosenfeld, A. Smith, M. Sisti, G. Ventura, M. Vanzini, and L. Zanotti, "Cuore: a cryogenic underground observatory for rare events," *Nuclear Instruments and Methods in Physics Research Section A: Accelerators, Spectrometers, Detectors and Associated Equipment*, vol. 518, no. 3, pp. 775–798, 2004.

[23] S. Andringa *et al.*, "Current Status and Future Prospects of the SNO+ Experiment," *Adv. High Energy Phys.*, vol. 2016, p. 6194250, 2016.

[24] V. Álvarez, F. I. G. M. Borges, S. Cárcel, J. M. Carmona, J. Castel, J. M. Catalá, S. Cebrián, A. Cervera, D. Chan, C. A. N. Conde, T. Dafni, T. H. V. T. Dias, J. Díaz, M. Egorov, R. Esteve, P. Evtoukhovitch, L. M. P. Fernandes, P. Ferrario, A. L. Ferreira, E. Ferrer-Ribas, E. D. C. Freitas, V. M. Gehman, A. Gil, I. Giomataris, A. Goldschmidt, H. Gómez, J. J. Gómez-Cadenas, K. González,

D. González-Díaz, R. M. Gutiérrez, J. Hauptman, J. A. H. Morata, D. C. Herrera, V. Herrero, F. J. Iguaz, I. G. Irastorza, V. Kalinnikov, D. Kiang, L. Labarga, I. Liubarsky, J. A. M. Lopes, D. Lorca, M. Losada, G. Luzón, A. Marí, J. Martín-Albo, A. Martínez, T. Miller, A. Moiseenko, F. Monrabal, C. M. B. Monteiro, J. M. Monzó, F. J. Mora, L. M. Moutinho, J. M. Vidal, H. N. da Luz, G. Navarro, M. Nebot, D. Nygren, C. A. B. Oliveira, R. Palma, J. Pérez, J. L. P. Aparicio, J. Renner, L. Ripoll, A. Rodríguez, J. Rodríguez, F. P. Santos, J. M. F. dos Santos, L. Segui, L. Serra, D. Shuman, C. Sofka, M. Sorel, J. F. Toledo, A. Tomás, J. Torrent, Z. Tsamalaidze, D. Vázquez, E. Velicheva, J. F. C. A. Veloso, J. A. Villar, R. C. Webb, T. Weber, J. White, and N. Yahlali, "NEXT-100 technical design report (TDR). executive summary," *Journal of Instrumentation*, vol. 7, pp. T06001–T06001, jun 2012.

[25] J. B. Albert, G. Anton, I. J. Arnquist, I. Badhrees, P. Barbeau, D. Beck, V. Belov, F. Bourque, J. P. Brodsky, E. Brown, T. Brunner, A. Burenkov, G. F. Cao, L. Cao, W. R. Cen, C. Chambers, S. A. Charlebois, M. Chiu, B. Cleveland, M. Coon, A. Craycraft, W. Cree, M. Côté, J. Dalmasson, T. Daniels, S. J. Daugherty, J. Daughhetee, S. Delaquis, A. Der Mesrobian-Kabakian, R. DeVoe, T. Didberidze, J. Dilling, Y. Y. Ding, M. J. Dolinski, A. Dragone, L. Fabris, W. Fairbank, J. Farine, S. Feyzbakhsh, R. Fontaine, D. Fudenberg, G. Giacomini, R. Gornea, K. Graham, G. Gratta, E. V. Hansen, D. Harris, M. Hasan, M. Heffner, E. W. Hoppe, A. House, P. Hufschmidt, M. Hughes, J. Hößl, Y. Ito, A. Iverson, A. Jamil, M. Jewell, X. S. Jiang, T. N. Johnson, S. Johnston, A. Karelin, L. J. Kaufman, R. Killick, T. Koffas, S. Kravitz, R. Krücken, A. Kuchenkov, K. S. Kumar, Y. Lan, D. S. Leonard, G. Li, S. Li, Z. Li, C. Licciardi, Y. H. Lin, R. MacLellan, T. Michel, B. Mong, D. Moore, K. Murray, R. J. Newby, Z. Ning, O. Njoya, F. Nolet, K. Odgers, A. Odian, M. Oriunno, J. L. Orrell, I. Ostrovskiy, C. T. Overman, G. S. Ortega, S. Parent, A. Piepke, A. Pocar, J.-F. Pratte, D. Qiu, V. Radeka, E. Raguzin, T. Rao, S. Rescia, F. Retiere, A. Robinson, T. Rossignol, P. C. Rowson, N. Roy, R. Saldanha, S. Sangiorgio, S. Schmidt, J. Schneider, A. Schubert, D. Sinclair, K. Skarpaas, A. K. Soma, G. St-Hilaire, V. Stekhanov, T. Stiegler, X. L. Sun, M. Tarka, J. Todd, T. Tolba, R. Tsang, T. Tsang, F. Vachon, V. Veeraraghavan, G. Visser, P. Vogel, J.-L. Vuilleumier, M. Wagenpfeil, Q. Wang, M. Weber, W. Wei, L. J. Wen, U. Wichoski, G. Wrede, S. X. Wu, W. H. Wu, L. Yang, Y.-R. Yen, O. Zeldovich, J. Zettlemoyer, X. Zhang, J. Zhao, Y. Zhou, and T. Ziegler, "Sensitivity and discovery potential of the proposed nexo experiment to neutrinoless double-β decay," *Phys. Rev. C*, vol. 97, p. 065503, Jun 2018.

[26] T. Araki, K. Eguchi, S. Enomoto, K. Furuno, K. Ichimura, H. Ikeda, K. Inoue, K. Ishihara, T. Iwamoto, T. Kawashima, Y. Kishimoto, M. Koga, Y. Koseki, T. Maeda, T. Mitsui, M. Motoki, K. Nakajima, H. Ogawa, K. Owada, J.-S. Ricol, I. Shimizu, J. Shirai, F. Suekane, A. Suzuki, K. Tada, O. Tajima, K. Tamae, Y. Tsuda, H. Watanabe, J. Busenitz, T. Classen, Z. Djurcic, G. Keefer, K. McKinny, D.-M. Mei, A. Piepke, E. Yakushev, B. E. Berger, Y. D. Chan, M. P. Decowski,

D. A. Dwyer, S. J. Freedman, Y. Fu, B. K. Fujikawa, J. Goldman, F. Gray, K. M. Heeger, K. T. Lesko, K.-B. Luk, H. Murayama, A. W. P. Poon, H. M. Steiner, L. A. Winslow, G. A. Horton-Smith, C. Mauger, R. D. McKeown, P. Vogel, C. E. Lane, T. Miletic, P. W. Gorham, G. Guillian, J. G. Learned, J. Maricic, S. Matsuno, S. Pakvasa, S. Dazeley, S. Hatakeyama, A. Rojas, R. Svoboda, B. D. Dieterle, J. Detwiler, G. Gratta, K. Ishii, N. Tolich, Y. Uchida, M. Batygov, W. Bugg, Y. Efremenko, Y. Kamyshkov, A. Kozlov, Y. Nakamura, C. R. Gould, H. J. Karwowski, D. M. Markoff, J. A. Messimore, K. Nakamura, R. M. Rohm, W. Tornow, R. Wendell, A. R. Young, M.-J. Chen, Y.-F. Wang, and F. Piquemal, "Measurement of neutrino oscillation with kamland: Evidence of spectral distortion," *Phys. Rev. Lett.*, vol. 94, p. 081801, Mar 2005.

[27] C. Giunti, M. Laveder, Y. F. Li, and H. W. Long, "Pragmatic view of short-baseline neutrino oscillations," *Phys. Rev. D*, vol. 88, p. 073008, Oct 2013.

[28] L. Wolfenstein, "Neutrino oscillations in matter," *Phys. Rev. D*, vol. 17, pp. 2369–2374, May 1978.

[29] K. Abe, J. Adam, H. Aihara, T. Akiri, C. Andreopoulos, S. Aoki, A. Ariga, S. Assylbekov, D. Autiero, M. Barbi, G. J. Barker, G. Barr, P. Bartet-Friburg, M. Bass, M. Batkiewicz, F. Bay, V. Berardi, B. E. Berger, S. Berkman, S. Bhadra, F. d. M. Blaszczyk, A. Blondel, S. Bolognesi, S. Bordoni, S. B. Boyd, D. Brailsford, A. Bravar, C. Bronner, N. Buchanan, R. G. Calland, J. Caravaca Rodríguez, S. L. Cartwright, R. Castillo, M. G. Catanesi, A. Cervera, D. Cherdack, N. Chikuma, G. Christodoulou, A. Clifton, J. Coleman, S. J. Coleman, G. Collazuol, K. Connolly, L. Cremonesi, A. Dabrowska, I. Danko, R. Das, S. Davis, P. de Perio, G. De Rosa, T. Dealtry, S. R. Dennis, C. Densham, D. Dewhurst, F. Di Lodovico, S. Di Luise, S. Dolan, O. Drapier, T. Duboyski, K. Duffy, J. Dumarchez, S. Dytman, M. Dziewiecki, S. Emery-Schrenk, A. Ereditato, L. Escudero, C. Ferchichi, T. Feusels, A. J. Finch, G. A. Fiorentini, M. Friend, Y. Fujii, Y. Fukuda, A. P. Furmanski, V. Galymov, A. Garcia, S. Giffin, C. Giganti, K. Gilje, D. Goeldi, T. Golan, M. Gonin, N. Grant, D. Gudin, D. R. Hadley, L. Haegel, A. Haesler, M. D. Haigh, P. Hamilton, D. Hansen, T. Hara, M. Hartz, T. Hasegawa, N. C. Hastings, T. Hayashino, Y. Hayato, C. Hearty, R. L. Helmer, M. Hierholzer, J. Hignight, A. Hillairet, A. Himmel, T. Hiraki, S. Hirota, J. Holeczek, S. Horikawa, F. Hosomi, K. Huang, A. K. Ichikawa, K. Ieki, M. Ieva, M. Ikeda, J. Imber, J. Insler, T. J. Irvine, T. Ishida, T. Ishii, E. Iwai, K. Iwamoto, K. Iyogi, A. Izmaylov, A. Jacob, B. Jamieson, M. Jiang, S. Johnson, J. H. Jo, P. Jonsson, C. K. Jung, M. Kabirnezhad, A. C. Kaboth, T. Kajita, H. Kakuno, J. Kameda, Y. Kanazawa, D. Karlen, I. Karpikov, T. Katori, E. Kearns, M. Khabibullin, A. Khotjantsev, D. Kielczewska, T. Kikawa, A. Kilinski, J. Kim, S. King, J. Kisiel, P. Kitching, T. Kobayashi, L. Koch, T. Koga, A. Kolaceke, A. Konaka, A. Kopylov, L. L. Kormos, A. Korzenev, Y. Koshio, W. Kropp, H. Kubo, Y. Kudenko, R. Kurjata, T. Kutter, J. Lagoda, I. Lamont, E. Larkin, M. Laveder, M. Lawe, M. Lazos,

T. Lindner, C. Lister, R. P. Litchfield, A. Longhin, J. P. Lopez, L. Ludovici, L. Magaletti, K. Mahn, M. Malek, S. Manly, A. D. Marino, J. Marteau, J. F. Martin, P. Martins, S. Martynenko, T. Maruyama, V. Matveev, K. Mavrokoridis, E. Mazzucato, M. McCarthy, N. McCauley, K. S. McFarland, C. McGrew, A. Mefodiev, C. Metelko, M. Mezzetto, P. Mijakowski, C. A. Miller, A. Minamino, O. Mineev, A. Missert, M. Miura, S. Moriyama, T. A. Mueller, A. Murakami, M. Murdoch, S. Murphy, J. Myslik, T. Nakadaira, M. Nakahata, K. G. Nakamura, K. Nakamura, S. Nakayama, T. Nakaya, K. Nakayoshi, C. Nantais, C. Nielsen, M. Nirkko, K. Nishikawa, Y. Nishimura, J. Nowak, H. M. O'Keeffe, R. Ohta, K. Okumura, T. Okusawa, W. Oryszczak, S. M. Oser, T. Ovsyannikova, R. A. Owen, Y. Oyama, V. Palladino, J. L. Palomino, V. Paolone, D. Payne, O. Perevozchikov, J. D. Perkin, Y. Petrov, L. Pickard, E. S. Pinzon Guerra, C. Pistillo, P. Plonski, E. Poplawska, B. Popov, M. Posiadala-Zezula, J.-M. Poutissou, R. Poutissou, P. Przewlocki, B. Quilain, E. Radicioni, P. N. Ratoff, M. Ravonel, M. A. M. Rayner, A. Redij, M. Reeves, E. Reinherz-Aronis, C. Riccio, P. A. Rodrigues, P. Rojas, E. Rondio, S. Roth, A. Rubbia, D. Ruterbories, A. Rychter, R. Sacco, K. Sakashita, F. Sánchez, F. Sato, E. Scantamburlo, K. Scholberg, S. Schoppmann, J. D. Schwehr, M. Scott, Y. Seiya, T. Sekiguchi, H. Sekiya, D. Sgalaberna, R. Shah, F. Shaker, D. Shaw, M. Shiozawa, S. Short, Y. Shustrov, P. Sinclair, B. Smith, M. Smy, J. T. Sobczyk, H. Sobel, M. Sorel, L. Southwell, P. Stamoulis, J. Steinmann, B. Still, Y. Suda, A. Suzuki, K. Suzuki, S. Y. Suzuki, Y. Suzuki, R. Tacik, M. Tada, S. Takahashi, A. Takeda, Y. Takeuchi, H. K. Tanaka, H. A. Tanaka, M. M. Tanaka, D. Terhorst, R. Terri, L. F. Thompson, A. Thorley, S. Tobayama, W. Toki, T. Tomura, C. Touramanis, T. Tsukamoto, M. Tzanov, Y. Uchida, A. Vacheret, M. Vagins, G. Vasseur, T. Wachala, K. Wakamatsu, C. W. Walter, D. Wark, W. Warzycha, M. O. Wascko, A. Weber, R. Wendell, R. J. Wilkes, M. J. Wilking, C. Wilkinson, Z. Williamson, J. R. Wilson, R. J. Wilson, T. Wongjirad, Y. Yamada, K. Yamamoto, C. Yanagisawa, T. Yano, S. Yen, N. Yershov, M. Yokoyama, J. Yoo, K. Yoshida, T. Yuan, M. Yu, A. Zalewska, J. Zalipska, L. Zambelli, K. Zaremba, M. Ziembicki, E. D. Zimmerman, M. Zito, and J. Żmuda, "Measurements of neutrino oscillation in appearance and disappearance channels by the t2k experiment with 6.6×10^{20} protons on target," *Phys. Rev. D*, vol. 91, p. 072010, Apr 2015.

[30] R. Patterson, "The nova experiment: status and outlook," *Nuclear Physics B - Proceedings Supplements*, vol. 235-236, pp. 151–157, 2013. The XXV International Conference on Neutrino Physics and Astrophysics.

[31] B. Abi, R. Acciarri, M. A. Acero, G. Adamov, D. Adams, M. Adinolfi, Z. Ahmad, J. Ahmed, T. Alion, S. A. Monsalve, C. Alt, J. Anderson, C. Andreopoulos, M. P. Andrews, F. Andrianala, S. Andringa, A. Ankowski, M. Antonova, S. Antusch, A. Aranda-Fernandez, A. Ariga, L. O. Arnold, M. A. Arroyave, J. Asaadi, A. Aurisano, V. Aushev, D. Autiero, F. Azfar, H. Back, J. J. Back, C. Backhouse, P. Baesso, L. Bagby, R. Bajou, S. Balasubramanian, P. Baldi, B. Bambah, F. Barao, G. Barenboim, G. J. Barker, W. Barkhouse, C. Barnes, G. Barr, J. B. Monarca,

N. Barros, J. L. Barrow, A. Bashyal, V. Basque, F. Bay, J. L. B. Alba, J. F. Beacom, E. Bechetoille, B. Behera, L. Bellantoni, G. Bellettini, V. Bellini, O. Beltramello, D. Belver, N. Benekos, F. B. Neves, J. Berger, S. Berkman, P. Bernardini, R. M. Berner, H. Berns, S. Bertolucci, M. Betancourt, Y. Bezawada, M. Bhattacharjee, B. Bhuyan, S. Biagi, J. Bian, M. Biassoni, K. Biery, B. Bilki, M. Bishai, A. Bitadze, A. Blake, B. B. Siffert, F. D. M. Blaszczyk, G. C. Blazey, E. Blucher, J. Boissevain, S. Bolognesi, T. Bolton, M. Bonesini, M. Bongrand, F. Bonini, A. Booth, C. Booth, S. Bordoni, A. Borkum, T. Boschi, N. Bostan, P. Bour, S. B. Boyd, D. Boyden, J. Bracinik, D. Braga, D. Brailsford, A. Brandt, J. Bremer, C. Brew, E. Brianne, S. J. Brice, C. Brizzolari, C. Bromberg, G. Brooijmans, J. Brooke, A. Bross, G. Brunetti, N. Buchanan, H. Budd, D. Caiulo, P. Calafiura, J. Calcutt, M. Calin, S. Calvez, E. Calvo, L. Camilleri, A. Caminata, M. Campanelli, D. Caratelli, G. Carini, B. Carlus, P. Carniti, I. C. Terrazas, H. Carranza, A. Castillo, C. Castromonte, C. Cattadori, F. Cavalier, F. Cavanna, S. Centro, G. Cerati, A. Cervelli, A. C. Villanueva, M. Chalifour, C. Chang, E. Chardonnet, A. Chatterjee, S. Chattopadhyay, J. Chaves, H. Chen, M. Chen, Y. Chen, D. Cherdack, C. Chi, S. Childress, A. Chiriacescu, K. Cho, S. Choubey, A. Christensen, D. Christian, G. Christodoulou, E. Church, P. Clarke, T. E. Coan, A. G. Cocco, J. A. B. Coelho, E. Conley, J. M. Conrad, M. Convery, L. Corwin, P. Cotte, L. Cremaldi, L. Cremonesi, J. I. Crespo-Anadón, E. Cristaldo, R. Cross, C. Cuesta, Y. Cui, D. Cussans, M. Dabrowski, H. da Motta, L. D. S. Peres, C. David, Q. David, G. S. Davies, S. Davini, J. Dawson, K. De, R. M. D. Almeida, P. Debbins, I. D. Bonis, M. P. Decowski, A. de Gouvêa, P. C. D. Holanda, I. L. D. I. Astiz, A. Deisting, P. D. Jong, A. Delbart, D. Delepine, M. Delgado, A. Dell'Acqua, P. D. Lurgio, J. R. T. de Mello Neto, D. M. DeMuth, S. Dennis, C. Densham, G. Deptuch, A. D. Roeck, V. D. Romeri, J. J. D. Vries, R. Dharmapalan, M. Dias, F. Diaz, J. S. Díaz, S. D. Domizio, L. D. Giulio, P. Ding, L. D. Noto, C. Distefano, R. Diurba, M. Diwan, Z. Djurcic, N. Dokania, M. J. Dolinski, L. Domine, D. Douglas, F. Drielsma, D. Duchesneau, K. Duffy, P. Dunne, T. Durkin, H. Duyang, O. Dvornikov, D. A. Dwyer, A. S. Dyshkant, M. Eads, D. Edmunds, J. Eisch, S. Emery, A. Ereditato, C. O. Escobar, L. E. Sanchez, J. J. Evans, E. Ewart, A. C. Ezeribe, K. Fahey, A. Falcone, C. Farnese, Y. Farzan, J. Felix, E. Fernandez-Martinez, P. F. Menendez, F. Ferraro, L. Fields, A. Filkins, F. Filthaut, R. S. Fitzpatrick, W. Flanagan, B. Fleming, R. Flight, J. Fowler, W. Fox, J. Franc, K. Francis, D. Franco, J. Freeman, J. Freestone, J. Fried, A. Friedland, S. Fuess, I. Furic, A. P. Furmanski, A. Gago, H. Gallagher, A. Gallego-Ros, N. Gallice, V. Galymov, E. Gamberini, T. Gamble, R. Gandhi, R. Gandrajula, S. Gao, D. Garcia-Gamez, M. Á. García-Peris, S. Gardiner, D. Gastler, G. Ge, B. Gelli, A. Gendotti, S. Gent, Z. Ghorbani-Moghaddam, D. Gibin, I. Gil-Botella, C. Girerd, A. K. Giri, D. Gnani, O. Gogota, M. Gold, S. Gollapinni, K. Gollwitzer, R. A. Gomes, L. V. G. Bermeo, L. S. G. Fajardo, F. Gonnella, J. A. Gonzalez-Cuevas, M. C. Goodman, O. Goodwin, S. Goswami, C. Gotti, E. Goudzovski, C. Grace, M. Graham, E. Gramellini, R. Gran, E. Granados, A. Grant, C. Grant, D. Gratieri, P. Green, S. Green, L. Greenler, M. Greenwood, J. Greer, W. C. Griffith, M. Groh, J. Grudzin-

ski, K. Grzelak, W. Gu, V. Guarino, R. Guenette, A. Guglielmi, B. Guo, K. K. Guthikonda, R. Gutierrez, P. Guzowski, M. M. Guzzo, S. Gwon, A. Habig, A. Hackenburg, H. Hadavand, R. Haenni, A. Hahn, J. Haigh, J. Haiston, T. Hamernik, P. Hamilton, J. Han, K. Harder, D. A. Harris, J. Hartnell, T. Hasegawa, R. Hatcher, E. Hazen, A. Heavey, K. M. Heeger, J. Heise, K. Hennessy, S. Henry, M. A. H. Morquecho, K. Herner, L. Hertel, A. S. Hesam, J. Hewes, A. Higuera, T. Hill, S. J. Hillier, A. Himmel, J. Hoff, C. Hohl, A. Holin, E. Hoppe, G. A. Horton-Smith, M. Hostert, A. Hourlier, B. Howard, R. Howell, J. Huang, J. Huang, J. Hugon, G. Iles, N. Ilic, A. M. Iliescu, R. Illingworth, A. Ioannisian, R. Itay, A. Izmaylov, E. James, B. Jargowsky, F. Jediny, C. Jesùs-Valls, X. Ji, L. Jiang, S. Jiménez, A. Jipa, A. Joglekar, C. Johnson, R. Johnson, B. Jones, S. Jones, C. K. Jung, T. Junk, Y. Jwa, M. Kabirnezhad, A. Kaboth, I. Kadenko, F. Kamiya, G. Karagiorgi, A. Karcher, M. Karolak, Y. Karyotakis, S. Kasai, S. P. Kasetti, L. Kashur, N. Kazaryan, E. Kearns, P. Keener, K. J. Kelly, E. Kemp, W. Ketchum, S. H. Kettell, M. Khabibullin, A. Khotjantsev, A. Khvedelidze, D. Kim, B. King, B. Kirby, M. Kirby, J. Klein, K. Koehler, L. W. Koerner, S. Kohn, P. P. Koller, M. Kordosky, T. Kosc, U. Kose, V. A. Kostelecký, K. Kothekar, F. Krennrich, I. Kreslo, Y. Kudenko, V. A. Kudryavtsev, S. Kulagin, J. Kumar, R. Kumar, C. Kuruppu, V. Kus, T. Kutter, A. Lambert, K. Lande, C. E. Lane, K. Lang, T. Langford, P. Lasorak, D. Last, C. Lastoria, A. Laundrie, A. Lawrence, I. Lazanu, R. LaZur, T. Le, J. Learned, P. LeBrun, G. L. Miotto, R. Lehnert, M. A. L. de Oliveira, M. Leitner, M. Leyton, L. Li, S. Li, S. W. Li, T. Li, Y. Li, H. Liao, C. S. Lin, S. Lin, A. Lister, B. R. Littlejohn, J. Liu, S. Lockwitz, T. Loew, M. Lokajicek, I. Lomidze, K. Long, K. Loo, D. Lorca, T. Lord, J. M. LoSecco, W. C. Louis, K. B. Luk, X. Luo, N. Lurkin, T. Lux, V. P. Luzio, D. MacFarland, A. A. Machado, P. Machado, C. T. Macias, J. R. Macier, A. Maddalena, P. Madigan, S. Magill, K. Mahn, A. Maio, J. A. Maloney, G. Mandrioli, J. Maneira, L. Manenti, S. Manly, A. Mann, K. Manolopoulos, M. M. Plata, A. Marchionni, W. Marciano, D. Marfatia, C. Mariani, J. Maricic, F. Marinho, A. D. Marino, M. Marshak, C. Marshall, J. Marshall, J. Marteau, J. Martin-Albo, N. Martinez, D. A. M. Caicedo, S. Martynenko, K. Mason, A. Mastbaum, M. Masud, S. Matsuno, J. Matthews, C. Mauger, N. Mauri, K. Mavrokoridis, R. Mazza, A. Mazzacane, E. Mazzucato, E. McCluskey, N. McConkey, K. S. McFarland, C. McGrew, A. McNab, A. Mefodiev, P. Mehta, P. Melas, M. Mellinato, O. Mena, S. Menary, H. Mendez, A. Menegolli, G. Meng, M. D. Messier, W. Metcalf, M. Mewes, H. Meyer, T. Miao, G. Michna, T. Miedema, J. Migenda, R. Milincic, W. Miller, J. Mills, C. Milne, O. Mineev, O. G. Miranda, S. Miryala, C. S. Mishra, S. R. Mishra, A. Mislivec, D. Mladenov, I. Mocioiu, K. Moffat, N. Moggi, R. Mohanta, T. A. Mohayai, N. Mokhov, J. Molina, L. M. Bueno, A. Montanari, C. Montanari, D. Montanari, L. M. M. Zetina, J. Moon, M. Mooney, A. Moor, D. Moreno, B. Morgan, C. Morris, C. Mossey, E. Motuk, C. A. Moura, J. Mousseau, W. Mu, L. Mualem, J. Mueller, M. Muether, S. Mufson, F. Muheim, A. Muir, M. Mulhearn, H. Muramatsu, S. Murphy, J. Musser, J. Nachtman, S. Nagu, M. Nalbandyan, R. Nandakumar, D. Naples, S. Narita, D. Navas-Nicolás, N. Nayak, M. Nebot-Guinot, L. Necib, K. Negishi, J. K. Nel-

son, J. Nesbit, M. Nessi, D. Newbold, M. Newcomer, D. Newhart, R. Nichol, E. Niner, K. Nishimura, A. Norman, A. Norrick, R. Northrop, P. Novella, J. A. Nowak, M. Oberling, A. O. D. Campo, A. Olivier, Y. Onel, Y. Onishchuk, J. Ott, L. Pagani, S. Pakvasa, O. Palamara, S. Palestini, J. M. Paley, M. Pallavicini, C. Palomares, E. Pantic, V. Paolone, V. Papadimitriou, R. Papaleo, A. Papanestis, S. Paramesvaran, S. Parke, Z. Parsa, M. Parvu, S. Pascoli, L. Pasqualini, J. Pasternak, J. Pater, C. Patrick, L. Patrizii, R. B. Patterson, S. J. Patton, T. Patzak, A. Paudel, B. Paulos, L. Paulucci, Z. Pavlovic, G. Pawloski, D. Payne, V. Pec, S. J. M. Peeters, Y. Penichot, E. Pennacchio, A. Penzo, O. L. G. Peres, J. Perry, D. Pershey, G. Pessina, G. Petrillo, C. Petta, R. Petti, F. Piastra, L. Pickering, F. Pietropaolo, J. Pillow, J. Pinzino, R. Plunkett, R. Poling, X. Pons, N. Poonthottathil, S. Pordes, M. Potekhin, R. Potenza, B. V. K. S. Potukuchi, J. Pozimski, M. Pozzato, S. Prakash, T. Prakash, S. Prince, G. Prior, D. Pugnere, K. Qi, X. Qian, J. L. Raaf, R. Raboanary, V. Radeka, J. Rademacker, B. Radics, A. Rafique, E. Raguzin, M. Rai, M. Rajaoalisoa, I. Rakhno, H. T. Rakotondramanana, L. Rakotondravohitra, Y. A. Ramachers, R. Rameika, M. A. R. Delgado, B. Ramson, A. Rappoldi, G. Raselli, P. Ratoff, S. Ravat, H. Razafinime, J. S. Real, B. Rebel, D. Redondo, M. Reggiani-Guzzo, T. Rehak, J. Reichenbacher, S. D. Reitzner, A. Renshaw, S. Rescia, F. Resnati, A. Reynolds, G. Riccobene, L. C. J. Rice, K. Rielage, Y. Rigaut, D. Rivera, L. Rochester, M. Roda, P. Rodrigues, M. J. R. Alonso, J. R. Rondon, A. J. Roeth, H. Rogers, S. Rosauro-Alcaraz, M. Rossella, J. Rout, S. Roy, A. Rubbia, C. Rubbia, B. Russell, J. Russell, D. Ruterbories, R. Saakyan, S. Sacerdoti, T. Safford, N. Sahu, P. Sala, N. Samios, M. C. Sanchez, D. A. Sanders, D. Sankey, S. Santana, M. Santos-Maldonado, N. Saoulidou, P. Sapienza, C. Sarasty, I. Sarcevic, G. Savage, V. Savinov, A. Scaramelli, A. Scarff, A. Scarpelli, T. Schaffer, H. Schellman, P. Schlabach, D. Schmitz, K. Scholberg, A. Schukraft, E. Segreto, J. Sensenig, I. Seong, A. Sergi, F. Sergiampietri, D. Sgalaberna, M. H. Shaevitz, S. Shafaq, M. Shamma, H. R. Sharma, R. Sharma, T. Shaw, C. Shepherd-Themistocleous, S. Shin, D. Shooltz, R. Shrock, L. Simard, N. Simos, J. Sinclair, G. Sinev, J. Singh, J. Singh, V. Singh, R. Sipos, F. W. Sippach, G. Sirri, A. Sitraka, K. Siyeon, D. Smargianaki, A. Smith, A. Smith, E. Smith, P. Smith, J. Smolik, M. Smy, P. Snopok, M. S. Nunes, H. Sobel, M. Soderberg, C. J. S. Salinas, S. Söldner-Rembold, N. Solomey, V. Solovov, W. E. Sondheim, M. Sorel, J. Soto-Oton, A. Sousa, K. Soustruznik, F. Spagliardi, M. Spanu, J. Spitz, N. J. C. Spooner, K. Spurgeon, R. Staley, M. Stancari, L. Stanco, H. M. Steiner, J. Stewart, B. Stillwell, J. Stock, F. Stocker, T. Stokes, M. Strait, T. Strauss, S. Striganov, A. Stuart, D. Summers, A. Surdo, V. Susic, L. Suter, C. M. Sutera, R. Svoboda, B. Szczerbinska, A. M. Szelc, R. Talaga, H. A. Tanaka, B. T. Oregui, A. Tapper, S. Tariq, E. Tatar, R. Tayloe, A. M. Teklu, M. Tenti, K. Terao, C. A. Ternes, F. Terranova, G. Testera, A. Thea, J. L. Thompson, C. Thorn, S. C. Timm, A. Tonazzo, M. Torti, M. Tortola, F. Tortorici, D. Totani, M. Toups, C. Touramanis, J. Trevor, W. H. Trzaska, Y. T. Tsai, Z. Tsamalaidze, K. V. Tsang, N. Tsverava, S. Tufanli, C. Tull, E. Tyley, M. Tzanov, M. A. Uchida, J. Urheim, T. Usher, M. R. Vagins, P. Vahle, G. A. Valdiviesso, E. Valencia, Z. Vallari, J. W. F. Valle,

S. Vallecorsa, R. V. Berg, R. G. V. de Water, D. V. Forero, F. Varanini, D. Vargas, G. Varner, J. Vasel, G. Vasseur, K. Vaziri, S. Ventura, A. Verdugo, S. Vergani, M. A. Vermeulen, M. Verzocchi, H. V. de Souza, C. Vignoli, C. Vilela, B. Viren, T. Vrba, T. Wachala, A. V. Waldron, M. Wallbank, H. Wang, J. Wang, Y. Wang, Y. Wang, K. Warburton, D. Warner, M. Wascko, D. Waters, A. Watson, P. Weatherly, A. Weber, M. Weber, H. Wei, A. Weinstein, D. Wenman, M. Wetstein, M. R. While, A. White, L. H. Whitehead, D. Whittington, M. J. Wilking, C. Wilkinson, Z. Williams, F. Wilson, R. J. Wilson, J. Wolcott, T. Wongjirad, K. Wood, L. Wood, E. Worcester, M. Worcester, C. Wret, W. Wu, W. Wu, Y. Xiao, G. Yang, T. Yang, N. Yershov, K. Yonehara, T. Young, B. Yu, J. Yu, R. Zaki, J. Zalesak, L. Zambelli, B. Zamorano, A. Zani, L. Zazueta, G. P. Zeller, J. Zennamo, K. Zeug, C. Zhang, M. Zhao, E. Zhivun, G. Zhu, E. D. Zimmerman, M. Zito, S. Zucchelli, J. Zuklin, V. Zutshi, and R. Zwaska, "Long-baseline neutrino oscillation physics potential of the DUNE experiment," *The European Physical Journal C*, vol. 80, oct 2020.

[32] B. Armbruster, I. M. Blair, B. A. Bodmann, N. E. Booth, G. Drexlin, J. A. Edgington, C. Eichner, K. Eitel, E. Finckh, H. Gemmeke, J. Hößl, T. Jannakos, P. Jünger, M. Kleifges, J. Kleinfeller, W. Kretschmer, R. Maschuw, C. Oehler, P. Plischke, J. Reichenbacher, C. Ruf, M. Steidl, J. Wolf, and B. Zeitnitz, "Upper limits for neutrino oscillations $\overline{\nu}_\mu \to \overline{\nu}_e$ from muon decay at rest," *Phys. Rev. D*, vol. 65, p. 112001, Jun 2002.

[33] J. E. Hill, "An alternative analysis of the lsnd neutrino oscillation search data on $\overline{\nu}_\mu \to \overline{\nu}_e$," *Phys. Rev. Lett.*, vol. 75, pp. 2654–2657, Oct 1995.

[34] M. Abbes, B. Achkar, S. Ait-Boubker, R. Aleksan, M. Avenier, G. Bagieu, J. Ballansat, C. Barnoux, R. Bazzoli, J. Berger, M. Bermond, P. Besson, M. Billault, J. Boucher, J. Bouchez, M. Bouriant, R. Brissot, B. Camberlin, J. Cavaignac, P. Charvin, J. Collot, A. Commerçon, M.-C. Cousinou, J. Cussonneau, G. Daguin-Moynot, Y. Declais, T. Desanlis, J.-M. Dubois, Y. Dufour, G. Farrache, J. Favier, Y. Gally, F. Garciaz, L. Giacobone, B. Guerre-Chaley, J.-P. Jobez, D. Jourde, E. Kajfasz, H. de Kerret, D. Koang, B. Lefièvre, F. Léon, E. Lesquoy, J. Mallet, A. Menthe, A. Metref, J. Mullié, E. Nagy, M. Obolensky, P. Ollive, A. Oriboni, H. Pessard, F. Pierre, J. Poinsignon, R. Potheau, R. Provasi, A. Stutz, J. Thion, J.-F. Thomas, and J. Wuthrick, "The bugey 3 neutrino detector," *Nuclear Instruments and Methods in Physics Research Section A: Accelerators, Spectrometers, Detectors and Associated Equipment*, vol. 374, no. 2, pp. 164–187, 1996.

[35] S. Gariazzo, C. Giunti, M. Laveder, Y. F. Li, and E. M. Zavanin, "Light sterile neutrinos," *Journal of Physics G: Nuclear and Particle Physics*, vol. 43, p. 033001, mar 2015.

[36] I. Stancu, "The miniboone detector technical design report," 4 2003.

[37] A. A. Aguilar-Arevalo, C. E. Anderson, A. O. Bazarko, S. J. Brice, B. C. Brown, L. Bugel, J. Cao, L. Coney, J. M. Conrad, D. C. Cox, A. Curioni, Z. Djurcic,

D. A. Finley, B. T. Fleming, R. Ford, F. G. Garcia, G. T. Garvey, J. Gonzales, J. Grange, C. Green, J. A. Green, T. L. Hart, E. Hawker, R. Imlay, R. A. Johnson, G. Karagiorgi, P. Kasper, T. Katori, T. Kobilarcik, I. Kourbanis, S. Koutsoliotas, E. M. Laird, S. K. Linden, J. M. Link, Y. Liu, Y. Liu, W. C. Louis, K. B. M. Mahn, W. Marsh, C. Mauger, V. T. McGary, G. McGregor, W. Metcalf, P. D. Meyers, F. Mills, G. B. Mills, J. Monroe, C. D. Moore, J. Mousseau, R. H. Nelson, P. Nienaber, J. A. Nowak, B. Osmanov, S. Ouedraogo, R. B. Patterson, Z. Pavlovic, D. Perevalov, C. C. Polly, E. Prebys, J. L. Raaf, H. Ray, B. P. Roe, A. D. Russell, V. Sandberg, R. Schirato, D. Schmitz, M. H. Shaevitz, F. C. Shoemaker, D. Smith, M. Soderberg, M. Sorel, P. Spentzouris, J. Spitz, I. Stancu, R. J. Stefanski, M. Sung, H. A. Tanaka, R. Tayloe, M. Tzanov, R. G. V. de Water, M. O. Wascko, D. H. White, M. J. Wilking, H. J. Yang, G. P. Zeller, and E. D. Zimmerman, "Measurement of ν_μ and $\overline{\nu}_\mu$ induced neutral current single π^0 production cross sections on mineral oil at $E_\nu \sim \mathcal{O}$ (1 gev)," *Phys. Rev. D*, vol. 81, p. 013005, Jan 2010.

[38] W. Hampel *et al.*, "GALLEX solar neutrino observations: Results for GALLEX IV," *Phys. Lett. B*, vol. 447, pp. 127–133, 1999.

[39] J. N. Abdurashitov, V. N. Gavrin, S. V. Girin, V. V. Gorbachev, T. V. Ibragimova, A. V. Kalikhov, N. G. Khairnasov, T. V. Knodel, V. N. Kornoukhov, I. N. Mirmov, A. A. Shikhin, E. P. Veretenkin, V. M. Vermul, V. E. Yants, G. T. Zatsepin, Y. S. Khomyakov, A. V. Zvonarev, T. J. Bowles, J. S. Nico, W. A. Teasdale, D. L. Wark, M. L. Cherry, V. N. Karaulov, V. L. Levitin, V. I. Maev, P. I. Nazarenko, V. S. Shkol'nik, N. V. Skorikov, B. T. Cleveland, T. Daily, R. Davis, K. Lande, C. K. Lee, P. S. Wildenhain, S. R. Elliott, and J. F. Wilkerson, "Measurement of the response of a gallium metal solar neutrino experiment to neutrinos from a ^{51}Cr source," *Phys. Rev. C*, vol. 59, pp. 2246–2263, Apr 1999.

[40] C. Giunti and M. Laveder, "Statistical significance of the gallium anomaly," *Phys. Rev. C*, vol. 83, p. 065504, Jun 2011.

[41] J. Kostensalo, J. Suhonen, C. Giunti, and P. Srivastava, "The gallium anomaly revisited," *Physics Letters B*, vol. 795, pp. 542–547, 2019.

[42] T. A. Mueller, D. Lhuillier, M. Fallot, A. Letourneau, S. Cormon, M. Fechner, L. Giot, T. Lasserre, J. Martino, G. Mention, A. Porta, and F. Yermia, "Improved predictions of reactor antineutrino spectra," *Phys. Rev. C*, vol. 83, p. 054615, May 2011.

[43] P. Huber, "Determination of antineutrino spectra from nuclear reactors," *Phys. Rev. C*, vol. 84, p. 024617, Aug 2011.

[44] J. Kopp, P. A. N. Machado, M. Maltoni, and T. Schwetz, "Sterile neutrino oscillations: the global picture," *Journal of High Energy Physics*, vol. 2013, may 2013.

[45] G. Mention, M. Fechner, T. Lasserre, T. A. Mueller, D. Lhuillier, M. Cribier, and A. Letourneau, "Reactor antineutrino anomaly," *Phys. Rev. D*, vol. 83, p. 073006, Apr 2011.

[46] M. Archidiacono, N. Fornengo, C. Giunti, S. Hannestad, and A. Melchiorri, "Sterile neutrinos: Cosmology versus short-baseline experiments," *Phys. Rev. D*, vol. 87, p. 125034, Jun 2013.

[47] R. A. Battye and A. Moss, "Evidence for massive neutrinos from cosmic microwave background and lensing observations," *Phys. Rev. Lett.*, vol. 112, p. 051303, Feb 2014.

[48] C. Pena-Garay and A. Serenelli, "Solar neutrinos and the solar composition problem," 2008.

[49] A. Diaz, C. Argüelles, G. Collin, J. Conrad, and M. Shaevitz, "Where are we with light sterile neutrinos?," *Physics Reports*, vol. 884, pp. 1–59, nov 2020.

[50] C. Llewellyn Smith, "Neutrino reactions at accelerator energies," *Physics Reports*, vol. 3, no. 5, pp. 261–379, 1972.

[51] J. Nieves, J. E. Amaro, and M. Valverde, "Inclusive quasielastic charged-current neutrino-nucleus reactions," *Phys. Rev. C*, vol. 70, p. 055503, Nov 2004.

[52] J. Nieves, I. Ruiz Simo, and M. Vicente Vacas, "The nucleon axial mass and the miniboone quasielastic neutrino–nucleus scattering problem," *Physics Letters B*, vol. 707, no. 1, pp. 72–75, 2012.

[53] D. Rein and L. M. Sehgal, "Neutrino-excitation of baryon resonances and single pion production," *Annals of Physics*, vol. 133, no. 1, pp. 79–153, 1981.

[54] C. Berger and L. M. Sehgal, "Lepton mass effects in single pion production by neutrinos," *Phys. Rev. D*, vol. 76, p. 113004, Dec 2007.

[55] M. S. Athar and J. G. Morfín, "Neutrino(antineutrino)–nucleus interactions in the shallow- and deep-inelastic scattering regions," *Journal of Physics G: Nuclear and Particle Physics*, vol. 48, p. 034001, jan 2021.

[56] C. Andreopoulos, A. Bell, D. Bhattacharya, F. Cavanna, J. Dobson, S. Dytman, H. Gallagher, P. Guzowski, R. Hatcher, P. Kehayias, A. Meregaglia, D. Naples, G. Pearce, A. Rubbia, M. Whalley, and T. Yang, "The genie neutrino monte carlo generator," *Nuclear Instruments and Methods in Physics Research Section A: Accelerators, Spectrometers, Detectors and Associated Equipment*, vol. 614, no. 1, pp. 87–104, 2010.

[57] T. Katori, "Meson exchange current (mec) models in neutrino interaction generators," *AIP Conference Proceedings*, vol. 1663, no. 1, p. 030001, 2015.

[58] H. Faissner, E. Frenzel, M. Grimm, T. Hansl-Kozanecka, D. Hoffmann, E. Radermacher, D. Rein, H. Reithler, U. Samm, L. Sehgal, H. Tuchscherer, H. de Witt, M. Baldo-Ceolin, F. Bobisut, H. Huzita, M. Loreti, and G. Puglierin, "Observation of neutrino and antineutrino induced coherent neutral pion production off al27," *Physics Letters B*, vol. 125, no. 2, pp. 230–236, 1983.

[59] K. Lackner, "Coherent meson production as a test for neutral weak currents of exotic space-time structure," *Nuclear Physics B*, vol. 153, pp. 526–545, 1979.

[60] D. Rein and L. M. Sehgal, "Coherent 0 production in neutrino reactions," *Nuclear Physics B*, vol. 223, no. 1, pp. 29–44, 1983.

[61] P. Marage *et al.*, "Coherent Single Pion Production by Anti-neutrino Charged Current Interactions and Test of PCAC," *Z. Phys. C*, vol. 31, pp. 191–197, 1986.

[62] S. L. Adler, "Consistency conditions on the strong interactions implied by a partially conserved axial-vector current," *Phys. Rev.*, vol. 137, pp. B1022–B1033, Feb 1965.

[63] D. Rein and L. Sehgal, "Pcac and the deficit of forward muons in + production by neutrinos," *Physics Letters B*, vol. 657, no. 4, pp. 207–209, 2007.

[64] A. Mislivec, A. Higuera, L. Aliaga, L. Bellantoni, A. Bercellie, M. Betancourt, A. Bodek, A. Bravar, H. Budd, G. F. R. Caceres V., T. Cai, D. A. Martinez Caicedo, M. F. Carneiro, E. Chavarria, H. da Motta, S. A. Dytman, G. A. Díaz, J. Felix, L. Fields, R. Fine, A. M. Gago, R. Galindo, H. Gallagher, A. Ghosh, R. Gran, D. A. Harris, K. Hurtado, D. Jena, J. Kleykamp, M. Kordosky, T. Le, E. Maher, S. Manly, W. A. Mann, C. M. Marshall, K. S. McFarland, B. Messerly, J. Miller, J. G. Morfín, J. Mousseau, D. Naples, J. K. Nelson, C. Nguyen, A. Norrick, Nuruzzaman, V. Paolone, G. N. Perdue, M. A. Ramírez, R. D. Ransome, H. Ray, L. Ren, D. Rimal, P. A. Rodrigues, D. Ruterbories, H. Schellman, C. J. Solano Salinas, M. Sultana, S. Sánchez Falero, N. Tagg, E. Valencia, M. Wospakrik, B. Yaeggy, and G. Zavala, "Measurement of total and differential cross sections of neutrino and antineutrino coherent $\pi^{\pm}$ production on carbon," *Phys. Rev. D*, vol. 97, p. 032014, Feb 2018.

[65] K. Hiraide, "A study of charged current single charged pion productions on carbon in a few-gev neutrino beam." `https://www-he.scphys.kyoto-u.ac.jp/theses/doctor/hiraide_dt.pdf`, 2009.

[66] L. Alvarez-Ruso, L. S. Geng, S. Hirenzaki, and M. J. V. Vacas, "Erratum: Charged current neutrino-induced coherent pion production [phys. rev. c 75, 055501 (2007)]," *Phys. Rev. C*, vol. 80, p. 019906, Jul 2009.

[67] L. Alvarez-Ruso, L. S. Geng, and M. J. V. Vacas, "Erratum: Neutral current coherent pion production [phys. rev. c 76, 068501 (2007)]," *Phys. Rev. C*, vol. 80, p. 029904, Aug 2009.

[68] J. N. Marx and D. R. Nygren, "The time projection chamber," *Physics Today*, vol. 31, p. 46, mar 1978.

[69] C. Rubbia, "The Liquid Argon Time Projection Chamber: A New Concept for Neutrino Detectors," 5 1977.

[70] A. Marchionni, "Status and new ideas regarding liquid argon detectors," *Annual Review of Nuclear and Particle Science*, vol. 63, pp. 269–290, oct 2013.

[71] M. Miyajima, T. Takahashi, S. Konno, T. Hamada, S. Kubota, H. Shibamura, and T. Doke, "Average energy expended per ion pair in liquid argon," *Phys. Rev. A*, vol. 9, pp. 1438–1443, Mar 1974.

[72] M. Miyajima, T. Takahashi, S. Konno, T. Hamada, S. Kubota, H. Shibamura, and T. Doke, "Erratum: Average energy expended per ion pair in liquid argon," *Phys. Rev. A*, vol. 10, pp. 1452–1452, Oct 1974.

[73] W. P. Jesse and J. Sadauskis, "Alpha-particle ionization in mixtures of the noble gases," *Phys. Rev.*, vol. 88, pp. 417–418, Oct 1952.

[74] J. Thomas and D. A. Imel, "Recombination of electron-ion pairs in liquid argon and liquid xenon," *Phys. Rev. A*, vol. 36, pp. 614–616, Jul 1987.

[75] W. Jaffé, *Alexander Baumann (1814-1857): ein Beitrag zum Wiener literarischen Vormärz und zum volkstümlichen Lied in Österreich*, vol. 42. A. Duncker, 1913.

[76] L. Onsager, "Initial recombination of ions," *Phys. Rev.*, vol. 54, pp. 554–557, Oct 1938.

[77] P. Cennini *et al.*, "Performance of a 3-ton liquid argon time projection chamber," *Nucl. Instrum. Meth. A*, vol. 345, pp. 230–243, 1994.

[78] S. Amoruso *et al.*, "Study of electron recombination in liquid argon with the ICARUS TPC," *Nucl. Instrum. Meth. A*, vol. 523, pp. 275–286, 2004.

[79] R. Acciarri, C. Adams, R. An, A. Aparicio, S. Aponte, J. Asaadi, M. Auger, N. Ayoub, L. Bagby, B. Baller, R. Barger, G. Barr, M. Bass, F. Bay, K. Biery, M. Bishai, A. Blake, V. Bocean, D. Boehnlein, V. Bogert, T. Bolton, L. Bugel, C. Callahan, L. Camilleri, D. Caratelli, B. Carls, R. C. Fernandez, F. Cavanna, S. Chappa, H. Chen, K. Chen, C.-Y. Chi, C. Chiu, E. Church, D. Cianci, G. Collin, J. Conrad, M. Convery, J. Cornele, P. Cowan, J. Crespo-Anadón, G. Crutcher, C. Darve, R. Davis, M. D. Tutto, D. Devitt, S. Duffin, S. Dytman, B. Eberly, A. Ereditato, D. Erickson, L. E. Sanchez, J. Esquivel, S. Farooq, J. Farrell, D. Featherston, B. Fleming, W. Foreman, A. Furmanski, V. Genty, M. Geynisman, D. Goeldi, B. Goff, S. Gollapinni, N. Graf, E. Gramellini, J. Green, A. Greene, H. Greenlee, T. Griffin, R. Grosso, R. Guenette, A. Hackenburg, R. Haenni, P. Hamilton, P. Healey, O. Hen, E. Henderson, J. Hewes, C. Hill, K. Hill, L. Himes, J. Ho,

G. Horton-Smith, D. Huffman, C. Ignarra, C. James, E. James, J. J. de Vries, W. Jaskierny, C.-M. Jen, L. Jiang, B. Johnson, M. Johnson, R. Johnson, B. Jones, J. Joshi, H. Jostlein, D. Kaleko, L. Kalousis, G. Karagiorgi, T. Katori, P. Kellogg, W. Ketchum, J. Kilmer, B. King, B. Kirby, M. Kirby, E. Klein, T. Kobilarcik, I. Kreslo, R. Krull, R. Kubinski, G. Lange, F. Lanni, A. Lathrop, A. Laube, W. Lee, Y. Li, D. Lissauer, A. Lister, B. Littlejohn, S. Lockwitz, D. Lorca, W. Louis, G. Lukhanin, M. Luethi, B. Lundberg, X. Luo, G. Mahler, I. Majoros, D. Makowiecki, A. Marchionni, C. Mariani, D. Markley, J. Marshall, D. M. Caicedo, K. McDonald, D. McKee, A. McLean, J. Mead, V. Meddage, T. Miceli, G. Mills, W. Miner, J. Moon, M. Mooney, C. Moore, Z. Moss, J. Mousseau, R. Murrells, D. Naples, P. Nienaber, B. Norris, N. Norton, J. Nowak, M. O'Boyle, T. Olszanowski, O. Palamara, V. Paolone, V. Papavassiliou, S. Pate, Z. Pavlovic, R. Pelkey, M. Phipps, S. Pordes, D. Porzio, G. Pulliam, X. Qian, J. Raaf, V. Radeka, A. Rafique, R. A. Rameika, B. Rebel, R. Rechenmacher, S. Rescia, L. Rochester, C. R. von Rohr, A. Ruga, B. Russell, R. Sanders, W. S. III, M. Sarychev, D. Schmitz, A. Schukraft, R. Scott, W. Seligman, M. Shaevitz, M. Shoun, J. Sinclair, W. Sippach, T. Smidt, A. Smith, E. Snider, M. Soderberg, M. Solano-Gonzalez, S. Söldner-Rembold, S. Soleti, J. Sondericker, P. Spentzouris, J. Spitz, J. S. John, T. Strauss, K. Sutton, A. Szelc, K. Taheri, N. Tagg, K. Tatum, J. Teng, K. Terao, M. Thomson, C. Thorn, J. Tillman, M. Toups, Y.-T. Tsai, S. Tufanli, T. Usher, M. Utes, R. V. de Water, C. Vendetta, S. Vergani, E. Voirin, J. Voirin, B. Viren, P. Watkins, M. Weber, T. Wester, J. Weston, D. Wickremasinghe, S. Wolbers, T. Wongjirad, K. Woodruff, K. Wu, T. Yang, B. Yu, G. Zeller, J. Zennamo, C. Zhang, and M. Zuckerbrot, "Design and construction of the MicroBooNE detector," *Journal of Instrumentation*, vol. 12, pp. P02017–P02017, feb 2017.

[80] S. Agostinelli, J. Allison, K. Amako, J. Apostolakis, H. Araujo, P. Arce, M. Asai, D. Axen, S. Banerjee, G. Barrand, F. Behner, L. Bellagamba, J. Boudreau, L. Broglia, A. Brunengo, H. Burkhardt, S. Chauvie, J. Chuma, R. Chytracek, G. Cooperman, G. Cosmo, P. Degtyarenko, A. Dell'Acqua, G. Depaola, D. Dietrich, R. Enami, A. Feliciello, C. Ferguson, H. Fesefeldt, G. Folger, F. Foppiano, A. Forti, S. Garelli, S. Giani, R. Giannitrapani, D. Gibin, J. Gómez Cadenas, I. González, G. Gracia Abril, G. Greeniaus, W. Greiner, V. Grichine, A. Grossheim, S. Guatelli, P. Gumplinger, R. Hamatsu, K. Hashimoto, H. Hasui, A. Heikkinen, A. Howard, V. Ivanchenko, A. Johnson, F. Jones, J. Kallenbach, N. Kanaya, M. Kawabata, Y. Kawabata, M. Kawaguti, S. Kelner, P. Kent, A. Kimura, T. Kodama, R. Kokoulin, M. Kossov, H. Kurashige, E. Lamanna, T. Lampén, V. Lara, V. Lefebure, F. Lei, M. Liendl, W. Lockman, F. Longo, S. Magni, M. Maire, E. Medernach, K. Minamimoto, P. Mora de Freitas, Y. Morita, K. Murakami, M. Nagamatu, R. Nartallo, P. Nieminen, T. Nishimura, K. Ohtsubo, M. Okamura, S. O'Neale, Y. Oohata, K. Paech, J. Perl, A. Pfeiffer, M. Pia, F. Ranjard, A. Rybin, S. Sadilov, E. Di Salvo, G. Santin, T. Sasaki, N. Savvas, Y. Sawada, S. Scherer, S. Sei, V. Sirotenko, D. Smith, N. Starkov, H. Stoecker, J. Sulkimo, M. Takahata, S. Tanaka, E. Tcherniaev, E. Safai Tehrani, M. Tropeano, P. Truscott, H. Uno,

L. Urban, P. Urban, M. Verderi, A. Walkden, W. Wander, H. Weber, J. Wellisch, T. Wenaus, D. Williams, D. Wright, T. Yamada, H. Yoshida, and D. Zschiesche, "Geant4—a simulation toolkit," *Nuclear Instruments and Methods in Physics Research Section A: Accelerators, Spectrometers, Detectors and Associated Equipment*, vol. 506, no. 3, pp. 250–303, 2003.

[81] E. Snider and G. Petrillo, "LArSoft: toolkit for simulation, reconstruction and analysis of liquid argon TPC neutrino detectors," *Journal of Physics: Conference Series*, vol. 898, p. 042057, oct 2017.

[82] J. Marshall and M. Thomson, "The pandora software development kit for pattern recognition," *The European Physical Journal C*, vol. 75, 06 2015.

[83] C. Adams, M. Alrashed, R. An, J. Anthony, J. Asaadi, A. Ashkenazi, M. Auger, S. Balasubramanian, B. Baller, C. Barnes, G. Barr, M. Bass, F. Bay, A. Bhat, K. Bhattacharya, M. Bishai, A. Blake, T. Bolton, L. Camilleri, D. Caratelli, I. Caro Terrazas, R. Carr, R. Castillo Fernandez, F. Cavanna, G. Cerati, Y. Chen, E. Church, D. Cianci, E. O. Cohen, G. H. Collin, J. M. Conrad, M. Convery, L. Cooper-Troendle, J. I. Crespo-Anadón, M. Del Tutto, D. Devitt, A. Diaz, K. Duffy, S. Dytman, B. Eberly, A. Ereditato, L. Escudero Sanchez, J. Esquivel, J. J. Evans, A. A. Fadeeva, R. S. Fitzpatrick, B. T. Fleming, D. Franco, A. P. Furmanski, D. Garcia-Gamez, V. Genty, D. Goeldi, S. Gollapinni, O. Goodwin, E. Gramellini, H. Greenlee, R. Grosso, R. Guenette, P. Guzowski, A. Hackenburg, P. Hamilton, O. Hen, J. Hewes, C. Hill, G. A. Horton-Smith, A. Hourlier, E.-C. Huang, C. James, J. Jan de Vries, X. Ji, L. Jiang, R. A. Johnson, J. Joshi, H. Jostlein, Y.-J. Jwa, G. Karagiorgi, W. Ketchum, B. Kirby, M. Kirby, T. Kobilarcik, I. Kreslo, I. Lepetic, Y. Li, A. Lister, B. R. Littlejohn, S. Lockwitz, D. Lorca, W. C. Louis, M. Luethi, B. Lundberg, X. Luo, A. Marchionni, S. Marcocci, C. Mariani, J. Marshall, J. Martin-Albo, D. A. Martinez Caicedo, A. Mastbaum, V. Meddage, T. Mettler, K. Mistry, A. Mogan, J. Moon, M. Mooney, C. D. Moore, J. Mousseau, M. Murphy, R. Murrells, D. Naples, P. Nienaber, J. Nowak, O. Palamara, V. Pandey, V. Paolone, A. Papadopoulou, V. Papavassiliou, S. F. Pate, Z. Pavlovic, E. Piasetzky, D. Porzio, G. Pulliam, X. Qian, J. L. Raaf, A. Rafique, L. Ren, L. Rochester, M. Ross-Lonergan, C. Rudolf von Rohr, B. Russell, G. Scanavini, D. W. Schmitz, A. Schukraft, W. Seligman, M. H. Shaevitz, R. Sharankova, J. Sinclair, A. Smith, E. L. Snider, M. Soderberg, S. Söldner-Rembold, S. R. Soleti, P. Spentzouris, J. Spitz, J. St. John, T. Strauss, K. Sutton, S. Sword-Fehlberg, A. M. Szelc, N. Tagg, W. Tang, K. Terao, M. Thomson, R. T. Thornton, M. Toups, Y.-T. Tsai, S. Tufanli, T. Usher, W. Van De Pontseele, R. G. Van de Water, B. Viren, M. Weber, H. Wei, D. A. Wickremasinghe, K. Wierman, Z. Williams, S. Wolbers, T. Wongjirad, K. Woodruff, T. Yang, G. Yarbrough, L. E. Yates, G. P. Zeller, J. Zennamo, and C. Zhang, "Deep neural network for pixel-level electromagnetic particle identification in the microboone liquid argon time projection chamber," *Phys. Rev. D*, vol. 99, p. 092001, May 2019.

[84] P. Abratenko, M. Alrashed, R. An, J. Anthony, J. Asaadi, A. Ashkenazi, S. Balasubramanian, B. Baller, C. Barnes, G. Barr, V. Basque, L. Bathe-Peters, O. B. Rodrigues, S. Berkman, A. Bhanderi, A. Bhat, M. Bishai, A. Blake, T. Bolton, L. Camilleri, D. Caratelli, I. C. Terrazas, R. C. Fernandez, F. Cavanna, G. Cerati, Y. Chen, E. Church, D. Cianci, J. Conrad, M. Convery, L. Cooper-Troendle, J. Crespo-Anadó n, M. D. Tutto, D. Devitt, R. Diurba, L. Domine, R. Dorrill, K. Duffy, S. Dytman, B. Eberly, A. Ereditato, L. E. Sanchez, J. Evans, G. F. Aguirre, R. Fitzpatrick, B. Fleming, N. Foppiani, D. Franco, A. Furmanski, D. Garcia-Gamez, S. Gardiner, G. Ge, S. Gollapinni, O. Goodwin, E. Gramellini, P. Green, H. Greenlee, W. Gu, R. Guenette, P. Guzowski, E. Hall, P. Hamilton, O. Hen, G. Horton-Smith, A. Hourlier, E. Huang, R. Itay, C. James, J. J. de Vries, X. Ji, L. Jiang, J. Jo, R. Johnson, Y.-J. Jwa, N. Kamp, G. Karagiorgi, W. Ketchum, B. Kirby, M. Kirby, T. Kobilarcik, I. Kreslo, R. LaZur, I. Lepetic, K. Li, Y. Li, B. Littlejohn, D. Lorca, W. Louis, X. Luo, A. Marchionni, S. Marcocci, C. Mariani, D. Marsden, J. Marshall, J. Martin-Albo, D. M. Caicedo, K. Mason, A. Mastbaum, N. McConkey, V. Meddage, T. Mettler, K. Miller, J. Mills, K. Mistry, A. Mogan, T. Mohayai, J. Moon, M. Mooney, A. Moor, C. Moore, J. Mousseau, M. Murphy, D. Naples, A. Navrer-Agasson, R. Neely, P. Nienaber, J. Nowak, O. Palamara, V. Paolone, A. Papadopoulou, V. Papavassiliou, S. Pate, A. Paudel, Z. Pavlovic, E. Piasetzky, I. Ponce-Pinto, D. Porzio, S. Prince, X. Qian, J. Raaf, V. Radeka, A. Rafique, M. Reggiani-Guzzo, L. Ren, L. Rochester, J. R. Rondon, H. Rogers, M. Rosenberg, M. Ross-Lonergan, B. Russell, G. Scanavini, D. Schmitz, A. Schukraft, M. Shaevitz, R. Sharankova, J. Sinclair, A. Smith, E. Snider, M. Soderberg, S. Söldner-Rembold, S. Soleti, P. Spentzouris, J. Spitz, M. Stancari, J. S. John, T. Strauss, K. Sutton, S. Sword-Fehlberg, A. Szelc, N. Tagg, W. Tang, K. Terao, C. Thorpe, M. Toups, Y.-T. Tsai, S. Tufanli, M. Uchida, T. Usher, W. V. D. Pontseele, B. Viren, M. Weber, H. Wei, Z. Williams, S. Wolbers, T. Wongjirad, M. Wospakrik, W. Wu, T. Yang, G. Yarbrough, L. Yates, H. Yu, G. Zeller, J. Zennamo, and C. Zhang, "Neutrino event selection in the MicroBooNE liquid argon time projection chamber using wire-cell 3d imaging, clustering, and charge-light matching," *Journal of Instrumentation*, vol. 16, p. P06043, jun 2021.

[85] D. Caratelli, "Neutrino identification with scintillation light in MicroBooNE," *Journal of Instrumentation*, vol. 15, p. C03023, Mar. 2020.

[86] MicroBooNE Collaboration, R. Acciarri, C. Adams, R. An, J. Anthony, J. Asaadi, M. Auger, L. Bagby, S. Balasubramanian, B. Baller, C. Barnes, G. Barr, M. Bass, F. Bay, M. Bishai, A. Blake, T. Bolton, L. Camilleri, D. Caratelli, B. Carls, R. C. Fernandez, F. Cavanna, H. Chen, E. Church, D. Cianci, E. Cohen, G. H. Collin, J. M. Conrad, M. Convery, J. I. Crespo-Anadon, M. Del Tutto, D. Devitt, S. Dytman, B. Eberly, A. Ereditato, L. E. Sanchez, J. Esquivel, A. A. Fadeeva, B. T. Fleming, W. Foreman, A. P. Furmanski, D. Garcia-Gomez, G. T. Garvey, V. Genty, D. Goeldi, S. Gollapinni, N. Graf, E. Gramellini, H. Greenlee, R. Grosso, R. Guenette, A. Hackenburg, P. Hamilton, O. Hen, J. Hewes, C. Hill, J. Ho,

G. Horton-Smith, A. Hourlier, E. C. Huang, C. James, J. J. de Vries, C. M. Jen, L. Jiang, R. A. Johnson, J. Joshi, H. Jostlein, D. Kaleko, G. Karagiorgi, W. Ketchum, B. Kirby, M. Kirby, T. Kobilarcik, I. Kreslo, A. Laube, Y. Li, A. Lister, B. R. Littlejohn, S. Lockwitz, D. Lorca, W. C. Louis, M. Luethi, B. Lundberg, X. Luo, A. Marchionni, C. Mariani, J. Marshall, D. A. M. Caicedo, V. Meddage, T. Miceli, G. B. Mills, J. Moon, M. Mooney, C. D. Moore, J. Mousseau, R. Murrells, D. Naples, P. Nienaber, J. Nowak, O. Palamara, V. Paolone, V. Papavassiliou, S. F. Pate, Z. Pavlovic, E. Piasetzky, D. Porzio, G. Pulliam, X. Qian, J. L. Raaf, A. Rafique, L. Rochester, C. R. von Rohr, B. Russell, D. W. Schmitz, A. Schukraft, W. Seligman, M. H. Shaevitz, J. Sinclair, A. Smith, E. L. Snider, M. Soderberg, S. Soldner-Rembold, S. R. Soleti, P. Spentzouris, J. Spitz, J. S. John, T. Strauss, A. M. Szelc, N. Tagg, K. Terao, M. Thomson, M. Toups, Y. T. Tsai, S. Tufanli, T. Usher, W. Van De Pontseele, R. G. Van de Water, B. Viren, M. Weber, D. A. Wickremasinghe, S. Wolbers, T. Wongjirad, K. Woodruff, T. Yang, L. Yates, G. P. Zeller, J. Zennamo, and C. Zhang, "The pandora multi-algorithm approach to automated pattern recognition of cosmic-ray muon and neutrino events in the microboone detector," 2017.

[87] P. Abratenko, R. Acciarri, C. Adams, R. An, J. Anthony, J. Asaadi, M. Auger, L. Bagby, S. Balasubramanian, B. Baller, C. Barnes, G. Barr, M. Bass, F. Bay, M. Bishai, A. Blake, T. Bolton, L. Bugel, L. Camilleri, D. Caratelli, B. Carls, R. C. Fernandez, F. Cavanna, H. Chen, E. Church, D. Cianci, E. Cohen, G. Collin, J. Conrad, M. Convery, J. Crespo-Anadón, M. D. Tutto, D. Devitt, S. Dytman, B. Eberly, A. Ereditato, L. E. Sanchez, J. Esquivel, B. Fleming, W. Foreman, A. Furmanski, D. Garcia-Gamez, G. Garvey, V. Genty, D. Goeldi, S. Gollapinni, N. Graf, E. Gramellini, H. Greenlee, R. Grosso, R. Guenette, A. Hackenburg, P. Hamilton, O. Hen, J. Hewes, C. Hill, J. Ho, G. Horton-Smith, E.-C. Huang, C. James, J. J. de Vries, C.-M. Jen, L. Jiang, R. Johnson, J. Joshi, H. Jostlein, D. Kaleko, L. Kalousis, G. Karagiorgi, W. Ketchum, B. Kirby, M. Kirby, T. Kobilarcik, I. Kreslo, A. Laube, Y. Li, A. Lister, B. Littlejohn, S. Lockwitz, D. Lorca, W. Louis, M. Luethi, B. Lundberg, X. Luo, A. Marchionni, C. Mariani, J. Marshall, D. M. Caicedo, V. Meddage, T. Miceli, G. Mills, J. Moon, M. Mooney, C. Moore, J. Mousseau, R. Murrells, D. Naples, P. Nienaber, J. Nowak, O. Palamara, V. Paolone, V. Papavassiliou, S. Pate, Z. Pavlovic, E. Piasetzky, D. Porzio, G. Pulliam, X. Qian, J. Raaf, A. Rafique, L. Rochester, C. R. von Rohr, B. Russell, D. Schmitz, A. Schukraft, W. Seligman, M. Shaevitz, J. Sinclair, E. Snider, M. Soderberg, S. Söldner-Rembold, S. Soleti, P. Spentzouris, J. Spitz, J. S. John, T. Strauss, A. Szelc, N. Tagg, K. Terao, M. Thomson, M. Toups, Y.-T. Tsai, S. Tufanli, T. Usher, R. V. de Water, B. Viren, M. Weber, D. Wickremasinghe, S. Wolbers, T. Wongjirad, K. Woodruff, T. Yang, L. Yates, G. Zeller, J. Zennamo, and C. Zhang, "Determination of muon momentum in the MicroBooNE LArTPC using an improved model of multiple coulomb scattering," *Journal of Instrumentation*, vol. 12, pp. P10010–P10010, oct 2017.

[88] A. A. Aguilar-Arevalo, C. E. Anderson, A. O. Bazarko, S. J. Brice, B. C. Brown, L. Bugel, J. Cao, L. Coney, J. M. Conrad, D. C. Cox, A. Curioni, Z. Djurcic, D. A. Finley, B. T. Fleming, R. Ford, F. G. Garcia, G. T. Garvey, C. Green, J. A. Green, T. L. Hart, E. Hawker, R. Imlay, R. A. Johnson, G. Karagiorgi, P. Kasper, T. Katori, T. Kobilarcik, I. Kourbanis, S. Koutsoliotas, E. M. Laird, S. K. Linden, J. M. Link, Y. Liu, Y. Liu, W. C. Louis, K. B. M. Mahn, W. Marsh, P. S. Martin, G. McGregor, W. Metcalf, P. D. Meyers, F. Mills, G. B. Mills, J. Monroe, C. D. Moore, R. H. Nelson, V. T. Nguyen, P. Nienaber, J. A. Nowak, S. Ouedraogo, R. B. Patterson, D. Perevalov, C. C. Polly, E. Prebys, J. L. Raaf, H. Ray, B. P. Roe, A. D. Russell, V. Sandberg, R. Schirato, D. Schmitz, M. H. Shaevitz, F. C. Shoemaker, D. Smith, M. Soderberg, M. Sorel, P. Spentzouris, I. Stancu, R. J. Stefanski, M. Sung, H. A. Tanaka, R. Tayloe, M. Tzanov, R. Van de Water, M. O. Wascko, D. H. White, M. J. Wilking, H. J. Yang, G. P. Zeller, and E. D. Zimmerman, "Neutrino flux prediction at miniboone," *Phys. Rev. D*, vol. 79, p. 072002, Apr 2009.

[89] T. M. Collaboration, "Measurement of the electronegative contaminants and drift electron lifetime in the microboone experiment." `https://microboone.fnal.gov/wp-content/uploads/MICROBOONE-NOTE-1003-PUB.pdf`, 2016.

[90] R. Acciarri, C. Adams, J. Asaadi, B. Baller, T. Bolton, C. Bromberg, F. Cavanna, E. Church, D. Edmunds, A. Ereditato, S. Farooq, B. Fleming, H. Greenlee, G. Horton-Smith, C. James, E. Klein, K. Lang, P. Laurens, D. McKee, R. Mehdiyev, B. Page, O. Palamara, K. Partyka, G. Rameika, B. Rebel, M. Soderberg, J. Spitz, A. M. Szelc, M. Weber, M. Wojcik, T. Yang, and G. P. Zeller, "A study of electron recombination using highly ionizing particles in the ArgoNeuT liquid argon TPC," *Journal of Instrumentation*, vol. 8, pp. P08005–P08005, aug 2013.

[91] P. Abratenko, R. An, J. Anthony, L. Arellano, J. Asaadi, A. Ashkenazi, S. Balasubramanian, B. Baller, C. Barnes, G. Barr, V. Basque, L. Bathe-Peters, O. B. Rodrigues, S. Berkman, A. Bhanderi, A. Bhat, M. Bishai, A. Blake, J. Book, L. Camilleri, D. Caratelli, I. C. Terrazas, F. Cavanna, G. Cerati, Y. Chen, D. Cianci, J. Conrad, M. Convery, L. Cooper-Troendle, J. Crespo-Anadón, M. D. Tutto, S. Dennis, P. Detje, A. Devitt, R. Diurba, R. Dorrill, K. Duffy, S. Dytman, B. Eberly, A. Ereditato, J. Evans, R. Fine, G. F. Aguirre, R. Fitzpatrick, B. Fleming, N. Foppiani, D. Franco, A. Furmanski, D. Garcia-Gamez, S. Gardiner, G. Ge, S. Gollapinni, O. Goodwin, E. Gramellini, P. Green, H. Greenlee, W. Gu, R. Guenette, P. Guzowski, L. Hagaman, O. Hen, C. Hilgenberg, G. Horton-Smith, A. Hourlier, R. Itay, C. James, X. Ji, L. Jiang, J. Jo, R. Johnson, Y.-J. Jwa, D. Kalra, N. Kamp, N. Kaneshige, G. Karagiorgi, W. Ketchum, M. Kirby, T. Kobilarcik, I. Kreslo, I. Lepetic, K. Li, Y. Li, K. Lin, B. Littlejohn, W. Louis, X. Luo, K. Manivannan, C. Mariani, D. Marsden, J. Marshall, D. M. Caicedo, K. Mason, A. Mastbaum, N. McConkey, V. Meddage, T. Mettler, K. Miller, J. Mills, K. Mistry, A. Mogan, T. Mohayai, J. Moon, M. Mooney, A. Moor, C. Moore, L. M. Lepin, J. Mousseau, M. Murphy, D. Naples, A. Navrer-Agasson, M. Nebot-Guinot, R. Neely, D. Newmark, J. Nowak, M. Nunes, O. Palamara, V. Paolone, A. Papadopoulou, V. Pa-

pavassiliou, S. Pate, N. Patel, A. Paudel, Z. Pavlovic, E. Piasetzky, I. Ponce-Pinto, S. Prince, X. Qian, J. Raaf, V. Radeka, A. Rafique, M. Reggiani-Guzzo, L. Ren, L. Rice, L. Rochester, J. R. Rondon, M. Rosenberg, M. Ross-Lonergan, G. Scanavini, D. Schmitz, A. Schukraft, W. Seligman, M. Shaevitz, R. Sharankova, J. Shi, J. Sinclair, A. Smith, E. Snider, M. Soderberg, S. Söldner-Rembold, P. Spentzouris, J. Spitz, M. Stancari, J. John, T. Strauss, K. Sutton, S. Sword-Fehlberg, A. Szelc, W. Tang, K. Terao, C. Thorpe, D. Totani, M. Toups, Y.-T. Tsai, M. Uchida, T. Usher, W. V. D. Pontseele, B. Viren, M. Weber, H. Wei, Z. Williams, S. Wolbers, T. Wongjirad, M. Wospakrik, K. Wresilo, N. Wright, W. Wu, E. Yandel, T. Yang, G. Yarbrough, L. Yates, H. Yu, G. Zeller, J. Zennamo, and C. Z. and, "New genie model tune for MicroBooNE," *Physical Review D*, vol. 105, apr 2022.